eCAM
Evidence-Based Complementary and Alternative Medicine

The Role of Complementary and Alternative Medicine in Regenerative Medicine

Guest Editors: Yueh-Sheng Chen, Wei-Chiang Lin, and Cheryl Miller

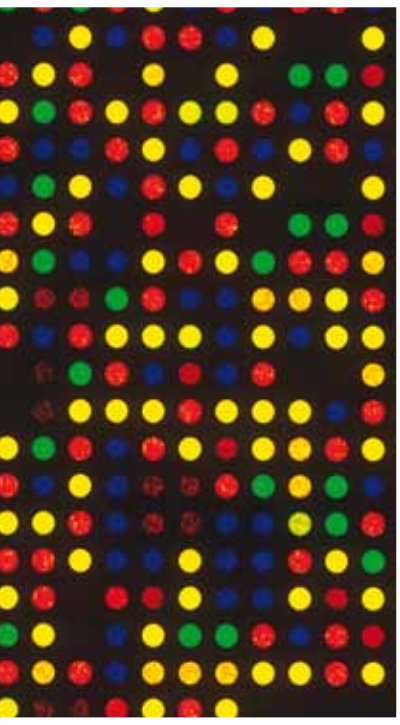

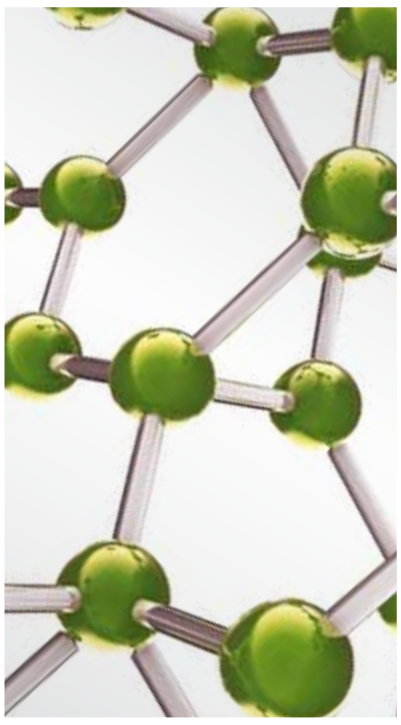


The Role of Complementary and Alternative Medicine in Regenerative Medicine

Evidence-Based Complementary and Alternative Medicine

The Role of Complementary and Alternative Medicine in Regenerative Medicine

Guest Editors: Yueh-Sheng Chen, Wei-Chiang Lin, and Cheryl Miller

Editorial Board

Contents

Hindawi Publishing Corporation
Evidence-Based Complementary and Alternative Medicine
Volume 2013, Article ID 420458, 2 pages
http://dx.doi.org/10.1155/2013/420458

Editorial

The Role of Complementary and Alternative Medicine in Regenerative Medicine

Yueh-Sheng Chen,[1] Wei-Chiang Lin,[2] and Cheryl Miller[3]

[1] *School of Chinese Medicine, China Medical University, Taichung 40402, Taiwan*
[2] *Department of Biomedical Engineering, Florida International University, Miami, FL 33174, USA*
[3] *Department of Surgery, Saint Louis University, St. Louis, MO 63103, USA*

Correspondence should be addressed to Yueh-Sheng Chen; yuehsc@mail.cmu.edu.tw

Received 1 August 2013; Accepted 1 August 2013

Regenerative medicine is the process of replacing or regenerating animal cells, tissues, or organs to restore or establish normal function. This field has the potential to solve the problem of the shortage of organs available for donation and of organ transplant rejection. Recently, application of Complementary and Alternative Medicine (CAM) as a means to accelerate the process of regeneration is a new approach. The CAM therapies offer a natural and cost-effective intervention to change the course of chronic disease and may regenerate failing organ systems.

The paper by Dr. Y.–J. Chen et al. explores how the Hepatitis B virus-encoded X regulates the expression of epidermal growth factor receptor, an important gene for growth of hepatocytes. Dr. H.–Y. Liu et al. demonstrated the regenerative potentials of deep sea water on osteogenesis, showing that deep sea water could potentially be applied in osteoporosis therapy. Dr. S. –H. Hsu et al. prepared peripheral nerve conduits containing the negatively charged *Tremella fuciformis* polysaccharide (TF) and successfully used the TF-immobilized conduits to repair a large (15 mm) critical gap defect in rats. Y. Lee et al. found that L-glutamate-induced neurotoxicity could be suppressed by the treatment with constituents of *Rhodiola rosea*, indicating that the *Rhodiola rosea* may have therapeutic potential for the treatment of inflammation and neurodegenerative disease. Dr. B.–Y. Yang et al. tried to apply percutaneous electrical stimulation to improve bone remodeling and bone healing in rats. X-ray and micro-CT showed that the electrical treatment could increase the amount of newly formed cranial bone. W. Liu et al. examined the contribution of side population (SP) cells from kidney and bone marrow to the reconstitution of kidney SP pools after ischemia-reperfusion injury (IRI). They found that following renal IRI, kidney SP cells were acutely depleted and then progressively restorated to baseline levels by both self-proliferation and extrarenal source, that is, bone marrow-derived cell homing. Dr. F. Yahya et al. showed that methanol extract of *Bauhinia purpurea* leaves could exert potential hepatoprotective activity in rats via its antioxidant activity and high phenolic content. T. Jayakumar et al. reviewed the effects of andrographolide, a major bioactive chemical constituent in *Andrographis paniculata* (Burm.f.) Nees, against cardiovascular disease, platelet activation, infertility, and NF-kB activation. Dr. H.–M. Chiang et al. showed the antioxidant activity of a *Neonauclea reticulata* water extract against ultraviolet B (UVB) irradiation in human skin fibroblast cell cultures (Hs68) by inhibiting MMP-1, -3, and -9 expressions and increasing levels of collagen activity. Dr. W.–Y. Su et al. developed a biphasic calcium phosphate cement, consisting of α-tricalcium phosphate (α-TCP) and hydroxyapatite (HAP), which is a potential biomaterial for bone repair. C. Y. Ho et al. showed that acupuncture and electroacupuncture could have positive effects on regeneration of median nerve in rats. J. Xiao et al. demonstrated that administration of garlic-derived antioxidant S-allylmercaptocysteine (SAMC) could ameliorate hepatic injury in a nonalcoholic fatty liver disease rat model. Dr. S.–C. Lee et al. investigated the effect of ferulic acid (FA) against peripheral nerve injury. They found that FA appears to promote peripheral nerve regeneration

across a 15 mm critical defect gap in the rat sciatic nerve injury model. Suppression of macrophages by FA at the site of peripheral nerve injury may contribute to its nerve growth-promoting capability.

By compiling these articles, we hope to stimulate our readers and researchers to provide continuing efforts to fully understand the effects of CAM therapies on regenerating tissues or organs.

Yueh-Sheng Chen
Wei-Chiang Lin
Cheryl Miller

Hindawi Publishing Corporation
Evidence-Based Complementary and Alternative Medicine
Volume 2013, Article ID 959261, 12 pages
http://dx.doi.org/10.1155/2013/959261

Research Article

Long-Term Regeneration and Functional Recovery of a 15mm Critical Nerve Gap Bridged by *Tremella fuciformis* Polysaccharide-Immobilized Polylactide Conduits

Shan-hui Hsu,[1,2,3] Shan-Ho Chan,[4,5] Chih-tsung Weng,[4] Shu-Hui Yang,[6] and Ching-Fen Jiang[7]

[1] *Institute of Polymer Science and Engineering, National Taiwan University, No. 1, Section 4, Roosevelt Road, Taipei 10617, Taiwan*
[2] *Rehabilitation Engineering Research Center, National Taiwan University, Taipei 10617, Taiwan*
[3] *Institute of Cellular and System Medicine, National Health Research Institutes, Miaoli County 35053, Taiwan*
[4] *Department of Chemical Engineering, National Chung Hsing University, Taichung 40227, Taiwan*
[5] *Department of Medical Imaging and Radiology, Shu-Zen Junior College of Medicine and Management, Kaohsiung 82144, Taiwan*
[6] *Fengshan Tropical Horticultural Experimental Station, Council of Agriculture, Executive Yuan, Kaohsiung 83052, Taiwan*
[7] *Department of Biomedical Engineering, I-Shou University, Kaohsiung 84001, Taiwan*

Correspondence should be addressed to Shan-hui Hsu; shhsu@ntu.edu.tw

Received 18 December 2012; Revised 17 June 2013; Accepted 27 June 2013

Academic Editor: Wei-Chiang Lin

Novel peripheral nerve conduits containing the negatively charged *Tremella fuciformis* polysaccharide (TF) were prepared, and their efficacy in bridging a critical nerve gap was evaluated. The conduits were made of poly(D,L-lactide) (PLA) with asymmetric microporous structure. TF was immobilized on the lumen surface of the nerve conduits after open air plasma activation. The TF-modified surface was characterized by the attenuated total reflection Fourier-transformed infrared spectroscopy and the scanning electron microscopy. TF modification was found to enhance the neurotrophic gene expression of C6 glioma cells in vitro. TF-modified PLA nerve conduits were tested for their ability to bridge a 15 mm gap of rat sciatic nerve. Nerve regeneration was monitored by the magnetic resonance imaging. Results showed that TF immobilization promoted the nerve connection in 6 weeks. The functional recovery in animals receiving TF-immobilized conduits was greater than in those receiving the bare conduits during an 8-month period. The degree of functional recovery reached ~90% after 8 months in the group of TF-immobilized conduits.

1. Introduction

Peripheral nerve injuries are commonly caused by trauma. The nerve would degrade in distal and renew in proximal portion. A common approach to regenerate the nerve is to bridge the defect by an autograft [1, 2], an allograft, or a biomaterial conduit. Autografts have been considered as the "clinical golden standard." However, they have unavoidable disadvantages, such as the limited availability and donor-site morbidity. Allografts on the other hand require immunosuppression therapy which causes another problem in the long term. Therefore, a biomaterial nerve conduit that helps to bridge the nerve gap is highly desired for clinical treatment. Traditional conduits are made of nonbiodegradable silicone rubber. Recent efforts have been devoted in developing biodegradable conduits [3–5] with microporosity. For example, biodegradable poly(D,L-lactide) (PLA) conduits with asymmetric microporous structure were developed to facilitate peripheral nerve regeneration [6–9]. Nerve conduits can be loaded with biologically active components such as the Schwann cells [10] or factors analogous to neurotrophic factors [11, 12] to increase the peripheral nerve regeneration.

Due to the hydrophobic nature of polymeric conduits, the method of loading for these components should be carefully designed so as not to decrease their bioactivities [13].

The bioactive herbal fruiting bodies of *Tremella fuciformis* are very popular in China as a medicinal remedy with nutritive and tonic actions for treating exhaustion. Attention has been drawn to the immunomodulating activities exhibited by their nonstarch polysaccharide components [14]. The polysaccharide fractions of *Tremella fuciformis* (TF) demonstrated pharmacological activities such as stimulation of the immune system [14, 15], antitumor [16, 17], hypoglycemic [18], hypocholesterolemic [19], anti-inflammatory [20], and antioxidant [21] effects. TF could induce human monocytes to produce interleukins and tumor necrosis factor in vitro [15, 22, 23]. In particular, TF (50–250 μg/mL) was reported to significantly enhance the neurite outgrowth of nerve growth factor-(NGF-) induced PC12 h cells [24]. So far, there has been no report regarding the efficacy of TF on the regeneration of peripheral nerve.

TF is quite available and cost efficient. Moreover, the bioactivity of TF, unlike those of neurotrophic proteins, is less likely to be influenced by combination with a polymer. In this study, TF was immobilized on the PLA conduits after the surface was activated by air plasma treatment. The ability of TF-modified conduits to bridge a large (15 mm) critical gap defect in rats was evaluated by the magnetic resonance imaging (MRI) [25], electrophysiology, histology, and dynamic walking analysis following a period of 8 months. The bioactive TF-containing conduits were demonstrated to promote peripheral nerve regeneration in short as well as in long term.

2. Materials and Methods

2.1. Fabrication of the Asymmetric Microporous PLA Substrates. Fabrication of PLA substrates followed that described in the previous literature [8]. 10% solution of PLA (Mw 180 kDa, Cargill, USA) was prepared in 1,4-dioxane (Sigma, USA) and poured in glass dish. The dish was then placed in 40% ethanol (as the nonsolvent). The asymmetric porous structure was generated as a result of the immersion-precipitation phase inversion process. The precipitated substrate was washed in water and dried in air. The asymmetric permeability of the PLA substrate was determined by the diffusion of albumin in each direction (inflow and outflow with respect to the conduit).

2.2. Immobilization of TF onto PLA by Plasma-Assisted Grafting. TF was extracted from fruiting bodies of *Tremella fuciformis* berk above 80°C for a few hours and centrifuged at 3000–5000 rpm for about 2–5 min. The residues were resuspended in water, heated, and centrifuged repeatedly to obtain more polysaccharide extracts. Extracts obtained from this process have an average molecular weight of about 3000 kDa and are readily soluble in water due to the abundant negative charge [26]. To immobilize TF on PLA, the top surface of PLA substrate was first activated by open air plasma (Plasmatreat, Steinhagen, Germany). The parameters (power, pressure, distance, and scan rate) of plasma treatment are supplied in the Supplementary Information (see Figure 1S available online at http://dx.doi.org/10.1155/2013/959261) The TF-grafted PLA substrate prepared from the above process was abbreviated as "PLA/TF."

The water contact angle of the modified surface was measured in the air with a static contact angle analyzer (FTA-1000 B, First Ten Angstrom Company, USA). TF grafting was confirmed by a Fourier-transformed infrared (IR) spectrometer (Perkin, Paragon-500) equipped with an attenuated total reflection unit (ATR-IR). The grafted amount was determined by gravimetry, that is, measuring the weight increase using a high sensitivity balance (Sartorius, BP211D, Germany). The surface as well as the cross-section was examined by a scanning electron microscope (SEM; ABT-150S, Topcon, USA). The samples were weighed and analyzed again by ATR-IR after placed in phosphate buffered saline (PBS) at 37°C for 2 and 4 weeks.

2.3. Conditions of PLA/TF by Plasma-Assisted Grafting. The plasma source was the compressed dried air (21% oxygen and 79% nitrogen) ejected from a rotating nozzle. To optimize the plasma activation process, parameters such as the plasma power, distance, and operating speed of the nozzle had to be adjusted. For the current experiment, the optimized parameters were air pressure 2.5 kg/cm^2, plasma power 1000 W, distance 10 mm, and speed 15 m/min. Following plasma activation, the PLA substrate was immersed in 1% TF aqueous solution at 37°C for 1 h. The substrate was then rinsed with distilled water, washed extensively in an ultrasonic bath for 30 min, air-dried, and stored in a desiccator.

2.4. Cell Culture and Gene Expression. Rat C6 glioma cells (BCRC-60046; Bioresources Collection and Research and Research Center, Hsinchu, Taiwan) were employed for in vitro tests of the materials. C6 glioma cells were cultured in Dubeleco's modified Eagle medium (DMEM) supplemented with 44 mmol/L $NaHCO_3$, 10% fetal bioactive serum, 50 U/mL streptomycin-penicillin, and 1% sodium pyruvate. Before seeding the cells, PLA and PLA/TF substrates were sterilized by 70% alcohol, rinsed with phosphate buffered saline (PBS), and placed into 24-well culture plates. C6 glioma cells at a density of 1×10^4 per well were seeded. The cells were trypsinized at 24 h and 72 h, and the number was counted with a hemocytometer under an inverted microscope. A blank well (tissue culture polystyrene, TCP) was used as the control. Cells were analyzed for their neurotrophic gene expression. Total RNA was extracted from cells after 72 h. Trizol reagent (Invitrogen) was added after the cells were trypsinized. 5 μg of total RNA was reverse-transcribed with the first-strand cDNA synthesis kit (Fermentas, Germany) following the manufacturer's instructions. Polymerase chain reaction was performed in a 25 μL reaction volume containing 1 μL of the cDNA, 0.5 μL, and 10 μmol/L of each primer and 5 μL of 5x PCR Master Mix buffer (Gene Mark, Taiwan). Polymerase chain reaction was carried out in a GeneAmp PCR system 2700 thermal cycler (Applied Biosystems, ABI). The cycling parameters of cDNA were 35 cycles of 94°C for 30 seconds, 55°C for 30 seconds, and 72°C for 30 seconds, followed by a final extension at 72°C for 7 minutes. β-actin was used to confirm fidelity of the PCR reaction and

as an internal control for semiquantitative analysis. The amplified products were analyzed by electrophoresis on 1.5% agarose-TAE [10 mmol/L Tris (pH 7.5), 5.7% glacial acetic acid, and 1 mmol/L EDTA] gels and visualized by ethidium bromide staining. The image was recorded by an image analyzer (BioDoc-It System, UVP, Upland, CA, USA), and the intensities of the bands were quantified by the LabWorks software. The optimized plasma parameters for PLA/TF were determined from the cell studies.

2.5. Animal Implantation and Evaluation. Flat substrates were rolled into conduits by the assistance of a 1.5 mm diameter mandrel. The edges were adhered tightly by a small amount of 1,4-dioxane. After rolling, the top surface of the substrates became the internal surface of the conduits. The conduits were dried under vacuum overnight to remove any residual solvent. They were checked for the dimensional fidelity and sectioned into 17 mm segments before implantation.

Forty male Sprague-Dawley rats weighing 300–350 g were used for in vivo studies. They were divided into two experimental groups. Each experimental group received PLA or PLA/TF conduits (~1.53 mm ID, ~0.21 mm in wall thickness, and ~17 mm long). The conduits were sterilized by 70% alcohol for 20 min and washed by PBS for 5 min before surgery.

Animals were deeply anesthetized with isoflurane (Halocarbon, USA) throughout the surgical procedures. Surgery was conducted on the left hind leg for each rat under aseptic conditions. After an incision had been made in the skin, the sciatic nerve was exposed by making a muscle splitting incision. A 15 mm nerve segment was excised with microscissors. The conduit (17 mm) was interposed into the 15 mm nerve defect, respectively. (The proximal nerve was anchored in the conduit by 7-0 nylon microsutures. The distal end was then sutured into the other end of the conduit. Nerve stumps at both ends were sutured into the conduit to a length of approximately 1 mm. The wound was then closed in layers using 3-0 Dexon sutures. The animals were housed in temperature-(25°C) and humidity-(45%) controlled rooms with 12 h light cycles. All procedures followed the ethical guidelines and were approved by the Animal Care and Use Committee of the university. While 15 mm gap is considered as a critical gap, results from smaller (10 mm) nerve gap (6-week) studies are included in the Supplementary Information.

Peripheral nerve regeneration across the gap defect was monitored by the MRI technique for a long term (at 2, 4, 6, and 8 months). MRI examination was performed for 30 min. Animals were anesthetized by and maintained with isoflurane (Halocarbon, USA) throughout the imaging procedures. The MRI equipment was a 1.5 Tesla Sonata system from Simens (Germany). The image employed a 5-inch surface coil (small loop coil) to acquire the images of the transected sciatic nerve. The parameters of MRI were T1 weighted images (T1WI), T2 weighted image (T1WI), and T2 weighted short time image of inversion recovery (STIR). The time parameters were repeat time (TR) and echo time (TE). The field size was 80 mm × 80 mm. The matrix resolution was 256 × 256 pixels. All experimental parameters of MRI should be refined by different animal sizes.

Walking track analysis was performed on all animals weekly up to 2 months and every 2 months before the animals were sacrificed. Preoperatively, the animals were trained to walk down a 150 × 8 cm track in a darkened enclosure. The sciatic functional index (SFI) that assessed the functional muscle reinnervation was calculated based on the walking track analysis, by the equation SFI = −38.3(PLF) + 109.5(TSF) + 13.3(ITF) − 8.8, where PLF (print length function) = (experimental PL − normal PL)/normal PL, TSF (toe spread function) = (experimental TS − normal TS)/normal TS (1st to 5th toes), and ITF (intermedian toe spread function) = (experimental IT − normal IT)/normal IT (2nd to 4th toes) [27, 28].

The walking behavior of rats was recorded as videos and rats were trained to walk down the 150 × 8 cm track to perform the video recordings. The walking behavior was analyzed by a semiautomation program using MATLAB 7.4.0. In the analysis, the video with the mpg/mpeg format was converted into a sequence of static images with the frames rate of frame per second. In walking behavior analysis, vector $\vec{a}$ was defined manually to select two points horizontal to the ground in the first frame. Vector $\vec{a}$ was originated from the rat ankle. Vector $\vec{a}$ had consistent directions in the rest of the frames steadily. Another vector $\vec{b}$ was defined as the central axis of the lower limb of the rat. Vector $\vec{b}$ was varied with the swing of the lower limb. The motion angle θ between the two vectors $\vec{a}$ and $\vec{b}$ was calculated based on the equation $\theta = \cos^{-1}(\vec{a} \cdot \vec{b})/(|\vec{a}| \cdot |\vec{b}|)$, $0^\circ \leq \theta \leq 180^\circ$. A completed swing cycle composed the changes of θ corresponding to the movement of the lower limb. A map indicating the different variations of θ versus time in terms of frame numbers could be used to evaluate the function of the limb. The extension range of the lower limb was denoted as Θ and defined as the absolute value of the gap between the maximum and the minimum of the θ during a swing cycle. The two parameters, Θ and the average θ, obtained from each map may be used to evaluate the degree of recovery of the limb after implantation of the conduit. Comparison was made to the control side (right side) of the same rat at 2, 4, 6, and 8 months.

Electrophysiological evaluation was performed before animals were sacrificed. Under anesthesia with chloral hydrate (360 mg/kg, intraperitoneal injection), the left sciatic nerve interposed by the conduit was carefully reexposed and dissected from surrounding tissues. The recording needle electrodes were placed in the anterior tibial muscle and the distal of nerve conduit. The sciatic nerve was stimulated by a pair of needle electrodes, which was placed directly on the proximal of nerve conduit and connected with DC electrical stimulator (PowerLab ML866, AD Instrument, Australia). The nerve stimulation parameter used was 1 to 10 mV and 0.2 ms duration. The ground electrode was placed in surrounding muscle tissues to remove conduction of stimulation through muscle tissues. The compound action potentials (CAPs) were recorded by a software (Scope for Windows, AD Instrument, Australia). Based on the nerve-to-nerve distances and time (from stimulation point to the maximum pulse amplitude), the nerve conduction velocity (NCV) for each group of conduits was determined.

Animals were euthanatized by CO_2 overdose treatment after 2, 4, 6, or 8 months. The implanted grafts were harvested and immediately fixed in cold buffered 3% glutaraldehyde solution. After two days, the nerve conduits were cut open longitudinally. The specimens were then washed in PBS, postfixed in 1% osmium tetroxide (Polysciences, USA), dehydrated in a graded series of ethanol solutions, and finally embedded. The embedded samples were cut to 3 μm thickness and stained with 1% toluidine blue, which did not stain PLA. All nerve sections were observed under the optical microscope, and photographs were taken using a digital camera (Nikon H666L, Japan). The cross-sectional area of regenerated nerve as well as the numbers of individual myelinated axons and blood vessels in the regenerated tissue at the midconduit was quantified by an image analysis system (Image-Pro Lite, Media Cybernetics, USA) [8].

2.6. Statistical Analysis. Forty rats underwent nerve conduit implantation. Ten rats were evaluated by MRI and sacrificed at 8 months. The average diameters of the regenerated nerve based on axial MR images at the midconduit were the mean values from the rats. The walking analysis and electrophysiological measurement were performed at 2, 4, 6, and 8 months ($n = 5$ for each group, the normal side as the control) before sacrifice for histological analysis. The results obtained from multiple samples were expressed as mean ± standard deviation. Statistical differences were analyzed by one-way analysis of variance (ANOVA). $P < 0.05$ was considered as statistically significant.

3. Results

3.1. Analysis of PLA/TF. To confirm that TF was successfully immobilized on the surface of PLA, physicochemical characterization was performed. The water contact angle of the original PLA was 76° and was reduced to 54° in PLA/TF, suggesting that the hydrophilic TF was immobilized on the surface. The corresponding ATR-FTIR spectra are shown in Figure 1(a). The original PLA surface did not show obvious absorption bands near 3394 cm^{-1} or 1751 cm^{-1}. These bands were the characteristic absorption bands in TF. The surface of TF-modified PLA (PLA/TF) also demonstrated these bands, indicating that TF was successfully immobilized on PLA. Figure 1(a) also showed that the characteristic absorption bands near 3394 and 1751 cm^{-1} decreased to about one half when the TF-immobilized PLA substrate was placed in PBS for 2 weeks. These bands were small but remained visible after 4 weeks. The grafted amount of TF on PLA was 237.67 ± 40.0 $\mu g/cm^2$, based on the weight analysis. The amount of TF on the surface was 163.21 ± 32 $\mu g/cm^2$ after being placed in PBS for 2 weeks and was not detectable after 4 weeks.

The SEM images of the cross-section of the PLA/TF substrate are shown in Figure 1(b). The skin layer and the asymmetric porous structure were well kept in the modified substrate (Figure 1(b)). These changes did not influence the characteristic asymmetric permeability of the original PLA substrate (Figure 1(c)). This was important because permeability of the conduit could also affect the nerve repair.

Table 1: The average diameter of regenerative nerve in PLA/TF and PLA conduits determined from the axial views of MRI at 2, 4, 6, and 8 months.

Months	Nerve diameter (mm)	
	PLA/TF	PLA
2	0.4 ± 0.08	0.3 ± 0.10
4	1.0 ± 0.12*	0.7 ± 0.12
6	1.3 ± 0.16*	1.0 ± 0.08
8	2.1 ± 0.1*	1.5 ± 0.14

*$P < 0.05$ between PLA/TF and PLA.

3.2. Effect of TF Modification on Cell Proliferation and Gene Expression. The cytocompatibility was tested in vitro by analyzing the proliferation and gene expression of both C6 glioma cells on different materials. The results are shown in Figure 2. The attachment and proliferation of C6 cells on PLA and on PLA/TF were similar (Figure 2(a)). The expression of BDNF, GDNF, and NGF genes of C6 cells on PLA/TF was upregulated compared with that on PLA (Figure 2(b)). These results indicated that PLA/TF was superior to the bare PLA in promoting the neurotrophic gene expression of C6 glioma cells.

3.3. In Vivo Nerve Regeneration across the 15 mm Gap Defect. MR images taken at different postimplantation periods are shown in Figure 3. Based on the MR sagittal views (Figure 3(A)), the sciatic nerve was at about 8 mm below the femur bone. The nerve conduit was at about 10 mm deep inside the rat body. The conduit was parallel to the femur bone. The blood vessels were observed near the distal end of the nerve conduit (indicated by the shortest arrows in Figure 3(A)). The regenerated nerves were very thin at 4 months in both PLA and PLA/TF groups (Figure 3A (a-b)). The size (diameter) of the regenerated nerve increased at 6 and 8 months (Figure 3A (c–f)). At this time, the regenerated nerve was thicker on both ends and still thin in the midsection. Based on the MR axial views (Figure 3(B)), the newly regenerated nerve inside all PLA and PLA/TF conduits was connected before 2 months (Figure 3B (a-b)). Among the five rats followed with MRI in the PLA group, the nerve of two rats was connected between 4 and 6 weeks, that is, connection not observed at 4 weeks but observed at 6 weeks. The nerve of the other three rats was connected between 6 and 8 weeks (connected nerve visualized at 8 weeks). In the PLA/TF group, the nerve in all rats was successfully connected between 4 and 6 weeks (connected nerve visualized at 6 weeks). Therefore, the success rate of nerve connection at 6 weeks was 40% for PLA conduits but was 100% for PLA/TF conduits. The newly regenerated nerves inside the conduits grew gradually thicker after connection. The average diameter of regenerative nerve in PLA/TF conduits was always greater than that in PLA conduits at each time point, as shown in Table 1.

SFI data from 1 week to 8 months are shown in Figure 4(a). The value of SFI increased for both PLA and PLA/TF groups during this period. Rats receiving PLA/TF conduits showed greater SFI in average than those receiving

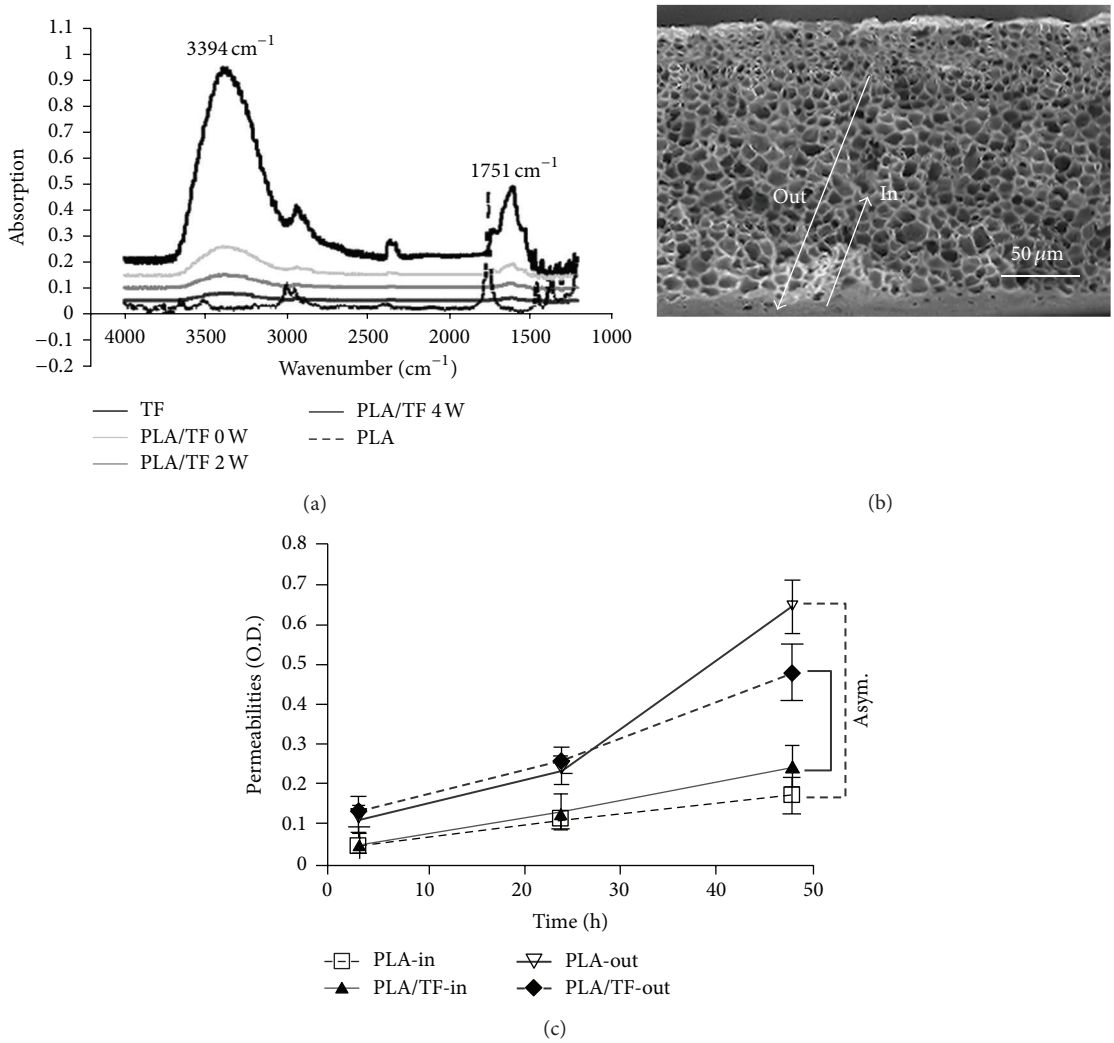

Figure 1: (a) ATR-IR spectra of PLA surface immobilized with TF (PLA/TF) after air plasma activation. The original spectrum is marked as "0 wk," while spectra marked "2 wk" and "4 wk" indicate those obtained after the sample was put in PBS for 2 and 4 weeks. (b) SEM image for the cross-section of TF modified PLA. (c) The permeabilities of the original and TF-immobilized PLA substrates are shown.

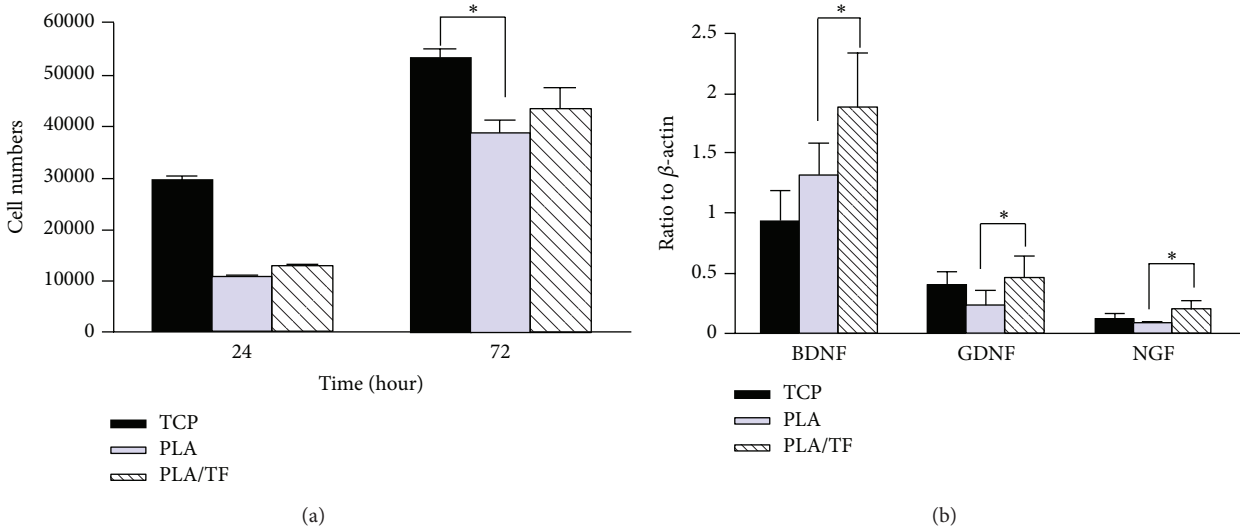

Figure 2: The effect of TF immobilization on the (a) proliferation and (b) gene expression of C6 cells. The gene expression was analyzed at 72 h. $^{*}P < 0.05$, $n = 3$. PLA/TF: TF-immobilized PLA; TCP: tissue culture polystyrene (blank control).

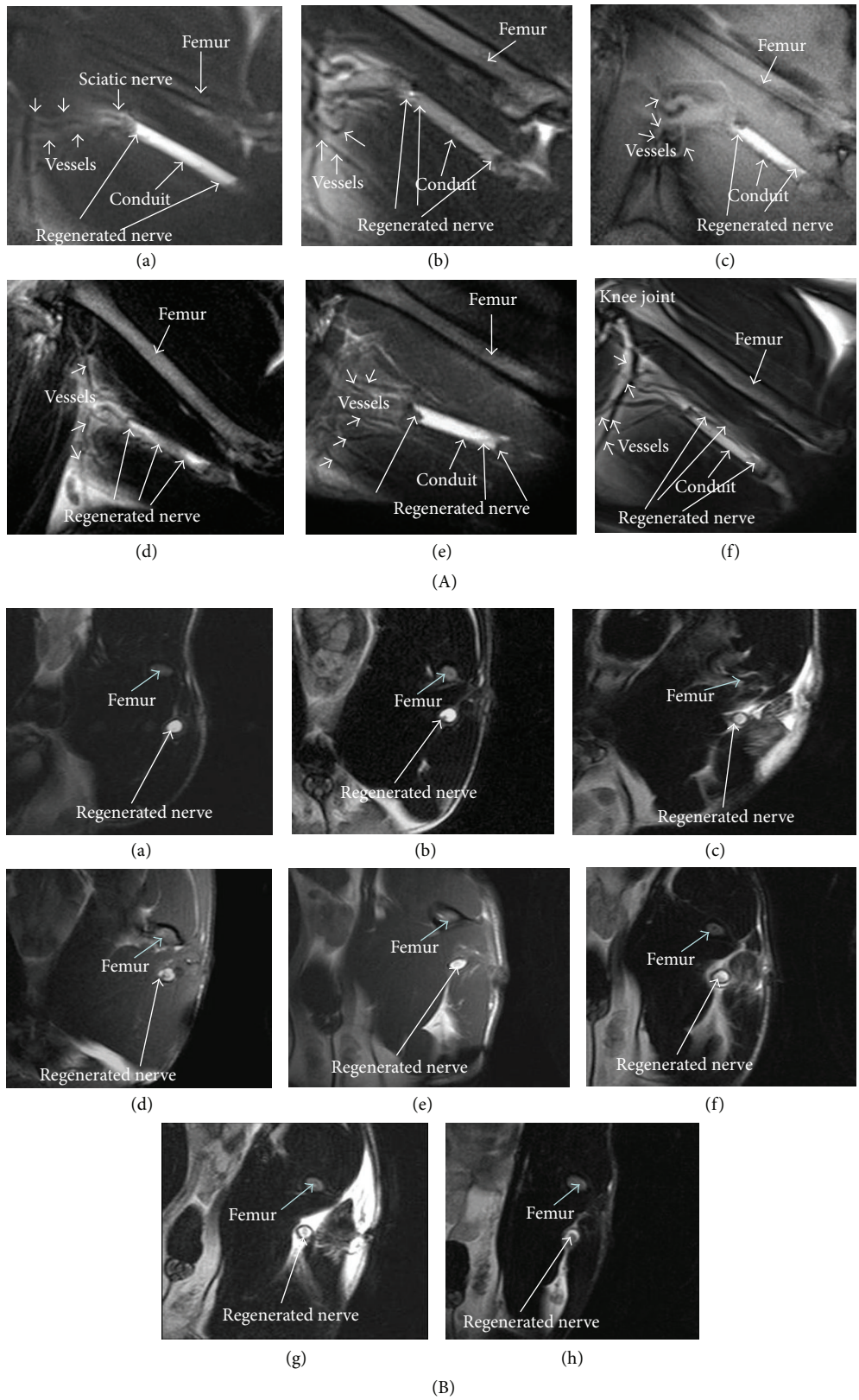

Figure 3: MR images for the regenerated nerve after transection (15 mm gap). (A) The sagittal views at (a), (b) 4 months, (c), (d) 6 months, and (e), (f) 8 months, for rats receiving PLA (a), (c), (e) or PLA/TF (b), (d), (f) conduits. (B) The axial views at (a), (b) 2 months, (c), (d) 4 months, (e), (f) 6 months, and (g), (h) 8 months, for rats receiving PLA (a), (c), (e), (g) or PLA/TF (b), (d), (f), (g) conduits. The regenerated nerve was indicated by long white arrows in the images. The axial views (B) were clearer than the sagittal views (A) in identifying the newly regenerated nerve.

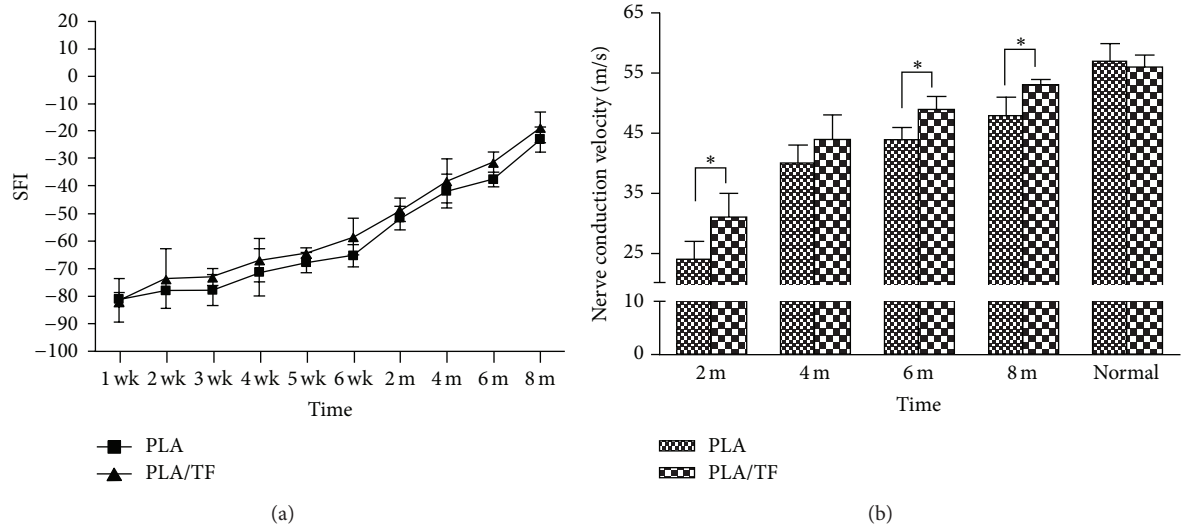

Figure 4: (a) SFI based on walking track analysis for rats receiving PLA and PLA/TF conduits during a period from 1 week (1 wk) to 8 months (8 m). (b) NCV obtained from electrophysiology for PLA and PLA/TF groups at different periods.

PLA conduits during the whole period though statistical significance could not be obtained. The values of nerve conduction velocity (NCV) are shown in Figure 4(b). For the normal rat sciatic nerve, NCV was about 55 ± 3 m/s ($n = 10$). After nerve connection (2 months), the value was small for the newly regenerated nerve but increased with the time. The NCV of the regenerated nerve in the PLA/TF group was significantly larger than that in the PLA group at 2, 6, and 8 months ($n = 5$ each). The functional recovery of rats at 2 months based on the data of NCV was about 42% for the group of PLA and about 55% for the group of PLA/TF. After 8 months, the functional recovery based on NCV was 84% for the group of PLA and 93% for the group of PLA/TF.

Results from dynamic walking analysis are shown in Figure 5. During a swing, the motion angle (θ) was recorded. The typical curves of θ versus frames at 4 months (for PLA/TF) and the normal limb (control side) are shown in Figures 5(c) and 5(d). The extension angle (Θ) during a swing cycle was calculated, listed with panels C-D, and summarized in Figure 5(e) ($n = 5$). The average θ is shown in Figure 5(f) ($n = 5$). It was obvious that the mean values of Θ and average θ increased from 1 week to 8 months for both PLA and PLA/TF groups. At 4, 6, and 8 months, the PLA/TF group had greater Θ as well as greater average θ values than the PLA group ($P < 0.05$, with one exception of Θ at 6 months where $P = 0.07$). The percent functional recovery of rats based on the restoration of Θ (versus normal) was 65% at 4 months, 77% at 6 months, and 90% at 8 months for the PLA/TF group, compared with 56% at 4 months, 72% at 6 months, and 81% at 8 months for the PLA group. These values were very close to those obtained based on the restoration of average θ (67% at 4 months, 80% at 6 months, and 91% at 8 months for the PLA/TF groups; 56% at 4 months, 72% at 6 months, and 81% at 8 months for the PLA group). Overall in this 15 mm critical gap rat sciatic nerve model, the PLA/TF group was superior to the PLA group in the long-term rehabilitation of walking function.

Histological results of the regenerated nerve in Figure 6 showed formations of blood vessels and myelins in both PLA and PLA/TF groups at 4, 6, and 8 months. All subjects had successful connection ($n = 5$ each group). At 4 months, the myelins in the regenerated nerve were very thin. The outer contour of the regenerated nerve was irregular in shape, especially in the PLA group (Figure 6(a)). The morphology was different from the intact and homogeneous morphology of myelins in the normal sciatic nerve. The accumulation of fat tissue around the regenerated nerve was observed at 4 and 6 months but was less frequent at 8 months in both groups.

From 4 to 8 months, both PLA and PLA/TF groups showed improvement in the sizes of blood vessels and myelins (Figure 6(b)). The myelins were larger in size (i.e. better morphology) in the group of PLA/TF than those in the group of PLA, especially at 4 and 8 months (Figure 6(b)). Blood vessels were larger and more abundant in the group of PLA/TF, and multierythrocytes could be clearly visualized at 8 months (Figure 6(b)). At the same time, the myelins in the group of PLA/TF formed self-organized bundles, as denoted by the dotted boxes in the image. This phenomenon was not as obvious in the group of PLA. Quantitative analyses of the histology revealed a significantly larger area of regenerated nerve as well as greater numbers of myelinated axons and blood vessels in the groups of PLA/TF, as compared to PLA, during a period of 8 months (Figure 7). These results indicated that TF immobilization enhanced peripheral nerve regeneration over a critical gap defect.

4. Discussion

This study employed a very convenient strategy to immobilize TF on the nerve conduits by treatment with air plasma. When PLA surface was activated by air plasma, the oxygen and nitrogen in air plasma could attack the weak bonds on the surface of PLA to form free radicals. Since TF was a hydrophilic material, the water contact angle of the PLA

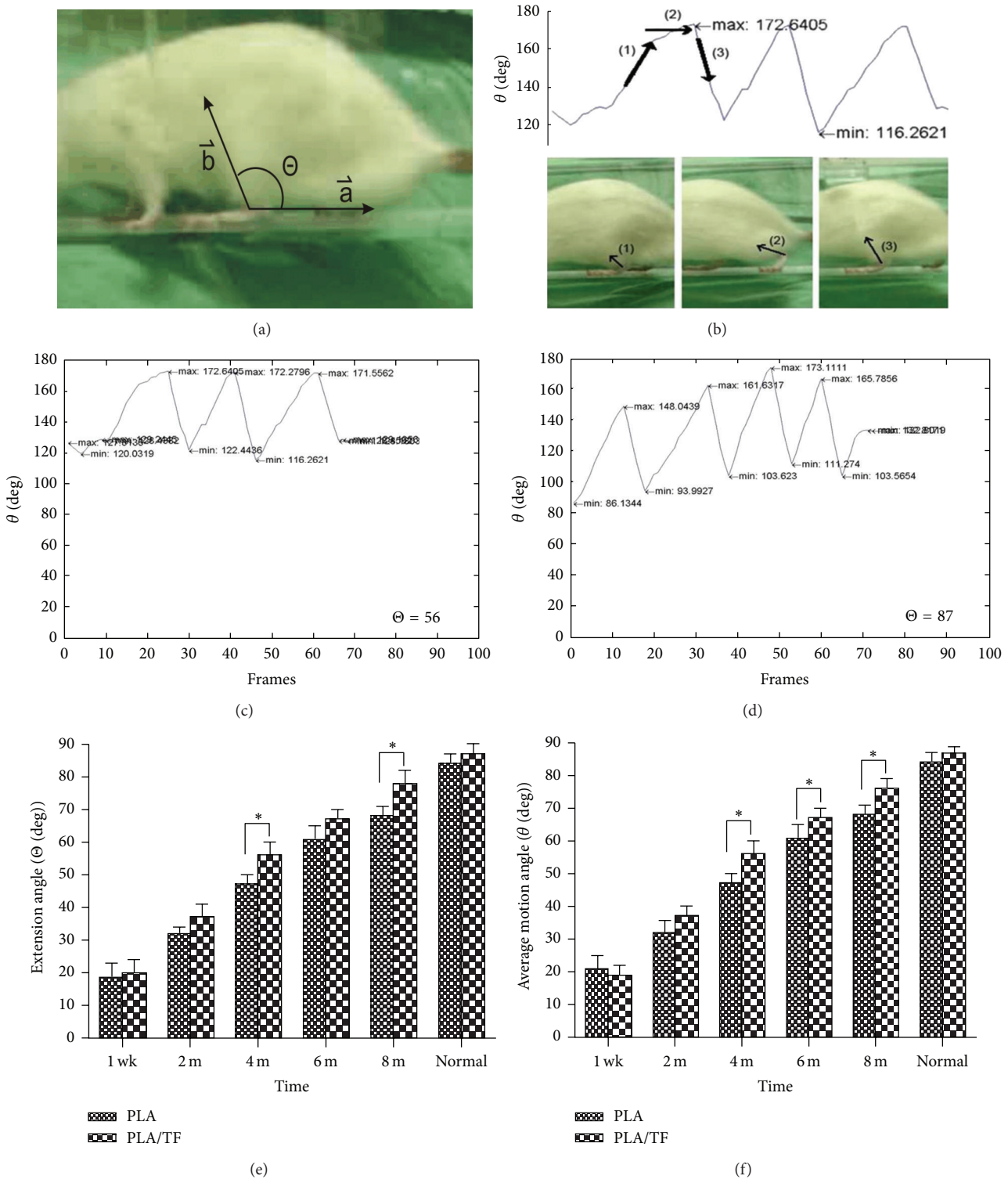

Figure 5: Dynamic walking analysis for rats with 15 mm transectional gap bridged by the conduit. (a) The motion angle (θ) was defined as the angle between vectors $\vec{a}$ and $\vec{b}$. (b) During a swing (from (1) and (2) to (3)), θ was recorded. Typical curves of θ versus frames are demonstrated for (c) the PLA/TF group at 4 months and (d) the control normal side. (e) shows the mean extension range (Θ) for PLA and PLA/TF groups at different time periods. (f) shows the mean values of average θ for PLA and PLA/TF groups at different time periods.

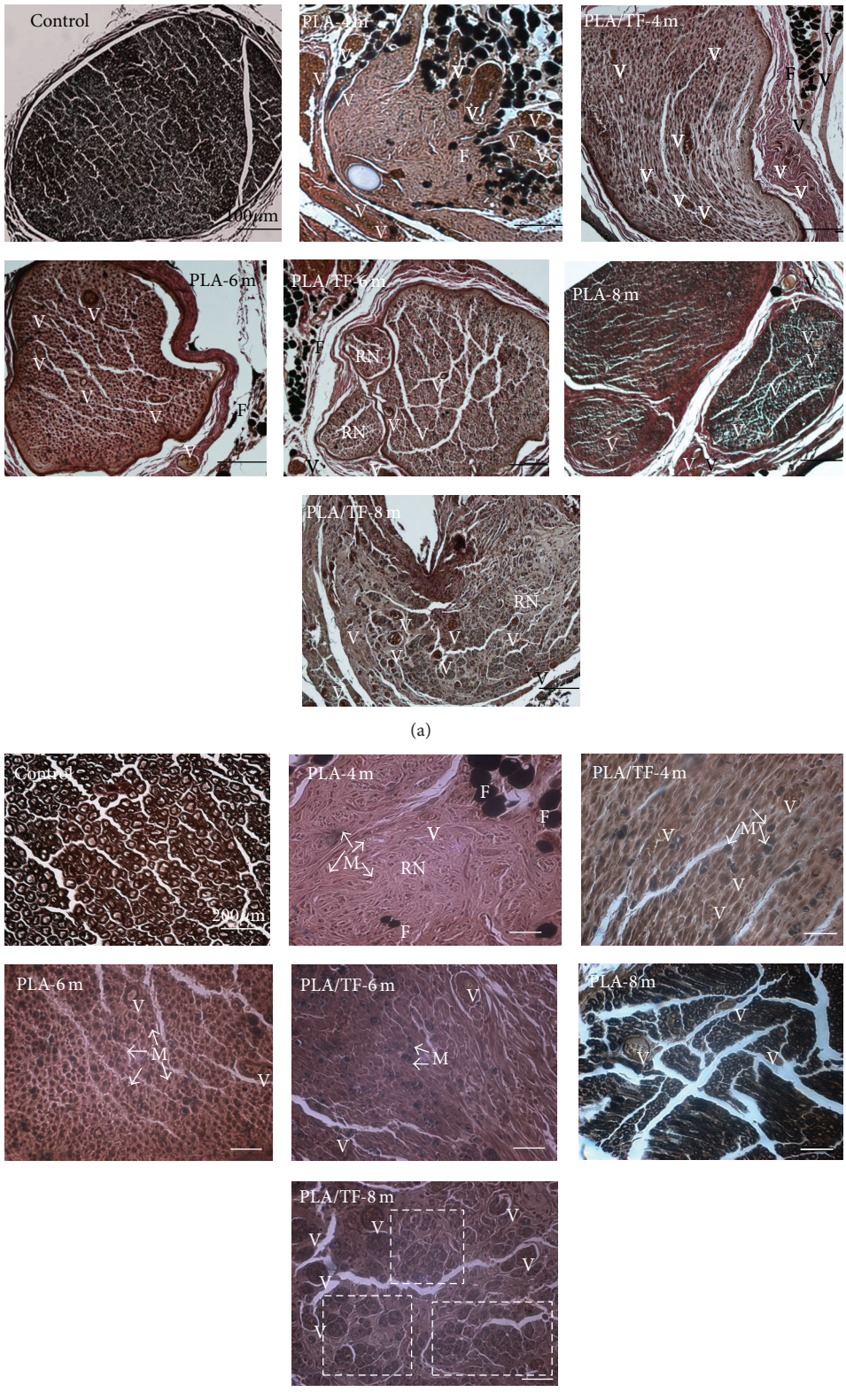

Figure 6: Histology for the nerve sections at the midconduit of PLA and PLA/TF conduits (15 mm gap) after 4, 6, and 8 months of implantation. (a) Images at low magnification showed the contour and shape of the regenerated tissue. (b) Images at higher magnification showed myelins and more detailed morphology. Blood vessel (V), myelin (M), fat tissue (F), and regenerated nerve (RN). Scar bars in (a) represent 100 μm, and those in (b) represent 200 μm. Dotted boxes in (b) indicate the formation of self-organized bundles.

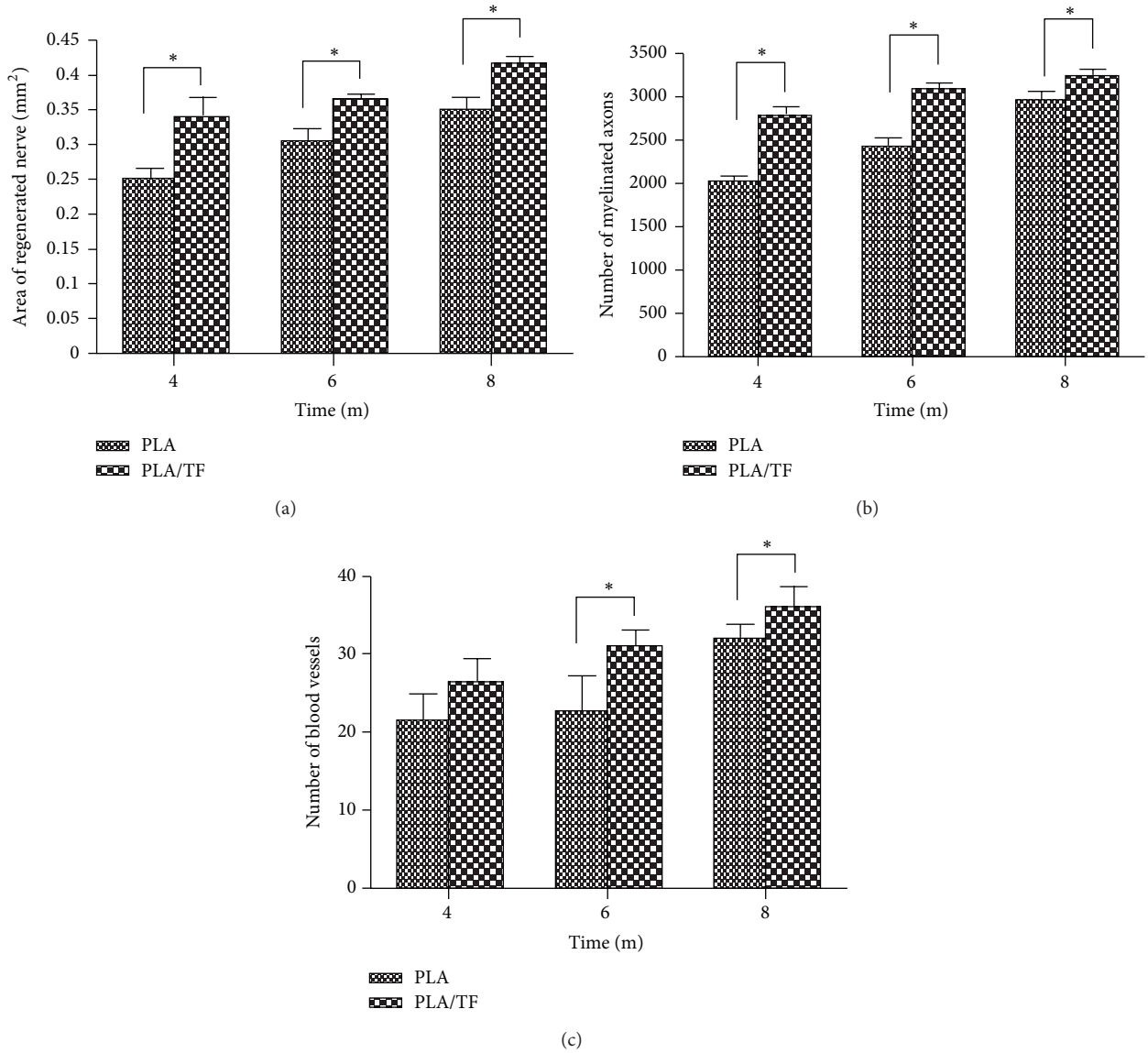

Figure 7: Quantitative analyses of the histological sections at the midconduit of PLA and PLA/TF conduits, showing a comparison of the (a) area of regenerated nerve, (b) number of myelinated axons, and (c) number of blood vessels between the two groups after 4, 6, and 8 months of implantation. $^*P < 0.05$.

surface decreased to 54° after TF modification. ATR-IR analysis also confirmed the grafting of TF. The current study demonstrated that TF could also be immobilized on PLA by air plasma. Besides, TF grafted on the surface of PLA was slowly released in PBS but remained to be detectable on the surface by ATR-IR after 4 weeks. This suggested that TF grafted on PLA may have endured for 4 weeks in vivo.

The rat model of sciatic nerve injury and defect was the most common animal model. The largest gap that could be created in rats was 15 mm [11]. MRI was employed in this study to monitor the long-term nerve regeneration within the conduit in the 15 mm gap nerve injury model. The images of the regenerated nerve and small blood vessels (100–200 μm) in the neighborhood were obtained by the MRI technique. Evaluation of crush injury in rat sciatic nerve by MRI was recently reported in the literature [29]. In this literature, the proximal sciatic nerve of adult rats was ligated by a tight suture that was removed 1 week later to induce complete anatomy and nerve regeneration. The images in our study not only demonstrated nerve sporting from the sagittal view but also identified the cross-section of the connected nerve by the axial view. Nerve connection was directly visualized at about 2 months from the sagittal view and from the axial view. The MRI axial views also revealed that the PLA/TF group had clearer images and larger cross-section of the regenerated nerve from 2 to 8 months than those of the PLA group.

The NCV in the PLA/TF group after 4 months of implantation was over 70% of that in normal nerve. Kim et al. reported that the nerve conduction velocity of regenerated nerve through a cellular nerve graft including growth factor

(nerve gap 8 mm) after implantation in rats for 6 months was about 60% [30] of that in normal nerve. The recovery degree for our PLA/TF conduits across a much larger gap (15 mm versus their 8 mm) in a shorter period (4 months versus their 6 months) was better than that previously reported.

The novel dynamic walking analysis and the resulted motion angle (θ) and extension range (Θ) showed the rehabilitation of walking function in rats. The data were more reliable than SFI. The SFI data had large standard deviation that statistically significant difference could not be identified between the two groups. Results from dynamic walking analysis were consistent with the tendency of SFI. Moreover, significant differences between PLA and PLA/TF groups could be demonstrated. This suggested that the analysis of extension range or average motion angle may be more appropriate to analyze the functional recovery in sciatic nerve defected animals.

Histological results showed a correlation between blood vessel formation and the number of new myelinated axons. Research has indicated that angiogenesis and neurogenesis are coupled processes [31]. TF was reported to function like NGF and promote the neurite outgrowth of PC12 h cells [24, 30]. NGF also contributes to angiogenesis [32, 33]. In our study, the vessels and myelins of regenerated nerves were evident in both PLA and PLA/TF groups at 4, 6, and 8 months. The histology of the PLA/TF group was better than that of the PLA group. While abundant blood vessels, multierythrocytes, and self-assembly of myelinated axons were usually observed in 6 weeks for the 10 mm gap [8], these features did not show up in histology until 6–8 months in the present study. It has been shown that the ligated sciatic nerve in rats recovered and had virtually the same histology as normal nerve after 12 weeks (~3 months) [11]. The evolutions and restoration of histology for the 15 mm large gap defected nerve obviously took much longer time (6–8 months in this study versus 6 weeks for the 10 mm gap). Histological results were consistent with the slow functional recovery demonstrated by the SFI, electrophysiology, and dynamic walking analysis.

In summary, our study demonstrated for the first time that TF modification was an efficient way to promote the peripheral nerve connection across a large gap in short term as well as nerve regeneration over an extensive period of time. The MRI technique successfully acquired the images of the regenerated sciatic nerve bridged by the conduits in rats. The new dynamic walking analysis provided the information of functional recovery in rats during a longer term.

5. Conclusion

TF was successfully grafted on the PLA nerve conduit after open air plasma treatment. The immobilization allowed TF to be retained on the conduit for more than 4 weeks. Nerve regeneration promoted by TF immobilization was evaluated in a 15 mm rat sciatic nerve transection model. MRI techniques were used to monitor the sciatic nerve regeneration within the conduit in the experimental rats during an 8-month period. TF-immobilized PLA (PLA/TF) conduits promoted the early nerve connection (6 weeks) from the two stumps. The superior efficacy of PLA/TF conduits over the bare PLA conduits was demonstrated in long term (8 months). The functional recovery after 8 months was ~84% based on electrophysiology and ~81% based on dynamic walking analysis for the bare PLA conduits, while that for PLA/TF conduits was ~93% based on electrophysiology and ~90% based on dynamic walking analysis.

Conflict of Interests

The authors confirm that there is no known conflict of interests associated with this paper.

Acknowledgments

This research was supported by the Program for Stem Cell and Regenerative Medicine Frontier Research (NSC101-2321-B-002-039) sponsored by the National Science Council, Taiwan. The authors thank Chih-Ming Chiang, Clayton Chi-Chang Chen, and the MRI Center, Department of Radiology, Taichung Veterans General Hospital, for their group support in MRI.

References

[1] J. Brandt, L. B. Dahlin, M. Kanje, and G. Lundborg, "Functional recovery in a tendon autograft used to bridge a peripheral nerve defect," *Scandinavian Journal of Plastic and Reconstructive Surgery and Hand Surgery*, vol. 36, no. 1, pp. 2–8, 2002.

[2] H. Millesi, "Progress in peripheral nerve reconstruction," *World Journal of Surgery*, vol. 14, no. 6, pp. 733–747, 1990.

[3] R. Deumens, A. Bozkurt, M. F. Meek et al., "Repairing injured peripheral nerves: bridging the gap," *Progress in Neurobiology*, vol. 92, no. 3, pp. 245–276, 2010.

[4] S. Hisasue, R. Kato, Y. Sato, T. Suetomi, Y. Tabata, and T. Tsukamoto, "Cavernous nerve reconstruction with a biodegradable conduit graft and collagen sponge in the rat," *Journal of Urology*, vol. 173, no. 1, pp. 286–291, 2005.

[5] Y. Zhu, A. Wang, S. Patel et al., "Engineering bi-layer nanofibrous conduits for peripheral nerve regeneration," *Tissue Engineering C*, vol. 17, no. 7, pp. 705–715, 2011.

[6] C. Chang and S. Hsu, "The effect of high outflow permeability in asymmetric poly(DL-lactic acid-co-glycolic acid) conduits for peripheral nerve regeneration," *Biomaterials*, vol. 27, no. 7, pp. 1035–1042, 2006.

[7] S. Hsu, S. Chan, C. Chiang, C. C. Chen, and C. Jiang, "Peripheral nerve regeneration using a microporous polylactic acid asymmetric conduit in a rabbit long-gap sciatic nerve transection model," *Biomaterials*, vol. 32, no. 15, pp. 3764–3775, 2011.

[8] S. Hsu and H. Ni, "Fabrication of the microgrooved/microporous polylactide substrates as peripheral nerve conduits and in vivo evaluation," *Tissue Engineering A*, vol. 15, no. 6, pp. 1381–1390, 2009.

[9] S. H. Oh, J. H. Kim, K. S. Song et al., "Peripheral nerve regeneration within an asymmetrically porous PLGA/Pluronic F127 nerve guide conduit," *Biomaterials*, vol. 29, no. 11, pp. 1601–1609, 2008.

[10] G. R. D. Evans, K. Brandt, S. Katz et al., "Bioactive poly(L-lactic acid) conduits seeded with Schwann cells for peripheral nerve regeneration," *Biomaterials*, vol. 23, no. 3, pp. 841–848, 2002.

[11] C. Chang, "The effect of pulse-released nerve growth factor from genipin-crosslinked gelatin in schwann cell-seeded polycaprolactone conduits on large-gap peripheral nerve regeneration," *Tissue Engineering A*, vol. 15, no. 3, pp. 547–557, 2009.

[12] K. Fu, L. Dai, I. Chiu, J. Chen, and S. Hsu, "Sciatic nerve regeneration by microporous nerve conduits seeded with glial cell line-derived neurotrophic factor or brain-derived neurotrophic factor gene transfected neural stem cells," *Artificial Organs*, vol. 35, no. 4, pp. 363–372, 2011.

[13] H.-C. Ni, Z.-Y. Lin, S.-H. Hsu, and I.-M. Chiu, "The use of air plasma in surface modification of peripheral nerve conduits," *Acta Biomaterialia*, vol. 6, no. 6, pp. 2066–2076, 2010.

[14] F. C. Guo, R. P. Kwakkel, B. A. Williams, X. Suo, W. K. Li, and M. W. A. Verstegen, "Coccidiosis immunization: effects of mushroom and herb polysaccharides on immune responses of chickens infected with Eimeria tenella," *Avian Diseases*, vol. 49, no. 1, pp. 70–73, 2005.

[15] Q. Gao, R. Seljelid, H. Chen, and R. Jiang, "Characterisation of acidic heteroglycans from Tremella fuciformis Berk with cytokine stimulating activity," *Carbohydrate Research*, vol. 288, pp. 135–142, 1996.

[16] B. Chen, "Optimization of extraction of Tremella fuciformis polysaccharides and its antioxidant and antitumour activities in vitro," *Carbohydrate Polymers*, vol. 81, no. 2, pp. 420–424, 2010.

[17] L. Tong, T. Y. Huang, and J. L. Li, "Effects of plant polysaccharides on cell proliferation and cell membrane contents of sialic acid, phospholipid and cholesterol in S 180 and K 562 cells," *Zhongguo Zhong Xi Yi Jie He Za Zhi*, vol. 14, no. 8, pp. 482–484, 1994.

[18] S. W. Kim, H. J. Hwang, Y. M. Baek, H. S. Hwang, and J. W. Yun, "Proteomic analysis in ob/ob mice before and after hypoglycemic polysaccharide treatments," *Journal of Microbiology and Biotechnology*, vol. 19, no. 10, pp. 1109–1121, 2009.

[19] H. Cheng, W. Hou, and M. Lu, "Interactions of lipid metabolism and intestinal physiology with Tremella fuciformis Berk edible mushroom in rats fed a high-cholesterol diet with or without nebacitin," *Journal of Agricultural and Food Chemistry*, vol. 50, no. 25, pp. 7438–7443, 2002.

[20] S. Ukai, T. Kiho, C. Hara, I. Kuruma, and Y. Tanaka, "Polysaccharides in fungi. XIV. Anti-inflammatory effect of the polysaccharides from the fruit bodies of several fungi," *Journal of Pharmacobio-Dynamics*, vol. 6, no. 12, pp. 983–990, 1983.

[21] J.-L. Mau, G.-R. Chao, and K.-T. Wu, "Antioxidant properties of methanolic extracts from several ear mushrooms," *Journal of Agricultural and Food Chemistry*, vol. 49, no. 11, pp. 5461–5467, 2001.

[22] Q. Gao, M. K. Killie, H. Chen, R. Jiang, and R. Seljelid, "Characteriza-tion and Cytokine-stimulating activities of acidic heteroglycans from Tremella fociformis," *Planta Medica*, vol. 63, no. 5, pp. 457–460, 1997.

[23] Q. Gao, G. Berntzen, R. Jiang, M. K. Killie, and R. Seljelid, "Conjugates of Tremella polysaccharides with microbeads and their TNF-stimulating activity," *Planta Medica*, vol. 64, no. 6, pp. 551–554, 1998.

[24] J. H. Kim, H. Ha, M. Lee et al., "Effect of Tremella fuciformis on the neurite outgrowth of PC12h cells and the improvement of memory in rats," *Biological and Pharmaceutical Bulletin*, vol. 30, no. 4, pp. 708–714, 2007.

[25] J. Shen, C. Zhou, X. Zhong et al., "MR neurography: T1 and T2 measurements in acute peripheral nerve traction injury in rabbits," *Radiology*, vol. 254, no. 3, pp. 729–738, 2010.

[26] S. -H. Yang, H. -I. Liu, and S. -J. Tsai, "Edible Tremella polysaccharide for skin care," 2006, Agricultural Research Institute, assignee, Taichung, Taiwan.

[27] J. R. Bain, S. E. Mackinnon, and D. A. Hunter, "Functional evaluation of complete sciatic, peroneal, and posterior tibial nerve lesions in the rat," *Plastic and Reconstructive Surgery*, vol. 83, no. 1, pp. 129–136, 1989.

[28] G. M. T. Hare, P. J. Evans, S. E. Mackinnon et al., "Walking track analysis: a long-term assessment of peripheral nerve recovery," *Plastic and Reconstructive Surgery*, vol. 89, no. 2, pp. 251–258, 1992.

[29] H. C. Lehmann, J. Zhang, S. Mori, and K. A. Sheikh, "Diffusion tensor imaging to assess axonal regeneration in peripheral nerves," *Experimental Neurology*, vol. 223, no. 1, pp. 238–244, 2010.

[30] B. Kim, J. J. Yoo, and A. Atala, "Peripheral nerve regeneration using acellular nerve grafts," *Journal of Biomedical Materials Research A*, vol. 68, no. 2, pp. 201–209, 2004.

[31] H. Teng, Z. G. Zhang, L. Wang et al., "Coupling of angiogenesis and neurogenesis in cultured endothelial cells and neural progenitor cells after stroke," *Journal of Cerebral Blood Flow and Metabolism*, vol. 28, no. 4, pp. 764–771, 2008.

[32] G. Cantarella, L. Lempereur, M. Presta et al., "Nerve growth factor-endothelial cell interaction leads to angiogenesis in vitro and in vivo," *The FASEB Journal*, vol. 16, no. 10, pp. 1307–1309, 2002.

[33] X. Liu, D. Wang, Y. Liu et al., "Neuronal-driven angiogenesis: role of NGF in retinal neovascularization in an oxygen-induced retinopathy model," *Investigative Ophthalmology and Visual Science*, vol. 51, no. 7, pp. 3749–3757, 2010.

Hindawi Publishing Corporation
Evidence-Based Complementary and Alternative Medicine
Volume 2013, Article ID 161976, 11 pages
http://dx.doi.org/10.1155/2013/161976

Research Article

Potential Osteoporosis Recovery by Deep Sea Water through Bone Regeneration in SAMP8 Mice

Hen-Yu Liu,[1,2] Ming-Che Liu,[3,4] Ming-Fu Wang,[5] Wei-Hong Chen,[1,2] Ching-Yu Tsai,[1,2] Kuan-Hsien Wu,[1,2] Che-Tong Lin,[6] Ying-Hua Shieh,[7] Rong Zeng,[8] and Win-Ping Deng[1,2,9,10]

[1] *Stem Cell Research Center, Taipei Medical University, Taipei, Taiwan*
[2] *Graduate Institute of Biomedical Materials and Tissue Engineering, Taipei Medical University, Taipei, Taiwan*
[3] *School of Dentistry, College of Oral Medicine, Taipei Medical University, Taipei, Taiwan*
[4] *Department of Urology, Taipei Medical University Hospital, Taipei, Taiwan*
[5] *Department of Food and Nutrition, Providence University, Taichung, Taiwan*
[6] *Graduate Institute of Oral Rehabilitation Sciences, Taipei Medical University, Taipei, Taiwan*
[7] *Department of Family Medicine, Taipei Medical University, Wan Fang Hospital, Taipei, Taiwan*
[8] *Department of Orthopedic Surgery, The Affiliated Hospital, Guangdong Medical College, Zhanjiang 524001, China*
[9] *Translational Research Laboratory, Cancer Center, Taipei Medical University, Taipei, Taiwan*
[10] *Cancer Center, Taipei Medical University Hospital, Taipei, Taiwan*

Correspondence should be addressed to Rong Zeng; 13802825311@139.com and Win-Ping Deng; wpdeng@ms41.hinet.net

Received 3 January 2013; Revised 22 June 2013; Accepted 27 June 2013

Academic Editor: Wei-Chiang Lin

The aim of this study is to examine the therapeutic potential of deep sea water (DSW) on osteoporosis. Previously, we have established the ovariectomized senescence-accelerated mice (OVX-SAMP8) and demonstrated strong recovery of osteoporosis by stem cell and platelet-rich plasma (PRP). Deep sea water at hardness (HD) 1000 showed significant increase in proliferation of osteoblastic cell (MC3T3) by MTT assay. For *in vivo* animal study, bone mineral density (BMD) was strongly enhanced followed by the significantly increased trabecular numbers through micro-CT examination after a 4-month deep sea water treatment, and biochemistry analysis showed that serum alkaline phosphatase (ALP) activity was decreased. For stage-specific osteogenesis, bone marrow-derived stromal cells (BMSCs) were harvested and examined. Deep sea water-treated BMSCs showed stronger osteogenic differentiation such as BMP2, RUNX2, OPN, and OCN, and enhanced colony forming abilities, compared to the control group. Interestingly, most untreated OVX-SAMP8 mice died around 10 months; however, approximately 57% of DSW-treated groups lived up to 16.6 months, a life expectancy similar to the previously reported life expectancy for SAMR1 24 months. The results demonstrated the regenerative potentials of deep sea water on osteogenesis, showing that deep sea water could potentially be applied in osteoporosis therapy as a complementary and alternative medicine (CAM).

1. Introduction

Osteoporosis, a common disease caused by imbalanced bone remodeling, is a global public health problem. Patients with osteoporosis are often accompanied with pain, disability, and decline in the quality of life, rise in mortality, and depletion of local health care budget [1–4]. The major type of osteoporosis occurred in postmenopausal women with an age range of 50–70 [5]. Bone density index rapidly decreased after the menopause, due to sex hormone imbalance and the lack of estrogen. The imbalance of homeostasis between osteoclasts and osteoblasts also leads to increased bone resorption [6, 7]. In addition, senile osteoporosis with increased age and the reduction of growth hormone (GH) which stimulates renal-synthesized 1 alpha,25-dihydroxyvitamin D3 (1,25(OH)2D3) is also another cause of osteoporosis [8, 9]. Age-related bone loss causes bone trabecular thinning as well as the loss of cortical layer of bone tissue, and the cortex becomes porous which will increase the femoral neck fracture rate [10]. For osteoporosis, supplemental dietary calcium and vitamin D may reduce the risk of fractures in postmenopausal women [11]. Drugs, lifestyle changes, home safety, and hip protection

are viable approaches for the prevention of osteoporosis. According to the World Health Organization Criteria (WHO) statistics, the penetration rate of osteoporosis in women over the age of 65 is up to 35%; hence, the advanced treatment for osteoporosis has become emergent.

Deep sea water (DSW) generally refers to sea water from a depth of more than 200 meters (m). It could be characterized by its purity, abundant nutrients, and minerals. Currently, DSW has been applied in the ground of food, agriculture, cosmetic, and medical field due to its high contents of unique minerals including sodium (Na), magnesium (Mg), calcium (Ca), potassium (K), zinc (Zn), and vanadium (V) [12]. DSW has been reported to stimulate both osteoblastogenesis and osteoclastogenesis in bone turnover [13]. NaCl from DSW also improves the biochemical properties of bone. DSW combined with soluble silicon as natural material could promote cell proliferation of osteoblast and enhance the osteogenesis-related gene expression in animal studies [13]. The DSW utilized in this study is drawn from the Pacific Ocean at a depth of 662 m and a distance of 5 kilometers (km) off the coast of Hualien County, Taiwan [14, 15], which contains abundant amounts of trace elements, including high concentrations of four essential minerals: Mg (96200 mg/L), K (10800 mg/L), Na (9010 mg/L), and Ca (39 mg/L).

Our previous study has demonstrated that transplantation of platelet-rich plasma- (PRP-) treated NIH3T3-G cells into OVX-SAMP8 mice significantly reversed osteoporosis. We also showed that PRP could not only increase bone regeneration but also reduce bone marrow adiposity in the osteoporotic mice [16–18]. In this study, we investigated the possibility of the treatment of osteoporosis by DSW. For osteoporotic model, SAMP8 mice received bilateral salpingo-oophorectomy at 4 months old and subsequently fed with DSW for 15 days. The effects of DSW on bone regeneration were then analyzed by bone mineral density, micro-CT, bone structure with HE stain, and the activities of isolated bone marrow stromal cells. Here, we demonstrated that DSW not only induced bone regeneration but also strongly recovered bone loss in OVX-SAMP8 mice. In addition, we have observed that DSW would be effective in prevention of osteoporosis and might be a complementary and alternative medicine (CAM).

2. Materials and Methods

2.1. Characterization of Deep Sea Water (DSW). DSW was obtained from the Pacific Ocean at a depth of 662 m [14, 15]. The obtained DSW was subjected to filtration to remove microorganism and virus and then concentrated. The elements contained in concentrated DSW were measured by inductively coupled plasma mass spectroscopy. As shown in Supplemental Table 1, the concentrated DSW contained high amounts of several essential minerals such as magnesium (Mg), potassium (K), sodium (Na), and calcium (Ca) (see Supplementary Material availbale online at http://dx.doi.org/10.1155/2013/161976). The final hardness of concentrated DSW was determined as 400,000 mg/L by using calcium and magnesium concentrations.

2.2. Cell Line and Cell Viability. Mouse preosteoblast cell line (MC3T3-E1, ATCC CRL-2593) was provided by Dr. Alexander T.H Wu (Taipei medical University, Taipei, Taiwan) and was cultured in 96 well plates (1×10^4 cells/well) in alpha minimum essential medium (α-MEM) supplemented with 10% fetal bovine serum (FBS) or/and different concentration of DSW (ranged from 500 to 2000 HD). MTT reagent was added into each well on day 3 of cell growth in culture, and cell viability was detected by Multiskan PC (Thermo Lab). For the cell counting assay, MC3T3 (1×10^4) were seeded in 6 cm dish containing DSW-derived medium (hardness of 1000 mg/L)and incubated at 37°C in 5% CO_2 atmosphere. After 72 hrs, MC3T3 were collected, and the cell numbers were counted by trypsin and ethylenediaminetetraacetic acid treatment.

2.3. Experimental Animals. All the animal experiment protocol was approved by the Institutional Animal Care and Use Committee of Taipei medical University. SAMP8 mice were ovariectomized (OVX) at 4 months of age to induce osteoporosis and then used in this experiments. Mice were grouped into the following (six mice per group): control group (CTRL, receiving PBS) and DSW group (receiving DSW). Both mice were suggested for daily water uptake which is based on a 22 g mouse consuming 5.2 mL water per day.

2.4. Serum ALP, Mg, and Ca Analyses. All mice were sacrificed and the extracted blood specimens were obtained at 4 months. The plasma concentrations for ALP, Mg, and Ca were then determined by a photometric method according to the manufacturer's instructions (Fuji Dri-Chem Clinical Chemistry Analyzer FDC 3500).

2.5. Bone Mineral Density and Micro-CT Analysis. Dual-energy X-ray absorptiometry (DEXA) analysis was used for the measurement of bone mass in the spine, left/right knee, and left/right femurs. BMD (XR-36; Norland Corp.; host software revision 2.5.3, scanner software revision 2.0.0) was performed 4 months after DSW treatment. All mice were sacrificed and their femurs and tibia bones were collected at 4 months for detecting the trabecular bone and bone volume by micro-CT (Skyscan-1076, Skyscan, Belgium). For trabecular bone analysis and 3D imaging, construction was operated at 50 KV, 200 uA, 0.4° of rotation step, 0.5 mm AI filter, and 9 μm/pixel of scan resolution. Each group contains 6 animals.

2.6. Histological Analysis. For histological determination, bone sample was fixed in 10% formalin and decalcified in 14% EDTA for 3 days. Bone sections (10 μm) were subjected to paraffin-embedding and then stained with hematoxylin and eosin (H&E) staining to detect the trabecular bone in the bone tissue.

2.7. Isolation of Bone Marrow Cells. Bone marrow stromal cells (BMSCs) were harvested from femurs and tibias of

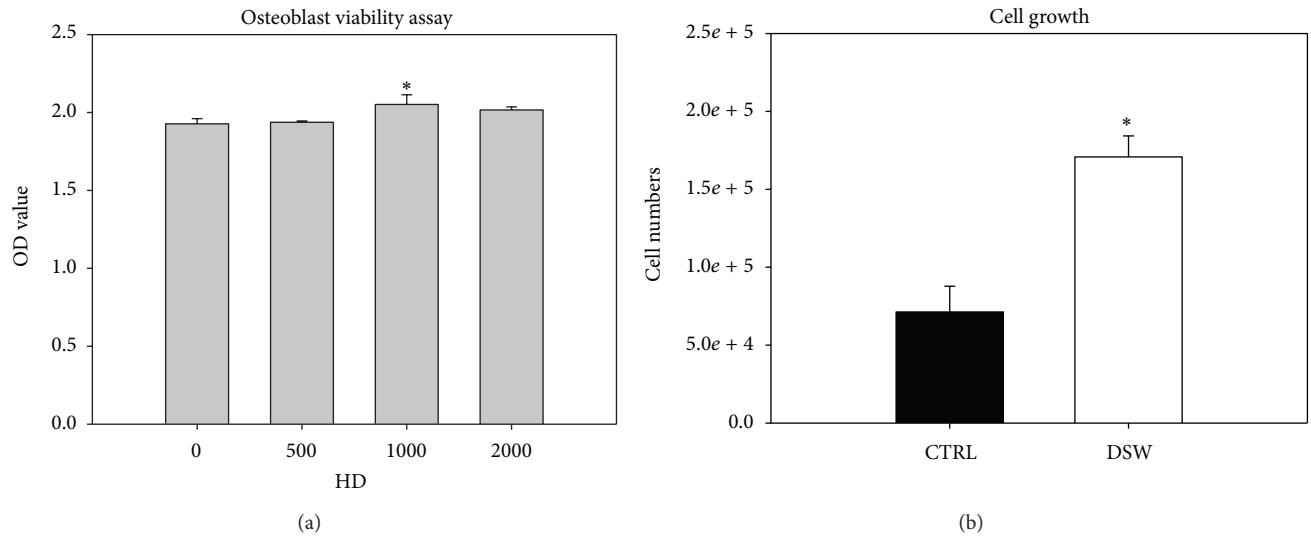

Figure 1: Optimization of hardness of DSW by cell viability of preosteoblast. Comparative proliferation profiles of preosteoblast (MC3T3) in DSW-enriched medium were analyzed by MTT assay (optical densities, mean 6 SD for 3 separate replicates). The MC3T3 cells treated with DSW of hardness (HD) 1000 showed the highest cell viability; t-test, $^{*}P < 0.05$.

DSW-treated mice and vehicle-treated mice (CTRL) after 4 months treatment. BMSCs were washed out in the bone marrow and centrifuged at 1000 rpm for 5 min. Cells were all cultured in α-MEM supplemented with 10% FBS for one week to remove the nonadherent cells and then washed with PBS. The adherent cells, indicated the BMSCs, were collected for ethylenediaminetetraacetic acid treatment.

2.8. Cell Proliferation and Colony-Forming Unit of BMSCs In Vivo. BMSCs were cultured in α-MEM supplemented with 10% FBS and/or DSW treatment for 3 days, and the cell numbers were counted for evaluating their proliferation. For colony formation assay, BMSCs were cultured in maintenance medium after 14 days and then fixed with 4% formaldehyde. Fixed cells were then stained with 0.5% crystal violet in methanol for 10 min, and formed colonies were then counted.

2.9. RT-PCR Analysis. Total RNA from BMSCs was extracted using TRIzol regent (Invitrogen Life Technologies). Gene expression levels were measured by RT-PCR. Primer sequences were indicated as follows: bone morphogenetic protein (BMP2): forward primer 5′-GGTCCTTGCACCAAGATGAAC-3′; reverse primer 5′-CAACCCTCCACAACCATGTC-3′, and temperature 62°C; osteopontin (OPN): forward primer 5′-ATGAGATTGGCAGTGATT-3′, reverse primer 5′-GTTGACCTCAGAAGATGA-3′, and temperature 48.8°C; osteocalcin (OCN): forward primer 5′-CAGCTTGGTGCACACCTAAGC-3′, reverse primer 5′-AGGGTTAAGCTCACACTGCTCC-3′, and temperature 55°C; runt-related transcription factor 2 (RUNX2): forward primer 5′-ACTTTCTCCAGGAAGACTGC-3′; reverse primer 5′-GCTGTTGTTGCTGTTGCTGT-3′, and temperature 55°C; glyceraldehyde 3-phosphate dehydrogenase (GAPDH): was used as an internal control (CTRL) forward primer 5′-GCTCTCCAGAACATCATCCCTGCC-3′; reverse primer 5′-CGTTGTCATACCAGGAAATGAGCTT-3′, and temperature, 55°C. PCR products were separated by electrophoresis on 1% agarose gels (Agarose I; AMRESCO) and visualized with ethidium bromide staining.

2.10. Statistical Analysis. All results were represented as mean ± standard deviation (SD). Significant differences between the two groups were determined by Student's t-test, P value < 0.05.

3. Results

3.1. Effect of Deep Sea Water (DSW) Hardness on the Cell Growth of Preosteoblast. To determine the effects of different hardness of DSW water on the cell viability of preosteoblasts, MC3T3 cells were cultured in DSW-derived medium for 48 hrs and analyzed by MTT assay. As shown in Figure 1(a), the DSW with hardness of 50 and 2000 mg/L did not affect the cell viability of preosteoblasts, yet DSW with hardness of 1000 mg/L slightly increased the cell viability of MC3T3 cells. Hence, we further evaluated the cell growth effects of DSW with hardness of 1000 mg/L on MC3T3 cells by using cell-counting assay. After 72 hrs of culture, MC3T3 cells showed 2- to 3-fold enhanced cell growth in DSW-derived medium (hardness of 1000 mg/L) compared to the control medium (Figure 1(b)). These results indicated that 1000 mg/L displays the optimal hardness of DSW for the cell growth of preosteoblasts. Therefore, we utilized DSW with hardness of 1000 mg/L in the following experiments.

3.2. Effect of DSW on Serum Alkaline Phosphatase (ALP), Calcium (Ca), and Magnesium (Mg) Activity in OVX-SAMP8 Mice. Based on the *in vitro* results, DSW of hardness 1000 was applied to OVX-SAMP8 mice for 4 months. We first evaluated the *in vivo* osteogenic effects of DSW by using

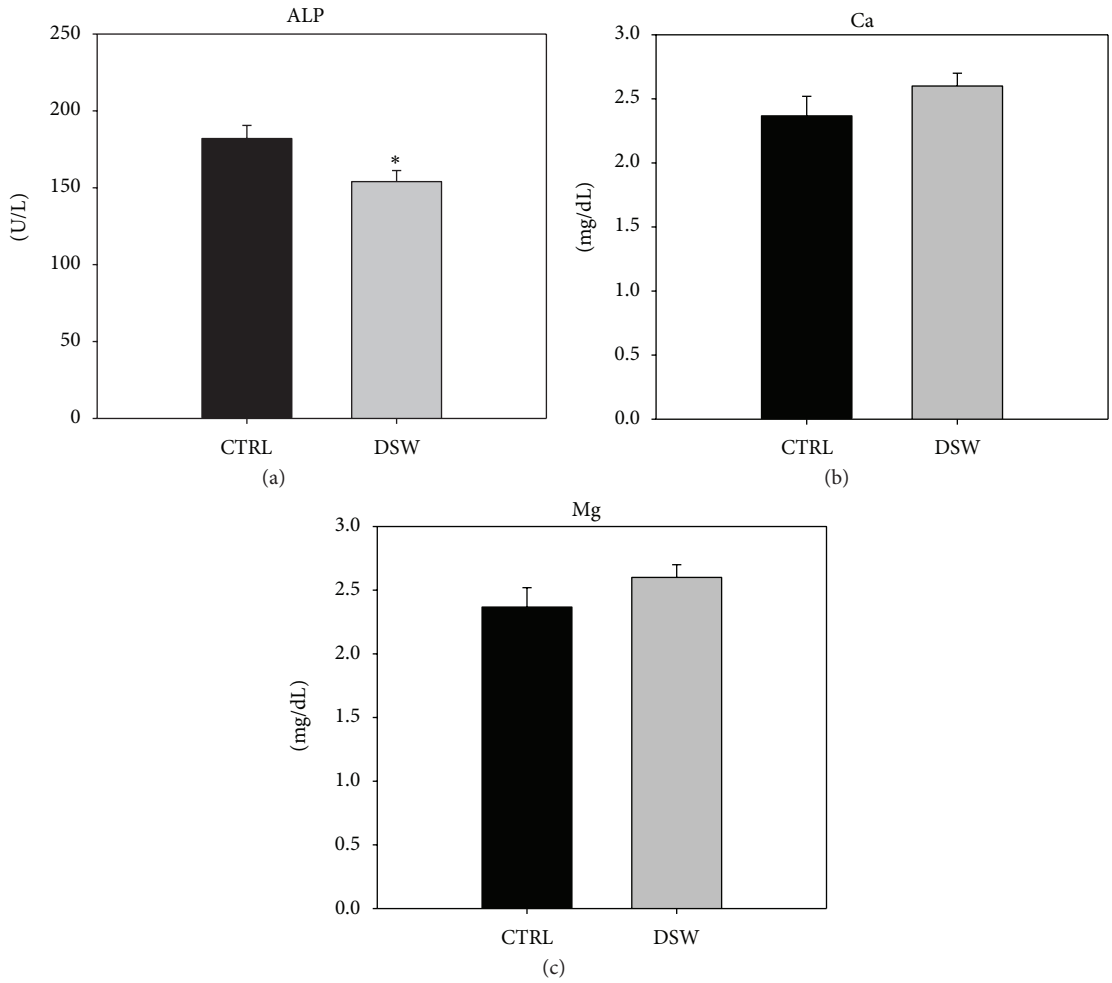

Figure 2: The effect of DSW treatment on serum ALP, Ca, and Mg activity. The serum ALP, Ca and Mg levels after 4 months DSW treatment was measured by ELISA assay. Serum ALP levels presented a significant decrease in DSW-treated mice (a). In contract, Ca and Mg showed no significant different in DSW group compared with control mice ((b) and (c)). Each bar represents the average from six animals; t-test, $^{*}P < 0.05$ versus CTRL group.

serum levels of ALP, Ca, and Mg. Serum ALP values reflect the increased turnover associated with bone destruction of aging, menopause, and various conditions affecting bone metabolism. Increased serum ALP levels are associated with an increased risk of rapid bone loss in peri- and postmenopausal women [19–21]. Ca and Mg play important roles in bone homeostasis and metabolism. Decreased serum levels of Ca and Mg have been shown to contribute to the risk of osteoporosis [22–24]. After 4 months DSW treatment, significantly lower ALP activity was evident in the DSW group as compared to control group (Figure 2(a)), which means that DSW could recover the bone loss in OVX-SAMP8 mice. Meanwhile, no significant difference was found in Ca and Mg levels between the DSW and control group (Figures 2(b) and 2(c)).

3.3. Quantitative Analysis of BMD in DSW-Treated Mice. DSW was used for prevention of OVX-SAMP8 osteoporotic mice, and bone density scores of spine, knee (right/left), and femurs (right/left) were determined by dual-energy X-ray absorptiometry (general scheme, Figure 3(a)). As demonstrated in Figure 3, 4 months after treatment, DSW of hardness 1000 significantly improved BMD of OVX-SAMP8 mice, compared with vehicle-treated OVX-SAMP8 mice, indicating that DSW induced bone regeneration and recovered bone mass loss in these osteoporotic mice (Figure 3(b)).

3.4. Photomicrographs for Bone Recovery in OVX-SAMP8 Mice by DSW. The improvement in BMD scores in DSW-treated animals was further supported by bone morphological analysis. Both micro-CT 2D and 3D imaging demonstrated higher trabecular area and volume in DSW-treated OVX-SAMP8 animals (left and middle two columns, resp., Figure 4(a)). Meanwhile, histological sections of bone tissues from DSW-treated mice also showed more trabecular bone areas in the bone marrow (right two columns, Figure 4(a)). After the relative trabecular bone volume ratio to the total bone volume (BV/TV) was measured, it was clear that a higher percent bone volume ratio (upper panel, Figure 4(b)) and trabecular bone number (lower panel, Figure 4(b)) were also found in DSW-treated OVX-SAMP8 mice.

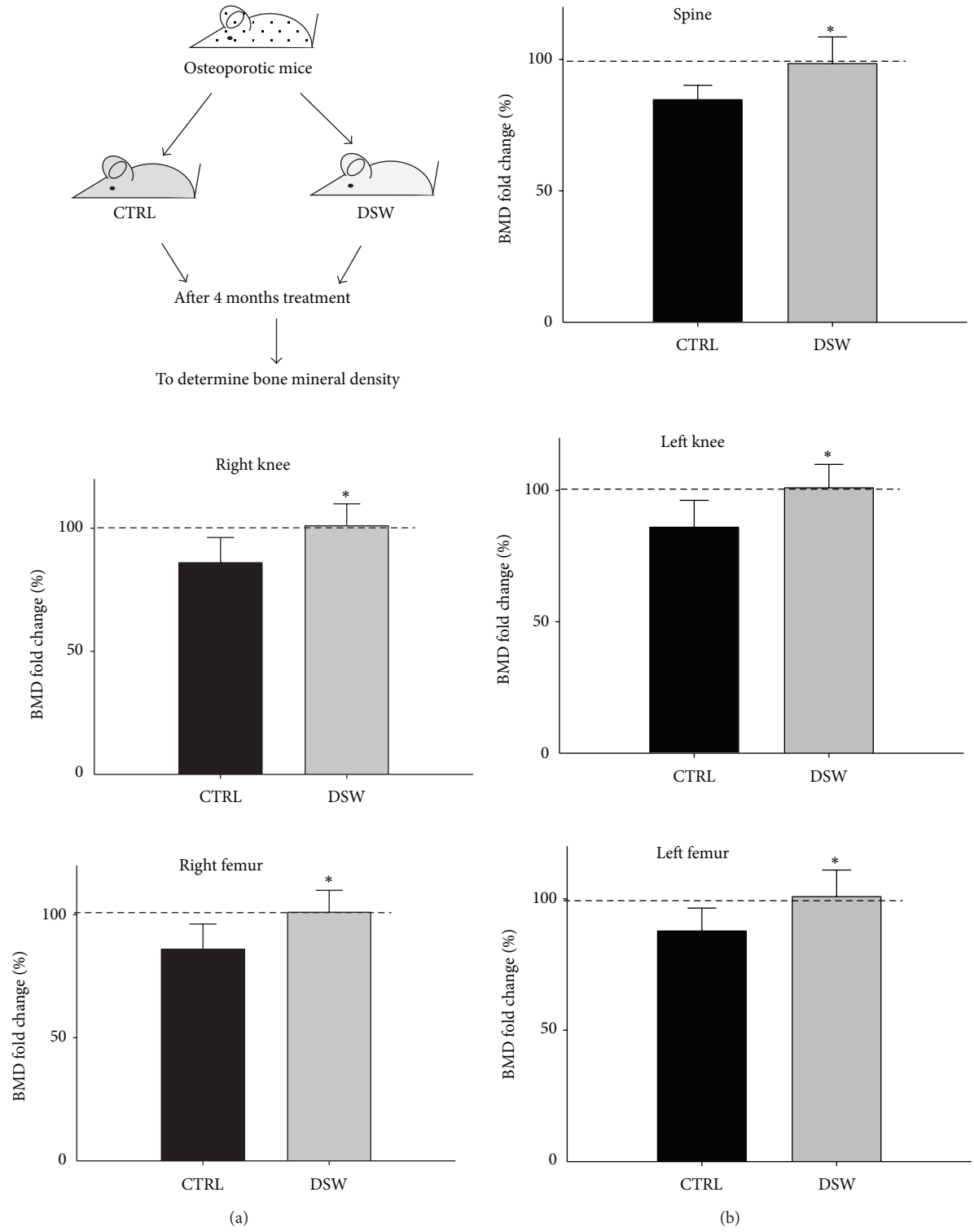

Figure 3: Quantitative analysis of BMD in DSW-treated and control mice. Bone density scores (BMD) of spine, knee (right/left), and femurs (right/left) were measured by Dual-energy X-ray absorptiometry after 4 months treatment (a). DSW-induced bone formation and decreased bone loss were observed in the DSW-treated OVX-SAMP8 mice (b). Values (means + SD) indicate relative BMD levels normalized to month 0 BMD (before operation = 100%; dashed line), respectively; $^{*}P < 0.05$ determined by t-tests; $n = 6$ of each group.

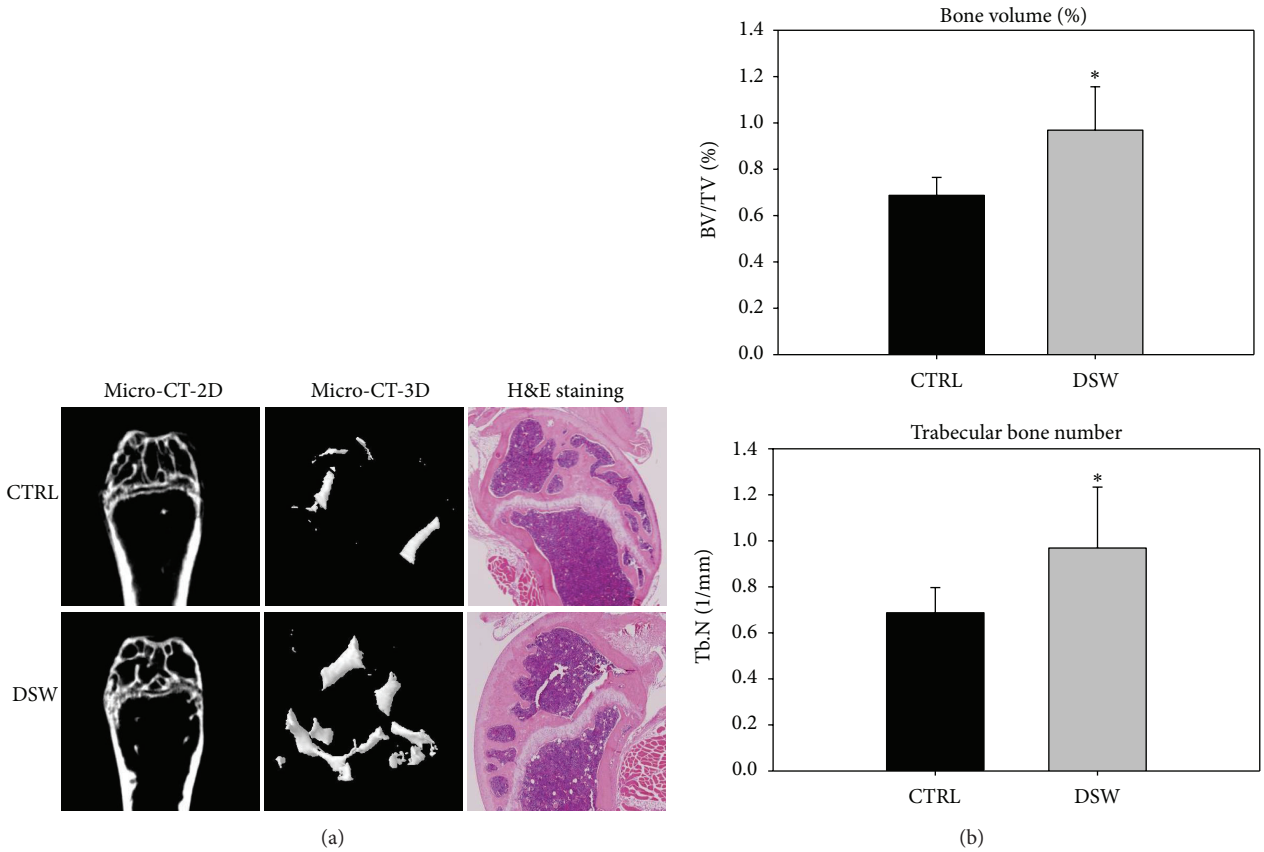

Figure 4: Effects of DSW on bone structure of OVX-SAMP8 mice. Comparative analyses of bone structure between control and DSW-treated OVX-SAMP8 mice. Micro-CT imaging observed that bone structure (trabecular/cortical bone, 2D), trabecular bone volume (3D), and trabecular bone mass were increased in the DSW-treated OVX-SAMP8 mice after 4 months treatment. H&E staining represented a higher ratio of bone mass in DSW-treated mice (a). The volume of trabecular bone (bone volume/total bone volume (BV/TV)), and the numbers of trabecular bone (Tb.N) were calculated (right panel), and bars represented the average from six animals (b); t-test, $^{*}P < 0.05$ versus CTRL group.

3.5. The Proliferation and Colony-Forming Ability of Bone Marrow Stem Cell (BMSC) Derived from DSW-Treated Mice. To validate these observations and determine the effect of DSW on bone microenvironment in OVX-SAMP8 mice, BMSCs in DSW-treated mice were isolated and examined for cell proliferation and colony-forming ability (general scheme, Figure 5(a)). The BMSCs from DSW-treated SAMP8 mice demonstrated significantly higher proliferative activity and higher numbers of colonies as compared to those from vehicle-treated mice after 7 days incubation (Figures 5(b) and 5(c)). This finding suggested that the BMSCs from DSW-treated SAMP8 mice had statistically significant proliferative and colony-forming abilities.

3.6. Effects of DSW on Osteogenic Differentiation of BMSCs In Vivo. Following the characterization scheme in Figure 5, osteogenic differentiation markers, including BMP2 (regulate the transcription factor Runx2 expression), RUNX2 (an early stage marker for osteogenesis), OPN (an intermediate marker for osteogenesis), and OCN (a late stage marker for osteogenesis) mRNA transcripts of BMSCs from DSW-treated OVX-SAMP8, were examined and compared. The mRNA level of RUNX2, BMP2, OPN, and OCN was significantly upregulated in DSW-treated mice when compare to control mice (Figure 6(a)). Moreover, the Alizarin Red S staining showed an increased level of matrix mineralization in the BMSCs isolated from the DSW-treated group, as compared to the control group (Figure 6(b)).

3.7. Survival of Osteoporotic Mice Treated with DSW. In addition to significantly improving bone trabecular architecture and BMD, the DSW could extend the life span of OVX-SAMP8 mice, which was markedly longer than that of the untreated OVX-SAMP8 (Figure 7). Most untreated OVX-SAMP8 mice died around 10 months; however, approximately 57% of DSW-treated groups lived up to 16.6 months, a life expectancy similar to the previously reported life expectancy for SAMR1 24 months [16].

4. Discussion

Previously, we have demonstrated the osteogenic regeneration mechanism by stem cells and platelet-rich plasma in OVX-SAMP8 mice [16]. In this study, we extended to

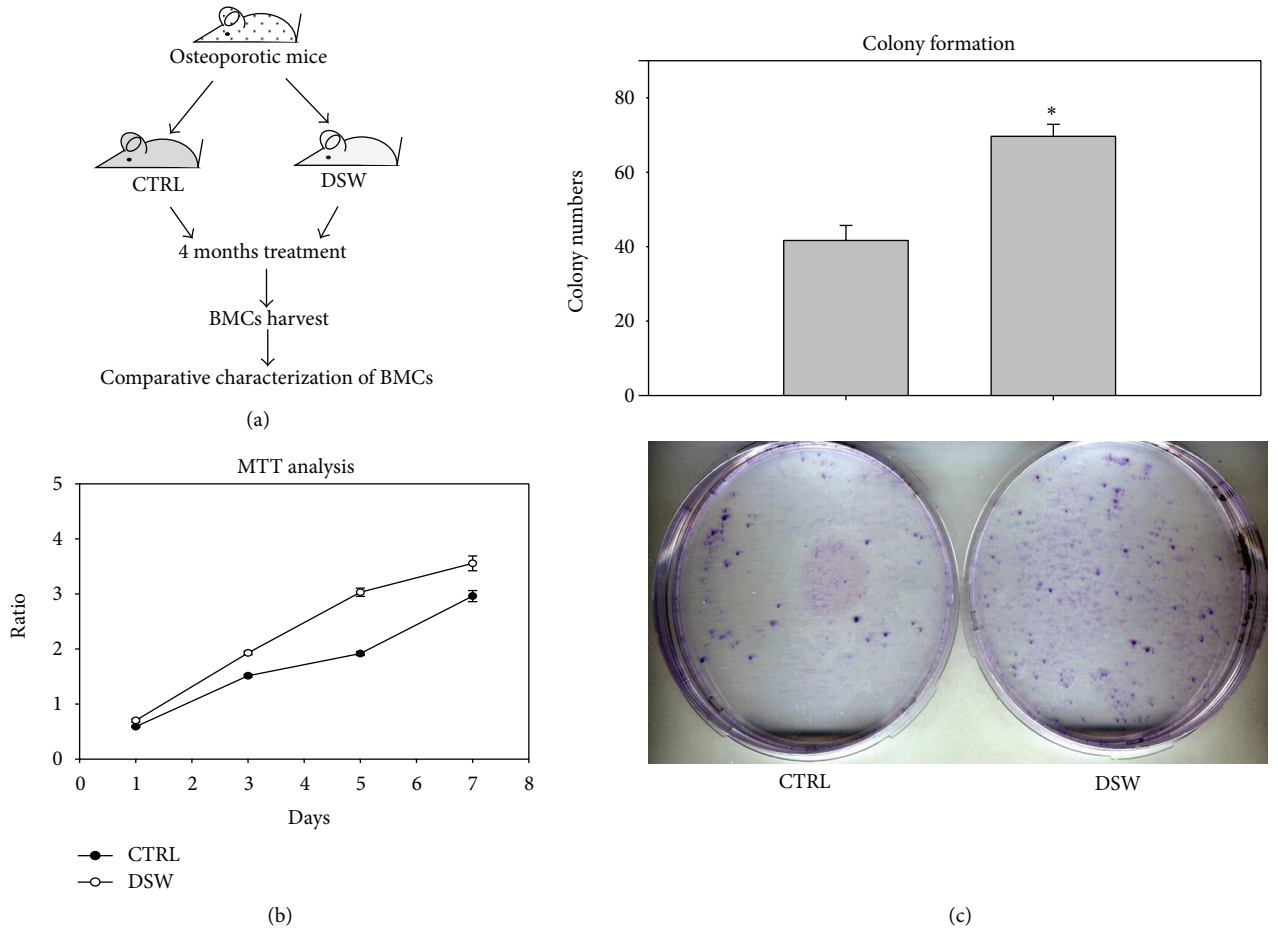

Figure 5: *Ex vivo* proliferation and colony-forming ability of isolated BMSCs. Comparative proliferation profiles of BMSCs from DSW and vehicle-treated mice were demonstrated by MTT assay ((a) and (b)). BMSCs were cultured for 14 days, and their colony forming abilities were assayed. Data was expressed quantitatively in the upper panel (c). Representative results of 3 experiments are demonstrated; t-test, $^{*}P < 0.05$ versus CTRL group.

examine the feasibility of using deep sea water (DSW) as a molecular cocktail to modulate the osteogenesis in osteoporotic mouse model. DSW contained major trace elements such as magnesium (Mg) and calcium (Ca), that have been reported to regulate bone metabolism. Mg and Ca were also found to induce murine osteoblast differentiation in MC3T3 cells. When MC3T3 cells were cultured in Mg- and Ca-free medium, their osteoblast differentiation marker osteocalcin (OCN) was reduced [25]. Epidemiologic studies showed a good correlation between Mg/Ca and bone density, in which low Mg and Ca intake might decrease bone mass [26, 27], bone turnover, and also cause high risk of fracture and osteoporosis. Moreover, the hardness (HD) of DSW which resulted from the composition of Mg and Ca also reported to modulate osteogenesis [28, 29]. In this study, our result showed that DSW of hardness 1000 (1000HD) appeared to be the optimal condition for osteoblast proliferation (Figure 1) and was applied for later experiments.

Serum alkaline phosphatase (ALP) is a group of enzymes found primarily in bone tissue. The primary importance of measuring ALP is to check the possibility of bone disease such as fractures and bone loss [30, 31]. The decreased serum ALP activity and bone mass recovery were found in early postmenopausal woman with osteoporosis after hormone replacement therapy [32]. From the biochemical analysis, OVX-SAMP8 mice exhibited decreased ALP activity after 4 months DSW treatment (Figure 2). The decreased ALP activities were evidenced by bone mineral density (BMD) which indicated that bone quality in OVX-SAMP8 mice was enhanced by DSW (Figure 3). Interestingly, there was no significant difference in Ca and Mg levels after DSW treatment compared to control group. In the present study, OVX-SAMP8 mice exhibited increased BMD and decreased bone loss after 4 months treatment with DSW. The histological and micro-CT 2D and 3D imaging data also demonstrated that BV/TV ratio, trabecular bone numbers, and volume were strongly enhanced in DSW-treated OVX-SAMP8 animals (Figure 4). BMD has been shown to be an important factor to determine the strength of cancellous bone and trabecular bone [33, 34]. In addition to BMD, trabecular structural parameters, such as fractal dimension or tissue volume, could enhance the prediction of bone mechanical quality [35, 36]. These analyses indicated that DSW treatment reduced the bone loss and induced the bone recovery.

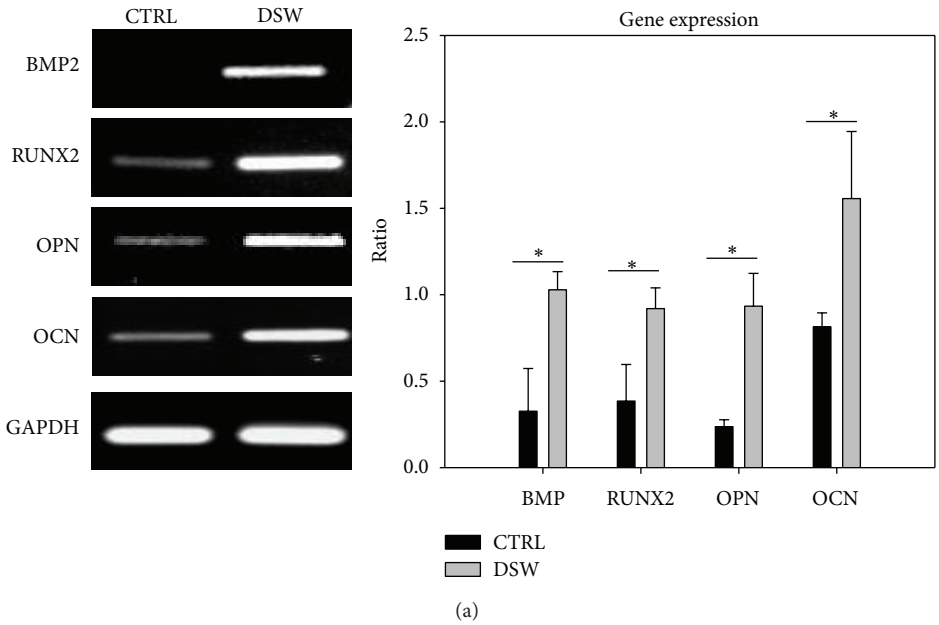

(a)

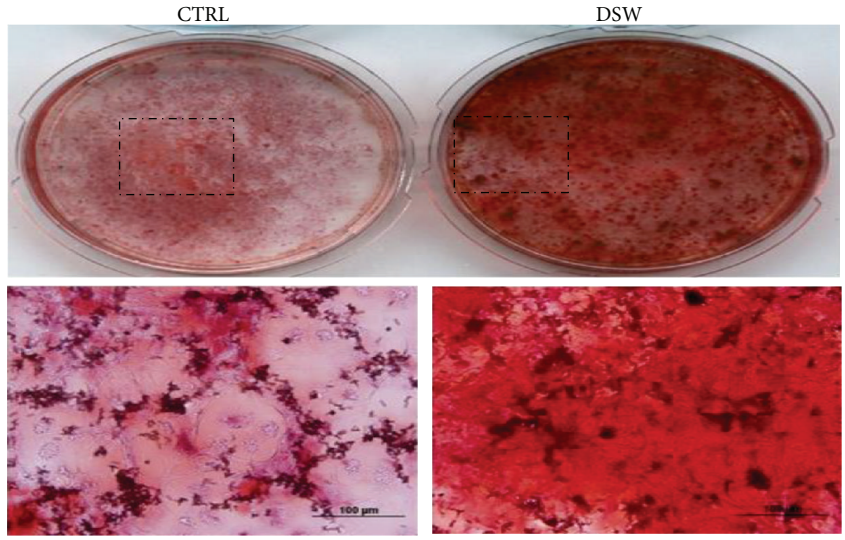

(b)

Figure 6: Comparative expression profile of osteogenic differentiation markers of BMSCs in osteoporotic mice. Effect of DSW on osteogenic mRNA expression in specific genes including bone morphogenetic protein 2 (BMP2), runt-related transcription factor 2 (RUNX2), Osteopontin (OPN) and Osteocalcin (OCN) of BMSCs was quantitatively measured ((a), right/left panel). The maturation of osteogenic differentiation was then examined by Alizarin Red S staining (b), and more calcium nodules were formed in DSW group. Representative results of 3 experiments are demonstrated; $^{*}P < 0.05$ versus CTRL group.

Interestingly, we initially used *in vitro* osteoblast cell culture to determine the effects of DSW on cell proliferation and colony formation; however, no effects were found (data not shown). Metabolism would be an important factor to be considered. Therefore, an alternative approach was designed and shown in general scheme of Figure 5(a). After administration of DSW, BMSCs in DSW-treated mice were then isolated and examined for cell proliferation and colony-forming ability. BMSCs obtained from DSW-treated mice showed markedly induction in osteogenesis-related molecules including BMP2, RUNX2, OPN, and OCN (Figure 6). BMP2 has been shown to regulate osterix via RUNX2 [37], an essential transcription factor for osteoblast differentiation [38]. During osteogenesis, OPN is an intermediate marker, while OCN is a late stage marker of osteoblasts [39]. DSW was found to strongly modulate the molecular determinants in bone microenvironment for osteogenesis. Meanwhile, the higher cell growth and colony formation were also detected in bone marrow cells isolated from DSW-treated mice (Figure 5). Taken together, DSW treatment enhanced bone formation in OVX-SAMP8 mice through metabolism.

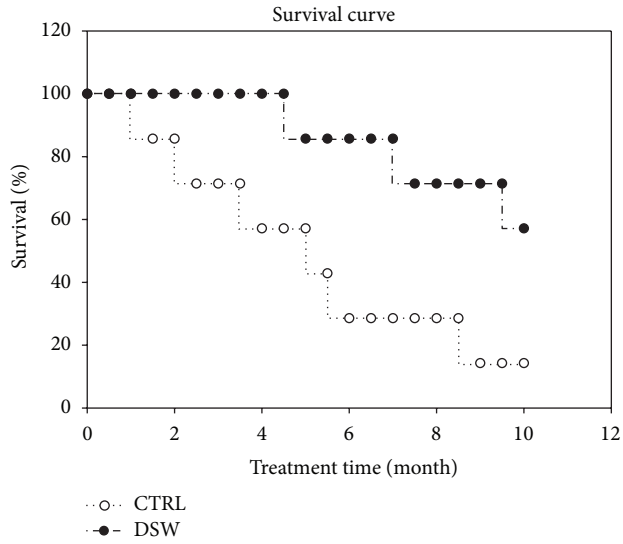

Figure 7: Survival of DSW-treated OVX-SAMP8 mice. The Kaplan-Meyer survival plots of mice from DSW (-•-) and vehicle groups (-○-) were shown.

Our data demonstrated that therapy with DSW appeared to prolong the life span of OVX-SAMP8 mice (Figure 7). Previously, we have shown that cell therapy with growth factors (PRP/NIH3T3-G) prolonged the life span of the osteoporotic mice through the bone mass recovery [16]. Epidemiologic studies indicated that the high mortality of hip fractures patients was 3-fold higher than those of general population. In contrast, the increased bone mass can also reduce the risk of bone fracture and subsequently increase the life expectancy in osteoporotic patients [40–42]. DSW treatment strongly indicated that not only bone mass was recovered but also osteogenesis was induced in osteoporotic mice and then potentially improving (regenerating) their structure and function in degenerative lesions, aging tissue, and organs. Furthermore, DSW treatment could be applied for rejuvenation therapy and bone regeneration for prolongation of life.

5. Conclusion

In this study, the potential effects of DSW on bone regeneration in osteoporosis recovery were investigated; we found that DSW promoted osteoblast viability and increased BMD scores, trabecular bone numbers, and ameliorated symptoms of osteoporosis. These findings suggest that DSW could be a useful treatment for preventing osteoporosis in the near future.

Abbreviations

DSW: Deep sea water
BMD: Bone mineral density
BMSCs: Bone marrow stromal cells.

Conflict of Interests

None of the authors have any conflict of interests with the mentioned trademarks, or companies.

Authors' Contribution

Hen-Yu Liu, Ming-che Liu, Rong Zeng, and Win-Ping Deng contributed equally to this work.

Acknowledgments

The authors thank the Taiwan Mouse Clinic which is funded by the National Research Program for Genomic Medicine (NRPGM) at the National Science Council (NSC) of Taiwan for technical support in bioimaging (micro-CT) and pathology (Histopathology) experiment and gratefully acknowledge Chi-Ming Lee, Wen-Tien Hsiao, and Milligrams Instruments Co., Ltd., for their excellent technical assistance in BMD measurement. Finally, the authors also thank the Taiwan Yes Deep Ocean Water Co., Ltd., for kindly providing the DSW (Deep Ocean Minerals, DOM) for this study. This research was supported by the following grants and agencies: National Science Council (101-2811-B-038-005), (NSC101-2314-B-038-023) and (99-2628-B-038-010-MY3), the Department of Health (DOH) to Taipei Medical University-Center of Excellence for Cancer Research (TMU-CECR, DOH102-TD-C-111-008), the Department of Health (DOH, DOH101-TD-PB-111-NSC010), Teaching Resource Center of Excellence, Taipei Medical University (A0070-1200), and Stem Cell Research Center and Cancer Center, Taipei Medical University Hospital, Taipei, Taiwan.

References

[1] J. D. Adachi, G. Ioannidis, L. Pickard et al., "The association between osteoporotic fractures and health-related quality of life as measured by the Health Utilities Index in the Canadian Multicentre Osteoporosis Study (CaMos)," *Osteoporosis International*, vol. 14, no. 11, pp. 895–904, 2003.

[2] J. A. Robbins, M. L. Biggs, and J. Cauley, "Adjusted mortality after hip fracture: from the cardiovascular health study," *Journal of the American Geriatrics Society*, vol. 54, no. 12, pp. 1885–1891, 2006.

[3] R. S. Braithwaite, N. F. Col, and J. B. Wong, "Estimating hip fracture morbidity, mortality and costs," *Journal of the American Geriatrics Society*, vol. 51, no. 3, pp. 364–370, 2003.

[4] M. E. Wiktorowicz, R. Goeree, A. Papaioannou, J. D. Adachi, and E. Papadimitropoulos, "Economic implications of hip fracture: health service use, institutional care and cost in Canada," *Osteoporosis International*, vol. 12, no. 4, pp. 271–278, 2001.

[5] J. M. Lane, E. H. Riley, and P. Z. Wirganowicz, "Osteoporosis: Diagnosis and treatment," *Journal of Bone and Joint Surgery A*, vol. 78, no. 4, pp. 618–632, 1996.

[6] D. J. Hadjidakis and I. I. Androulakis, "Bone remodeling," *Annals of the New York Academy of Sciences*, vol. 1092, pp. 385–396, 2006.

[7] C. C. Johnston Jr. and C. W. Slemenda, "Changes in skeletal tissue during the aging process," *Nutrition Reviews*, vol. 50, no. 12, pp. 385–387, 1992.

[8] G. Duque, M. Macoritto, N. Dion, L. Ste-Marie, and R. Kremer, "1,25(OH)2D3 acts as a bone-forming agent in the hormone-independent senescence-accelerated mouse (SAM-P/6)," *American Journal of Physiology*, vol. 288, no. 4, pp. E723–E730, 2005.

[9] P. B. Saadeh, B. J. Mehrara, D. S. Steinbrech et al., "Transforming growth factor-β1 modulates the expression of vascular endothelial growth factor by osteoblasts," *American Journal of Physiology*, vol. 277, no. 4, part 1, pp. C628–C637, 1999.

[10] G. Baczyk, T. Opala, P. Kleka, and M. Chuchracki, "Multifactorial analysis of risk factors for reduced bone mineral density among postmenopausal women," *Archives of Medical Science*, vol. 8, no. 2, pp. 332–341, 2012.

[11] R. P. Heaney, "Osteoporosis: management and treatment strategies for orthopaedic surgeons," *Journal of Bone and Joint Surgery A*, vol. 90, no. 11, pp. 2544–2545, 2008.

[12] H. S. Hwang, H. A. Kim, S. H. Lee, and J. W. Yun, "Anti-obesity and antidiabetic effects of deep sea water on ob/ob mice," *Marine Biotechnology*, vol. 11, no. 4, pp. 531–539, 2009.

[13] F. Maehira, Y. Iinuma, Y. Eguchi, I. Miyagi, and S. Teruya, "Effects of soluble silicon compound and deep-sea water on biochemical and mechanical properties of bone and the related gene expression in mice," *Journal of Bone and Mineral Metabolism*, vol. 26, no. 5, pp. 446–455, 2008.

[14] Z. Y. Fu, F. L. Yang, H. W. Hsu, and Y. F. Lu, "Drinking deep seawater decreases serum total and low-density lipoprotein-cholesterol in hypercholesterolemic subjects," *Journal of Medicinal Food*, vol. 15, no. 6, pp. 535–541, 2012.

[15] C. Lee, Y. Kung, J. Wang, T. Lung, and T. Pan, "Enhanced hypolipidemic effect and safety of red mold dioscorea cultured in deep ocean water," *Journal of Agricultural and Food Chemistry*, vol. 59, no. 15, pp. 8199–8207, 2011.

[16] W. Lo, J. Chiou, J. G. Gelovani et al., "Transplantation of embryonic fibroblasts treated with platelet-rich plasma induces osteogenesis in SAMP8 mice monitored by molecular imaging," *Journal of Nuclear Medicine*, vol. 50, no. 5, pp. 765–773, 2009.

[17] H. Liu, A. T. H. Wu, C. Tsai et al., "The balance between adipogenesis and osteogenesis in bone regeneration by platelet-rich plasma for age-related osteoporosis," *Biomaterials*, vol. 32, no. 28, pp. 6773–6780, 2011.

[18] H. Y. Liu, J. F. Chiou, A. T. Wu et al., "The effect of diminished osteogenic signals on reduced osteoporosis recovery in aged mice and the potential therapeutic use of adipose-derived stem cells," *Biomaterials*, vol. 33, no. 26, pp. 6105–6112, 2012.

[19] N. B. Watts, D. K. Jenkins, J. M. Visor, D. C. Casal, and P. Geusens, "Comparison of bone and total alkaline phosphatase and bone mineral density in postmenopausal osteoporotic women treated with alendronate," *Osteoporosis International*, vol. 12, no. 4, pp. 279–288, 2001.

[20] A. Rogers, R. A. Hannon, and R. Eastell, "Biochemical markers as predictors of rates of bone loss after menopause," *Journal of Bone and Mineral Research*, vol. 15, no. 7, pp. 1398–1404, 2000.

[21] P. D. Ross and W. Knowlton, "Rapid bone loss is associated with increased levels of biochemical markers," *Journal of Bone and Mineral Research*, vol. 13, no. 2, pp. 297–302, 1998.

[22] J. Y. Reginster, L. Strause, R. Deroisy, M. P. Lecart, P. Saltman, and P. Franchimont, "Preliminary report of decreased serum magnesium in postmenopausal osteoporosis," *Magnesium*, vol. 8, no. 2, pp. 106–109, 1989.

[23] R. K. Rude and M. Olerich, "Magnesium deficiency: possible role in osteoporosis associated with gluten-sensitive enteropathy," *Osteoporosis International*, vol. 6, no. 6, pp. 453–461, 1996.

[24] G. Candelas, J. A. Martinez-Lopez, M. P. Rosario, L. Carmona, and E. Loza, "Calcium supplementation and kidney stone risk in osteoporosis: a systematic literature review," *Clinical and Experimental Rheumatology*, vol. 30, no. 6, pp. 954–961, 2012.

[25] E. Abed, C. Martineau, and R. Moreau, "Role of melastatin transient receptor potential 7 channels in the osteoblastic differentiation of murine MC3T3 cells," *Calcified Tissue International*, vol. 88, no. 3, pp. 246–253, 2011.

[26] A. Creedon, A. Flynn, and K. Cashman, "The effect of moderately and severely restricted dietary magnesium intakes on bone composition and bone metabolism in the rat," *British Journal of Nutrition*, vol. 82, no. 1, pp. 63–71, 1999.

[27] T. O. Carpenter, S. J. Mackowiak, N. Troiano, and C. M. Gundberg, "Osteocalcin and its message: relationship to bone histology in magnesium-deprived rats," *American Journal of Physiology*, vol. 263, no. 1, part 1, pp. E107–E114, 1992.

[28] J. E. Sojka and C. M. Weaver, "Magnesium supplementation and osteoporosis," *Nutrition Reviews*, vol. 53, no. 3, pp. 71–74, 1995.

[29] A. Cagnacci, B. Bagni, A. Zini, M. Cannoletta, M. Generali, and A. Volpe, "Relation of folates, vitamin B12 and homocysteine to vertebral bone mineral density change in postmenopausal women. A five-year longitudinal evaluation," *Bone*, vol. 42, no. 2, pp. 314–320, 2008.

[30] S. Mora, L. Cafarelli, P. Erba et al., "Differential effect of age, gender and puberty on bone formation rate assessed by measurement of bone-specific alkaline phosphatase in healthy Italian children and adolescents," *Journal of Bone and Mineral Metabolism*, vol. 27, no. 6, pp. 721–726, 2009.

[31] P. Garnero and P. D. Delmas, "Assessment of the serum levels of bone alkaline phosphatase with a new immunoradiometric assay in patients with metabolic bone disease," *Journal of Clinical Endocrinology and Metabolism*, vol. 77, no. 4, pp. 1046–1053, 1993.

[32] R. Dresner-Pollak, M. Mayer, and D. Hochner-Celiniker, "The decrease in serum bone-specific alkaline phosphatase predicts bone mineral density response to hormone replacement therapy in early postmenopausal women," *Calcified Tissue International*, vol. 66, no. 2, pp. 104–107, 2000.

[33] E.-M. Lochmüller, D. Bürklein, V. Kuhn et al., "Mechanical strength of the thoracolumbar spine in the elderly: Prediction from in situ dual-energy X-ray absorptiometry, quantitative computed tomography (QCT), upper and lower limb peripheral QCT, and quantitative ultrasound," *Bone*, vol. 31, no. 1, pp. 77–84, 2002.

[34] C. L. Benhamou, S. Poupon, E. Lespessailles et al., "Fractal analysis of radiographic trabecular bone texture and bone mineral density: two complementary parameters related to osteoporotic fractures," *Journal of Bone and Mineral Research*, vol. 16, no. 4, pp. 697–704, 2001.

[35] Y. Jiang, J. Zhao, P. Augat et al., "Trabecular bone mineral and calculated structure of human bone specimens scanned by peripheral quantitative computed tomography: relation to biomechanical properties," *Journal of Bone and Mineral Research*, vol. 13, no. 11, pp. 1783–1790, 1998.

[36] S. E. Tomten, J. A. Falch, K. I. Birkeland, P. Hemmersbach, and A. T. Høstmark, "Bone mineral density and menstrual irregularities. A comparative study on cortical and trabecular bone structures in runners with alleged normal eating behavior," *International Journal of Sports Medicine*, vol. 19, no. 2, pp. 92–97, 1998.

[37] K. Nakashima, X. Zhou, G. Kunkel et al., "The novel zinc finger-containing transcription factor Osterix is required for osteoblast differentiation and bone formation," *Cell*, vol. 108, no. 1, pp. 17–29, 2002.

[38] T. Komori, H. Yagi, S. Nomura et al., "Targeted disruption of Cbfa1 results in a complete lack of bone formation owing to

maturational arrest of osteoblasts," *Cell*, vol. 89, no. 5, pp. 755–764, 1997.

[39] D. C. Wan, Y. Shi, R. P. Macamuli, N. Quarto, K. M. Lyons, and M. T. Longaker, "Osteogenic differentiation of mouse adipose-derived adult stromal cells requires retinoic acid and bone morphogenetic protein receptor type IB signaling," *Proceedings of the National Academy of Sciences of the United States of America*, vol. 103, no. 33, pp. 12335–12340, 2006.

[40] J. Panula, H. Pihlajamäki, V. M. Mattila et al., "Mortality and cause of death in hip fracture patients aged 65 or older—a population-based study," *BMC Musculoskeletal Disorders*, vol. 12, article 105, 2011.

[41] A. Trombetti, F. Herrmann, P. Hoffmeyer, M. A. Schurch, J. P. Bonjour, and R. Rizzoli, "Survival and potential years of life lost after hip fracture in men and age-matched women," *Osteoporosis International*, vol. 13, no. 9, pp. 731–737, 2002.

[42] J. Empana, P. Dargent-Molina, and G. Bréart, "Effect of hip fracture on mortality in elderly Wwomen: The EPIDOS Prospective Study," *Journal of the American Geriatrics Society*, vol. 52, no. 5, pp. 685–690, 2004.

Hindawi Publishing Corporation
Evidence-Based Complementary and Alternative Medicine
Volume 2013, Article ID 370961, 9 pages
http://dx.doi.org/10.1155/2013/370961

Research Article

Reconstitution of Kidney Side Population Cells after Ischemia-Reperfusion Injury by Self-Proliferation and Bone Marrow-Derived Cell Homing

Hongbao Liu,[1] Weihui Liu,[2] Shuibing Liu,[3] Qiuhong Meng,[3] Ning Zhang,[4] Hanmin Wang,[1] Rong Li,[1] Limin Wang,[5] Peng Zhang,[1] and Shiren Sun[1]

[1] *Department of Nephrology, Xijing Hospital, The Fourth Military Medical University, Xi'an 710032, China*
[2] *PLA Center of General Surgery, General Hospital of Chengdu Army Region, Chengdu 610083, China*
[3] *School of Pharmacy, Fourth Military Medical University, Xi'an 710032, China*
[4] *Department of Hepatobiliary Surgery, Xijing Hospital, Fourth Military Medical University, Xi'an 710032, China*
[5] *Foreign Language Department, Bethune Military Medical NCO's Academy, Shijiazhuang 050081, China*

Correspondence should be addressed to Peng Zhang; xjsnzp@126.com and Shiren Sun; xjsnssr@126.com

Received 29 October 2012; Accepted 16 May 2013

Academic Editor: Yueh-Sheng Chen

The aim of this study was to examine the contribution of side population (SP) cells from kidney and bone marrow for reconstitution of kidney SP pools after ischemia-reperfusion injury (IRI). The SP and non-SP cells in kidneys following IRI were isolated and serially assessed by fluorescence-activated cell sorting. The apoptosis, proliferation, phenotype, and paracrine actions of SP cells were evaluated *in vitro* and *in vivo*. Results indicated that the SP cells from ischemic kidney were acutely depleted within one day following renal IRI and were progressively restored to baseline within 7 days after IRI, through both proliferation of remaining kidney SP cells and homing of bone marrow-derived cells to ischemic kidney. Either hypoxia or serum deprivation alone increased apoptosis of SP cells, and a combination of both further aggravated it. Furthermore, hypoxia *in vivo* and *in vitro* induced the increase in the secretion of vascular endothelial growth factor, insulin-like growth factor 1, hepatocyte growth factor, and stromal cell-derived factor-1α in kidney SP but not non-SP cells. In summary, these results suggest that following renal IRI, kidney SP cells are acutely depleted and then progressively restored to baseline levels by both self-proliferation and extrarenal source, that is, bone marrow-derived cell homing.

1. Introduction

Renal ischemia/reperfusion injury (IRI) is the most common cause for acute kidney injury (AKI) and is associated with high morbidity and mortality [1]. A large number of studies have focused on the endogenous and exogenous mechanisms of kidney repair after ischemic/hypoxic injury [2, 3]. A single step purification method for hematopoietic stem cells, based on the efflux of the DNA binding dye Hoechst 33342, has been reported [4]. The isolated cells were called side population (SP) cells, and they were also found in other nonhematopoietic organs including kidney [5–13]. The kidney SP cells can differentiate into multilineage and ameliorate acute kidney injury [6, 7, 9, 12], suggesting that kidney SP cells are a good target for clinical renal regenerative therapy. Several studies have demonstrated that the kidney SP cells were decreased in the kidney of several kidney injury animal models [7, 9, 13]. The possibility as to whether the depletion of resident SP cells in the injured kidney is provisional or permanent remains to be determined. During renal repair from ischemic injury, the proliferative activity of remaining renal cells increases dramatically and the mobilization of bone marrow-derived cells (BMCs) into the injured kidney improves significantly, which reflects the intrinsic ability of these cells to replace damaged cells with new ones [14–16]. The SP cells, including kidney SP and bone marrow-derived SP, probably have similar responses, as mentioned above, during repair from an ischemic insult, which needs to be determined. Our previous

study has reported that, for the animals with renal IRI, the infusion of exogenous kidney SP cells can significantly improve renal function, accelerate mitogenic response, and reduce cell apoptosis [12]. However, the response of endogenous SP cells to renal IRI still remains unknown; especially, the knowledge about proliferation, reconstitution, and paracrine actions of endogenous SP cells after IRI has not been evaluated *in vivo*.

In the present study, therefore, we attempted to investigate serial changes of the SP cell numbers during renal IRI and to validate the relative relevance among proliferation, restoration, and paracrine actions of SP cells.

2. Materials and Methods

2.1. Animals. C57BL/6 mice (age from 6 to 8 weeks) were provided by the Experimental Animal Center of the Fourth Military Medical University (Xi'an, China). All procedures involving animals were approved by the Institutional Animal Care and Use Committees of the university. Animals bred in the house with constant temperature and humidity, with a 12/12 h light/dark cycle, could freely ingest standard diet and tap water. The results for all experiments had been demonstrated at least six times.

2.2. Induction of Renal IRI. Renal IRI was induced in isoflurane anaesthetized female C57BL/6 mice, and rectal temperature was maintained at 37°C. After a mid-abdominal laparotomy, kidneys were exposed and left kidney pedicles were clamped with atraumatic vascular microclamps for 30 min followed by clamp release to allow reperfusion, as described earlier [12, 17]. Before and 1, 3, and 7 days after unilateral renal IRI, kidney SP and non-SP cells were, respectively, isolated from the ischemic (left) and nonischemic (right) kidneys.

2.3. Histological Score of Kidney (HSK). The excised kidneys were fixed in phosphate-buffered 10% formalin, sectioned, and then stained with hematoxylin and eosin. Evaluation of HSK was performed in a blind manner by a pathologist. HSK was graded on a 4-point scale [2, 18]: 0 = normal histology; 1 = mild damage (less than onethird of nuclear loss (necrosis) per tubular cross section); 2 = moderate damage (greater than one-third and less than two-thirds of tubular cross section showing nuclear loss (necrosis)); 3 = severe damage (greater than two-thirds of tubular cross section showing nuclear loss (necrosis)). The total score per kidney section was calculated by addition of all 10 scores with a maximum possible injury score of 30.

2.4. Isolation of Kidney SP Cells. The protocol was based on a report by Challen et al. [6]. Briefly, anesthetized mice were perfused via the abdominal aorta with normal saline, and the minced kidneys were digested enzymatically in Hank's balanced salt solution (HBSS) (Invitrogen, Sweden) containing 1.2 U/mL Dispase II (Roche, Italy), 0.01% DNAse type I (Sigma, USA), and 7.5 mg/mL collagenase B (Roche) for 20 min at 37°C. The cell suspension was filtered through 40 μm strainers (BD Falcon 2350; BD Pharmingen, USA) to remove debris and washed in HBSS containing 10 mmol/L HEPES (Sigma) and 2% fetal bovine serum (FBS) (Gibco, USA). Cells were resuspended in Dulbecco's modified Eagle's medium (DMEM) (HyClone, USA) containing 2% FBS, 10 mM HEPES, and 5 μg/mL Hoechst 33342 (Sigma), with or without 50 μM verapamil (Sigma), at 1×10^6 cells/mL, incubated at 37°C for 90 min, and washed in cold phosphate-buffered saline (PBS) prior to cell surface antigen staining. Cell surface antigen staining was performed at 4°C for 20 min using monoclonal rat anti-mouse antibodies reactive to CD45-FITC, c-Kit-FITC, CD31-PE, and isotype controls (BD Pharmingen). Propidium iodide (PI, 2 μg/mL) (BD Pharmingen) was added prior to fluorescence-activated cell sorting (FACS) analysis to exclude dead cells.

2.5. Cell Culture. Cells were plated in DMEM containing 10% FBS, 5 μg/mL insulin, 5 μg/mL transferrin, 5 pM thyronine, 50 nM hydrocortisone, 50 nM selenium, and 50 nM prostaglandin (all Sigma) at 37°C in a 95% air/5% CO_2 incubator for 48 h. The conditions that might be observed in ischemia were simulated by hypoxia and by serum deprivation (SD) of the culture medium. For hypoxia exposure, cells were maintained under hypoxic conditions in an airtight chamber (Billups-Rothenberg, USA) containing a gas mixture composed of 95% N_2 and 5% CO_2 at 37°C for 6 h. For SD experiments, cells were washed with serum-free DMEM and placed in serum-free medium under normoxic or hypoxic conditions at 37°C for 6 h.

2.6. Apoptosis Assay. Apoptosis assay was performed by using an Annexin V = FITC apoptosis detection kit (BD Pharmingen) according to the manufacturer's instructions. In brief, cells were rinsed with ice-cold PBS, resuspended in binding buffer, incubated with Annexin V-FITC and PI in the dark for 15 min, and then immediately analyzed by using a FACScan flow cytometer.

2.7. Cell Cycle Assay. Cells were suspended in 1× PBS at a concentration of 1×10^6 cells/mL and then ice-cold 70% ethanol was dropwise added into cell solution. After incubating overnight at 4°C, the cells were resuspended with paraformaldehyde fixation solution and fixed on the surface of ice for 1 h. Cells were then collected by centrifugation and resuspended in PI staining solution containing 0.05% Triton X-100, 100 μg/mL RNase A, and 50 μg/mL PI. After incubating for 30 min at 37°C, cells were immediately analyzed by using the FACScan flow cytometer.

2.8. FACS Analysis. Cell analysis and sorting were performed on a dual-laser FACS Vantage (BD Biosciences, USA). Hoechst 33342 was excited at 355 nm UV light, and fluorescence emission was collected with a 675 nm long-pass filter (Hoechst red) and a 450/20 band-pass filter (Hoechst blue), and a 610 nm dichroic mirror short-pass was used to separate the emission wavelengths. PE, FITC, and PI fluorescence was detected by using a 488 nm argon laser, and live cell gate was defined as the cells being excluded from the cells positive for PI.

2.9. Enzyme Linked Immunosorbent Assay (ELISA). The production of vascular endothelial growth factor (VEGF), insulin- like growth factor 1 (IGF-1), hepatocyte growth factor (HGF), and stromal cell-derived factor-1 (SDF-1α) in the supernatants of SP and non-SP was determined by ELISA using a commercially available ELISA kit (R&D Systems, USA) according to the manufacturer's recommendation. About 1×10^6 cell suspension was cultivated in serum-free or serum-containing DMEM medium for 6 h under the conditions of normoxia or hypoxia. Protein was quantified by BCA protein assay reagent (Pierce, USA). Optical density was measured at 450 nm with wavelength correction at 570 nm. All samples and standards were measured twice.

2.10. Statistical Analysis. Data are presented as mean ± SD. Differences between data means were checked by analysis of variance (ANOVA) or Student's t-test using the SPSS statistical software package (SPSS, Inc., Chicago, IL, USA). A P value of less than 0.05 was considered statistically significant.

3. Results

3.1. Depletion of Kidney SP Cells after Acute Renal IRI. Whole kidney cells were isolated from C57BL/6 mice and stained with Hoechst 33342 dye (Figure 1(a)). FACS analysis of renal isolates from normal animals revealed that the Hoechst-extruding, verapamil-sensitive kidney SP cell fraction showed, on average, 1.36% of the total viable cell population (1.13% to 1.59%). Importantly, the kidney SP pools were significantly depleted by more than 40% within 1 day after IRI. To determine the response of endogenous kidney SP to ischemic kidney injury, adult animals received sham operation and unilateral renal IRI. Immunohistochemistry staining showed that left (ischemic) kidneys from mice at 1 d after IRI had significantly higher histological score of kidney (HSK) than sham-operated kidneys, and the increased HSK was decreased to 50.6 ± 9.1% at 7 d after IRI. In contrast, the HSK in the right (nonischemic) kidneys was not changed during all the observation times. All the above results indicated that the model for unilateral renal IRI had been successfully established (Figure 1(b)). In nonoperated and in sham-operated animals, regional kidney SP levels were similar in the left kidney (data not shown). Interestingly, after unilateral renal IRI, the ischemic (left) kidney, but not nonischemic (right) kidney, showed an acute depletion of SP cells within one day (Figures 1(c) and 1(d)). Importantly, left kidney SP cells were progressively restored to baseline levels within 7 days after IRI. For right kidney, a percentage of the kidney SP cells had no change over time.

3.2. In Vitro Apoptosis of Kidney SP Cells with Hypoxia and SD Alone or in Combination. Since hypoxia and SD are both components of ischemia-reperfusion *in vivo*, we further investigated the impact of the two components on kidney SP and non-SP cell apoptosis *in vitro*. To achieve this goal, kidney SP and non-SP cells were incubated in four kinds of culture conditions for 6 h as follows: DMEM medium supplemented with or without 10% FBS under normoxia or hypoxia (Figure 1(e)). Under hypoxia with FBS condition, it caused more apoptotic (Annexin V^+) cells (in both SP and non-SP groups) than under normoxia with FBS condition; however, hypoxia caused fewer apoptotic cells in SP group than in non-SP group. Meanwhile, under normoxia without FBS, it caused more apoptotic cells (similarly in both SP and non-SP groups) than under normoxia with FBS. Finally, the hypoxia without FBS condition generated the most apoptotic cells among four kinds of culture conditions. In one word, SD alone increased the level of apoptosis both in SP and non-SP cells, and hypoxia further aggravated the SD-induced cell apoptosis.

3.3. The Paracrine Actions of Kidney SP Cells after IRI. We first determined the effects of hypoxia on the secretion of chemokines and mitogenic factors in kidney SP cells. The result showed that hypoxia for 6 h significantly increased the release of VEGF, IGF-1, HGF, and SDF-1α when compared with normoxia in the serum-containing or serum-free media (Figure 2(a)). However, SD markedly reduced the hypoxia-induced increase in the production of these factors (Figure 2(a)). Furthermore, the secretion levels of these factors in non-SP cells did not change by hypoxia and/or SD (Figure 2(b)). Next, we wanted to determine whether hypoxia *in vivo* induced SP cell paracrine actions. In the left kidney, the secretion of growth factors in the SP but not in non-SP cells appeared to be increased within the first day of IRI, peaked on the third day, and rapidly downregulated on the seventh day after injury to the level observed in sham-operated kidneys (Figures 2(c)–2(f)). In the right kidney, however, the secretion levels of these factors in both SP and non-SP cells had no change over time.

3.4. The Proliferation of Kidney SP Cells after IRI. The cellular mechanisms being responsible for reconstituting kidney SP following IRI remain unknown. We, therefore, quantified kidney SP and non-SP in S-G_2M phase from sham-operated and IRI animals, using the cell cycling marker, the DNA binding dye, PI. After IRI, the SP cells in left kidney underwent self-proliferation and reentered the cell cycle on the first day, as marked by a 2.5-fold increase in PI, and remained cycling on the seventh day after IRI (Figure 3(a)). The proliferation of non-SP in left kidney was delayed, with increased PI staining on the seventh day after injury (Figure 3(a)). In the right kidney, the SP proliferation was also delayed and non-SP proliferation had no change over time (Figure 3(b)). In addition, the role of either hypoxia or SD *in vitro* in the proliferation of kidney SP and non-SP cells was also evaluated. The result showed that hypoxia but not SD induced the increase in proliferation *in vitro* in kidney SP cells. However, neither hypoxia nor SD had effect on the proliferation of the kidney non-SP cells (Figure 3(c)).

3.5. Phenotype of Kidney SP Cells after IRI. Characterization by flow cytometry confirmed that the SP cells from normal kidney expressed CD31 (17.5% ± 2.7%) and lacked hematopoietic stem cell markers such as CD45 (2.8% ± 0.7%) and c-Kit (0.7% ± 0.4%). In the kidney SP cells isolated from mice on the first day after IRI, the percentage of cells expressing

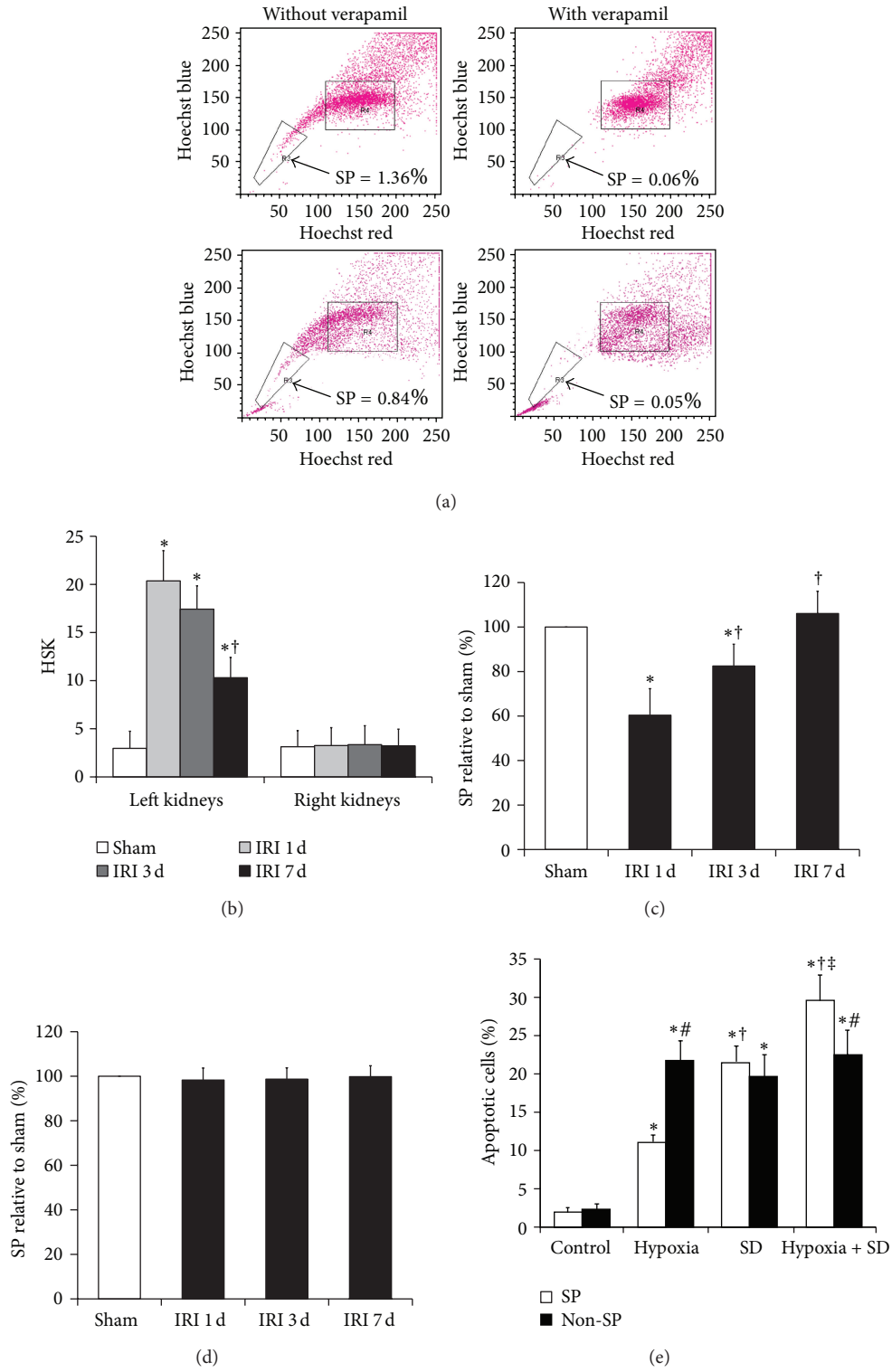

Figure 1: Depletion of SP cells in the ischemic kidney after IRI. (a) Fluorescence-activated cell sorting isolation of SP and non-SP cells in the left kidney from normal animals and IRI animals. Hoechst low SP cells are identified by the R3 area and demonstrate an a decrease in kidney SP cells within 1 day after IRI. (b) The histological score of kidney (HSK) in kidneys from sham-operated and IRI-mice was calculated. $^{*}P < 0.05$ versus sham; $^{\dagger}P < 0.05$ versus IRI 1 d. ((c) and (d)) The SP cells in left (c) and right (d) kidneys from sham-operated (white bars) and IRI (black bars) animals. $^{*}P < 0.05$ versus sham; $^{\dagger}P < 0.05$ versus IRI 1 d. (e) *In vitro* apoptosis analysis of kidney SP and non-SP cells in basal conditions and after simulated ischemia. Cultured kidney SP and non-SP cells were subjected to hypoxia and SD alone or in combination for 6 h. Bar graph described from the FACS-based Annexin V/propidium iodide apoptosis assay. The cells without both hypoxia and SD stimulation were used as controls. $^{*}P < 0.05$ versus control; $^{\dagger}P < 0.05$ versus hypoxia; $^{\ddagger}P < 0.05$ versus SD; $^{\#}P < 0.05$ versus non-SP.

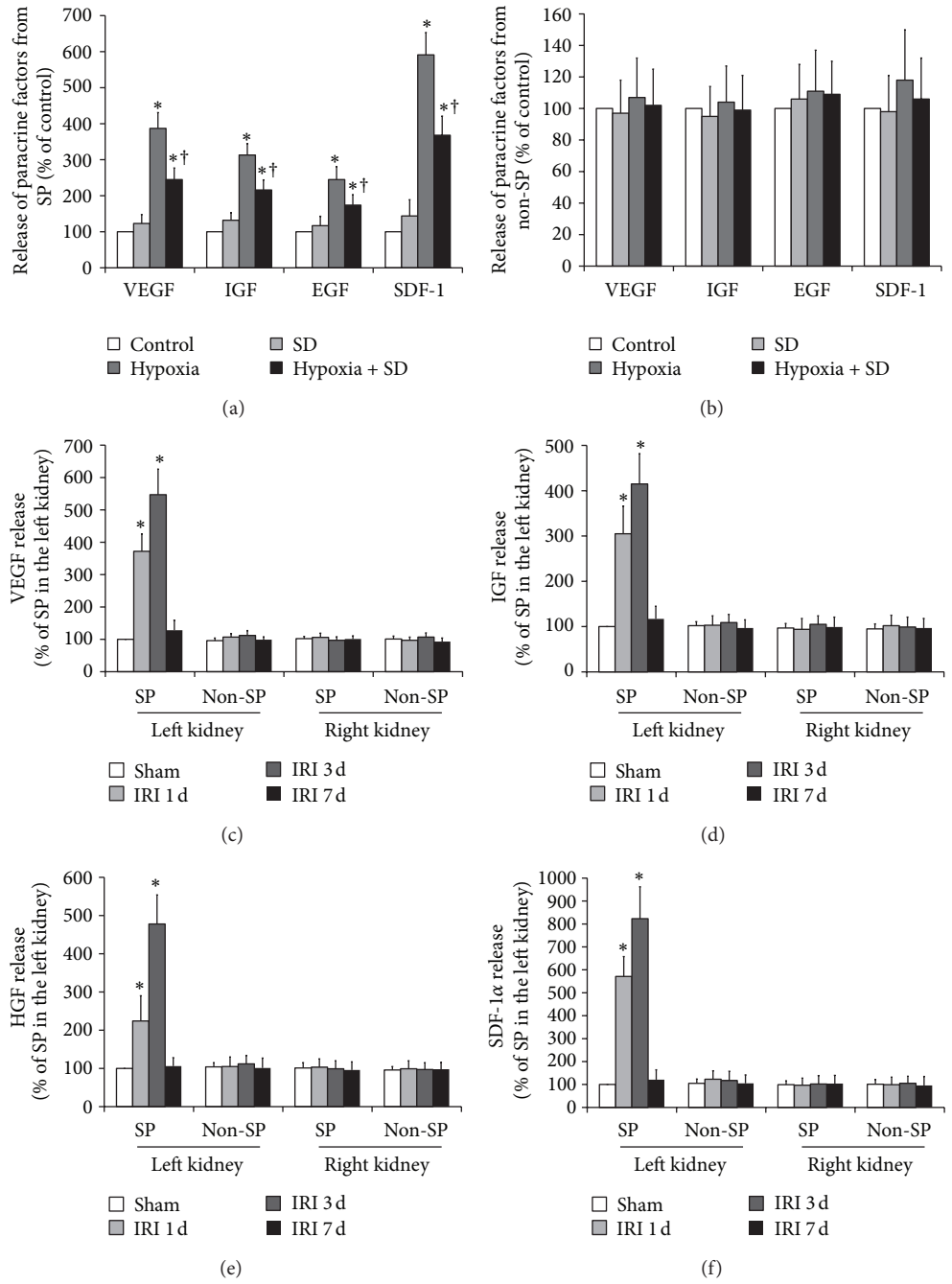

Figure 2: Hypoxia induces the increase in SP cell paracrine actions *in vitro* and *in vivo*. ((a) and (b)) Effect of hypoxia and SD alone or a combination of both on SP and non-SP cell paracrine actions *in vitro*. Cultured kidney SP (a) and non-SP (b) cells were subjected to hypoxia and SD alone or in combination for 6 h, and then the secretion levels of VEGF, IGF-1, HGF, and SDF-1α were quantified by ELISA. The cells without both hypoxia and SD stimulation were used as controls. $^{*}P < 0.05$ versus control; $^{\dagger}P < 0.05$ versus hypoxia. ((c)–(f)) ELISA was performed to detect the secretion levels of VEGF, IGF-1, HGF, and SDF-1α in the SP and non-SP cells separated from the ischemic (left) and nonischemic (right) kidneys of unilateral renal IRI mice. $^{*}P < 0.05$ versus sham.

CD45 and c-Kit was observed to increase in the left kidney compared with the right kidney (Figures 4(a) and 4(b)), suggesting the hematopoietic origin and bone marrow phenotype of these cells. With time following renal injury, the number of CD45 and c-Kit positive cells significantly decreased. Furthermore, CD31 expression was low among left kidney SP on the first day after IRI but increased significantly within 7 days (Figure 4(c)). In the right kidneys after IRI, the percentage of SP cells expressing CD45, c-Kit, and CD31 had no change over time (Figures 4(a)–4(c)). In addition, as shown in Figure 4(d), neither hypoxia *in vitro* nor SD *in vitro* had effect on the expression of CD45, c-Kit, and CD31

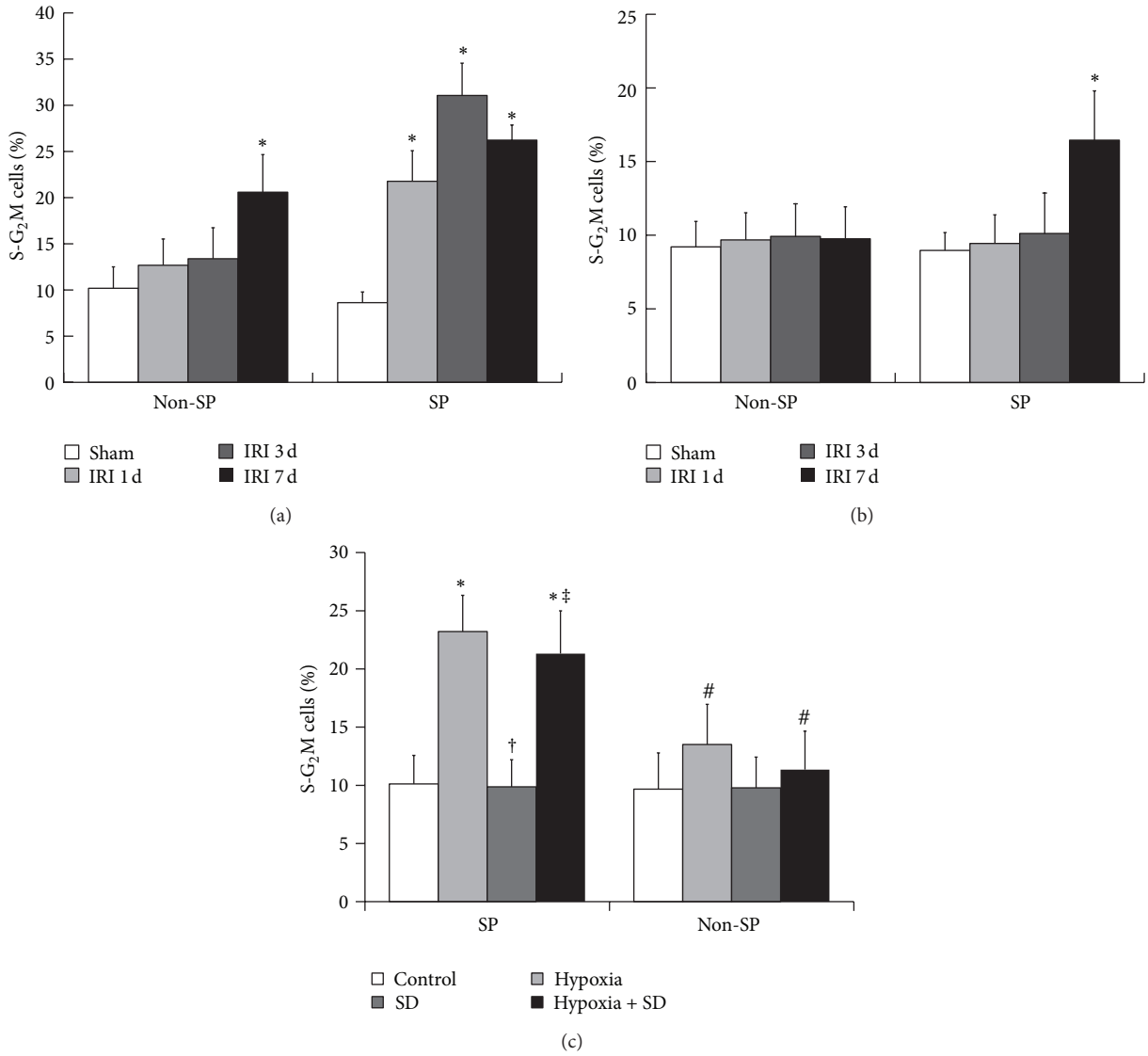

Figure 3: Proliferation of SP cells in the ischemic kidney after IRI. ((a) and (b)) Proliferation of the SP and non-SP cells in the ischemic (a) and nonischemic (b) kidney after IRI. Fractions of S-G_2M kidney SP and non-SP in sham-operated and IRI animals were obtained by propidium iodide staining. $^{*}P < 0.05$ versus sham. (c) Effect of hypoxia and SD alone or a combination of both on cell proliferation *in vitro*. The cells without both hypoxia and SD stimulation were used as controls. $^{*}P < 0.05$ versus control; $^{\dagger}P < 0.05$ versus hypoxia; $^{\ddagger}P < 0.05$ versus SD; $^{\#}P < 0.05$ versus SP.

in the kidney SP cells. In short, these results suggested the possibility about the BMC homing to ischemic kidney and about their immunophenotypic conversion from BMCs to kidney SP cells.

4. Discussion

SP cells have been found in various types of adult tissues including kidney and are presumed to be a stem cell-rich population [4–13]. Protective effects of kidney SP cells have been demonstrated by the findings that infusion of exogenous kidney SP cells can improve renal function in different models of renal injury [6, 7, 9, 12]. However, experiments based on the administration of exogenous SP do not necessarily reflect the physiological role of endogenous SP, and the response of the endogenous SP to renal injury remains incompletely understood.

We first identified the existence of SP cells in adult C57BL/6 mice kidneys and an acute depletion of kidney SP cells on the first day following renal IRI. Next, we wanted to determine whether hypoxia and SD, which were both components of ischemia *in vivo*, could induce the increase in SP apoptosis. As expected, either hypoxia or SD alone increased the level of SP cell apoptosis and a combination of both further aggravated it. Importantly, the hypoxia-induced increase in apoptosis was much less in SP cells than that in non-SP cells, suggesting that SD was the stronger one in kidney SP cells between the two stimuli on cell apoptosis. Because the SP cells were more survivable than non-SP cells under hypoxia conditions, we hypothesized that molecules or

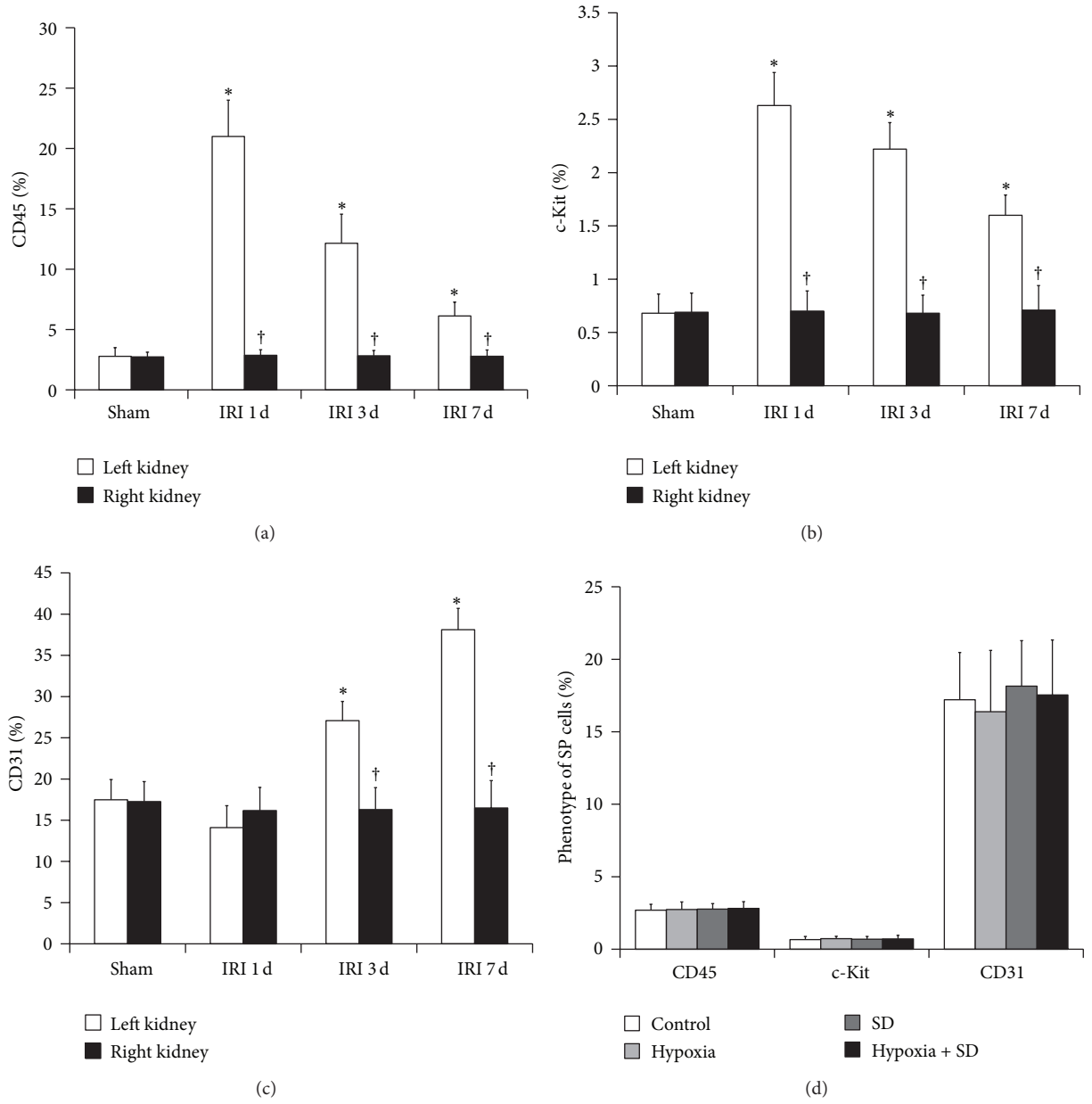

Figure 4: Phenotype of SP cells in the ischemic kidney after IRI. ((a)–(c)) The expression of CD45 (a), c-Kit (b), and CD31 (c) in left (white bars) and right (black bars) kidney SP from sham-operated and IRI animals. $^{*}P < 0.05$ versus sham. $^{\dagger}P < 0.05$ versus left kidney. (d) Effect of hypoxia and SD alone or a combination of both on the expression of CD45, c-Kit, and CD31 *in vitro*. The cells without both hypoxia and SD stimulation were used as controls.

proteins secreted by SP cells could inhibit hypoxia-induced cell apoptosis. As expected, our result showed that, at least in SP cells, hypoxia *in vitro* but not SD *in vitro* induced the enhanced secretion of VEGF, IGF-1, HGF, and SDF-1α. Furthermore, the increased secretion of growth factors was discovered in the SP but not non-SP cells in the ischemic kidney after acute renal IRI. These data suggest the potential role of SP cell paracrine actions in repair after acute renal IRI.

We also evaluated serial changes of kidney SP number during acute renal IRI and, for the first time, discovered that the initial depleted SP cells in the ischemic kidney were progressively restored to baseline levels within 7 days after IRI. Although the clear evidence has showed that renal recovery from ischemic injury requires regeneration of damaged tubular epithelium [14], the relative relevance of regeneration of kidney SP cells in physiopathological conditions still needs to be identified further. In the present study, we confirmed that the proliferation of SP cells was earlier than that of non-SP cells in the ischemic kidney and was delayed in the nonischemic kidney, suggesting that the proliferation of resident kidney SP cells might partially participate in the renewal of kidney SP cells following renal IRI.

Furthermore, immunophenotypic analysis showed that the SP cells obtained from normal kidneys contained very low

levels of cells that expressed CD45 and c-Kit, which were predominant in bone marrow SP cells, suggesting that the kidney SP cells, under physiologic conditions, were a resident nonhematopoietic cell population. Marumo et al. [13] confirmed that kidney SP fraction was reduced by 38% in tubulointerstitial injury caused by unilateral ureteral obstruction, and the number of cells expressing CD45 in kidney SP cells was conversely increased in obstructed kidneys. Although the possibility that BMCs might functionally contribute to the renal regeneration after inducing renal ischemia was still a matter of debate, mobilization of BMCs to injured kidney was clear [19–23]. To determine the possible contribution of SP fraction within BMCs to the injured kidney, the expression of CD45 and c-Kit on SP cells from kidneys was serially investigated. Our results showed that the expression of CD45 and c-Kit was significantly increased in the SP fraction in kidneys from IRI animals compared with sham-operated animals on the first day after surgery, suggesting that the SP cells of BMCs, which were positive for CD45 and c-Kit, might be mobilized and home to ischemic kidney and partly contribute, at least, to maintain and reconstitute the kidney SP pools under renal IRI. In addition, with time following renal injury, the percentage of cells expressing CD45 and c-Kit decreased significantly and the percentage of cells expressing CD31 (vascular endothelial cells marker) increased significantly within 7 days, suggesting that the SP cells in ischemic kidney, which probably originated from resident renal cells or BMCs, could undergo tissue-specific immunophenotypic conversion to participate in restoration of ischemic renal tissue.

In conclusion, these studies demonstrate that the initial depleted kidney SP cells are progressively restored to baseline levels within 7 days after IRI. The reconstitution of this cell population may come from the proliferation of existing SP cells and homing of bone marrow-derived SP cells to ischemic kidney. The kidney SP cells can be used as a therapeutic target which can modulate tissue regeneration in AKI by promoting their activation or preventing their depletion. Further investigation into the function and biological signals of the reconstituted SP cell population following injury is of clinical importance to promote renal regeneration.

Authors' Contribution

H. Liu, W. Liu, S. Liu, Q. Meng, N. Zhang, and H. Wang contributed equally to this work.

Acknowledgments

This work was supported by Grants from National Nature Science Foundation of China (nos. 81000309 and 30900277), Midwestern Excellent Young Scientist Foundation of Chinese Medical Doctor Association (2012), and Natural Science Basis Research Plan in Shaanxi Province of China (no. 2009K12-02).

References

[1] T. Z. Ali, I. Khan, W. Simpson et al., "Incidence and outcomes in acute kidney injury: a comprehensive population-based study," *Journal of the American Society of Nephrology*, vol. 18, no. 4, pp. 1292–1298, 2007.

[2] H. Liu, S. Liu, Y. Li et al., "The role of SDF-1-CXCR4/CXCR7 axis in the therapeutic effects of hypoxia-preconditioned mesenchymal stem cells for renal ischemia/reperfusion injury," *PLoS One*, vol. 7, no. 4, article e34608, 2012.

[3] H. Liu, W. Xue, G. Ge et al., "Hypoxic preconditioning advances CXCR4 and CXCR7 expression by activating HIF-1α in MSCs," *Biochemical and Biophysical Research Communications*, vol. 401, no. 4, pp. 509–515, 2010.

[4] S. Zhou, J. D. Schuetz, K. D. Bunting et al., "The ABC transporter Bcrp1/ABCG2 is expressed in a wide variety of stem cells and is a molecular determinant of the side-population phenotype," *Nature Medicine*, vol. 7, no. 9, pp. 1028–1034, 2001.

[5] S. K. Addla, M. D. Brown, C. A. Hart, V. A. C. Ramani, and N. W. Clarke, "Characterization of the Hoechst 33342 side population from normal and malignant human renal epithelial cells," *American Journal of Physiology—Renal Physiology*, vol. 295, no. 3, pp. F680–F687, 2008.

[6] G. A. Challen, I. Bertoncello, J. A. Deane, S. D. Ricardo, and M. H. Little, "Kidney side population reveals multilineage potential and renal functional capacity but also cellular heterogeneity," *Journal of the American Society of Nephrology*, vol. 17, no. 7, pp. 1896–1912, 2006.

[7] K. Hishikawa, T. Marumo, S. Miura et al., "Musculin/MyoR is expressed in kidney side population cells and can regulate their function," *Journal of Cell Biology*, vol. 169, no. 6, pp. 921–928, 2005.

[8] K. Hishikawa, T. Marumo, S. Miura et al., "Leukemia inhibitory factor induces multi-lineage differentiation of adult stem-like cells in kidney via kidney-specific cadherin 16," *Biochemical and Biophysical Research Communications*, vol. 328, no. 1, pp. 288–291, 2005.

[9] N. Imai, K. Hishikawa, T. Marumo et al., "Inhibition of histone deacetylase activates side population cells in kidney and partially reverses chronic renal injury," *Stem Cells*, vol. 25, no. 10, pp. 2469–2475, 2007.

[10] T. Inowa, K. Hishikawa, T. Takeuchi, T. Kitamura, and T. Fujita, "Isolation and potential existence of side population cells in adult human kidney," *International Journal of Urology*, vol. 15, no. 3, pp. 272–274, 2008.

[11] H. Iwatani, T. Ito, E. Imai et al., "Hematopoietic and nonhematopoietic potentials of Hoechstlow/side population cells isolated from adult rat kidney," *Kidney International*, vol. 65, no. 5, pp. 1604–1614, 2004.

[12] W. Liu, H. Liu, D. Gao et al., "ABCG2 protects kidney side population cells from hypoxia/reoxygenation injury through activation of the MEK/ERK pathway," *Cell Transplantation*, 2013.

[13] T. Marumo, K. Hishikawa, Y. Matsuzaki et al., "Angiotensin II type 1 receptor blockade prevents decrease in adult stem-like cells in kidney after ureteral obstruction," *European Journal of Pharmacology*, vol. 573, no. 1–3, pp. 216–220, 2007.

[14] J. Guo and L. G. Cantley, "Cellular maintenance and repair of the kidney," *Annual Review of Physiology*, vol. 72, pp. 357–376, 2009.

[15] B. D. Humphreys and J. V. Bonventre, "Mesenchymal stem cells in acute kidney injury," *Annual Review of Medicine*, vol. 59, pp. 311–325, 2008.

[16] C. Sagrinati, E. Ronconi, E. Lazzeri, L. Lasagni, and P. Romagnani, "Stem-cell approaches for kidney repair: choosing the

right cells," *Trends in Molecular Medicine*, vol. 14, no. 7, pp. 277–285, 2008.

[17] B. Li, A. Cohen, T. E. Hudson, D. Motlagh, D. L. Amrani, and J. S. Duffield, "Mobilized human hematopoietic stem/progenitor cells promote kidney repair after ischemia/reperfusion injury," *Circulation*, vol. 121, no. 20, pp. 2211–2220, 2010.

[18] S. Gupta, S. Li, M. J. Abedin et al., "Effect of Notch activation on the regenerative response to acute renal failure," *American Journal of Physiology—Renal Physiology*, vol. 298, no. 1, pp. F209–F215, 2010.

[19] J. S. Duffield and J. V. Bonventre, "Kidney tubular epithelium is restored without replacement with bone marrow-derived cells during repair after ischemic injury," *Kidney International*, vol. 68, no. 5, pp. 1956–1961, 2005.

[20] J. S. Duffield, K. M. Park, L. Hsiao et al., "Restoration of tubular epithelial cells during repair of the postischemic kidney occurs independently of bone marrow-derived stem cells," *Journal of Clinical Investigation*, vol. 115, no. 7, pp. 1743–1755, 2005.

[21] E. L. Herzog, L. Chai, and D. S. Krause, "Plasticity of marrow-derived stem cells," *Blood*, vol. 102, no. 10, pp. 3483–3493, 2003.

[22] D. Krause and L. G. Cantley, "Bone marrow plasticity revisited: protection or differentiation in the kidney tubule?" *Journal of Clinical Investigation*, vol. 115, no. 7, pp. 1705–1708, 2005.

[23] R. Poulsom, S. J. Forbes, K. Hodivala-Dilke et al., "Bone marrow contributes to renal parenchymal turnover and regeneration," *Journal of Pathology*, vol. 195, no. 2, pp. 229–235, 2001.

Hindawi Publishing Corporation
Evidence-Based Complementary and Alternative Medicine
Volume 2013, Article ID 642920, 11 pages
http://dx.doi.org/10.1155/2013/642920

Research Article

Garlic-Derived S-Allylmercaptocysteine Ameliorates Nonalcoholic Fatty Liver Disease in a Rat Model through Inhibition of Apoptosis and Enhancing Autophagy

Jia Xiao,[1,2] Rui Guo,[2] Man-Lung Fung,[3] Emily C. Liong,[2] Raymond Chuen Chung Chang,[2] Yick-Pang Ching,[2] and George L. Tipoe[2]

[1] *Center for Gene and Cell Engineering, Shenzhen Institute of Advanced Technology, Chinese Academy of Sciences, Shenzhen 518055, China*
[2] *Department of Anatomy, Li Ka Shing Faculty of Medicine, The University of Hong Kong, Hong Kong*
[3] *Department of Physiology, Li Ka Shing Faculty of Medicine, The University of Hong Kong, Hong Kong*

Correspondence should be addressed to Jia Xiao; jia.xiao@siat.ac.cn and George L. Tipoe; tgeorge@hku.hk

Received 18 December 2012; Revised 11 March 2013; Accepted 12 March 2013

Academic Editor: Yueh-Sheng Chen

Our previous study demonstrated that administration of garlic-derived antioxidant S-allylmercaptocysteine (SAMC) ameliorated hepatic injury in a nonalcoholic fatty liver disease (NAFLD) rat model. Our present study aimed to investigate the mechanism of SAMC on NAFLD-induced hepatic apoptosis and autophagy. Adult female rats were fed with a high-fat diet for 8 weeks to develop NAFLD with or without intraperitoneal injection of 200 mg/kg SAMC for three times per week. During NAFLD development, increased apoptotic cells and caspase-3 activation were observed in the liver. Increased apoptosis was modulated through both intrinsic and extrinsic apoptotic pathways. NAFLD treatment also enhanced the expression of key autophagic markers in the liver with reduced activity of LKB1/AMPK and PI3K/Akt pathways. Increased expression of proapoptotic regulator p53 and decreased activity of antiautophagic regulator mTOR were also observed. Administration of SAMC reduced the number of apoptotic cells through downregulation of both intrinsic and extrinsic apoptotic mechanisms. SAMC also counteracted the effects of NAFLD on LKB1/AMPK and PI3K/Akt pathways. Treatment with SAMC further enhanced hepatic autophagy by regulating autophagic markers and mTOR activity. In conclusion, administration of SAMC during NAFLD development in rats protects the liver from chronic injury by reducing apoptosis and enhancing autophagy.

1. Introduction

Nonalcoholic fatty liver disease (NAFLD) is one of the most common chronic liver diseases in Western countries. It ranges from simple fatty liver (steatosis) to nonalcoholic steatohepatitis (NASH) and even cirrhosis [1]. At present, the pathogenesis of NAFLD is not fully understood. Key events that contribute to the initiation and progression of NAFLD are summarized in a "multi-hit" model [2, 3]. In this model, dysregulated metabolism of free fatty acids (FFAs) is considered as the "first-hit" of NAFLD pathogenesis, which leads to insulin resistance and fat accumulation in the liver. Inflammatory response, oxidative stress, apoptosis, and even autophagy serve as "following-hits" that contribute to the ongoing inflammation (NASH). Emerging data suggest that apoptosis plays a critical role in NAFLD-induced liver injury and in the progression from steatosis to NASH and cirrhosis [4–6]. Moreover, the degree of apoptosis is closely associated with the severity of NASH and the stage of fibrosis [7]. Thus, inhibition of apoptosis in the liver may be a useful treatment strategy of NAFLD.

There are two major apoptotic pathways: intrinsic (mitochondrial) and extrinsic (death receptor) pathways. Both pathways are involved in the pathogenesis of NAFLD [8]. p53 is a transcription factor that controls the activation of both intrinsic and extrinsic apoptotic pathways in response to a variety of stimuli including direct DNA damage, oncogenes,

hypoxia, and survival factor deprivation [9]. For intrinsic pathway, p53 enhances the expression of proapoptotic genes, such as Bak1 and Bax, to facilitate the mitochondria-mediated apoptosis. For extrinsic pathway, apart from the signal transduction of death receptors (e.g., Fas and FADD) on the cell membrane, p53 also activates caspase-8 in the cytosol to promote the caspase signaling cascade [9, 10]. Other members of the Bcl-2 family, such as Bcl-2 and Bcl-XL, antagonize the proapoptotic effects mediated by p53 to act as an antiapoptosis mechanism [11]. However, the relationship between the initiation of NAFLD and apoptosis is still poorly understood.

Macroautophagy (hereafter referred to as autophagy) refers to a process where cytoplasmic materials are sequestered and degraded by lysosomal pathway. As a terminal target of insulin signaling, mTOR negatively controls the activity of ULK1 complex and then regulates the autophagic sequestration via vps34 and beclin1. After that, autophagosomes fuse with lysosome to degrade target cytosolic contents through the action of Atg 5, 12, and LC3 [12]. In the liver, autophagy is believed to exert several important physiological functions, including starvation adaptation, quality control (to prevent the accumulation of degenerating proteins and organelles), and prevention of tumorigenesis [13]. However, the exact role of autophagy during NAFLD progression remains largely unknown.

S-allylmercaptocysteine (SAMC) is a water-soluble compound of aged garlic. It is a major *in vivo* metabolic product of diallyl disulfide and allicin, the organo-sulfur compounds of raw garlic [14]. SAMC has been characterized for its anticancer property both *in vivo* and *in vitro* [15–17]. In addition, SAMC also plays a preventive role in an acetaminophen-induced acute liver injury model through the inhibition of the activity of cytochrome P450 2E1 (CYP2E1) [18]. We previously demonstrated the protective properties of SAMC in both carbon tetrachloride-induced acute liver injury model [19] and NAFLD-induced chronic liver injury model [20]. In these studies, SAMC reduces the key events that contribute to the hepatic damage including oxidative stress, inflammation, and necrosis. However, whether the application of SAMC could alleviate apoptosis in NAFLD liver injury is still largely unknown. In the current study, we investigated the antiapoptotic and autophagic enhancing effects of SAMC in a NAFLD rat model. Signaling pathways regulated by SAMC on hepatic apoptosis and autophagy have also been characterized.

2. Materials and Methods

2.1. Reagents. SAMC pure powder was kindly given by Dr. Patrick M. T. Ling (Queensland University of Technology, Australia) and originally from Wakunaga Co. Ltd (Osaka, Japan). The purity of the SAMC powder is more than 95% by HPLC analysis. It does not contain any other garlic compound such as SAC or allicin. SAMC was dissolved in a phosphate buffered saline containing 10% L-dextrose and 1% gum Arabic (w/v) at pH 4.5. Antibodies against Bcl-2, Bcl-XL, Bak1, Bax, vps34, and phosphorylated phosphoinositide 3-kinase (PI3 K) p85α at Tyr508 were purchased from Santa Cruz Biotechnology (Santa Cruz, CA, USA). Antibodies of phosphorylated liver kinase B1 (LKB1) at Ser428, total LKB1, phosphorylated AMP-activated protein kinase (AMPK) at Thr172, total AMPK, phosphorylated p53 at Ser15, total p53, phosphorylated Akt at Ser473, total Akt, total PI3 K (p85 subunit), cytochrome c, TNF-related apoptosis-inducing ligand (TRAIL), Fas, Fas-associated protein with death domain (FADD), cleaved caspase-3, cleaved caspase-8, phosphorylated mTOR at Ser2448, mTOR, beclin 1, Atg12, LC3 II, and p62 were from Cell Signaling Technology (Danvers, MA, USA).

2.2. Animals and Treatments. Eight weeks healthy female SD rats with body weight ranging from 180–200 g were purchased from the Laboratory Animal Unit (LAU), The University of Hong Kong. Rats were kept under standard conditions for three days before starting of the experiment with free access to animal chow and tap water. The animals were divided into four groups ($n = 7$ in each group), namely, (1) control group; (2) NAFLD group; (3) SAMC treatment only group (200 mg/kg in solvent, intraperitoneal injection, three times per week); and (4) NAFLD and SAMC cotreatment group. Pilot studies on hepatic histology and serum ALT showed that this solvent had no hepatic toxicity. The development of NAFLD in rats, including the recipe and preparation protocols of diet, was performed based on our previously described voluntary oral feeding NAFLD animal model [18]. The optimum dosage of SAMC was previously shown to be effective in protecting the liver from both acute and chronic injury [19, 20]. Instead of oral administration in a dietary supplement form, SAMC was intraperitoneally injected to avoid possible degradation prior to absorption through the gastrointestinal tract (GIT). After eight weeks, the rats were euthanized by an overdose of anesthesia according to the protocols approved by the Committee on the Use of Live Animals in Teaching and Research at The University of Hong Kong. The Laboratory Animal Unit of the University of Hong Kong is fully accredited by the Association for Assessment and Accreditation of Laboratory Animal Care International (AAALAC international). Liver samples were collected for further analysis.

2.3. Processing of Tissue and TUNEL Assay. Liver tissue samples were fixed in 10% phosphate-buffered formalin processed for histology and embedded in paraffin blocks. Five-micrometer tissue sections were subjected to hematoxylin and eosin (H&E) staining and terminal deoxynucleotidyl transferase-mediated dUTP nick-end labeling (TUNEL) assay using an *in situ* cell death detection kit (Roche Diagnostics, Basel, Switzerland). After H&E staining, hepatic injury was evaluated by using the NAFLD activity score (NAS) system as previously described [20]. For TUNEL assay, TUNEL-positive parenchymal and nonparenchymal cell signals were quantified in terms of the intensity of the red stain. This parameter is represented by the mean optical density in ten random fields per section per animal using the ImageJ software (NIH, Bethesda, MD, USA).

2.4. Western Blot Analysis. Cytosolic protein of each liver sample was extracted by using NE-PER protein extraction system (Pierce Biotechnology, Rockford, IL, USA) with the addition of Halt phosphatase inhibitor cocktail (Pierce). Before Western blot, protein was diluted and mixed with 2× sample buffer (0.1 M Tris-HCl, pH 6.8, 20% glycerol, 4% sodium dodecyl sulfate, 0.2% Bromophenol Blue, 5.25% β-mercaptoethanol). The mixture was denatured at 99°C for 5 min and followed by electrophoresis in a 10% polyacrylamide gel. The protein was then transferred to an Immun-Blot PVDF Membrane (Bio-Rad) in a TE series transfer electrophoresis unit (Hoefer Inc., Holliston, MA, USA). The membrane was then incubated in blocking buffer (5% nonfat milk powder in TBST, 100 mM Tris-HCl, pH 7.5, 0.9% NaCl, 0.1% Tween 20) for 1 hour followed by incubation with appropriate primary antibodies in TBST overnight at 4°C with gentle agitation. On the following day, the membrane was washed with TBST and incubated with appropriate secondary antibodies for 2 h at room temperature. Beta-actin was used as the internal control. After washing off the unbound antibody with TBST, the expression of the antibody-linked protein was determined by an ECL Western Blotting Detection Reagents (GE Healthcare). The optical density of the bands was measured and quantified by ImageJ software (National Institute of Health, MD). The ratio of the optical density of the protein product to the internal control was calculated and was expressed as a percentage of the control expression by ImageJ.

2.5. Statistical Analysis. Data from each group were expressed as means ± SEM. Statistical comparison between groups was done using the Kruskal-Wallis test followed by Dunn's post hoc test to compare all groups. A $P < 0.05$ was considered to be statistically significant (Prism 5.0, Graphpad software, Inc., San Diego, CA, USA).

3. Results

3.1. SAMC Cotreatment Improved Hepatic Histology during NAFLD Development. Eight-week induction of NAFLD by high-fat diet induced showed increase in lipid accumulation and inflammatory foci deposition in the rat liver. SAMC cotreatment significantly improved the hepatic histology by reducing the fatty droplets and inflammatory foci number without influencing the healthy rats (Figures 1(a)–1(d)). NAS quantification of liver sections further confirmed the beneficial effects of SAMC cotreatment on hepatic histology (Figure 1(e)).

3.2. Addition of SAMC Reduced Apoptosis in the Liver during NAFLD Development. After 8 weeks of NAFLD induction using high-fat diet, hepatic apoptosis in NAFLD rats was more evident than that in other three groups (~3.5-fold), as shown by the quantification of TUNEL assay staining (Figure 2(e)). Cotreatment with 200 mg/kg SAMC significantly reduced the intensity of hepatic apoptotic positive signal comparable to the control level in the liver section (Figures 2(a)–2(d)). Vehicle-treated SAMC group rats did not show increase in the intensity of apoptotic signals when compared with the control group (Figure 2(c)). As the central apoptotic signaling pathway, caspase-3 is activated under the signals from both intrinsic and extrinsic apoptotic pathways [21]. In NAFLD rats, the expression level of cleaved (activated) caspase-3 was markedly higher than the control level (~7.2-fold), which was consistent with the TUNEL assay. Addition of SAMC significantly and markedly reduced the level of the activated caspase-3 induced by a high-fat diet (Figure 2(f)).

3.3. Intrinsic Apoptotic Signaling Pathway Components Involved in SAMC Attenuation. In NAFLD rats, the protein level of phosphorylated p53 was highly elevated, indicating an activation of the master regulator of cellular apoptosis. Cotreatment with SAMC during NAFLD development significantly reduced the phosphorylated p53 expression to the control level without significantly disturbing its baseline and the total form of p53 expressions (Figure 3(a)). As an important intrinsic intermediate in apoptosis, the protein level of cytochrome c was also upregulated in NAFLD rats but attenuated in SAMC cotreatment rats (Figure 3(b)). The antiapoptotic members of the Bcl-2 family (Bcl-2 and Bcl-XL) showed inhibited expression during the development of NAFLD, while the level of proapoptotic members (Bak1 and Bax) was upregulated (Figures 3(c)–3(f)). Administration of SAMC potently counter-acted the effects of NAFLD on these Bcl-2 family members through the intrinsic apoptotic pathway.

3.4. Extrinsic Apoptotic Signaling Pathways Components Involved in SAMC Attenuation. To further examine the effects of NAFLD and SAMC on the extrinsic apoptotic pathway, protein expressions of key extrinsic apoptotic pathway components, including Fas, TRAIL, FADD, and cleaved caspase-8, were measured by Western blot. The expression level of Fas, TRAIL, FADD, and cleaved caspase-8 was upregulated during the NAFLD progression by 7.1-fold, 2.0-fold, 3.2-fold, and 1.7-fold, respectively. Administration of SAMC significantly reduced the elevated expressions of these proteins comparable to the control levels (Figures 4(a)–4(d)). SAMC treatment alone did not influence the basal expression of TRAIL and cleaved caspase-8 but increased basal Fas level and decreased basal FADD level.

3.5. SAMC Alleviated Hepatic Apoptosis through Targeting LKB1/AMPK and PI3 K/Akt Pathways. To explore the signaling pathways involved in SAMC attenuated apoptosis, we measured the phosphorylation and total forms of key components from two kinase pathways, namely, LKB1/AMPK and PI3 K/Akt signaling pathways. Development of NAFLD in rats inhibited the phosphorylation of LKB1, AMPK, PI3 K, and Akt proteins (Figures 5(a)–5(d)). The influence of NAFLD on total LKB1, AMPK, and Akt was not obvious, while total PI3 K expression was inhibited by NAFLD. Addition of SAMC dramatically restored the phosphorylation form of LKB1 and Akt to levels that were higher than control (Figures 5(a) and 5(d)). Treatment of SAMC also upregulated

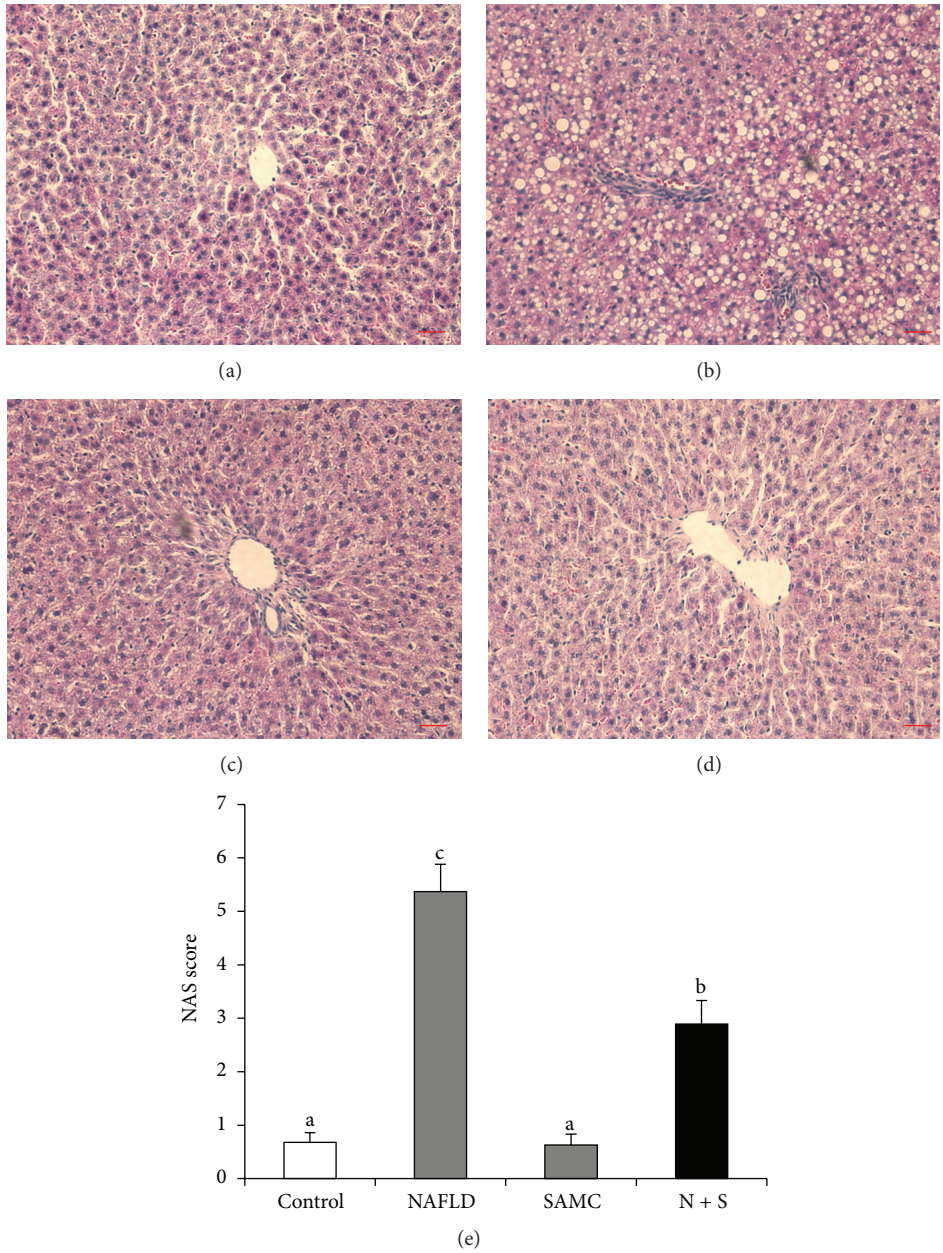

Figure 1: Cotreatment with SAMC during NAFLD development improved hepatic histology in rats. ((a)–(d)) Representative images of H&E staining in the rat liver sections ((a) control, (b) NAFLD, (c) SAMC, (d) NAFLD + SAMC) and (e) quantitative data of NAS score of H&E staining. Data presented are expressed as Mean ± SEM ($n = 7$) and experimental groups marked by different letters represented significant differences between groups at $P < 0.05$ (Kruskal-Wallis test followed by Dunn's post hoc test). Magnification: 200x. Bar: 20 microns. N + S: NAFLD + SAMC cotreatment.

the phosphorylated and total protein expressions of PI3 K when compared with the NAFLD group (Figure 5(c)). For phosphorylated AMPK, SAMC also slightly restored its level when compared with the NAFLD rat level, although the change was not statistically significant (Figure 5(b)).

3.6. SAMC Treatment Further Enhanced Autophagy through Inhibition of mTOR Activity. NAFLD rats showed increased expression level of autophagic markers during NAFLD progression, including vps34, beclin 1, Atg 12, and LC3 II, with inhibited phosphorylation level of autophagic inhibitor mTOR (Figures 6(a)–6(e)). Interestingly, cotreatment with SAMC further enhanced the expression level of vps34, beclin 1, Atg 12, and LC3 II. It also further decreased the phosphorylation of mTOR, indicating a further induction of hepatic autophagy after NAFLD progression through inhibition of mTOR activity (Figures 6(a)–6(e)). As an ubiquitin binding protein for autophagy, the protein expression of p62 was downregulated in the NAFLD group and further reduced by the cotreatment of SAMC (Figure 6(f)).

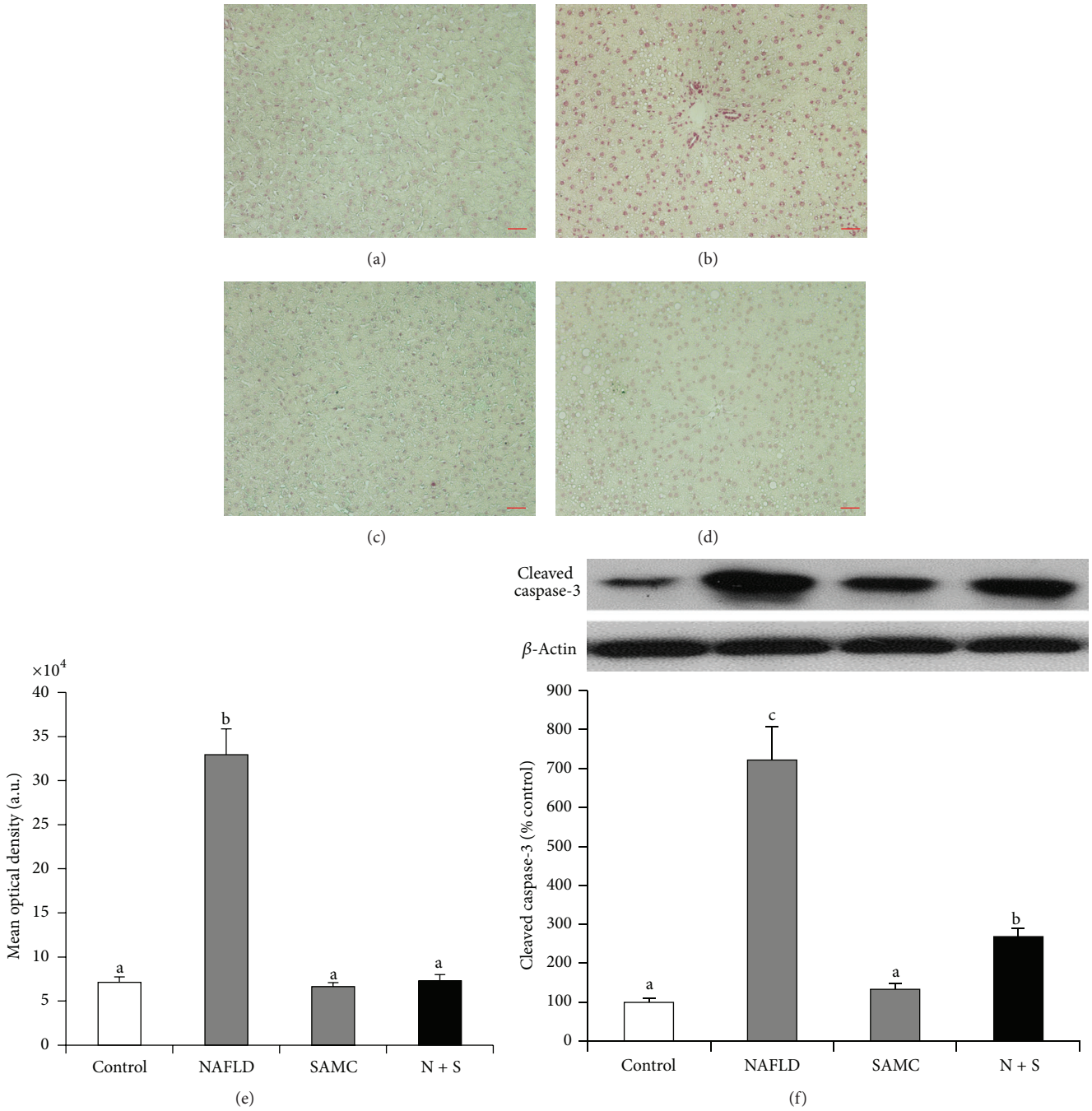

Figure 2: Addition of SAMC during the development of NAFLD reduced the hepatic apoptosis in rats. ((a)–(d)) Representative results of TUNEL assay in the rat liver sections by fast red staining ((a) control, (b) NAFLD, (c) SAMC, (d) NAFLD+SAMC) and (e) quantitative data of TUNEL assay results (a.u. = arbitrary unit). (f) Protein expression of cleaved (activated) caspase-3 was measured by Western blot and then quantified by ImageJ software. Data presented are expressed as mean ± SEM ($n = 7$), and experimental groups marked by different letters represented significant differences between groups at $P < 0.05$ (Kruskal-Wallis test followed by Dunn's post hoc test). Magnification: 200x. Bar: 20 microns. N + S: NAFLD + SAMC cotreatment.

4. Discussion

Despite the huge effort put in the prevention and treatment of NAFLD from researchers and clinicians, there are few options to retard or even reverse the progression of this disease. As to date, weight loss is the most recognized therapeutic method to improve liver injury induced by NAFLD [22]. Recently, several drugs have been assessed for the treatment of NAFLD, including antiobesity regimens, insulin sensitizers, antihyperlipidemics, and antioxidants. However,

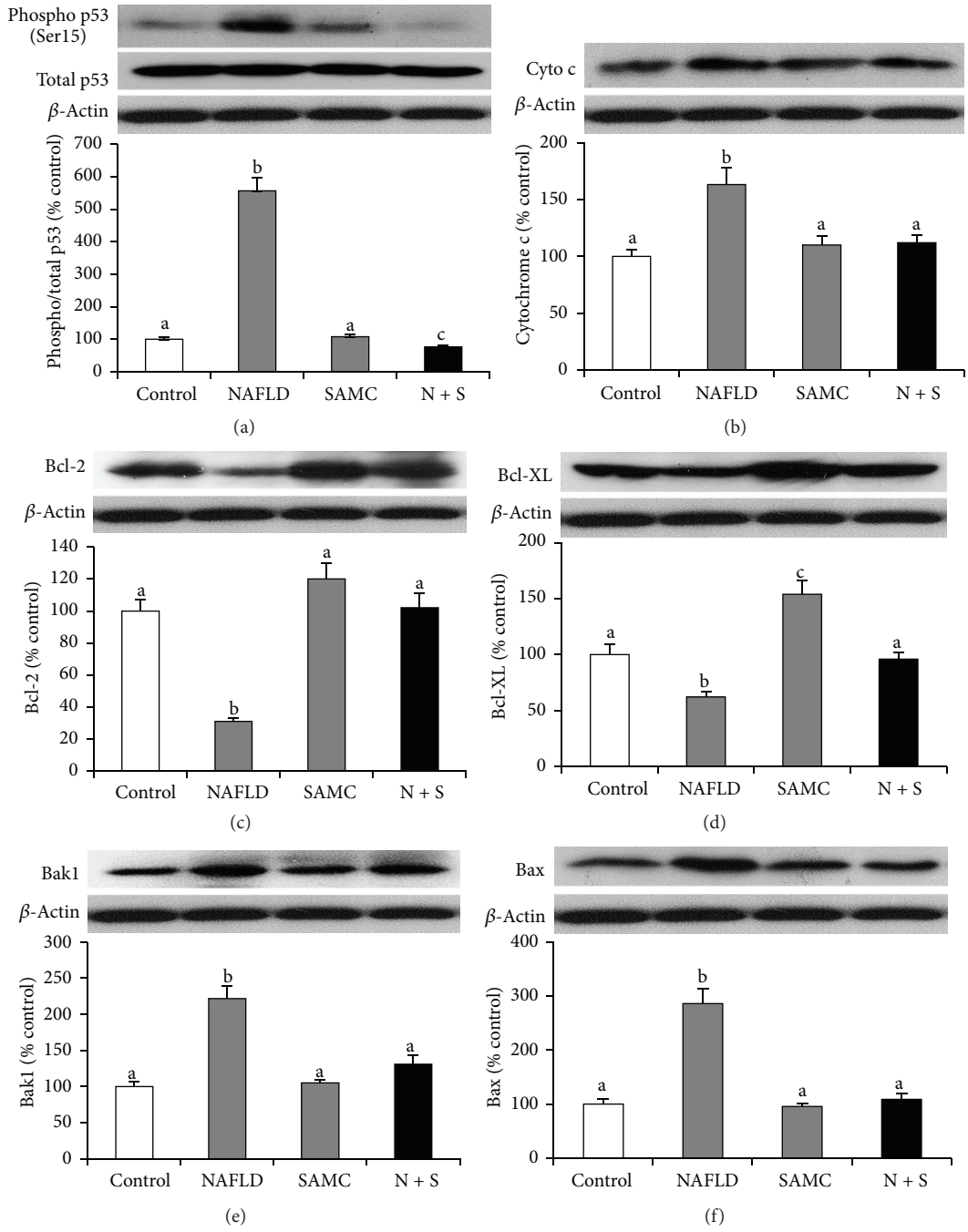

Figure 3: Addition of SAMC attenuated intrinsic apoptotic pathway components through p53 during the development of NAFLD. Protein expressions of (a) phosphorylated and total p53, (b) cytochrome c, (c) Bcl-2, (d) Bcl-XL, (e) Bak1, and (f) Bax were measured by Western blot and then quantified by ImageJ software. Data presented are expressed as mean ± SEM ($n = 7$), and experimental groups marked by different letters represented significant differences between groups at $P < 0.05$ (Kruskal-Wallis test followed by Dunn's post hoc test). N + S: NAFLD + SAMC cotreatment.

a few of them showed very positive outcomes [23]. We have reported that administration of 200 mg/kg SAMC during the development of NAFLD in a rat model could attenuate the histolopathogical changes, lipid metabolism dysfunction, oxidative stress, and inflammation through kinase- and transcription-factor-dependent pathways with minimal side effects on healthy animals [20]. In the current study, we demonstrated the antiapoptotic and proautophagic properties of SAMC cotreatment. During NAFLD development, both intrinsic and extrinsic apoptotic pathways have been activated to transduce death signals to the functional protein caspase-3 under the actions of p53. As the upstream regulating pathways, both LKB1/AMPK and PI3 K/Akt pathways were inhibited to further facilitate the process of apoptosis.

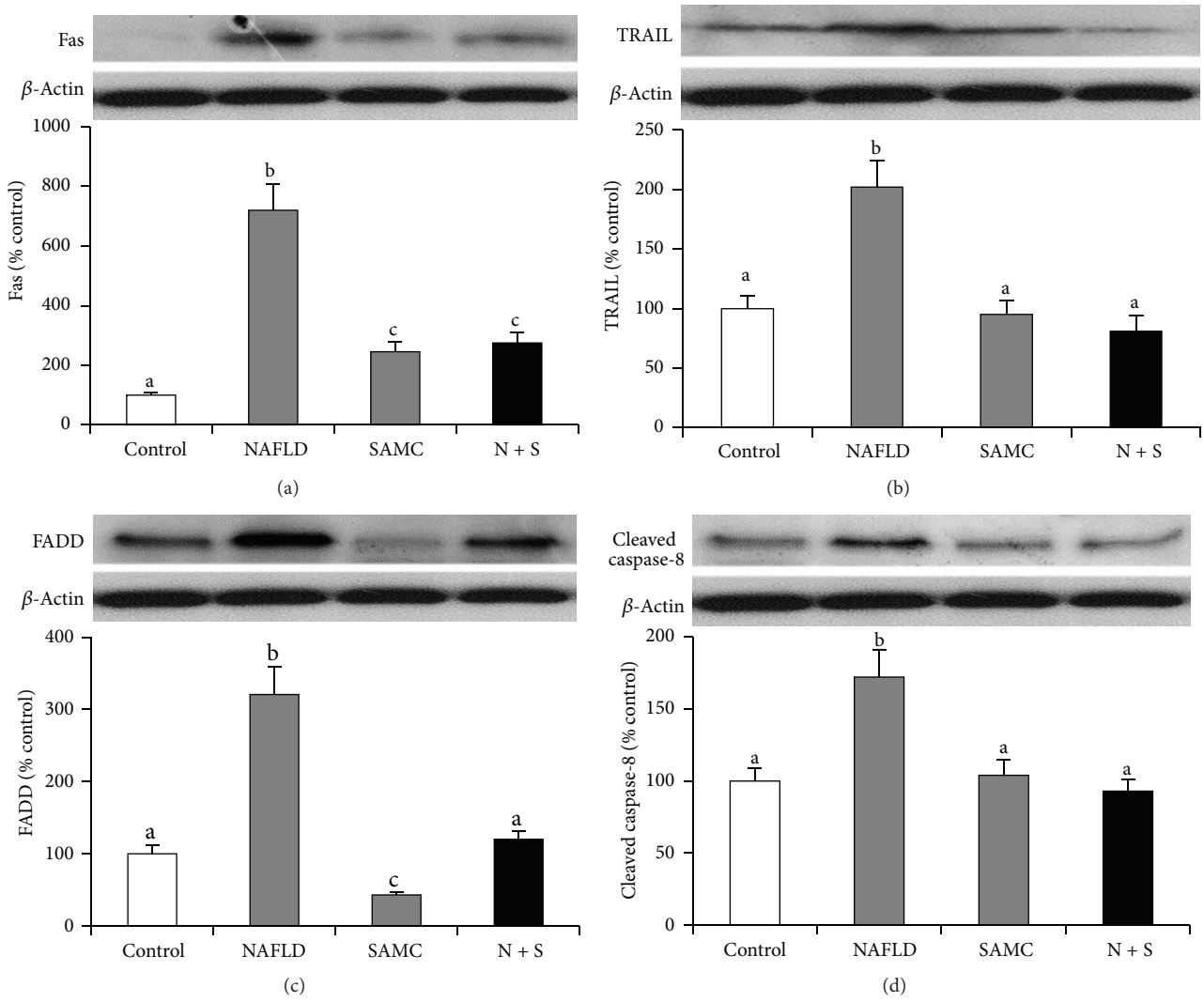

Figure 4: Addition of SAMC attenuated extrinsic apoptotic pathway components during the development of NAFLD. Protein expression of (a) Fas, (b) TRAIL, (c) FADD, and (d) cleaved caspase-8 were measured by Western blot and then quantified by ImageJ software. Data presented are expressed as mean ± SEM ($n = 7$), and experimental groups marked by different letters represented significant differences between groups at $P < 0.05$ (Kruskal-Wallis test followed by Dunn's post hoc test). N + S: NAFLD + SAMC cotreatment.

Addition of SAMC targeted both intrinsic and extrinsic pathways through restoring the LKB1/AMPK and PI3 K/Akt pathways, leading to reduced caspase-3 activity and apoptosis in the liver. In addition, treatment of SAMC further enhanced the hepatic autophagy through the inhibition of mTOR, contributing to the ameliorative effects of SAMC.

Apoptosis of liver cells and adipocytes is often found in NAFLD patients and experimental animals [4, 24]. It is considered as a critical factor for the progression of NAFLD to NASH [8]. Inhibition of excessive apoptosis in the liver may be helpful in the treatment of NASH experimentally and clinically. In response to cellular damage, such as hypoxia, DNA damage, and fat accumulation, the p53 tumor suppressor is activated to inhibit cell proliferation through promotion of intrinsic and extrinsic apoptotic pathways [9]. Previous study found that the extrinsic pathway of apoptosis (especially the activation of Fas/FasL system) may be a central event for the induction of apoptosis in NAFLD [7, 25]. Another report also showed that the activation of p53 and TRAIL receptor expression is associated with apoptosis in a methionine and choline deficient (MCD) diet model [26]. Therefore, it is very clear that both intrinsic and extrinsic pathways of apoptosis are activated in NAFLD despite the action of p53, which is consistent with our current findings of clinically relevant and not genetically modified NAFLD rat model [27]. Interestingly, several previous reports demonstrated that in cancer cell, addition of SAMC induced apoptosis by microtubule depolymerization, JNK1, and caspase-3 activation [17, 28]. The discrepancy of results between these reports and our current study may be due to different microenvironment. In cancer cells, apoptosis is a beneficial event which can retard the proliferation of tumor cells, whereas in NAFLD

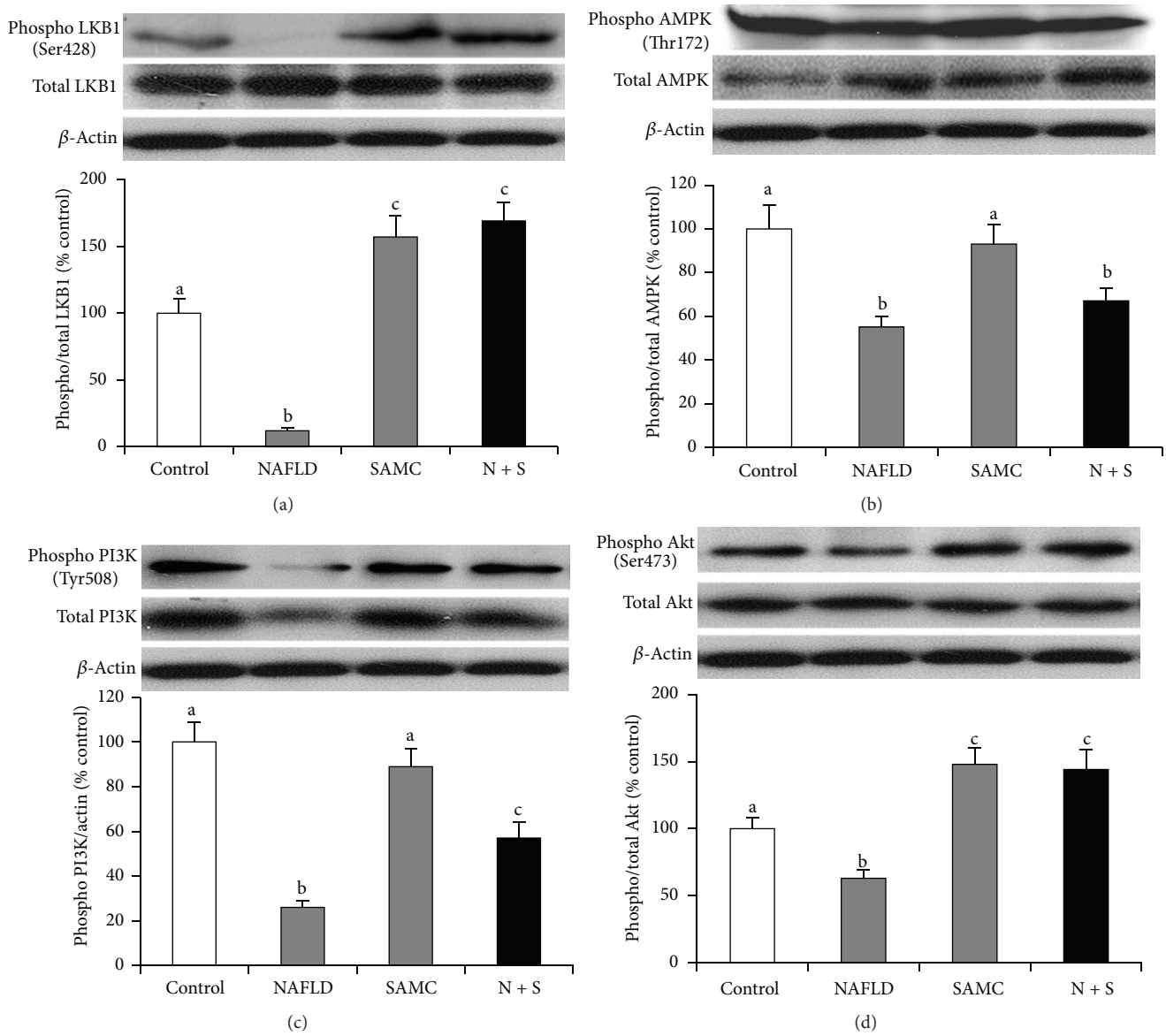

Figure 5: Addition of SAMC reduced NAFLD-induced hepatic apoptosis via modulating the LKB1/AMPK and PI3 K/Akt pathways. Protein expressions of phosphorylated and total (a) LKB1, (b) AMPK, (c) PI3 K, and (d) Akt were measured by Western blot and then quantified by ImageJ software. Data presented are expressed as mean ± SEM ($n = 7$), and experimental groups marked by different letters represented significant differences between groups at $P < 0.05$ (Kruskal-Wallis test followed by Dunn's post hoc test). N + S: NAFLD + SAMC cotreatment.

rats, apoptosis is a detrimental event responsible for the progression and severity of NAFLD. Therefore, SAMC may exert distinct action on apoptosis under different circumstances, whichever is more beneficial to the host. Indeed, the underlying mechanisms for this interesting phenomenon require further investigations.

The detailed function and mechanism of autophagy in NAFLD development are not fully elucidated. Recent studies pointed out that autophagy may selectively target lipid droplets within hepatocytes for degradation, leading to reduction of steatosis. This process is called lipophagy [29]. Pharmacological inhibition of vps34 by 3-methyladenine (3MA) increases the triglyceride (TG) contents in normal cell or cell treated with unsaturated fatty acid. Inhibition of negative regulator of autophagy, mTOR, by rapamycin decreases oleic acid-induced TG levels in cultured hepatocytes [29, 30] and fatty liver mouse model [31]. Therefore, enhancing autophagy is considered as a novel therapeutic strategy for NAFLD therapy [32]. In this study, SAMC enhanced the hepatic autophagy during NAFLD development, with further reduced activity of mTOR, indicating a mTOR-directed pathway. Whether this process is directly related to the reduction of lipid contents in hepatocytes needs future investigations.

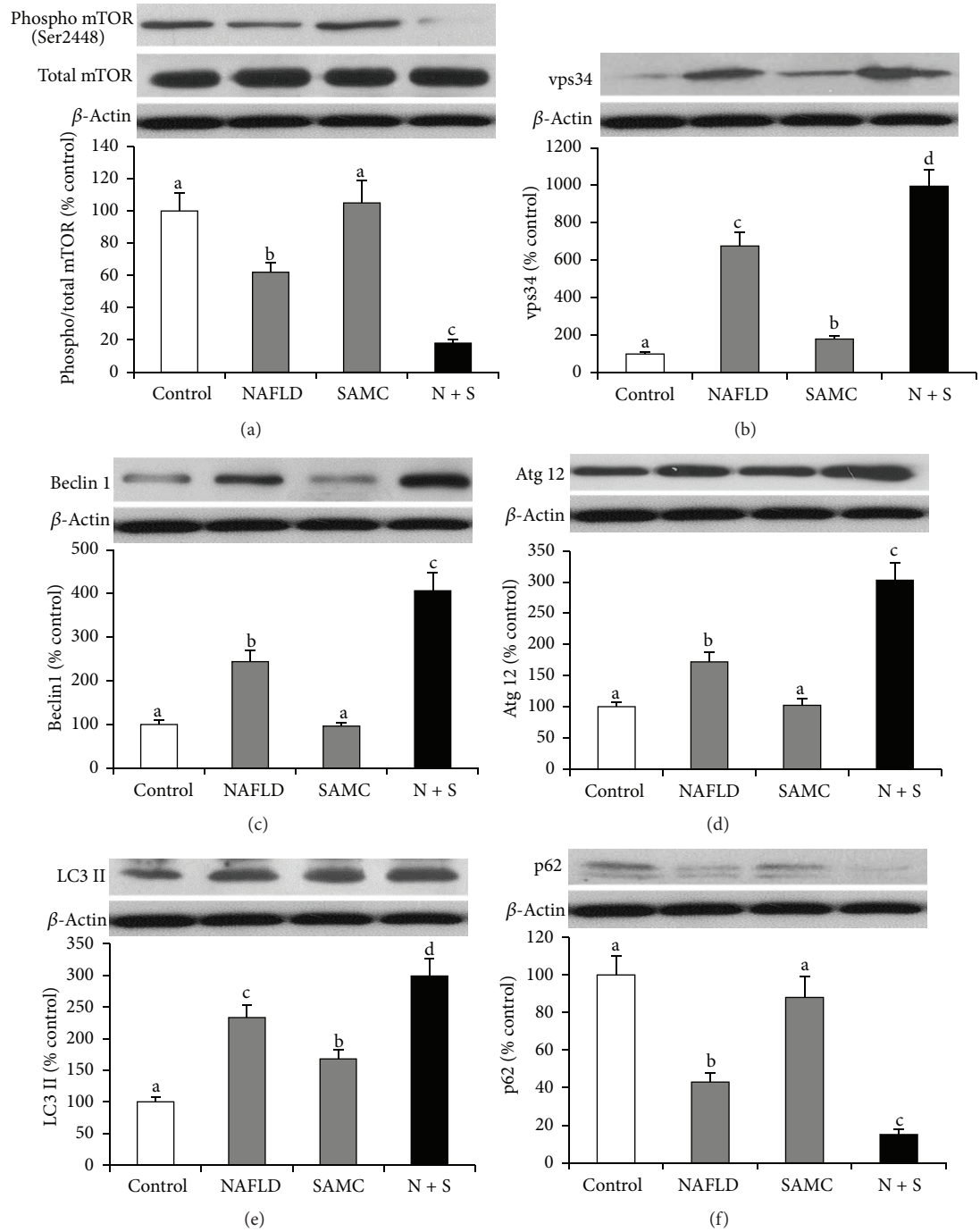

Figure 6: Cotreatment with SAMC further enhanced hepatic autophagy through inhibition of mTOR activity. Protein expressions of (a) phosphorylated and total mTOR, (b) vps34, (c) beclin 1, (d) Atg 12, (e) LC3 II and (f) p62 were measured by Western blot and then quantified by ImageJ software. Data presented are expressed as mean ± SEM ($n = 7$), and experimental groups marked by different letters represented significant differences between groups at $P < 0.05$ (Kruskal-Wallis test followed by Dunn's post hoc test). N + S: NAFLD + SAMC cotreatment.

To further investigate the upstream signaling regulators of apoptosis and autophagy in the liver, we assessed the phosphorylation and total forms of LKB1/AMPK and PI3 K/Akt pathways and found that reactivation of these two pathways contributed to the cell survival during NAFLD. AMPK is an important enzyme response to energy deprivation and, in some cases, cellular stress to induce apoptosis through the AMPK-p53 axis [33]. During NAFLD, AMPK increases the transport of FFAs into the mitochondria, as well as promotes β-oxidation, thus restoring energy balance [34]. In many cases, activation of AMPK protected cells from apoptosis. In an iron-induced hepatic oxidative stress and liver injury

model, addition of sauchinone, a bioactive lignan, activated the LKB1/AMPK pathway, resulting in inhibition of apoptosis in the liver [35]. Moreover, an *in vitro* study using HepG2 cell line found that resveratrol attenuates arachidonic acid and iron-induced apoptosis through activation of LKB1/AMPK pathway [36]. Recent study found that activation of hypothalamic autophagy PI3 K/Akt pathway has also been found to play an important role in the impairment of mitochondria during NAFLD development. In a high-fat diet fed NAFLD rat model, reduced phosphorylated form of PI3 K and Akt and total form of PI3 K were observed with hepatic apoptosis. Treatment of pharmacological inhibitors of PI3 K or Akt instead of high-fat diet mimicked such phenomena [37]. Thus, in this study, the modulation of the activity of LKB1/AMPK and PI3K/Akt pathways by SAMC administration may partly be involved in its antiapoptotic effect during NAFLD development. However, further investigations are needed to clarify the interactions between these pathways and p53, as well as the possible involvement of other apoptosis-related signaling pathways. In addition, it is not clear whether the antiapoptotic effects of SAMC on NAFLD are a direct effect or a consequence of "upstream" antioxidant and anti-inflammatory effects. Although some studies proposed the regulatory roles of LKB1/AMPK and PI3 K/Akt pathways in autophagy [38], in this study, it is suggested that the further enhancement of autophagy by SAMC cotreatment was not through these two pathways. Detailed mechanisms for distinct regulation of apoptosis and autophagy by SAMC are waiting for further study.

In conclusion, our results clearly showed the antiapoptotic and proautophagy properties of SAMC during the development of NAFLD in a rat model. The protective effect of SAMC was partly through modulating both p53-dependent intrinsic and extrinsic apoptotic pathways, as well as the inhibition of mTOR activity. Restoration of LKB1/AMPK and PI3 K/Akt pathways also contributed to this protective effect of SAMC.

Conflict of Interests

The authors declare that they have no conflict of interests.

Authors' Contribution

J. Xiao and R. Guo contributed equally to this work.

Acknowledgments

The authors thank Ms. Carman Leung for her technical help in this project. This study is supported by Seed Funding, University Research Committee, The University of Hong Kong and General Research Fund, University Grant Council, Hong Kong.

References

[1] N. Méndez-Sánchez, M. Arrese, D. Zamora-Valdés, and M. Uribe, "Current concepts in the pathogenesis of nonalcoholic fatty liver disease," *Liver International*, vol. 27, no. 4, pp. 423–433, 2007.

[2] J. Edmilson and A. J. Mccullough, "Pathogenesis of non-alcoholic steatohepatitis: human data," *Clinical Liver Disease*, vol. 11, no. 1, pp. 75–104, 2007.

[3] S. A. Polyzos, J. Kountouras, and C. Zavos, "The multi-hit process and the antagonistic roles of tumor necrosis factor-alpha and adiponectin in non alcoholic fatty liver disease," *Hippokratia*, vol. 13, no. 2, p. 127, 2009.

[4] N. Alkhouri, C. Carter-Kent, and A. E. Feldstein, "Apoptosis in nonalcoholic fatty liver disease: diagnostic and therapeutic implications," *Expert Review of Gastroenterology and Hepatology*, vol. 5, no. 2, pp. 201–212, 2011.

[5] M. Marzioni, S. S. Glaser, G. Alpini, and G. D. LeSage, "Role of apoptosis in development of primary biliary cirrhosis," *Digestive and Liver Disease*, vol. 33, no. 7, pp. 531–533, 2001.

[6] M. J. Ramírez, E. Titos, J. Clària, M. Navasa, J. Fernández, and J. Rodés, "Increased apoptosis dependent on caspase-3 activity in polymorphonuclear leukocytes from patients with cirrhosis and ascites," *Journal of Hepatology*, vol. 41, no. 1, pp. 44–48, 2004.

[7] A. E. Feldstein, A. Canbay, P. Angulo et al., "Hepatocyte apoptosis and Fas expression are prominent features of human nonalcoholic steatohepatitis," *Gastroenterology*, vol. 125, no. 2, pp. 437–443, 2003.

[8] A. E. Feldstein and G. J. Gores, "Apoptosis in alcoholic and nonalcoholic steatohepatitis," *Frontiers in Bioscience*, vol. 10, no. 3, pp. 3093–3099, 2005.

[9] S. Haupt, M. Berger, Z. Goldberg, and Y. Haupt, "Apoptosis—the p53 network," *Journal of Cell Science*, vol. 116, no. 20, pp. 4077–4085, 2003.

[10] J. D. Amaral, J. M. Xavier, C. J. Steer et al., "The role of p53 in apoptosis," *Discovery Medicine*, vol. 9, no. 45, pp. 145–152, 2010.

[11] J. C. Martinou and R. J. Youle, "Mitochondria in apoptosis: Bcl-2 family members and mitochondrial dynamics," *Developmental Cell*, vol. 21, no. 1, pp. 92–101, 2011.

[12] G. Kroemer, G. Mariño, and B. Levine, "Autophagy and the integrated stress response," *Molecular Cell*, vol. 40, no. 2, pp. 280–293, 2010.

[13] M. Komatsu, "Liver autophagy: physiology and pathology," *The Journal of Biochemistry*, vol. 152, no. 1, pp. 5–15, 2012.

[14] L. D. Lawson and Z. J. Wang, "Pre-hepatic fate of the organosulfur compounds derived from garlic (Allium sativum)," *Planta Medica*, vol. 59, no. 7, pp. A688–A689, 1993.

[15] E. W. Howard, M. T. Ling, W. C. Chee, W. C. Hiu, X. Wang, and C. W. Yong, "Garlic-derived S-allylmercaptocysteine is a novel in vivo antimetastatic agent for androgen-independent prostate cancer," *Clinical Cancer Research*, vol. 13, no. 6, pp. 1847–1856, 2007.

[16] D. Liang, Y. Qin, W. Zhao et al., "S-allylmercaptocysteine effectively inhibits the proliferation of colorectal cancer cells under in vitro and in vivo conditions," *Cancer Letters*, vol. 310, no. 1, pp. 69–76, 2011.

[17] D. Xiao, J. T. Pinto, J. W. Soh et al., "Induction of apoptosis by the garlic-derived compound S-allylmercaptocysteine (SAMC) Is associated with microtubule depolymerization and c-jun NH_2Kinase 1 activation," *Cancer Research*, vol. 63, no. 20, pp. 6825–6837, 2003.

[18] I. Sumioka, T. Matsura, and K. Yamada, "Therapeutic effect of S-allylmercaptocysteine on acetaminophen-induced liver injury in mice," *European Journal of Pharmacology*, vol. 433, no. 2-3, pp. 177–185, 2001.

[19] J. Xiao, E. C. Liong, M. T. Ling, Y. P. Ching, M. L. Fung, and G. L. Tipoe, "S-allylmercaptocysteine reduces carbon tetrachloride-induced hepatic oxidative stress and necroinflammation via nuclear factor kappa B-dependent pathways in mice," *European Journal of Nutrition*, vol. 51, no. 3, pp. 323–333, 2011.

[20] J. Xiao, Y. P. Ching, E. C. Liong et al., "Garlic-derived S-allylmercaptocysteine is a hepato-protective agent in non-alcoholic fatty liver disease in vivo animal model," *European Journal of Nutrition*, vol. 52, no. 1, pp. 179–191, 2013.

[21] J. G. Walsh, S. P. Cullen, C. Sheridan, A. U. Lüthi, C. Gerner, and S. J. Martin, "Executioner caspase-3 and caspase-7 are functionally distinct proteases," *Proceedings of the National Academy of Sciences of the United States of America*, vol. 105, no. 35, pp. 12815–12819, 2008.

[22] E. Centis, R. Marzocchi, S. Di Domizio, M. F. Ciaravella, and G. Marchesini, "The effect of lifestyle changes in non-alcoholic fatty liver disease," *Digestive Diseases*, vol. 28, no. 1, pp. 267–273, 2010.

[23] N. Rafiq and Z. M. Younossi, "Effects of weight loss on nonalcoholic fatty liver disease," *Seminars in Liver Disease*, vol. 28, no. 4, pp. 427–433, 2008.

[24] P. S. Ribeiro, H. Cortez-Pinto, S. Solá et al., "Hepatocyte apoptosis, expression of death receptors, and activation of NF-κB in the liver of nonalcoholic and alcoholic steatohepatitis patients," *American Journal of Gastroenterology*, vol. 99, no. 9, pp. 1708–1717, 2004.

[25] A. E. Feldstein, A. Canbay, M. E. Guicciardi, H. Higuchi, S. F. Bronk, and G. J. Gores, "Diet associated hepatic steatosis sensitizes to Fas mediated liver injury in mice," *Journal of Hepatology*, vol. 39, no. 6, pp. 978–983, 2003.

[26] G. C. Farrell, C. Z. Larter, J. Y. Hou et al., "Apoptosis in experimental NASH is associated with p53 activation and TRAIL receptor expression," *Journal of Gastroenterology and Hepatology*, vol. 24, no. 3, pp. 443–452, 2009.

[27] G. L. Tipoe, C. T. Ho, E. C. Liong et al., "Voluntary oral feeding of rats not requiring a very high fat diet is a clinically relevant animal model of non-alcoholic fatty liver disease (NAFLD)," *Histology and Histopathology*, vol. 24, no. 9, pp. 1161–1169, 2009.

[28] H. Shirin, J. T. Pinto, Y. Kawabata et al., "Antiproliferative effects of S-allylmercaptocysteine on colon cancer cells when tested alone or in combination with sulindac sulfide," *Cancer Research*, vol. 61, no. 2, pp. 725–731, 2001.

[29] R. Singh, S. Kaushik, Y. Wang et al., "Autophagy regulates lipid metabolism," *Nature*, vol. 458, no. 7242, pp. 1131–1135, 2009.

[30] S. Mei, H. M. Ni, S. Manley et al., "Differential roles of unsaturated and saturated fatty acids on autophagy and apoptosis in hepatocytes," *Journal of Pharmacology and Experimental Therapeutics*, vol. 339, no. 2, pp. 487–498, 2011.

[31] G. R. Chang, Y. S. Chiu, Y. Y. Wu et al., "Rapamycin protects against high fat diet-induced obesity in C57BL/6J mice," *Journal of Pharmacological Sciences*, vol. 109, no. 4, pp. 496–503, 2009.

[32] H. M. Ni, J. A. Williams, H. Yang et al., "Targeting autophagy for the treatment of liver diseases," *Pharmacological Research*, vol. 66, no. 6, pp. 463–474, 2012.

[33] G. Filomeni, S. Cardaci, A. M. Da Costa Ferreira, G. Rotilio, and M. R. Ciriolo, "Metabolic oxidative stress elicited by the copper(II) complex [Cu(isaepy)2] triggers apoptosis in SH-SY5Y cells through the induction of the AMP-activated protein kinase/p38MAPK/p53 signalling axis: Evidence for a combined use with 3-bromopyruvate in neuroblastoma treatment," *Biochemical Journal*, vol. 437, no. 3, pp. 443–453, 2011.

[34] J. H. Ix and K. Sharma, "Mechanisms linking obesity, chronic kidney disease, and fatty liver disease: the roles of fetuin-A, adiponectin, and AMPK," *Journal of the American Society of Nephrology*, vol. 21, no. 3, pp. 406–412, 2010.

[35] Y. W. Kim, S. M. Lee, S. M. Shin et al., "Efficacy of sauchinone as a novel AMPK-activating lignan for preventing iron-induced oxidative stress and liver injury," *Free Radical Biology and Medicine*, vol. 47, no. 7, pp. 1082–1092, 2009.

[36] M. S. Sang, J. C. Il, and G. K. Sang, "Resveratrol protects mitochondria against oxidative stress through AMP-activated protein kinase-mediated glycogen synthase kinase-3β inhibition downstream of poly(ADP-ribose) polymerase-LKB1 pathway," *Molecular Pharmacology*, vol. 76, no. 4, pp. 884–895, 2009.

[37] J. W. Han, X. R. Zhan, X. Y. Li et al., "Impaired PI3K/Akt signal pathway and hepatocellular injury in high-fat fed rats," *World Journal of Gastroenterology*, vol. 16, no. 48, pp. 6111–6118, 2010.

[38] R. Singh and A. M. Cuervo, "Lipophagy: connecting autophagy and lipid metabolism," *International Journal of Cell Biology*, vol. 2012, Article ID 282041, 12 pages, 2012.

Hindawi Publishing Corporation
Evidence-Based Complementary and Alternative Medicine
Volume 2013, Article ID 636580, 10 pages
http://dx.doi.org/10.1155/2013/636580

Research Article

Hepatoprotective Activity of Methanolic Extract of *Bauhinia purpurea* Leaves against Paracetamol-Induced Hepatic Damage in Rats

F. Yahya,[1] S. S. Mamat,[1] M. F. F. Kamarolzaman,[1] A. A. Seyedan,[1] K. F. Jakius,[1] N. D. Mahmood,[1] M. S. Shahril,[1] Z. Suhaili,[2] N. Mohtarrudin,[3] D. Susanti,[4] M. N. Somchit,[1] L. K. Teh,[5] M. Z. Salleh,[5] and Z. A. Zakaria[1,5]

[1] *Department of Biomedical Science, Faculty of Medicine and Health Sciences, Universiti Putra Malaysia, 43400 Serdang, Selangor, Malaysia*
[2] *Department of Animal Science, Faculty of Agriculture and Biotechnology, Universiti Sultan Zainal Abidin, Gong Badak Campus, 20300 Kuala Terengganu, Terengganu, Malaysia*
[3] *Department of Pathology, Faculty of Medicine & Health Sciences, Universiti Putra Malaysia, 43400 Serdang, Selangor, Malaysia*
[4] *Department of Biomedical Science, Kulliyyah of Science, International Islamic University Malaysia, Jl Sultan Ahmad Shah, Bandar Indera Mahkota, 25200 Kuantan, Pahang, Malaysia*
[5] *Pharmacogenomics Centre (PROMISE), Faculty of Pharmacy, Universiti Teknologi MARA, 42300 Puncak Alam, Selangor, Malaysia*

Correspondence should be addressed to Z. A. Zakaria; dr_zaz@yahoo.com

Received 20 October 2012; Revised 16 May 2013; Accepted 24 May 2013

Academic Editor: Wei-Chiang Lin

In an attempt to further establish the pharmacological properties of *Bauhinia purpurea* (Fabaceae), hepatoprotective potential of methanol extract of *B. purpurea* leaves (MEBP) was investigated using the paracetamol- (PCM-) induced liver toxicity in rats. Five groups of rats ($n = 6$) were used and administered orally once daily with 10% DMSO (negative control), 200 mg/kg silymarin (positive control), or MEBP (50, 250, and 500 mg/kg) for 7 days, followed by the hepatotoxicity induction using paracetamol (PCM). The blood samples and livers were collected and subjected to biochemical and microscopical analysis. The extract was also subjected to antioxidant study using the 2, 2-diphenyl-1-picrylhydrazyl (DPPH) radical scavenging assay with the total phenolic content (TPC) also determined. From the histological observation, lymphocyte infiltration and marked necrosis were observed in PCM-treated groups (negative control), whereas maintenance of the normal hepatic structural was observed in group pretreated with silymarin and MEBP. Hepatotoxic rats pretreated with silymarin or MEBP exhibited significant decrease ($P < 0.05$) in ALT and AST enzyme level. Moreover, the extract also exhibited antioxidant activity and contained high TPC. In conclusion, MEBP exerts potential hepatoprotective activity that could be partly attributed to its antioxidant activity and high phenolic content and thus warrants further investigation.

1. Introduction

Diverse range of bioactive molecules has been isolated from plant natural product, making them medicinally valuable sources [1]. There has been a revival of interest in plant-based medicines due to the increase awareness of the limited ability of synthetic pharmaceutical products to control major disease and the need to discover new molecular structures as the lead compounds from other sources, including the plant kingdom [2]. One of the plants that are currently under investigation for its potential pharmacological activities in our laboratory is *Bauhinia purpurea* (family Leguminosae). Known to the Malays as "*pokok tapak kerbau,*" *B. purpurea* leaves have been traditionally used by the Indians to treat stomach tumors, ulcers, wounds, glandular swellings, diarrhea, and fever [3]. Scientifically, *B. purpurea* has been proved to possess antidiarrheal activity [4], thyroid stimulating and antihypothyroidism [5, 6], and larvicidal [7] activities. Other

researchers have also reported the pharmacological benefit of *B. purpurea*. For example, the plant exhibited antimicrobial [8], antinociceptive, anti-inflammatory, and antipyretic [3, 9], antimycobacterial, antimalarial, antifungal, cytotoxic, and anti-inflammatory [10], anti-nephrotoxicity [11], and wound healing [12] activities. *In vitro* study has demonstrated that *B. purpurea* possesses antiproliferative [13], antioxidant [13, 14], and antimicrobial activities [14, 15], and also has potential as hepatocellular carcinoma inhibitor [16]. Interestingly, other studies have proved that *B. purpurea* leaf possesses antiulcer activity [17, 18]. We have also reported on the phytochemical constituents of *B. purpurea*, which indicate the presence of flavonoids, triterpenes, tannins, and steroids [3]. Flavonoids, in particular, are polyphenolic compounds, widely distributed in the plant kingdom, and exhibited various pharmacological activities including hepatoprotective activity [19]. Interestingly, there is a link between the hepatoprotective activity with the anti-inflammatory, antioxidation, and antiproliferative activities, which has been exerted by the leaves of *B. purpurea*.

Our literature survey revealed that no attempt has been made to this date to study the hepatoprotective activity of *B. purpurea* leaves. Thus, we take this opportunity to study the hepatoprotective activity of methanol extract of *B. purpurea* leaves (MEBP) using the paracetamol- (PCM-) induced liver damage in rats as the animal model.

2. Materials and Methods

2.1. Chemicals. Paracetamol (PCM; *Sigma*-Aldrich, USA) and silymarin (*Sigma*-Aldrich) were used in the present study. All other chemicals and reagents used were of analytical grade.

2.2. Collection of Plant Material. The leaves of *B. purpurea* were collected from their natural habitat around Universiti Putra Malaysia (UPM), Serdang campus, Selangor, Malaysia. A voucher specimen (SK 1985/11) was identified by comparison with specimens available at the Herbarium of the Laboratory of Natural Products, IBS, UPM, Serdang, Selangor, Malaysia. The leaves were dried under shade for 7 days at room temperature, segregated, and pulverized by mechanical grinder to form coarse powder.

2.3. Preparation of Plant Extract. The coarse powder of *B. purpurea* had undergone the maceration type of extraction using methanol as the solvent system. The coarse powder of air-dried leaves of *B. purpurea* was subjected to methanol extraction whereby 1 kg of powder leaves was macerated in 20 L of methanol in the ratio of 1 : 20 (w/v) for 72 hours, and the supernatant was filtered sequentially using cloth filter, cotton wool, and Whatman no. 1 filter paper. The solvent was then evaporated under reduced pressure (204 mbar) and controlled temperature (40°C) using a vacuum rotary evaporator (Buchi Rotavapor R210/215, Switzerland). The residue was collected and subjected to the similar extraction process for another two times [20].

2.4. Pharmacological Studies

2.4.1. Antioxidant Activity of MEBP

Total Phenolic Content. Determination of total phenolic content (TPC) was performed using Folin-Ciocalteu reagent according to the method of Singleton and Rossi [21] with slight modifications. Briefly, a 1.0 mg quantity of MEBP was extracted for 2 hours with 1.0 mL of 80% methanol containing 1.0% hydrochloric acid and 1.0% of distilled water at room temperature on the shaker set at 200 rpm. The hydrochloric acid was added at this stage as part of the extraction solution to increase solubility of insoluble plant compounds. The mixture was centrifuged at 6000 rpm for 15 minutes, and the supernatant decanted into vials. The supernatant was used for the determination of TPC. A 200.0 μL of supernatant extract was mixed with 400.0 μL of Folin-Ciocalteu reagent (0.1 mL/0.9 mL) and allowed to stand at room temperature for 5 minutes. Then, 400.0 μL of sodium bicarbonate (60.0 mg/mL) solution was added, and the mixture was allowed to stand at room temperature for 90 minutes. Absorbance was measured at 725 nm. A calibration curve was generated by using the gallic acid standard optical density (OD), and the levels in the samples were expressed as gallic acid equivalent (GAE)-TPC mg/100 g.

2.4.2. DPPH Radical Scavenging Activity. Antioxidant reducing activity on DPPH radical was estimated according to the method of Blois [22] with modification involving the use of high-throughput microplate system. Sample (50 μL of 1.0 mg/mL) was added to 50 μL of DPPH (FG: 384.32) (1 mM in ethanolic solution) and 150 μL of ethanol (absolute) in a 96-well microtiter plate in triplicates. The plate was shaken (15 seconds, 500 rpm) and left to stand at room temperature for 30 minutes. The absorbance of the resulting solution was measured spectrophotometrically at 520 nm.

2.5. Hepatoprotective Assay

2.5.1. PCM-Induced Hepatotoxicity Test. The *in vivo* hepatoprotective activity of MEBP was determined using the PCM-induced hepatotoxicity test in rats. The animals were divided into 6 groups ($n = 6$) and administered with test solutions as described below.

(i) Group I served as normal control and received 10% DMSO

(ii) Group II served as negative control and received 10% DMSO.

(iii) Group III served as positive control and received 200 mg/kg silymarin.

(iv) Pretreatment groups:

(1) Group IV received 50 mg/kg MEBP,
(2) Group V received 250 mg/kg MEBP, and
(3) Group VI received 500 mg/kg MEBP.

These doses of extract (50, 250, and 500 mg/kg) were used in the present study based on our previous reports on

the acute toxicity study performed using the single dose of orally administered 5000 mg/kg MEBP, which showed no sign of toxicity in rats. Furthermore, this dose range was chosen based on the antiulcer activity of *B. purpurea* leaves [14]. Based on these findings, the highest dose used in the present study (500 mg/kg) was set up to be 10% of the dose used in the acute toxicity study (5000 mg/kg). In our preliminary study, the 500 mg/kg MEBP, which exhibited significant antiulcer activity, also exerted significant hepatoprotective activity. Therefore, the other two doses (50 and 250 mg/kg, which were 10 and 2 folds reduction of 500 mg/kg (the highest dose) were selected based on the antiulcer findings [14], respectively.

The animals were fasted for 48 hours prior to the experiment under standard laboratory conditions. After 48 hours, each group of rats received the respective dose of test solution orally once daily for 7 consecutive days. The oral administration of PCM was performed 3 hours after the last extract administration on the 7th day except for group I, which received only 10% DMSO. Forty eight [23] hours after the hepatic injury induction, the animals were anesthetized using diethyl ether, and the blood was drained for biochemical parameters study. The animals were then sacrificed by cervical dislocation, and the liver was removed for histopathological studies.

2.6. Biochemical Studies. Biochemical parameters were assayed according to the standard methods. Alanine aminotransferase (ALT), alkaline phosphate (ALP), aspartate aminotransferase (AST), total were measured using the Hitachi 902 Automatic Chemical Analyser.

2.7. Histopathology. The liver tissue was dissected out and fixed in the 10% formalin, dehydrated in gradual ethanol (50–100%), cleared in xylene, and embedded in paraffin wax. The sections, which are 5-6 μm thick, were then prepared using rotary microtome (Leica RM 2125 RTS, Singapore) and stained with hematoxylin and eosin dye for microscopic observation of histopathological changes in the liver. Liver sections then will be scored and evaluated according to the severity of the hepatic injury as described by El-Beshbishy et al. [24] with modifications.

2.8. Phytochemical Screening and HPLC Analysis of MEBP. The phytochemical screening of MEBP was performed again according to the conventional protocols as adopted by Zakaria et al. [18]. The HPLC analysis of the extract was also carried out and performed according to the previous report [18] but with slight modifications. Briefly, 10 mg of MEBP was dissolved in 1 mL mETH and then filtered through the membrane filter (pore size 0.45 μm). A Waters Delta 600 with 600 Controller and Waters 2996 Photodiode Array (Milford, MA, USA) equipped with an autosampler, online degasser, and column heater was used to analyse the filtered sample. Data were evaluated and processed using the installed Millenium 32 Software (Waters Product). The filtered samples were separated at 27°C on a minibore Phenomenex Luna 5 μm C_{18} column (dimensions 250 × 4.60 mm) using a one-step linear gradient. The solvents were (A) 0.1% aqueous formic acid and (B) acetonitrile, and the elution system was as follows: initial conditions were 85% A and 15% B with a linear gradient reaching 25% B at $t = 12$ min. This was maintained for 10 min after which the programmed returned to the initial solvent composition at $t = 25$ min and continued for 10 min. The flow rate used was 1.0 mL/min, and the injection volume was 10 μL. The HPLC was monitored at 254 and 366 nm.

Table 1: Antioxidant profile of MEBP.

Sample	DPPH radical scavenging (%)
Ascorbic acid (200 μg/mL)	85.72 ± 0.97
MEBP (200 μg/mL)	61.06 ± 0.35

2.9. Statistical Analysis. Data obtained are presented in mean ± standard error of mean (SEM). The data were analysed using the one-way analysis of variance (ANOVA), and the differences between the groups were determined using the Dunnett post hoc test as provided by the Graph pad PRISM V5.02 software. The limit of significance was set at $P < 0.05$.

3. Results

3.1. In Vitro Antioxidant Studies

3.1.1. Total Phenolic Compound. The result obtained showed that the total phenolic content of MEBP (200 μg/mL) was 1194.35 ± 24.89 mg GAE/100 g. From the standard given, TPC value that higher than 1000 mg GAE/100 g is considered high total phenol compound.

3.1.2. DPPH Scavenging Assay. Free radicals scavenging capacity of MEBP was indicated by the bleaching of DPPH. Since the ability of MEBP to scavenge the free radical species in DPPH scavenging assay has been determined previously [13], the present study was carried out using only one concentration of the currently prepared MEBP with the aim of supporting the previous findings and, later, to propose the role of antioxidant effect as one of the possible mechanisms of hepatoprotective of MEBP. As can be seen from Table 1, the 200 μg/mL MEBP caused more than 50% antioxidant activity when assessed against the DPPH radical scavenging assay, which is in comparison to the standard drug, 200 μg/mL ascorbic acid.

3.2. In Vivo Hepatoprotective Study

3.2.1. Effect of MEBP on the Body Weight and Liver Weight after Induction with PCM. PCM administration following pretreatment with 10% DMSO significantly ($P < 0.05$) caused augmentation in liver weight and body weight when compared to the normal control group. Interestingly, pretreatment with 500 mg/kg significantly ($P < 0.05$) reduced the increased liver and body weight seen in the PCM-treated liver group. The reference hepatoprotective agent 200 mg/kg

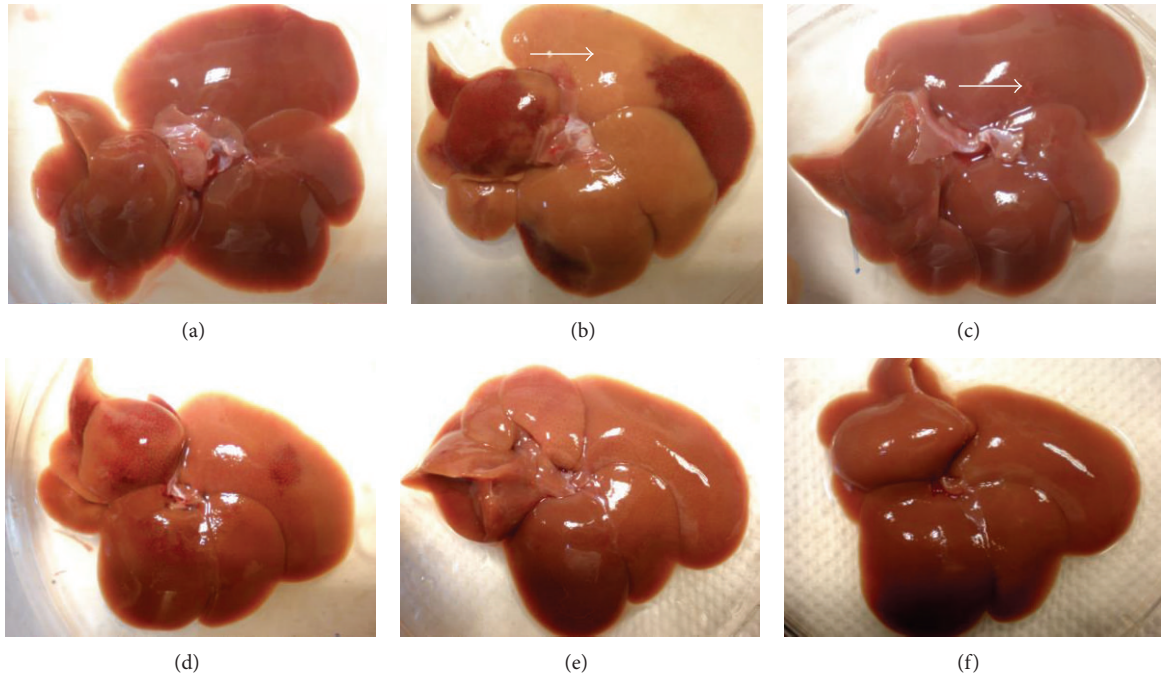

Figure 1: (a) Normal liver, (b) liver intoxicated with 3 g/kg PCM: gross image shows major color changes of liver lobes (arrow), (c) liver pretreated with 200 mg/kg silymarin and induced with PCM: spot of color changes was noted (arrow), (d) liver pretreated with 50 mg/kg MEBP and induced by PCM, (e) liver pretreated with 250 mg/kg MEBP and induced by PCM, (f) liver pretreated with 500 mg/kg MEBP and induced by PCM.

Table 2: Effect of MEBP on percentage change of body and liver weight in PCM-treated rats.

Treatment	Dose (mg/kg)	Change of body weight (%)	Liver weight (g/100 g)
Control	—	5.14 ± 0.43	2.89 ± 0.06
PCM		17.58 ± 2.10[a]	4.81 ± 0.40[a]
Silymarin + PCM	200	3.11 ± 0.67[b]	3.60 ± 0.11[b]
MEBP + PCM	50	15.57 ± 1.53[a]	5.66 ± 0.39[a]
	250	11.07 ± 0.73[ab]	4.29 ± 0.17[a]
	500	4.55 ± 0.91[b]	4.06 ± 0.24[ab]

Values are expressed as means ± S.E.M. of six replicates.
[a]Data differed significantly ($P < 0.05$) when compared to normal control within the respective column.
[b]Data differed significantly ($P < 0.05$) when compared to the negative control within the respective column.

silymarin as expected has also demonstrated significant reduction in liver weight to normal value (Table 2).

3.2.2. Histopathological Study of the PCM-Induced Hepatotoxic Liver with and without Pretreatment with MEBP. Gross necropsy and histopathological study were performed on the liver to observe any irregularities or abnormalities on the structure. Gross necropsy of normal liver demonstrated normal appearances (i.e., dark maroon in-color liver with smooth surfaces (Figure 1(a)). Meanwhile, the liver intoxicated with PCM showed major changes of the color of the lobes from maroon to brown (Figure 1(b)). Pre-treatment with 200 mg/kg silymarin (Figure 1(c)) or the MEBP (Figures 1(d)–1(f)) reversed the toxic effect of PCM with only mild spots of brown color changes observed.

Histopathologically, the non-PCM-intoxicated liver pretreated with 10% DMSO (normal) shows normal lobular architecture and normal hepatic cells with well preserved cytoplasm and well defined sinusoids line and nucleus around the perivenular area (Figure 2(a)). The section of PCM-intoxicated liver, pretreated with 10% DMSO, demonstrates infiltration of lymphocytes, the presence of haemorrhage and extensive coagulative necrosis of the perivenular, and midzonal region with periportal sparing (Figure 2(b)). Coagulative-type necrosis of hepatocytes in PCM-induced liver toxicity is present predominantly in the perivenular zone (zone 3). These pathological changes were found to be lesser as the dose of MEBP increased indicating the extract ability to reverse the PCM-induced intoxication (Figures 2(d)–2(f))). Table 3 shows the histopathological scoring of the liver tissues pretreated with the respective test solution. Interestingly, the presence of marked necrosis, inflammation, and hemorrhage following treatment with PCM (shown by the negative control group) was reduced remarkably when pretreated with the extract or silymarin.

3.2.3. Biochemical Study. In this study, gross necropsy and histopathological study of the PCM-intoxicated liver pretreated with the respective test solution showed a correlation with serum biochemical indices. Paracetamol administration

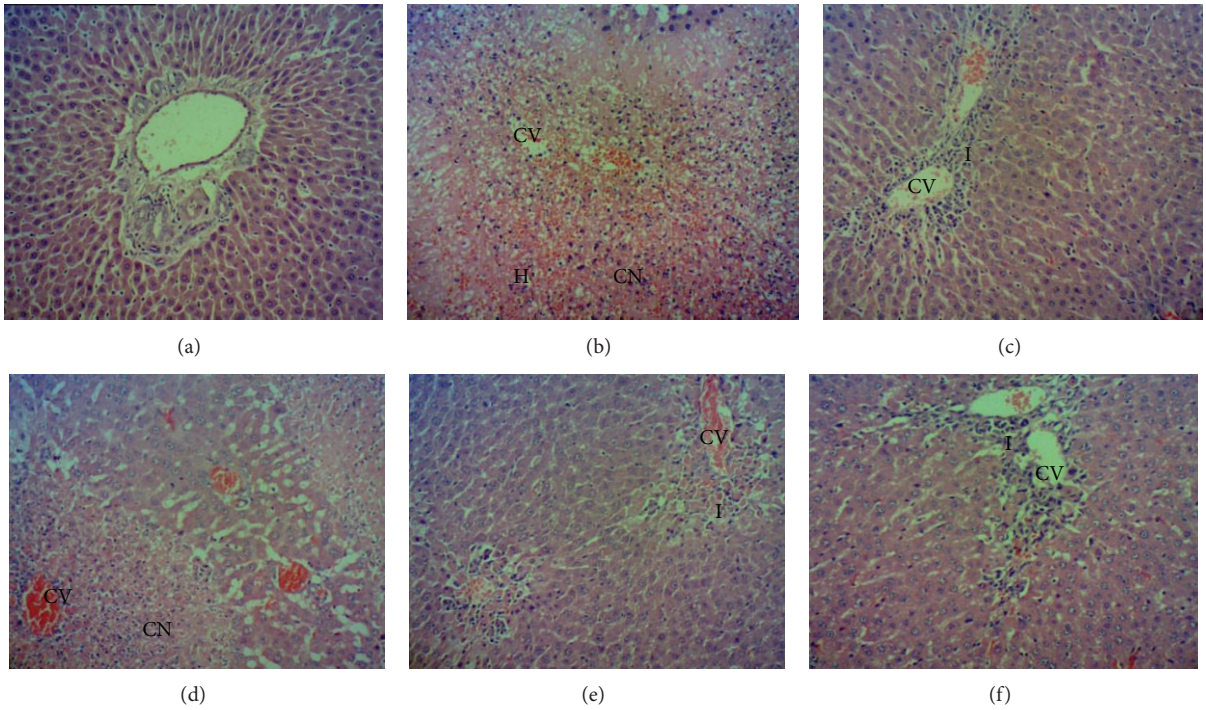

Figure 2: (a) Normal, (b) section of liver tissue of 3 g/kg PCM-treated group (p.o) showing massive coagulative necrosis, haemorrhage and inflammation. (c) Section of 200 mg/kg of silymarin liver tissue pretreated on the liver followed by PCM showing preservation of normal hepatocytes. (d) Section of pretreated 50 mg/kg MEBP liver tissue followed by PCM showing tissue necrosis and inflammation. (e) Section of pretreated 250 mg/kg MEBP liver tissue followed by PCM showing mild inflammation. (f) Section of pretreated 500 mg/kg MEBP liver tissue followed by PCM showing normal histology with mild inflammation. (100x magnification). CV: centrilobular. CN: coagulative necrosis. I: inflammation. H: haemorrhage.

Table 3: Histopathological evaluation of the effect of various doses of MEBP against PCM-induced hepatic injury in rats.

Treatment	Dose (mg/kg)	Steatosis	Necrosis	Inflammation	Haemorrhage
Normal	–	–	–	–	–
10% DMSO		–	+++	++	++
Silymarin	200	–	+	+	+
MEBP	50	–	++	+	+
	250	–	+	+	–
	500	–	+	+	+

The severity of various features of hepatic injury was evaluated based on those following scoring schemes: –: normal, +: mild effect, ++: moderate effect, +++: severe effect.

caused significant elevation in the ALT, AST, and ALP serum marker level in group pretreated with 10% DMSO as compared to the normal 10% DMSO-pretreated, non-PCM-intoxicated group (Table 4). However, oral administration of high dose MEBP (500 mg/kg) and silymarin (200 mg/kg) exhibited an ability to counteract the toxic effect of PCM by decreasing the level of these enzymes.

3.3. Phytochemical Constituents and HPLC Profile of MEBP. The phytochemical screening of MEBP is shown in Table 5. Several groups of bioactive constituents were detected, namely, saponins, flavonoids, tannins and polyphenolic compounds, triterpenes, and steroids, but not alkaloids. However, the presences of those compounds are very low as indicated by the low froth formation (for detection of saponins) and weak colour formation (for detection of flavonoids, tannins, and triterpenes).

The HPLC profile of MEBP measured at the wavelength of 254 and 366 nm is shown in Figure 2(a). The best wavelength wherein clear separation of peaks was obtained is 366 nm. At this wavelength, several peaks were separated with 5 major peaks (labelled as P1, P2 P3, P4, and P5) which were clearly detected in the chromatogram at the respective retention time (RT) of 2.75, 3.65, 4.94, 6.25, and 7.12 min, respectively. Further analysis demonstrated that the five peaks showed λ_{max} values in the region of 201.4–272.0, 192.0–268.5, 254.3–350.6, 264.9–344.6, and 254.3–351.7 nm, respectively (Figure 3(b)).

Table 4: Effect of MEBP pretreatment on ALT, AST and ALP (U/L) level.

Treatment	Dose (mg/kg)	ALT (U/L)	AST (U/L)	ALP (U/L)
Control	—	15.83 ± 2.862	95.13 ± 5.924	115.7 ± 6.994
PCM control (neg)		1714 ± 142.2[a]	3008 ± 210.7[a]	330.0 ± 42.35[a]
Silymarin (pos)	200	588.1 ± 193.7[ab]	959.2 ± 338.8[ab]	195.5 ± 11.06[ab]
MEBP	50	1222 ± 187.7[a]	2407 ± 294.9[a]	347.0 ± 29.40[a]
	250	1096 ± 221.1[ab]	2076 ± 409.4[ab]	264.8 ± 29.77[a]
	500	867.7 ± 101.2[ab]	1730 ± 256.6[ab]	256.3 ± 13.91[a]

Values are expressed as means ± S.E.M. of six replicates.
[a]Data differed significantly ($P < 0.05$) when compared to the normal control group within each respective column.
[b]Data differed significantly ($P < 0.05$) when compared to the negative control group within each respective column.

Table 5: Comparison on the phytochemical constituents between the leaves of *B. pururea* and MEBP.

Sample	Phytochemical constituent	Result
MEBP	Alkaloid	—
	Saponin	+
	Flavonoid	+
	Tannins and polyphenolic compounds	+
	Triterpene	+
	Steroid	++

For saponins—+: 1-2 cm froth; ++: 2-3 cm froth; +++: >3 cm froth.
For flavonoids, tannins, triterpenes, and steroids—+: weak colour; ++: mild colour; +++: strong colour.
For akalioids—+: negligible amount of precipitate; ++: weak precipitate; +++: strong precipitate.

4. Discussion and Conclusion

Hepatocytes are the main component that regulates various metabolic activities of liver. Distortion of this organ will result in disorder of body metabolism [25, 26]. An accidental over dosage administration of PCM as an antipyretic drug and over-the-counter analgesic [27] can result in hepatic damage [28]. *N*-acetyl-*p*-benzoquinoneimine (NAPQI), which is one of the metabolites of PCM after the latter undergoes metabolism in the liver via the action of cytochrome P450 (cyP450) monooxygenase [26, 29, 30], is highly responsible for the PCM toxic effect to the liver [31]. Several CYP450 enzymes have been known to participate in the bioactivation of NAPQI [30]. NAPQI is normally conjugated with glutathione (GSH) and excreted in urine. GSH has been highlighted to be responsible in the antioxidant defense of our body by scavenging the free radicals produced through the metabolism processes within the liver [32] in order to prevent any subsequent cell damage. Overdosage of PCM will result in accumulation of NAPQI, which will bind to GSH to form conjugates that will lead to the oxidation and conversion of GSH to glutathione disulfide (GSSG) resulting in the reduced level of blood and liver GSH [33]. Depletion of GSH level in blood and liver due to this process can result in mitochondrial dysfunction, increase of lipid peroxidation, and development of acute hepatic necrosis. Hepatocellular necrosis releases the enzymes such as AST and ALT into the circulation [34], and hence it can be measured in the serum [28]. Hepatic parenchymal cells produce pool of ALT that is regarded as specific enzyme for detection of liver abnormalities [35, 36]. Despite that, measurement of AST is still considered to be essential marker since it is sensitive to mitochondrial distortion predominantly in zone 3, centrilobular zone [35, 36]. Moreover, Somchit et al. [37] also suggested that NAPQI is involved in the formation of protein adducts via its action on DNA, proteins, cellular proteins, which in turn leads to the dysfunction and death of hepatocytes and finally liver necrosis.

PCM-intoxication model is a universally established model to study the potential hepatoprotective activity of extracts/compounds [26, 38]. From the results obtained in the present study, PCM, at the intoxicated dose of 3 g/kg, increased the body weight and subsequently liver weight of rats as expected and showed significant elevation of serum level of hepatic enzymes, ALT and AST. Histopathological observations provide evidence of reducing number of viable cells with massive necrotic cells around the centrilobular zone extending to parenchymal zone, which is characterized by pyknosis and karyolysis nuclear. Interestingly, administration of MEBP showed capability to reduce the liver weight and concurrently caused significant reduction of enzyme ALT and AST level in blood in a dose-dependent manner. It is further supported by the normalization of histopathological changes to preserve the histostructure of hepatocytes. This liver regeneration progress was almost comparable to silymarin pretreated group which showed increasing number of viable cells and declining of hepatic enzymes level in serum.

Based on the role of PCM metabolite, NAPQI, as described previously, the development of PCM-induced hepatotoxicity seems to depend partly on the existence of free radicals and oxidative processes. For that reason, it is hypothesized that extracts/compounds possessing free radical scavenging and/or antioxidant activities could also demonstrate hepatoprotective activity against the PCM toxic effect. This is supported by claim that the combination of hepatoprotective effect and antioxidant activity synergistically prevents the process of initiation and progress of hepatocellular damage [39]. Interestingly, our previous findings did demonstrate the MEBP ability to scavenge free radicals and to exert antioxidant activity [26], which is concurrent with our recent finding using the DPPH assay. Moreover, the inflammatory processes activated by PCM or other toxic agents are

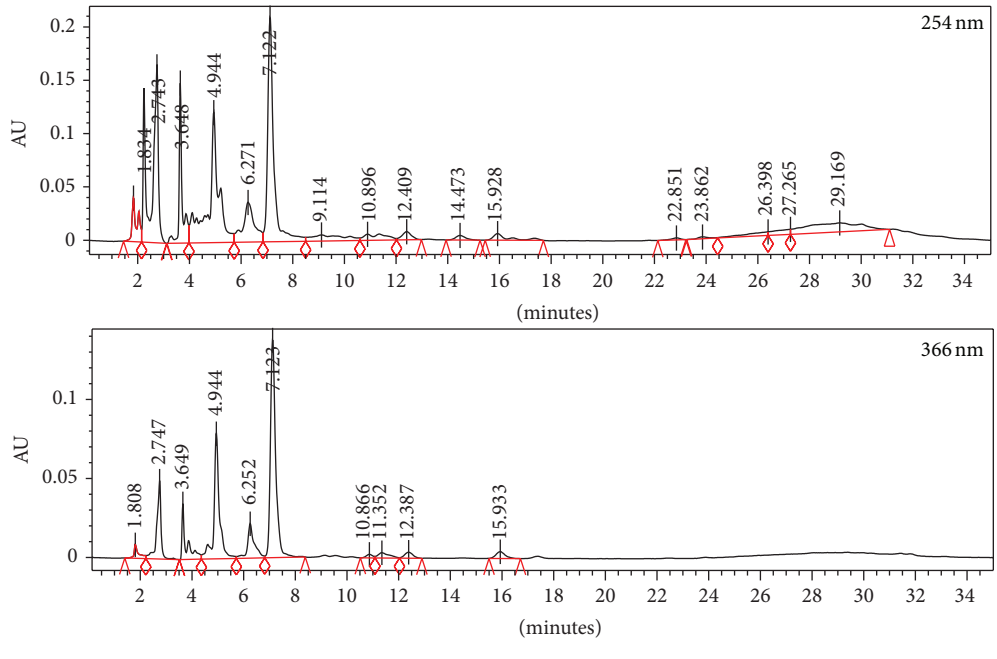

(a)

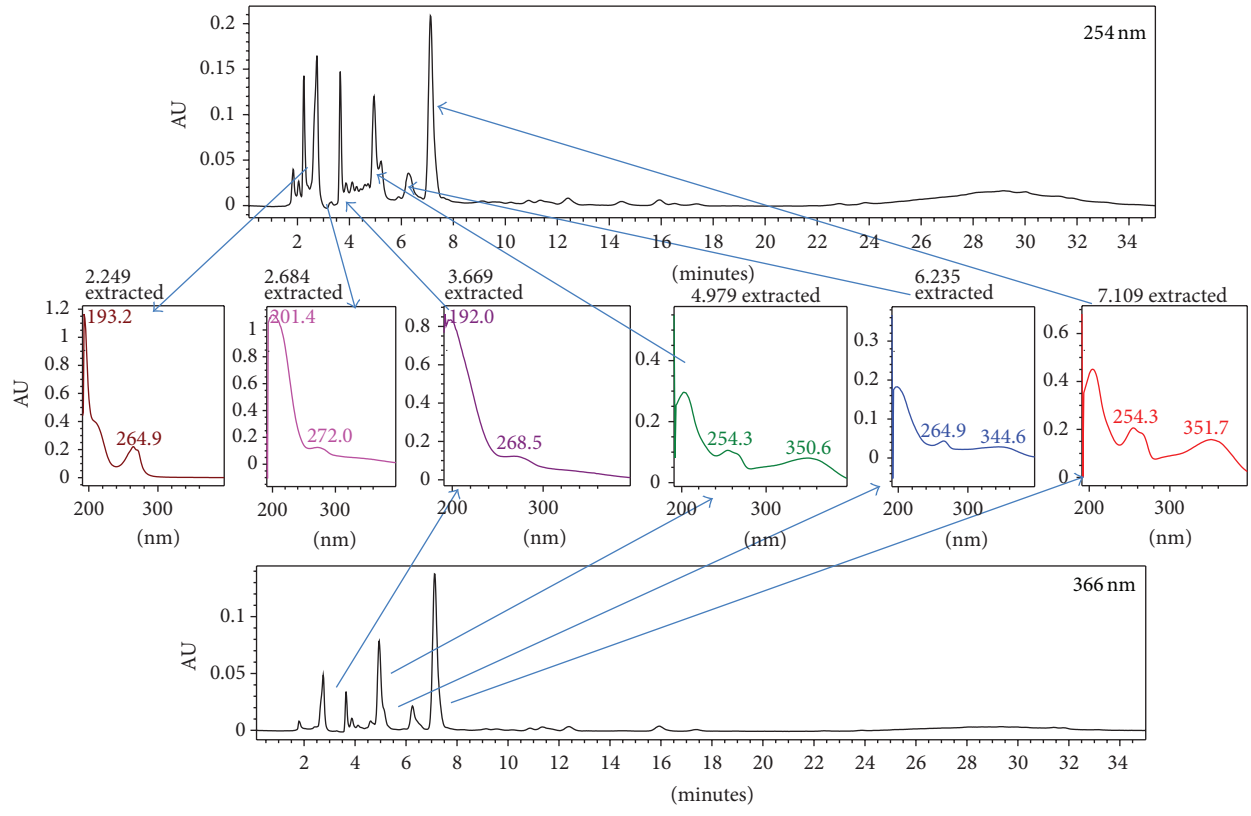

(b)

Figure 3: (a) The HPLC profile of MEBP at two different wavelengths, namely 254, and 366 nm. (b) The UV spectra analysis of peak 4 (RT = 4.94 min), peak 5 (RT = 6.27 min), and peak 6 (RT = 7.12 min) of the MEBP at 254 nm exhibiting the λ max at 254–351 nm, 264–345 nm,and 254–352 nm, respectively, suggesting, in part, the presence of flavonoid-based compounds.

intimately involved in the chemical-induced hepatotoxic processes [40]. The inflammatory processes are thought to be responsible for producing various mediators, which are involved in the production of ROS and NO that can affect liver damage or repair. Therefore, it is also possible to postulate that extracts/compounds possessing anti-inflammatory activity might also exhibit hepatoprotective activity. It is again interesting to highlight that we have previously demonstrated that the leaves of *B. purpurea* possess anti-inflammatory activity [3, 9].

Phytochemical screening of MEBP demonstrated the presence of flavonoids, saponins, condensed tannins, and steroids. In addition, the presence of high content of total phenolic compounds in the MEBP was reported in our previous and present study. The presence of flavonoids, in particular, has been confirmed earlier by Yadav and Bhadoria [41] followed by Zakaria et al. [18]. Flavonoids have been reported to exhibit antioxidant [42, 43], anti-inflammatory [44], and hepatoprotective [43, 44] activities. Furthermore, condensed tannins have been suggested to possess free radical scavenging and antioxidant, anti-inflammatory, and hepatoprotective activities [45], while saponins have been reported also to exhibit hepatoprotective activity via modulation of its antioxidant [46] and anti-inflammatory activities [47]. Taking all these reports into consideration, it is plausible to suggest that the hepatoprotective activity of MEMM involved, partly, synergistic action of flavonoids, condensed tannins, and saponins.

Furthermore, the MEBP successfully reversed PCM-induced hepatotoxic effect, which is supported by the extract ability to bring down the elevated levels of ALT, AST and ALP, suggesting that these biochemical restorations could be due to the extract's inhibitory effects on cytochrome P450 or/and promotion of the PCM glucuronidation [48]. Moreover, the ability to bring down the enzymes level could be associated with the ability of MEBP to prevent peroxidative degradation of membrane lipids of endoplasmic reticulum that is rich in polyunsaturated fatty acids by thwarting binding of activated radicals to the macromolecules. This process could be achieved via the antioxidant activity of MEBP [23]. Other than that, several possible mechanisms could partly be linked to the observed hepatoprotective activity of MEBP. Mehendale [49] suggested that any potential mechanisms must involve activation of peroxisome proliferators activated receptor-α (PPAR-α), which are ligand-activated transcription factors activated by xenobiotics and are highly expressed in hepatocytes. Interestingly, Manautou et al. [50] and Liang et al. [51] have demonstrated the ability of flavonoids and saponins, which are also found in the MEBP, to activate the PPAR-α system. This mechanism of action might relate to the role of these compounds in the attenuation of PCM-induced hepatotoxicity. Interestingly, Han et al. [52] suggested that in the PCM-induced hepatotoxicity, regardless of which cellular pathway is involved in hepatoprotective activity, all pathways depend on PPAR-α receptor activation. In addition, mechanisms of hepatoprotection that could take place include activation of hepatic regeneration via an enhanced synthesis of protein and glycoprotein or accelerated detoxification and excretion [38], prevention of the process of lipid peroxidation, and stabilization of the hepatocellular membrane [23]. However, further studies are warranted before we could conclude on the exact mechanism(s) involved in the hepatoprotective activity of the MEBP such as cytokine assessments, antimitochondrial swelling activity, evaluation of oxidative stress markers, and immunohistochemistry study.

Acknowledgments

This study was supported by the Science Fund Research Grant (Reference no. 06-01-04-SF1127) from the Ministry of Science Technology and Innovation, Malaysia, and the Research University Grant Scheme (Reference no. 04-01-11-1169RU) from the Universiti Putra Malaysia, Malaysia. The authors thank the Faculty of Medicine and Health Sciences, Universiti Putra Malaysia, Malaysia, for providing the facilities to carry out this study.

References

[1] C. Alagesaboopathi, "Phytochemical screening and antimicrobial potential of *Andrographis ovata*," *African Journal of Biotechnology*, vol. 10, no. 25, pp. 5033–5036, 2011.

[2] M. A. Hussain, M. Q. Khan, N. Hussain, and T. Habib, "Antibacterial and antifungal potential of leaves and twigs of *Viscum album* L.," *Journal of Medicinal Plant Research*, vol. 5, no. 23, pp. 5545–5549, 2011.

[3] Z. A. Zakaria, L. Y. Wen, N. I. Abdul Rahman, A. H. Abdul Ayub, M. R. Sulaiman, and H. K. Gopalan, "Antinociceptive, anti-inflammatory and antipyretic properties of the aqueous extract of *Bauhinia purpurea* leaves in experimental animals," *Medical Principles and Practice*, vol. 16, no. 6, pp. 443–449, 2007.

[4] P. K. Mukherjee, T. K. Gopal, T. Subburaju et al., "Studies on the anti-diarrheal profiles of *Bauhinia purpurea* linn leaves extract," *Natural Product Sciences*, vol. 4, no. 4, pp. 234–237, 1998.

[5] S. Panda and A. Kar, "*Withania somnifera* and *Bauhinia purpurea* in the regulation of circulating thyroid hormone concentrations in female mice," *Journal of Ethnopharmacology*, vol. 67, no. 2, pp. 233–239, 1999.

[6] R. Jatwa and A. Kar, "Amelioration of metformin-induced hypothyroidism by *Withania somnifera* and *Bauhinia purpurea* extracts in type 2 diabetic mice," *Phytotherapy Research*, vol. 23, no. 8, pp. 1140–1145, 2009.

[7] A. R. Gururaj, I. A. Urbandale, B. N. Kumar, and I. A. des Moines, *Derivatives of Bauhinia purpurea Lectin and Their Use as Larvicides*, United States Pioneer Hi-Bred International, Des Moines, Iowa, USA, 1999.

[8] M. Murugan and V. R. Mohan, "Evaluation of phytochemical analysis and antibacterial activity of *Bauhinia purpurea* L. and *Hiptage benghalensis* L. Kurz," *Journal of Applied Pharmaceutical Science*, vol. 1, pp. 157–160, 2011.

[9] Z. A. Zakaria, N. I. A. Rahman, Y. W. Loo et al., "Antinociceptive and anti-inflammatory activities of the chloroform extract of *Bauhinia purpurea* L., (Leguminosae) leaves in animal models," *International Journal of Tropical Medicine*, vol. 4, pp. 140–114, 2009.

[10] S. Boonphong, P. Puangsombat, A. Baramee, C. Mahidol, S. Ruchirawat, and P. Kittakoop, "Bioactive compounds from *Bauhinia purpurea* possessing antimalarial, antimycobacterial,

antifungal, anti-inflammatory, and cytotoxic activities," *Journal of Natural Products*, vol. 70, no. 5, pp. 795–801, 2007.

[11] B. V. S. Lakshmi, N. Neelima, N. Kasthuri, V. Umarani, and M. Sudhakar, "Protective effect of *Bauhinia purpurea* on gentamicin-induced nephrotoxicity in rats," *Indian Journal of Pharmaceutical Sciences*, vol. 71, no. 5, pp. 551–554, 2009.

[12] K. V. Ananth, M. Asad, N. P. Kumar, S. M. B. Asdaq, and G. S. Rao, "Evaluation of wound healing potential of *Bauhinia purpurea* leaf extracts in rats," *Indian Journal of Pharmaceutical Sciences*, vol. 72, no. 1, pp. 122–127, 2010.

[13] Z. A. Zakaria, M. S. Rofiee, L. K. Teh, M. Z. Salleh, M. R. Sulaiman, and M. N. Somchit, "*Bauhinia purpurea* leaves' extracts exhibited *in vitro* antiproliferative and antioxidant activities," *African Journal of Biotechnology*, vol. 10, no. 1, pp. 65–74, 2011.

[14] H. V. Annegowda, M. N. Mordi, S. Ramanathan, M. R. Hamdan, and S. M. Mansor, "Effect of extraction techniques on phenolic content, antioxidant and antimicrobial activity of *Bauhinia purpurea*: HPTLC determination of antioxidants," *Food Analytical Methods*, vol. 5, no. 2, pp. 226–233, 2012.

[15] B. S. Negi, B. P. Dave, and Y. K. Agarwal, "Evaluation of antimicrobial activity of *Bauhinia purpurea* leaves under *in vitro* conditions," *Indian Journal of Microbiology*, vol. 52, no. 3, pp. 360–365, 2012.

[16] E. F. Fang, C. S. F. Bah, J. H. Wong et al., "A potential human hepatocellular carcinoma inhibitor from *Bauhinia purpurea* L. seeds: from purification to mechanism exploration," *Archives of Toxicology*, vol. 86, no. 2, pp. 293–304, 2012.

[17] Z. A. Zakaria, E. E. Abdul Hisam, M. S. Rofiee et al., "*In vivo* antiulcer activity of the aqueous extract of *Bauhinia purpurea* leaf," *Journal of Ethnopharmacology*, vol. 137, no. 2, pp. 1047–1054, 2011.

[18] Z. A. Zakaria, E. E. Abdul Hisam, M. Norhafizah et al., "Methanol extract of *Bauhinia purpurea* leaf possesses Anti-Ulcer activity," *Medical Principles and Practice*, vol. 21, no. 5, pp. 476–482, 2012.

[19] K. R. Narayana, M. S. Reddy, M. R. Chaluvadi, and D. R. Krishna, "Bioflavonoids classification, pharmacological, biochemical effects and therapeutic potential," *Indian Journal of Pharmacology*, vol. 33, no. 1, pp. 2–16, 2001.

[20] Z. Zabidi, W. N. Wan Zainulddin, S. S. Mamat et al., "Antiulcer activity of methanol extract of *Melastoma malabathricum* leaves in rats," *Medical Principles and Practice*, vol. 21, no. 5, pp. 501–503, 2012.

[21] V. L. Singleton and J. A. Rossi Jr., "Colorimetry of total phenolics with phosphomolybdic-phosphotungstic acid reagents," *American Journal of Enology and Viticulture*, vol. 16, pp. 144–158, 1965.

[22] M. S. Blois, "Antioxidant determinations by the use of a stable free radical," *Nature*, vol. 181, no. 4617, pp. 1199–1200, 1958.

[23] M. Mujeeb, V. Aeri, P. Bagri, and S. Khan, "Hepatoprotective activity of the methanolic extract of *Tylophora indica* (Burm. f.) Merill. leaves," *International Journal of Green Pharmacy*, vol. 3, no. 2, pp. 125–127, 2009.

[24] H. A. El-Beshbishy, A. M. Mohamadin, A. A. Nagy, and A. B. Abdel-Naim, "Amelioration of tamoxifen-induced liver injury in rats by grape seed extract, black seed extract and curcumin," *Indian Journal of Experimental Biology*, vol. 48, no. 3, pp. 280–288, 2010.

[25] E. Shaker, H. Mahmoud, and S. Mnaa, "Silymarin, the antioxidant component and *Silybum marianum* extracts prevent liver damage," *Food and Chemical Toxicology*, vol. 48, no. 3, pp. 803–806, 2010.

[26] Z. A. Zakaria, M. S. Rofiee, M. N. Somchit et al., "Hepatoprotective activity of dried- and fermented-processed virgin coconut oil," *Evidence-Based Complementary and Alternative Medicine*, vol. 2011, Article ID 142739, 8 pages, 2011.

[27] E. Hazai, L. Vereczkey, and K. Monostory, "Reduction of toxic metabolite formation of acetaminophen," *Biochemical and Biophysical Research Communications*, vol. 291, no. 4, pp. 1089–1094, 2002.

[28] B. Rajkapoor, Y. Venugopal, J. Anbu, N. Harikrishnan, M. Gobinath, and V. Ravichandran, "Protective effect of *Phyllanthus polyphyllus* on acetaminophen induced hepatotoxicity in rats," *Pakistan Journal of Pharmaceutical Sciences*, vol. 21, no. 1, pp. 57–62, 2008.

[29] B. G. Katzung, *Basic and Clinical Pharmacology*, McGrawHill, New York, NY, USA, 9th edition, 2004.

[30] H. Ha, N. Lee, C. Seo et al., "Hepatoprotective and antioxidative activities of cornus officinalis against acetaminophen-induced hepatotoxicity in mice," *Evidence-Based Complementary and Alternative Medicine*, vol. 2012, Article ID 804924, 8 pages, 2012.

[31] H. S. Farghaly and M. A. Hussein, "Protective effect of curcumin against paracetamol-induced liver damage," *Australian Journal of Basic and Applied Sciences*, vol. 4, no. 9, pp. 4266–4274, 2010.

[32] C. Kerksick and D. Willoughby, "The antioxidant role of glutathione and N-acetyl-cysteine supplements and exercise-induced oxidative stress," *Journal of the International Society of Sports Nutrition*, vol. 2, no. 2, pp. 38–44, 2005.

[33] S. U. Yanpallewar, S. Sen, S. Tapas, M. Kumar, S. S. Raju, and S. B. Acharya, "Effect of *Azadirachta indica* on paracetamol-induced hepatic damage in Albino rats," *Phytomedicine*, vol. 10, no. 5, pp. 391–396, 2003.

[34] A. K. Shnoy, S. N. Somayaji, and K. L. Bairy, "Hepatoprotective activity of ethanolic extract of *Ginkgo biloba* against carbon tetrachloride induced hepatic injury in rats," *Indian Journal Pharmacology*, vol. 46, pp. 167–174, 2002.

[35] D. E. Amacher, "Serum transaminase elevations as indicators of hepatic injury following the administration of drugs," *Regulatory Toxicology and Pharmacology*, vol. 27, no. 2, pp. 119–130, 1998.

[36] N. Uma, S. Fakurazi, and I. Hairuszah, "*Moringa oleifera* enhances liver antioxidant status via elevation of antioxidant enzymes activity and counteracts paracetamol-induced hepatotoxicity," *Malaysian Journal of Nutrition*, vol. 16, no. 2, pp. 293–307, 2010.

[37] M. N. Somchit, A. Zuraini, A. A. Bustamam, N. Somchit, M. R. Sulaiman, and R. Noratunlina, "Protective activity of turmeric (*Curcuma longa*) in paracetamol-induced hepatotoxicity in rats," *International Journal of Pharmacology*, vol. 1, pp. 252–256, 2005.

[38] G. Kumar, G. S. Banu, P. V. Pappa, M. Sundararajan, and M. R. Pandian, "Hepatoprotective activity of *Trianthema portulacastrum* L. against paracetamol and thioacetamide intoxication in albino rats," *Journal of Ethnopharmacology*, vol. 92, no. 1, pp. 37–40, 2004.

[39] A. K. Gupta, H. Chitme, S. K. Dass, and N. Misra, "Hepatoprotective activity of *Rauwolfia serpentina* rhizome in paracetamol intoxicated rats," *Journal of Pharmacological and Toxicological*, vol. 1, pp. 82–88, 2006.

[40] M. I. Luster, P. P. Simeonova, R. M. Gallucci, J. M. Matheson, and B. Yucesoy, "Immunotoxicology: role of inflammation in chemical-induced hepatotoxicity," *International Journal of Immunopharmacology*, vol. 22, no. 12, pp. 1143–1147, 2000.

[41] S. Yadav and B. K. Bhadoria, "Two dimeric flavonoids from *Bauhinia purpurea*," *Indian Journal of Chemistry B*, vol. 44, no. 12, pp. 2604–2607, 2005.

[42] J. F. S. Ferreira, D. L. Luthria, T. Sasaki, and A. Heyerick, "Flavonoids from *Artemisia annua* L. As antioxidants and their potential synergism with artemisinin against malaria and cancer," *Molecules*, vol. 15, no. 5, pp. 3135–3170, 2010.

[43] A. R. Tapas, D. M. Sakarkar, and R. B. Kakde, "Flavonoids as nutraceuticals: a review," *Tropical Journal of Pharmaceutical Research*, vol. 7, no. 3, pp. 1089–1099, 2008.

[44] H. K. Sandhar, B. Kumar, S. Prasher, P. Tiwari, M. Salhan, and P. Sharma, "A review of phytochemistry and pharmacology of flavonoids," *Internationale Pharmaceutica Sciencia*, vol. 1, pp. 24–41, 2011.

[45] P. Pithayanukul, S. Nithitanakool, and R. Bavovada, "Hepatoprotective potential of extracts from seeds of *Areca catechu* and nutgalls of *Quercus infectoria*," *Molecules*, vol. 14, no. 12, pp. 4987–5000, 2009.

[46] O. O. Elekofehinti, I. G. Adanlawo, K. Komolafe, and O. C. Ejelonu, "Saponins from *Solanum anguivi* fruits exhibit antioxidant potential in Wistar rats," *Annals of Biological Research*, vol. 3, no. 7, pp. 3212–3217, 2012.

[47] E. K. Akkol, I. I. Tatli, and Z. S. Akdemir, "Antinociceptive and anti-inflammatory effects of saponin and iridoid glycosides from *Verbascum pterocalycinum* var. mutense Hub.-Mor.," *Zeitschrift fur Naturforschung C*, vol. 62, no. 11-12, pp. 813–820, 2007.

[48] E. Porchezhian and S. H. Ansari, "Hepatoprotective activity of *Abutilon indicum* on experimental liver damage in rats," *Phytomedicine*, vol. 12, no. 1-2, pp. 62–64, 2005.

[49] H. M. Mehendale, "PPAR-α: a key to the mechanism of hepatoprotection by clofibrate," *Toxicological Sciences*, vol. 57, no. 2, pp. 187–190, 2000.

[50] J. E. Manautou, S. G. E. Hart, E. A. Khairallah, and S. D. Cohen, "Protection against acetaminophen hepatotoxicity by a single dose of clofibrate: effects on selective protein arylation and glutathione depletion," *Fundamental and Applied Toxicology*, vol. 29, no. 2, pp. 229–237, 1996.

[51] Y. Liang, S. Tsai, D. Tsai, S. Lin-Shiau, and J. Lin, "Suppression of inducible cyclooxygenase and nitric oxide synthase through activation of peroxisome proliferator-activated receptor-γ by flavonoids in mouse macrophages," *FEBS Letters*, vol. 496, no. 1, pp. 12–18, 2001.

[52] K. L. Han, M. H. Jung, J. H. Sohn, and J. Hwang, "Ginsenoside 20(S)-protopanaxatriol (PPT) activates peroxisome proliferator-activated receptor γ (PPARγ) in 3T3-L1 adipocytes," *Biological and Pharmaceutical Bulletin*, vol. 29, no. 1, pp. 110–113, 2006.

Hindawi Publishing Corporation
Evidence-Based Complementary and Alternative Medicine
Volume 2013, Article ID 324864, 9 pages
http://dx.doi.org/10.1155/2013/324864

Research Article

Neonauclea reticulata (Havil.) Merr Stimulates Skin Regeneration after UVB Exposure via ROS Scavenging and Modulation of the MAPK/MMPs/Collagen Pathway

Hsiu-Mei Chiang,[1] Hsin-Chun Chen,[1] Hua-Hsien Chiu,[2] Chien-Wen Chen,[1] Ssu-Meng Wang,[1] and Kuo-Ching Wen[1]

[1] *Department of Cosmeceutics, China Medical University, Taichung 404, Taiwan*
[2] *Center for Biomedical Technology Research and Development, Fooyin University, Kaohsiung 83102, Taiwan*

Correspondence should be addressed to Hsiu-Mei Chiang; hmchiang@mail.cmu.edu.tw
and Kuo-Ching Wen; kcwen0520@mail.cmu.edu.tw

Received 3 January 2013; Accepted 29 May 2013

Academic Editor: Wei-Chiang Lin

In this study, we investigated whether the protective effects of *Neonauclea reticulata* water extract against ultraviolet B (UVB) irradiation in human skin fibroblast cell cultures (Hs68) are governed by its ability to protect against oxidative stress and expression of matrix metalloproteinases (MMPs). We found that *Neonauclea reticulata* extract exhibited DPPH scavenging activity and inhibited AAPH-induced haemolysis of erythrocytes in a dose- and time-dependent manner. We also found that pretreatment of fibroblasts with *Neonauclea reticulata* water extract resulted in markedly lower levels of MMP-1, -3, and -9 expressions. Furthermore, our results indicate that *Neonauclea reticulata* extract inhibits the expression of MMPs by inhibiting ERK, JNK, and p38 phosphorylation. Our results also demonstrate that treatment with *Neonauclea reticulata* extract protects against UVB-induced depletion of collagen. In addition, *Neonauclea reticulata* extract did not have a cytotoxic effect. These findings indicate that the antioxidant activity of *Neonauclea reticulata* extract resulted in inhibition of MMP-1, -3, and -9 expressions and in increased levels of collagen activity. Our results suggest that *Neonauclea reticulata* extract can protect against photoaging.

1. Introduction

Ultraviolet (UV) irradiation causes hazardous effects on the structure and function of skin, including sunburn, immune suppression, cancer, and photoaging [1, 2]. UV-induced oxidative damage and induction of matrix metalloproteinases (MMPs) have been implicated in skin photoaging. Photoaging is thought to occur by continuous damage to the collagenous extracellular matrix (ECM) that comprises the dermal connective tissue [3], and histological studies have demonstrated that the alterations are found in the dermal layer of photoaged skin. Collagen is the major insoluble fibrous protein in the extracellular matrix and in connective tissue, and type I collagen is the most abundant subtype of collagen. Collagen is synthesized primarily by fibroblasts residing within the dermis and is responsible for conferring strength and elasticity of skin [4]. Disorganization, fragmentation, and dispersion of collagen bundles are prominent features of photodamaged human skin.

Ultraviolet B (UVB) irradiation stimulates the generation of reactive oxygen species (ROS) and induces the overexpression of MMP-1, -3, and -9 in human fibroblasts, resulting in the destruction of collagen and, hence, wrinkle formation and sagging skin [5–8]. Increased levels of ROS are known to alter the structure and function of genes and proteins in skin and MMPs, which are involved in extracellular matrix (ECM) remodelling, play important roles in cell migration, skin ulceration, and photoaging [9].

The results from recent studies have shown that phytochemicals such as polyphenols are excellent antioxidant and antiphotoaging agents [7, 10, 11]. Polyphenols and flavonoids are abundant in fruits, vegetables, green tea, and red wine

and possess a variety of biological activities including antioxidants and the ability to inhibit the expression of MMPs in dermal fibroblasts. *Neonauclea reticulata* (Havil.) Merr is a member of the flavonoid-rich Rubiaceae family of flowering plants. In our previous studies, we found that *Coffea arabica* and *Ixora parviflora*, also members of the Rubiaceae family, were rich in polyphenols content and exhibited antiphotoaging activity by inhibiting the expression of MMPs and mitogen-activated protein kinases (MAPKs) [7, 8]. Therefore, we expected that plants who belonged to Rubiaceae family, such as *Neonauclea reticulate*, may exhibit similar activity. In our preliminary study, *Neonauclea reticulata* extract showed high total phenolic content and good ROS scavenging activity, suggesting that *Neonauclea reticulata* extract might be effective against UVB-induced photoaging. The aim of this study was to investigate the mechanisms through which *Neonauclea reticulata* extract protects against UVB-induced oxidative stress and photoaging in human skin fibroblast cell cultures. In addition, in our knowledge, this is the first report of the biological benefits of *Neonauclea reticulata*.

2. Materials and Methods

2.1. Materials. Human foreskin fibroblasts were obtained from the Bioresource Collection and Research Center (Hsinchu, Taiwan). Gelatin, agarose, hydrochloric acid, methanol, dimethyl sulfoxide (DMSO), doxycycline hyclate, calcium chloride ($CaCl_2$), DL-dithiothreitol, and Folin-Ciocalteu reagent were purchased from Sigma-Aldrich Chemicals (St. Louis, MO, USA). Fetal bovine serum (FBS), penicillin-streptomycin, trypsin-EDTA, and Dulbecco's Modified Eagle's Medium (DMEM) were purchased from Gibco, Invitrogen (Carlsbad, CA, USA). Coomassie blue R-250, dibasic sodium phosphate, igepal CA-630, tris, and 3-(4,5-dimethylthiazol-2-yl)-2,5-diphenyltetrazolium bromide (MTT) were purchased from USB (Cleveland, OH, USA). Collagenase was purchased from Calbiochem, Merck (Darmstadt, Germany). Fluorogenic peptide substrate I was purchased from R&D Systems (Wiesbaden, Germany), and Bradford reagent was supplied by Bio-Rad Laboratories (Hercules, CA, USA). Donkey anti-goat IgG-HRP, ERK 1 (C-16), JNK1 (G-13), MMP-1 (L-20), MMP-3 (1B4), MMP-9 (6-6B), p38 (A-12), p-p38 (Thr 180/Tyr 182)-R, p-JNK (Thr 183/Tyr 185), and p-ERK 1/2 (Thr 202/Tyr 204) were purchased from Santa Cruz Biotechnology, Inc. (CA, USA). All other chemicals used were of high purity biochemistry grade.

2.2. Preparation of Neonauclea reticulata Extract. Fresh leaves of *Neonauclea reticulata* were harvested and identified at the National Museum of Natural Science, Taichung, Taiwan. The leaves were identified by macroscopic and microscopic examination by Dr. T. Y. Aleck Yang, and the voucher specimen was deposited in the National Museum of Natural Science (no. TNM BS 00599). The leaves were dried, ground, and then extracted twice with a 30-fold volume of water or methanol ultrasonically for 1 h. The supernatant was filtered, and the filtrate was evaporated to dryness in vacuo. The *Neonauclea reticulata* extract was stored at −20°C before use.

2.3. Total Phenolic Content of Neonauclea reticulata Extract. Total phenolic content was determined by the Folin-Ciocalteu reaction as reported previously [7]. Briefly, a mixture of *Neonauclea reticulata* extract and Folin-Ciocalteu phenol reagent was prepared, and then sodium carbonate was added to the mixture. The resulting blue complex was then measured at 760 nm. Gallic acid was used as a standard for the calibration curve. The contents of phenolic compounds were expressed as mg gallic acid equivalent/g dry weight. The dry weight indicated was *Neonauclea reticulata* leaves dry weight.

2.4. The Antioxidant Effects of Neonauclea reticulata Preparations

2.4.1. DPPH Radical Scavenging Activity. In this assay, ascorbic acid (50 μg/mL) was used as a positive control. Reaction mixtures containing DPPH and serial dilutions of sample (amounts of sample ranging from 25 to 1000 μg/mL) were placed in a 96-well microplate at room temperature in the dark for 30 min. After incubation, the absorbance was read at 517 nm by ELISA. Scavenging activity was determined by the following:

$$\text{scavenging activity } (\%) = \left[1 - \left(\frac{A_{\text{sample}}}{A_{\text{control}}}\right)\right] \times 100. \quad (1)$$

2.4.2. Preparation of Erythrocyte Suspensions and Hemolysis Assay. Blood was obtained from male SD rats via cardiopuncture, and whole blood was collected in EDTA-containing tubes. This animal study adhered to The Guidebook for the Care and Use of Laboratory Animals (published by The Chinese Society for Laboratory Animal Science, Taiwan). The erythrocytes were isolated by centrifugation, washed with PBS, and then resuspended to the desired hematocrit level. In order to induce free radical chain oxidation in the erythrocytes, aqueous peroxyl radicals were generated by thermal decomposition of AAPH in oxygen. A erythrocyte suspension at 5% hematocrit was incubated with PBS (control) or preincubated with *Neonauclea reticulata* extract (10–50 μg/mL), followed by incubation with or without AAPH in PBS. This reaction mixture was shaken gently while being incubated for a fixed interval at 37°C. The reaction mixture was removed and centrifuged at 3000 ×g for 2 min, with absorbance of the supernatant determined at 540 nm. Reference values were determined using the same volume of erythrocytes in a hypotonic buffer. The hemolysis percentage was calculated using the formula $[(A_{\text{sample}}/A_{\text{control}})] \times 100$.

2.4.3. Peroxide Scavenging Assay. The ability of *Neonauclea reticulata* extract to scavenge H_2O_2 was determined spectrophotometrically as previously described [12]. Briefly, a 20 mM solution of H_2O_2 was prepared in PBS (pH 7.4), added to various concentrations of *Neonauclea reticulata* extract that had been dissolved in methanol (50 to 2000 μg/mL), and then allowed to stand at room temperature in the dark. The absorption was measured at 230 nm using an ELISA reader (Tecan, Grodig, Austria). The H_2O_2 scavenging

activity of *Neonauclea reticulata* extract was determined by the following:

$$\text{scavenging effect (\%)} = \left(\frac{A_{\text{control at 230 nm}} - A_{\text{sample at 230 nm}}}{A_{\text{control at 230 nm}}}\right) \times 100. \quad (2)$$

2.5. MMP Activity Assay by Fluorescent Gelatin. The MMP activity in samples exposed to *Neonauclea reticulata* was assessed using a fluorescent method. Various concentrations of *Neonauclea reticulata* extract were tested for its ability to digest a synthetic fluorogenic substrate. Each concentration of *Neonauclea reticulata* extract was incubated with substrate at 37°C. Fluorescence intensity was measured at 320 nm (excitation) and 405 nm (emission) with a fluorescence reader.

2.6. Cell Culture. Human foreskin fibroblasts (Hs68) cells were plated in a 10 cm dish and grown in DMEM supplemented with 10% FBS, 100 U/mL penicillin, and 100 U/mL streptomycin at 37°C in 5% CO_2 humidified air. The cells were subcultured following trypsinization. For UVB irradiation, the medium was removed and washed in PBS. All UVB irradiations were performed under a thin layer of PBS. After UVB irradiation, cells were rinsed twice with PBS and incubated in fresh culture media without serum in the presence of *Neonauclea reticulata* extract for a further 24 h.

2.7. UVB Irradiation Dose. The source of UVB radiation was a UV lamp with a digital controller to regulate UV dosage (CL-1000 M, UVP, USA). The peak emission was recorded at 302 nm. The UVB irradiation dose was 40 mJ/cm^2 (exposure time was 15 seconds). According to the results of our preliminary study, this UV dose induces the expression of MMPs and MAPKs but does not significantly affect cell viability (data not shown). After UVB irradiation, PBS was replaced with a serum-free medium, and cells were incubated for 24 h before subjecting them to the thiazolyl blue tetrazolium bromide (MTT) and MMP assays.

2.8. Cell Viability Test. Fibroblasts were plated at a density of 10^4 cells/well in 96-well plates per 100 μL medium and treated with 50 μL of various concentrations of *Neonauclea reticulata* extract dissolved in DMEM and a small amount of DMSO for 24 h (the final concentration of DMSO was lower than 0.1%). The cytotoxic effect of *Neonauclea reticulata* extract on cells exposed to UVB and on cells that were unexposed to UVB irradiation was evaluated in cells that had been cultured for 3 h in MTT solution. Metabolic activity was quantified by measuring light absorbance at 570 nm (Tecan, Grodig, Austria).

2.9. Fluorescence Assay of Intracellular ROS. This assay is based on the use of an established nonfluorescent (DCFDA)/fluorescent (DCF) system that measures the levels of ROS, which are in turn responsible for the generation of fluorescence [12]. Hs68 cells were seeded in a 24-well plate at a density of 10^5 cells/well for 24 h, rinsed once with 0.5 mL PBS, and then exposed to UVB irradiation (302 nm, CL-1000 M, UVP, USA). The UVB irradiation dose was 80 mJ/cm^2 (exposure time was about 30 seconds). After that, PBS was removed, and then various concentrations of *Neonauclea reticulata* extract (1, 5, 10, and 50 μg/mL) that had been prepared in serum-free DMEM were added. Cells were then allowed to incubate for 24 h at 37°C. The cells were then incubated for 30 min in the presence of 10 μM DCFDA. After that, the DMEM was removed and the cells were washed twice with PBS. The cells were then covered with PBS. Images were observed under a fluorescence microscope (Leica DMIL, German), and the fluorescence (emission 520 nm, excitation 488 nm) was measured using a microplate reader (Thermo Electron Corporation, Vantaa, Finland). The following equation was used to calculate the relative fluorescence:

$$\text{relative fluorescence (\%)} = \left(\frac{A_{\text{control}} - A_{\text{sample}}}{A_{\text{control}}}\right) \times 100. \quad (3)$$

2.10. Immunoblot Analysis. Cells were harvested and homogenized with lysis buffer [7]. Equal amounts of protein were separated on 10% SDS-PAGE gels and then transferred to a PVDF membrane (Hybond ECL, Amersham Pharmacia Biotech Inc., Piscataway, NJ, USA). Blots were blocked with nonfat milk in TBS buffer containing 0.05% Tween 20 (TBST). The membrane was incubated overnight at 4°C with specific antibodies. The antibodies comprised goat polyclonal antibodies against MMP-1 (1 : 500) and type I procollagen (1 : 500) and mouse polyclonal antibodies against MMP-3 (1 : 500), MMP-9 (1 : 500), ERK (1 : 500), JNK (1 : 500), p38 (1 : 500), p-ERK (1 : 500), p-JNK (1 : 500), and p-p38 (1 : 500) (Santa Cruz Biotechnology, Inc.). The membranes were washed with TBST, and the blots were then incubated with the corresponding conjugated anti-immunoglobulin G-horseradish peroxidase (Santa Cruz Biotechnology Inc.). Immunoreactive proteins were detected with the ECL Western blotting detection system (Fujifilm, LAS-4000). Signal strengths were quantified using a densitometric program (multi Gauge V2.2).

2.11. Measurement of Total Collagen Synthesis. Total collagen synthesis in fibroblasts after UVB exposure was measured by the Sircol soluble collagen assay kit (Biocolor Ltd., UK) according to the manufacturer's protocol. Briefly, cell culture medium was mixed with Sircol dye reagent and incubated at room temperature for 30 min. After centrifugation, ice-cold acid-salt washing reagent was added to the precipitate, and then the mixture was centrifuged. The precipitate was dissolved with Alka reagent, and the absorption was determined at 555 nm by an ELISA reader (Tecan, Grodig, Austria).

2.12. Statistical Analysis. Results are expressed as mean ± SD. Differences between groups were analyzed by ANOVA followed by the Scheffe's test. A p value <0.05 was considered to represent statistical significance.

3. Results

3.1. The Extraction Yield and Total Phenolic Content of Neonauclea reticulata Preparations. The extraction yield of *Neonauclea reticulata* leaves was 5.6% by methanol and 17.0% by water. The total phenolic content in the extract was determined by the Folin-Ciocalteu method. The total phenolic content, expressed as μg gallic acid equivalent per mg of dry weight (*Neonauclea reticulata* leaves) was 24.2 ± 1.6 μg/mg in the water extract and 9.2 ± 0.6 μg/mg in the methanol extract.

3.2. Fluorometric Analysis of the Inhibitory Effect of Neonauclea reticulata Preparations on Bacterial Collagenase-1. In order to elucidate the inhibitory effect of *Neonauclea reticulata* extract on bacterial collagenase-1, fluorescence-conjugated gelatin was used, and the results were compared with the positive control, namely, doxycycline hyclate (DC). In this study, a fluorescence-conjugated substrate was incubated with bacterial collagenase-1 for 20 h in the presence of different concentrations of water extract, methanol extract, or DC at 37°C. The inhibitory effects of *Neonauclea reticulata* preparations (10–500 μg/mL) were dose-dependent (Figure 1) and the highest dose of *Neonauclea reticulata* extract (500 μg/mL) inhibited bacterial collagenase-1 expression in 90% of cells.

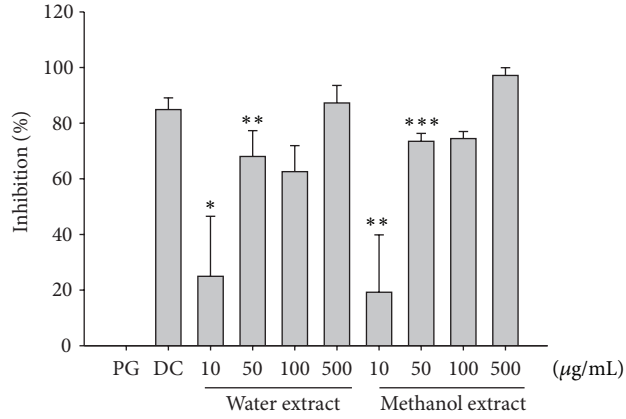

Figure 1: Collagenase fluorescence assay of methanol and water extracts of *Neonauclea reticulata extract* (1000 μg/mL). Methanol and water extracts of *Neonauclea reticulata* significantly reduced collagenase activity. ($^{*}P < 0.05$; $^{**}P < 0.01$; $^{***}P < 0.001$).

3.3. The Antioxidant Effect of Neonauclea reticulata Preparations

3.3.1. Scavenging of DPPH Radicals. Figure 2(a) shows the free radical (DPPH) scavenging activity of *Neonauclea reticulata* extract (10–100 μg/mL) and ascorbic acid (50 μg/mL). Our results indicate that *Neonauclea reticulata* water and methanol extracts exhibited DPPH radial scavenging activity in a dose-dependent manner. The DPPH scavenging activity was significant at 10 μg/mL and was similar to that of ascorbic acid at 50 μg/mL (Figure 2(a)).

3.3.2. Erythrocyte Hemolysis Assay. According to the results of the DPPH and MMP activity assays in a cell-free system, the activity of the water extract of *Neonauclea reticulata* was similar to those of methanol extract. Therefore, the water extract of *Neonauclea reticulata* was determined using an AAPH-induced erythrocyte hemolysis assay. The influence of the *Neonauclea reticulata* extract on *in vitro* erythrocyte hemolysis was examined by incubating rat erythrocytes in the presence of 25 mM AAPH as an initiator of oxidation. The *Neonauclea reticulata* extract exhibited a strong, dose-dependent inhibitory effect at concentrations greater than 50 μg/mL (50–500 μg/mL) against erythrocyte hemolysis when treated for more than 1.5 h (Figure 2(b)).

3.3.3. Peroxide Scavenging Assay. Peroxide is the primary product of oxidation produced during the initial stage of oxidation. The peroxide scavenging activities of *Neonauclea reticulata* extract and ascorbic acid are shown in Figure 2(c). The mean peroxide scavenging activity of various concentrations of *Neonauclea reticulata* extract (50, 100, 250, 500, 750, 1000, and 2000 μg/mL) ranged from 5.1% ± 0.3% to 99.6% ± 0.3% and that of ascorbic acid (1000 μg/mL) was 98.5 ± 0.1%. The activity of *Neonauclea reticulata* extract was similar to that of ascorbic acid at an equal concentration (500 μg/mL).

3.3.4. Fluorescence Assay of Intracellular ROS. DCFDA staining and fluorescence microscopy were used to qualitatively characterize the degree of ROS generation. Fibroblasts were exposed to UVB (80 mJ/cm^2) and then incubated with 10 μM of DCFDA for 30 min in a 24-well plate. After removing the DCFDA-containing medium, the cells were washed with PBS and treated with *Neonauclea reticulata* extract for 24 h. As shown in Figure 3, ROS levels were markedly higher in UVB-exposed fibroblasts than in control cells; however, this increase in ROS generation was attenuated in a dose-dependent manner in UVB-exposed fibroblasts that had been pretreated with various concentrations of *Neonauclea reticulata* extract (1–50 μg/mL).

3.4. Effect of Neonauclea reticulata Extract on the Cell Viability. According to the results obtained in the cell-free system mentioned above, *Neonauclea reticulata* water extract was chosen for the study in human foreskin fibroblasts (Hs68). Hs68 cells were treated with various concentrations of *Neonauclea reticulata* extract, and cell viability was measured using the MTT assay. As shown in Figure 4, the survival curve indicates that *Neonauclea reticulata* extract (5–200 μg/mL) did not exhibit cytotoxic effects on the proliferation of cells. In addition, the preparations at high concentration (>100 μg/mL) stimulated cell growth (140%).

3.5. Effects of Neonauclea reticulata Extract on UVB-Induced Photoaging and the Effect of Neonauclea reticulata Extract on Expression of MMPs and Type I Procollagen. UV irradiation at a UVB dose of 40 mJ/cm^2 resulted in overexpression of MMPs and a decrease in type I procollagen synthesis in untreated fibroblast cells (Figure 5). However, pretreatment

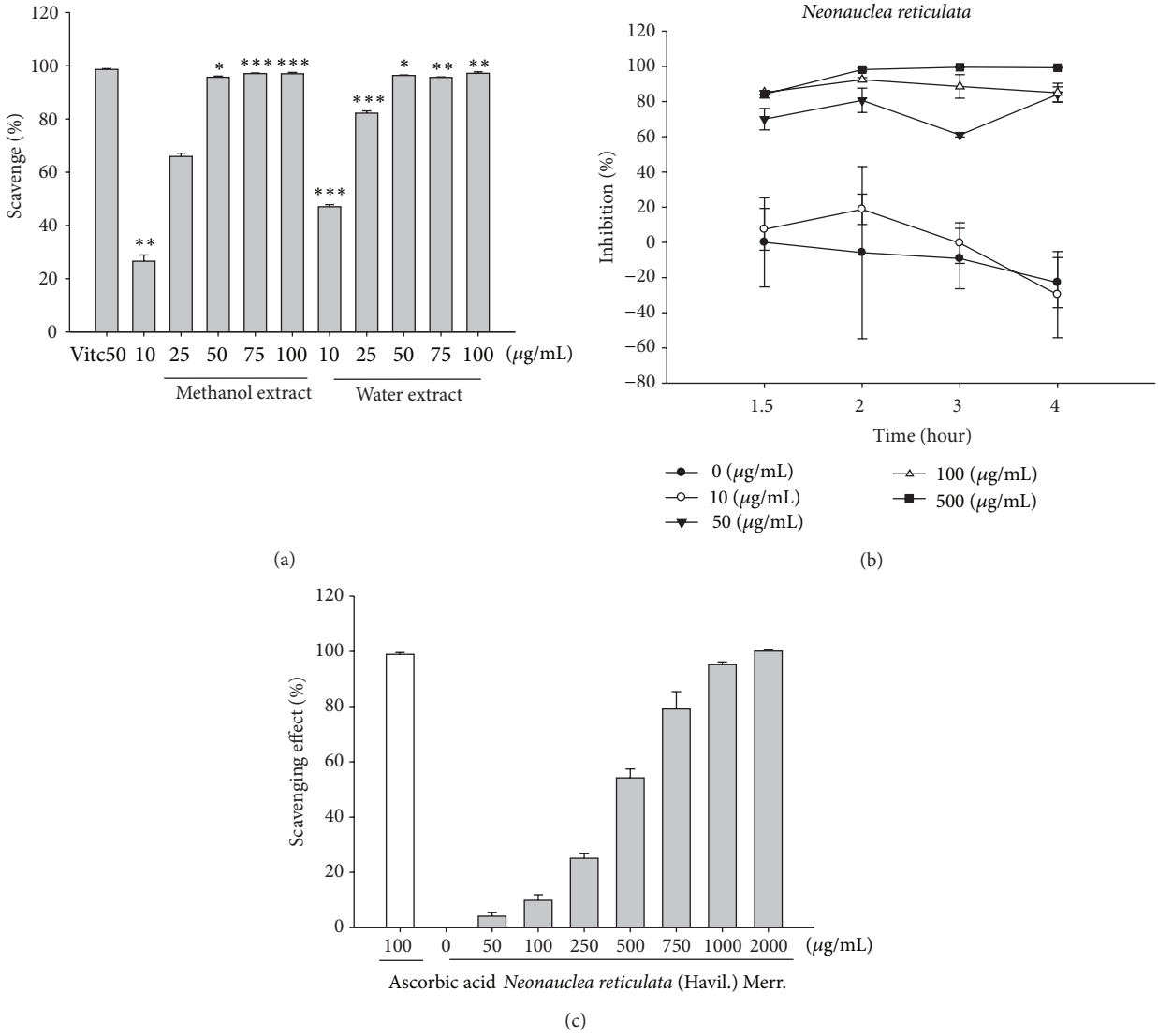

Figure 2: Antioxidant effect of *Neonauclea reticulata* preparation on DPPH radical scavenging and AAPH-induced hemolysis ($n = 6$). (a) Effects of methanol and water extracts of *Neonauclea reticulata* (10–100 μg/mL) on DPPH radical scavenging. (b) Scavenging of hydrogen peroxide by *Neonauclea reticulata*. (c) Time course inhibition of water extract of *Neonauclea reticulata* (10–100 μg/mL) on AAPH-induced hemolysis. *Neonauclea reticulata* preparations exhibited DPPH radial scavenging activity at doses higher than 50 μg/mL. The IC_{50} of *Neonauclea reticulata* extract on DPPH radical scavenging was 10.2 μg/mL. The *Neonauclea reticulata* extract inhibited erythrocyte hemolysis in a dose-dependent manner (10–50 μg/mL). The IC_{50} of *Neonauclea reticulata* extract on AAPH-induced lysis of rat erythrocytes was 33.5 μg/mL.

of cells with different concentrations of *Neonauclea reticulata* before exposure to UVB (40 mJ/cm^2) irradiation resulted in a dose-dependent reduction in expression of MMP-1, -3, -9 in cells (Figure 5). In addition, we found that UVB irradiation resulted in underexpression of type I procollagen and that pretreatment with *Neonauclea reticulata* extract did not result in a significant increase in expression of type I procollagen after exposure to UVB (Figure 5).

3.6. Effect of Neonauclea reticulata Extract on MAPK Expression. As shown in Figure 6, UVB (40 mJ/cm^2) induced the phosphorylation of p38, ERK, and JNK. The inhibitory effect of *Neonauclea reticulata* extract (5–50 μg/mL) on ERK phosphorylation was dose-dependent (Figure 6), and the effect was significant even at low doses (e.g., 5 μg/mL). Phosphorylation of p38 and ERK was suppressed in cells that had been pretreated with *Neonauclea reticulata* extract, even at low doses.

3.7. Pretreatment with Neonauclea reticulata Extract Attenuated UVB-Induced Reduction in Total Collagen Synthesis. Fibroblasts were pretreated with *Neonauclea reticulata* extract (1–50 μg/mL) for 1 h, exposed to UVB, and then treated with *Neonauclea reticulata* extract for 24 h. As shown in Figure 7,

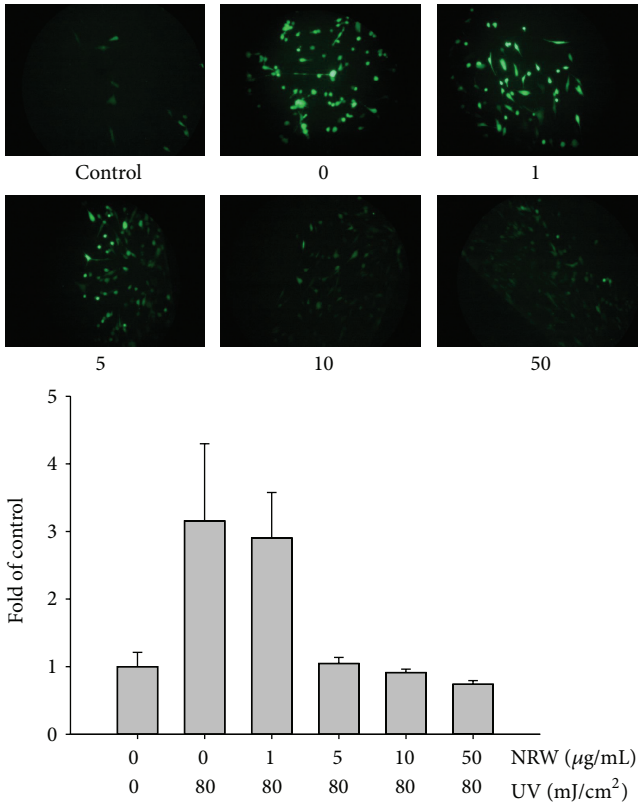

Figure 3: Repressive effect of *Neonauclea reticulata* extract (NRW) on intracellular oxidative stress in UV-irradiated Hs68 cells.

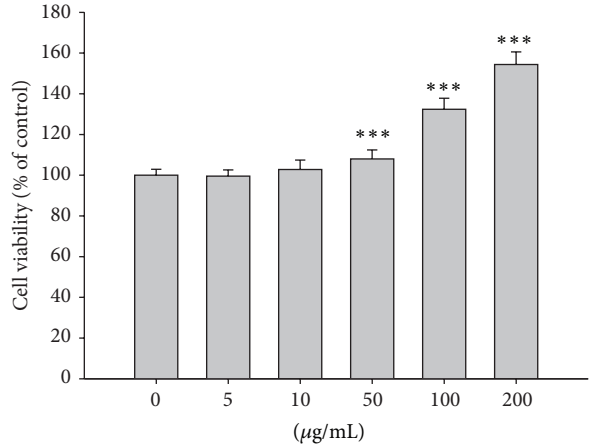

Figure 4: Viability (%) of human foreskin fibroblasts exposed to *Neonauclea reticulata* extract. *Neonauclea reticulata* extract (5–200 μg/mL) did not exhibit cytotoxic effects on the proliferation of cells. In addition, the preparations at high concentration (>100 μg/mL) stimulated cell growth (150%) (***$P < 0.001$).

Neonauclea reticulata extract treatment resulted in a dose-dependent restoration of collagen.

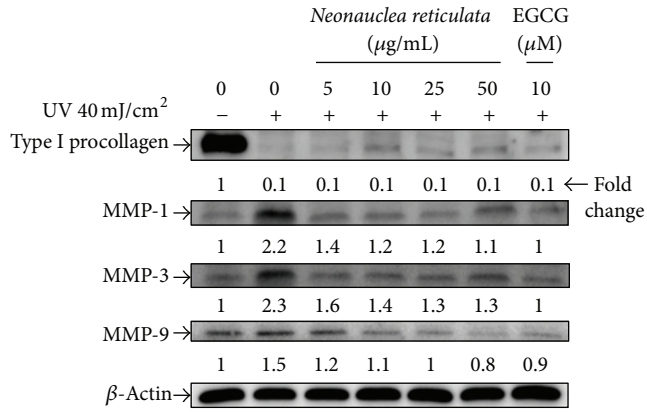

Figure 5: Effects of *Neonauclea reticulata* extract on UVB-induced expression of MMP-1, -3, and -9 and type I procollagen in human foreskin fibroblasts. Expression of MMPs increased and that of type I procollagen decreased after UVB irradiation. *Neonauclea reticulata* extract (5–50 μg/mL) treatment attenuated this effect.

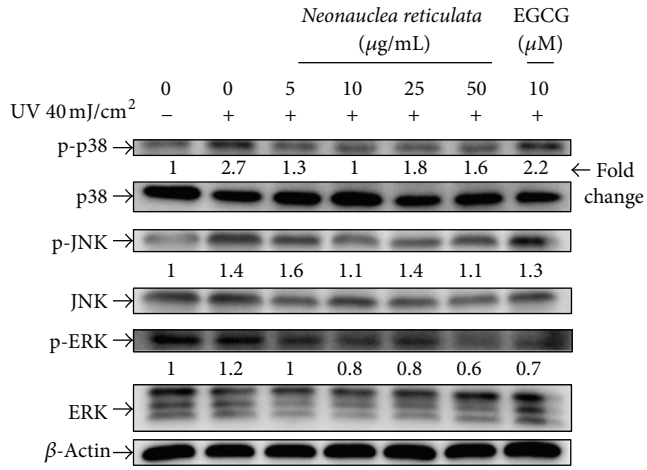

Figure 6: Effect of *Neonauclea reticulata* extract on UVB-induced expression of MAP kinases in human fibroblasts. *Neonauclea reticulata* extract inhibited ERK phosphorylation in a dose-dependent manner. In addition, the extract suppressed the activation of JNK at a dose of 10 μg/mL. *Neonauclea reticulata* extract at low doses (5 and 10 μg/mL) inhibited the phosphorylation of p38.

4. Discussion

UVB irradiation of human skin fibroblasts induces the expression of MMPs, which in turn degrades the extracellular matrix (ECM), causing photoaging. Some investigators have, therefore, focused on the development of MMP inhibitors as a promising antiphotoaging strategy [2]. In our previous study, we demonstrated that irradiation of human skin fibroblasts with UVB caused a decrease in cell viability and type I procollagen content and an increase in ROS production and expression of MMPs [7, 8]. In this study, we found that *Neonauclea reticulata* extract not only enhanced the proliferation of fibroblasts in a concentration-dependent manner but also exhibited a protective effect against UVB-induced

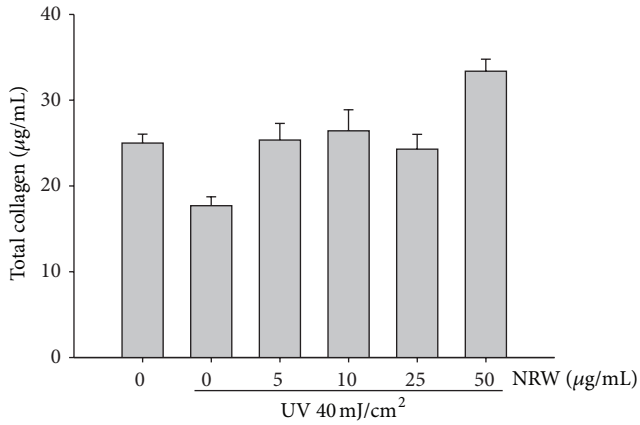

Figure 7: Effect of *Neonauclea reticulata* extract (NRW) on total collagen synthesis.

cytotoxicity. These results suggest that *Neonauclea reticulata* extract is a promising antiphotoaging agent.

UVB-induced inflammation and the resulting accumulation of ROS play an important role in chronologically aged and photoaged skin *in vivo* [13]. Studies have shown that intracellular generation of ROS such as superoxide anion (O_2^-), hydroxyl radical ($OH^\bullet$), singlet oxygen ($^1O_2$), and hydrogen peroxide (H_2O_2) lead to a state of cellular oxidative stress and that said ROS generation is a key mediator in the photoaging process [12, 14]. The mechanisms of action of most natural product- and vitamin-based treatments that are used for skin aging involve free radical scavenging. Studies of numerous natural compounds from plant sources have shown that their photoprotective effects are mediated by their ability to quench ROS generation and prevent DNA damage due to UVB irradiation [15, 16]. In addition, other studies on natural products have reported that the high polyphenol content in these products is responsible for some of the biological activities observed in these plants. Increased cellular levels of ROS can lead to cellular damage; however, studies have shown that natural products with high polyphenol content such as *Coffea arabica*, *Terminalia catappa*, and *Emblica officinalis* protect cells from such cellular damage by scavenging ROS [7, 17–21]. In this study, we found that *Neonauclea reticulata* extract, which is abundant in polyphenols, is a natural antioxidant and that it protects against photoaging. Polyphenols are good ROS scavengers because they contain a large number of OH groups [22]. In this study, *Neonauclea reticulata* extract showed good DPPH radical and peroxide scavenging activity and protected against AAPH-induced erythrocyte hemolysis. In addition, *Neonauclea reticulata* extract exhibited scavenging activity of intracellular ROS produced by UVB irradiation, indicating that *Neonauclea reticulata* extract is a potential candidate for the prevention of aging and photoaging.

UV irradiation also enhances collagenase activity and reduces the production of collagen, resulting in wrinkle formation through degradation of the collagen in the dermal extracellular matrix [6, 23]. Collagenase inhibitors have been identified as potential therapeutic candidates for antiphotoaging and prevention of wrinkle formation [24]. MMPs cause an imbalance between collagen synthesis and degradation [5, 25]. UV irradiation induces MMP-1, MMP-3, and MMP-9 expressions [6, 26]. MMP-1 initiates the degradation of types I and III fibrillar collagens, MMP-9 further degrades collagen fragments generated by collagenases, and MMP-3 activates pro-MMP-1 [27]. Our previous studies indicated that *Coffee arabica* and *Terminalia catappa* extracts protect against photoaging induced by UVB by inhibiting the MAPK pathway and, hence, the expression of MMP-1, -3, and -9 [7, 18]. It had been reported that *Melothria heterophylla* extract and esculetin isolated from *Fraxinus chinensis* inhibited UVB-induced expression of MMP-1 mRNA and protein [28]. The results from our study indicate that *Neonauclea reticulata* extract is not only a potent MMP inhibitor but also inhibits MMP-1-induced degradation of types I and III collagen. In addition, we found that *Neonauclea reticulata* extract inhibited MMP-9 expression, thereby preventing the degradation of collagen fragments generated by MMP-1 and inhibited MMP-3 expression, which in turn resulted in a reduction in pro-MMP-1 secretion. Our findings indicate that *Neonauclea reticulata* extract promotes skin regeneration.

MAPK activation is not only involved in photoaging but also plays a role in MMP production in fibroblasts. We found that *Neonauclea reticulata* extract inhibited JNK, ERK, and p38 activation. We speculate that the inhibition of collagen degradation by *Neonauclea reticulata* extract is related to its antioxidant activity, since the direct injury of UVB in skin is due to ROS. We also found that *Neonauclea reticulata* extract inhibits MAPK phosphorylation and causes modulation of c-Fos expression. JNK and p38 modulate c-Fos expression, and c-Fos accompanied by c-Jun synthesizes the transcription factor AP-1. The inhibition of ERK, JNK, and p38 expression by *Neonauclea reticulata* extract may also result in suppression of c-Fos and c-Jun expression, which in turn would inhibit AP-1, MMP, and type I procollagen expression. Based on our findings, we speculate that *Neonauclea reticulata* extract and its active components stimulate the proliferation of fibroblasts and TGF-β secretion, activate the signal transduction pathway of collagen synthesis, and suppress UVB-induced AP-1 activation.

5. Conclusions

Neonauclea reticulata extract attenuated UVB-induced overexpression of MMP-1, -3, and -9 in fibroblasts by inhibiting UVB-induced MAPK activation (Figure 8). Our results indicate that *Neonauclea reticulata* extract is a promising antiphotoaging agent.

Conflict of Interests

The authors declare no conflict of interests in this work.

Authors' Contribution

Hsin-Chun Chen and Hsiu-Mei Chiang contributed equally to this paper.

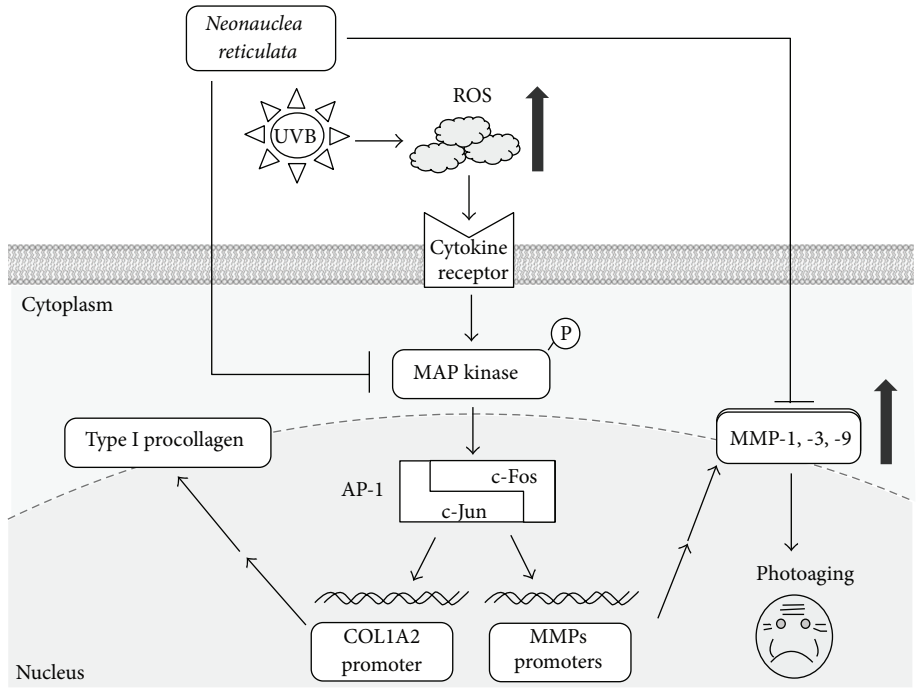

Figure 8: A simplified depiction of the proposed antiphotoaging mechanism of *Neonauclea reticulata* extract.

Acknowledgments

The authors are grateful to the National Museum of Natural Science and Dr. T. Y. Aleck Yang for supplying the material. This study was sponsored in part by the National Science Council (NSC99-2320-B-039-012-MY3; NSC99-2622-B-039-001-CC3), Taipei, Taiwan.

References

[1] E. A. Offord, J.-C. Gautier, O. Avanti et al., "Photoprotective potential of lycopene, β-carotene, vitamin E, vitamin C and carnosic acid in UVA-irradiated human skin fibroblasts," *Free Radical Biology and Medicine*, vol. 32, no. 12, pp. 1293–1303, 2002.

[2] H. J. Moon, S. R. Lee, S. N. Shim et al., "Fucoidan inhibits UVB-induced MMP-1 expression in human skin fibroblasts," *Biological and Pharmaceutical Bulletin*, vol. 31, no. 2, pp. 284–289, 2008.

[3] P. K. Vayalil, A. Mittal, Y. Hara, C. A. Elmets, and S. K. Katiyar, "Green tea polyphenols prevent ultraviolet light-induced oxidative damage and matrix metalloproteinases expression in mouse skin," *Journal of Investigative Dermatology*, vol. 122, no. 6, pp. 1480–1487, 2004.

[4] K. Gelse, E. Poschl, and T. Aigner, "Collagens—structure, function, and biosynthesis," *Advanced Drug Delivery Reviews*, vol. 55, pp. 1531–1546, 2003.

[5] J. H. Rabe, A. J. Mamelak, P. J. S. McElgunn, W. L. Morison, and D. N. Sauder, "Photoaging: mechanisms and repair," *Journal of the American Academy of Dermatology*, vol. 55, no. 1, pp. 1–19, 2006.

[6] K. K. Dong, N. Damaghi, S. D. Picart et al., "UV-induced DNA damage initiates release of MMP-1 in human skin," *Experimental Dermatology*, vol. 17, no. 12, pp. 1037–1044, 2008.

[7] H.-M. Chiang, T.-J. Lin, C.-Y. Chiu et al., "*Coffea arabica* extract and its constituents prevent photoaging by suppressing MMPs expression and MAP kinase pathway," *Food and Chemical Toxicology*, vol. 49, no. 1, pp. 309–318, 2011.

[8] K.-C. Wen, P.-C. Fan, S.-Y. Tsai, I.-C. Shih, and H.-M. Chiang, "*Ixora parviflora* protects against UVB-induced photoaging by inhibiting the expression of MMPs, MAP kinases, and COX-2 and by promoting type i procollagen synthesis," *Evidence-Based Complementary and Alternative Medicine*, vol. 2012, Article ID 417346, 11 pages, 2012.

[9] H. Birkedal-Hansen, "Proteolytic remodeling of extracellular matrix," *Current Opinion in Cell Biology*, vol. 7, no. 5, pp. 728–735, 1995.

[10] Q. Afnan, M. D. Adil, A. Nissar-Ul et al., "Glycyrrhizic acid (GA), a triterpenoid saponin glycoside alleviates ultraviolet-B irradiation-induced photoaging in human dermal fibroblasts," *Phytomedicine*, vol. 19, no. 7, pp. 658–664, 2012.

[11] H. S. Kim, J. H. Song, U. J. Youn et al., "Inhibition of UVB-induced wrinkle formation and MMP-9 expression by mangiferin isolated from *Anemarrhena asphodeloides*," *European Journal of Pharmacology*, vol. 689, pp. 38–44, 2012.

[12] K.-C. Wen, H.-H. Chiu, P.-C. Fan et al., "Antioxidant activity of *Ixora parviflora* in a cell/cell-free system and in UV-exposed human fibroblasts," *Molecules*, vol. 16, no. 7, pp. 5735–5752, 2011.

[13] A. Mastrofrancesco, M. Ottaviani, N. Aspite et al., "Azelaic acid modulates the inflammatory response in normal human keratinocytes through PPARγ activation," *Experimental Dermatology*, vol. 19, no. 9, pp. 813–820, 2010.

[14] S. A. Ham, J. S. Hwang, T. Yoo et al., "Ligand-activated PPARδ inhibits UVB-induced senescence of human keratinocytes via PTEN-mediated inhibition of superoxide production," *Biochemical Journal*, vol. 444, no. 1, pp. 27–38, 2012.

[15] J. Vostálová, A. Zdařilová, and A. Svobodová, "*Prunella vulgaris* extract and rosmarinic acid prevent UVB-induced DNA damage and oxidative stress in HaCaT keratinocytes," *Archives of Dermatological Research*, vol. 302, no. 3, pp. 171–181, 2010.

[16] V. A. Kostyuk, A. I. Potapovich, D. Lulli et al., "Modulation of human keratinocyte responses to solar UV by plant polyphenols as a basis for chemoprevention of non-melanoma skin cancers," *Current Medicinal Chemistry*, vol. 20, no. 7, pp. 869–879, 2013.

[17] M. D. Adil, P. Kaiser, N. K. Satti, A. M. Zargar, R. A. Vishwakarma, and S. A. Tasduq, "Effect of *Emblica officinalis* (fruit) against UVB-induced photo-aging in human skin fibroblasts," *Journal of Ethnopharmacology*, vol. 132, no. 1, pp. 109–114, 2010.

[18] K. C. Wen, I. C. Shih, J. C. Hu et al., "Inhibitory effects of *Terminalia catappa* on UVB-induced photo-damage in fibroblast cell line," *Evidence-Based Complementary and Alternative Medicine*. In press.

[19] J. Javanmardi, A. Khalighi, A. Kashi, H. P. Bais, and J. M. Vivanco, "Chemical characterization of basil (*Ocimum basilicum* L.) found in local accessions and used in traditional medicines in Iran," *Journal of Agricultural and Food Chemistry*, vol. 50, no. 21, pp. 5878–5883, 2002.

[20] J. Nazaruk, S. K. Czechowska, R. Markiewicz, and M. H. Borawska, "Polyphenolic compounds and in vitro antimicrobial and antioxidant activity of aqueous extracts from leaves of some Cirsium species," *Natural Product Research*, vol. 22, no. 18, pp. 1583–1588, 2008.

[21] Z. Hodzic, H. Pasalic, A. Memisevic, M. Srabovic, M. Saletovic, and M. Poljakovic, "The influence of total phenols content on antioxidant capacity in the whole grain extracts," *European Journal of Scientific Research*, vol. 28, no. 3, pp. 471–477, 2009.

[22] G.-S. Sim, B.-C. Lee, H. S. Cho et al., "Structure activity relationship of antioxidative property of flavonoids and inhibitory effect on matrix metalloproteinase activity in UVA-irradiated human dermal fibroblast," *Archives of Pharmacal Research*, vol. 30, no. 3, pp. 290–298, 2007.

[23] J. Uitto, "The role of elastin and collagen in cutaneous aging: intrinsic aging versus photoexposure," *Journal of Drugs in Dermatology*, vol. 7, no. 2, pp. s12–s16, 2008.

[24] S. Inomata, Y. Matsunaga, S. Amano et al., "Possible involvement of gelatinases in basement membrane damage and wrinkle formation in chronically ultraviolet B-exposed hairless mouse," *Journal of Investigative Dermatology*, vol. 120, no. 1, pp. 128–134, 2003.

[25] J.-Y. Bae, J.-S. Choi, Y.-J. Choi et al., "(-)epigallocatechin gallate hampers collagen destruction and collagenase activation in ultraviolet-B-irradiated human dermal fibroblasts: involvement of mitogen-activated protein kinase," *Food and Chemical Toxicology*, vol. 46, no. 4, pp. 1298–1307, 2008.

[26] S. Pillai, C. Oresajo, and J. Hayward, "Ultraviolet radiation and skin aging: roles of reactive oxygen species, inflammation and protease activation, and strategies for prevention of inflammation-induced matrix degradation—a review," *International Journal of Cosmetic Science*, vol. 27, no. 1, pp. 17–34, 2005.

[27] L. Rittie and G. J. Fisher, "UV-light-induced signal cascades and skin aging," *Ageing Research Reviews*, vol. 1, no. 4, pp. 705–720, 2002.

[28] P. K. Mukherjee, N. Maity, N. K. Nema, and B. K. Sarkar, "Bioactive compounds from natural resources against skin aging," *Phytomedicine*, vol. 19, no. 1, pp. 64–73, 2011.

Hindawi Publishing Corporation
Evidence-Based Complementary and Alternative Medicine
Volume 2013, Article ID 682380, 10 pages
http://dx.doi.org/10.1155/2013/682380

Research Article

Hepatitis B Virus-Encoded X Protein Downregulates EGFR Expression via Inducing MicroRNA-7 in Hepatocellular Carcinoma Cells

Yun-Ju Chen,[1,2] Pei-Hsuan Chien,[2] Wen-Shu Chen,[3,4] Yu-Fong Chien,[1] Ya-Ying Hsu,[1] Li-Yun Wang,[3] Jhen-Yu Chen,[4] Chih-Wen Lin,[5,6] Tzung-Chi Huang,[7] Yung-Luen Yu,[3,4,8,9] and Wei-Chien Huang[3,4,8,9]

[1] *Department of Biological Science and Technology, I-Shou University, Kaohsiung 824, Taiwan*
[2] *Department of Medical Research, E-Da Hospital, Kaohsiung 824, Taiwan*
[3] *Center for Molecular Medicine, China Medical University Hospital, Taichung 404, Taiwan*
[4] *Graduate Institute of Cancer Biology, China Medical University, Taichung 404, Taiwan*
[5] *The School of Chinese Medicine for Post-Baccalaureate, I-Shou University, Kaohsiung 824, Taiwan*
[6] *Division of Gastroenterology and Hepatology, Department of Medicine, E-Da Hospital, Kaohsiung 824, Taiwan*
[7] *Department of Biomedical Imaging and Radiological Science, China Medical University, Taichung 404, Taiwan*
[8] *The Ph.D. Program for Cancer Biology and Drug Discovery, China Medical University, Taichung 404, Taiwan*
[9] *Department of Biotechnology, Asia University, Taichung 413, Taiwan*

Correspondence should be addressed to Wei-Chien Huang; whuang@mail.cmu.edu.tw

Received 10 December 2012; Accepted 23 May 2013

Academic Editor: Wei-Chiang Lin

Hepatitis B virus (HBV) infection accounts for over a half of cases of hepatocellular carcinoma (HCC), the most frequent malignant tumor of the liver. HBV-encoded X (HBx) plays critical roles in HBV-associated hepatocarcinogenesis. However, it is unclear whether and how HBx regulates the expression of epidermal growth factor receptor (EGFR), an important gene for cell growth. Therefore, the study aimed to investigate the association between HBx and EGFR expression. In this study, we found that HBx upregulates miR-7 expression to target 3′UTR of EGFR mRNA, which in turn results in the reduction of EGFR protein expression in HCC cells. HBx-mediated EGFR suppression renders HCC cells a slow-growth behavior. Deprivation of HBx or miR-7 expression or restoration of EGFR expression can increase the growth rate of HCC cells. Our data showed the miR-7-dependent EGFR suppression by HBx, supporting an inhibitory role of HBx in the cell growth of HCC. These findings not only identify miR-7 as a novel regulatory target of HBx, but also suggest HBx-miR-7-EGFR as a critical signaling in controlling the growth rate of HCC cells.

1. Introduction

Hepatocellular carcinoma (HCC), the third leading cause of cancer-associated death worldwide, is a heterogeneous and complex disease [1]. Chronic infections of hepatitis virus, such as hepatitis B virus (HBV) and hepatitis C virus (HCV), are known to contribute to the tumorigenesis in most of HCC [2]. Particularly, HBV infection-associated HCC accounts for over a half of HCC cases and is endemically observed in Asia and Africa [3, 4]. HBV-associated hepatocyte transformation is attributed to inflammatory responses, destruction and regeneration of hepatocytes, and pleiotropic activities of HBV-encoded proteins [5]. When HBV-infected insults are destroyed, hepatocyte regeneration is activated for the replacement of damaged or destroyed hepatocytes by replication of mature hepatocytes [6]. Similar to wound healing, deposition of extracellular matrix components occurrs during liver regeneration and thereby causes liver fibrosis

and cirrhosis [7]. In the potentially mutagenic environment caused by continual inflammation, repeated proliferation of hepatocytes and constant liver regeneration may eventually be selected for transformed hepatocytes and could link HBV infections to the development of HCC [6].

In addition to HBV-initiated immune and inflammatory responses, HBV-encoded proteins *per se* may also regulate proliferation and regeneration of hepatocytes by altering multiple cellular signaling transduction pathways [8]. The HBV genome contains four overlapping open reading frames (ORFs), which encode pre-S1/pre-S2/S, viral polymerase, HBV X protein (HBx), and pre-C/C, respectively. Among them, the HBx protein is the smallest one with 154 amino acids and is thought to make the most significant contribution to the development of HBV-associated HCC [9, 10]. However, the roles of HBx in proliferation, apoptosis, and liver regeneration remain controversial. Results from two studies using transgenic HBx mouse models reveal its oncogenic function in enhancing tumor growth [11, 12]. Introduction of HBx into HCC cell lines can cause cells to enter cell cycle through activation of Src kinase, Ras, and MAPKs [13] or through induction of cyclin expression and cyclin-dependent kinase activity [14]. Inhibition of apoptosis by HBx by elevation of transcription factor nuclear factor Kappa B (NF-κB) has also been linked to the development of HCC [15]. However, the results from several other HBx-transgenic mouse studies do not support the direct link between HBx and tumorigenesis of HCC [16, 17]. In contrast, an inhibitory activity of HBx in hepatoma cell growth has been shown both *in vivo* and *in vitro* [18–21]. Inhibition of proliferation via GSK-3β/β-Catenin cascade [21], induction of apoptosis via releasing cytochrome c from mitochondria [22], and inactivating FLICE inhibitor protein (c-FLIP) [23] have been proposed for the antigrowth activity of HBx. To develop a complete understanding of HBx-associated liver disease and hepatocarcinogenesis, it will be important to reconcile these apparently conflicting data.

Besides inflammatory mediators, such as interleukin-6 and interleukin-1, accumulating evidence indicates a critical role of dysregulated growth and survival-related pathways in HCC development [24]. Aberrant activation of Raf-MEK-ERK and PI3K-Akt pathways driven by epidermal growth factor receptor (EGFR) is commonly observed and implicated in the tumor growth and progression of many human cancer types, including HCC [25]. Moreover, activation of EGFR signaling pathways via the overexpression of either its cognate ligands or itself is strongly associated with the poor prognosis of HCC [26, 27]. Interestingly, the poor prognosis is particularly observed in HBV-infected HCC patients with EGFR expression [27, 28]. Activation of oncogenic MAPK and PI3K/Akt signaling pathways is also frequently observed in HBx-expressing HCC cells [29, 30]. These observations imply an association between EGFR and HBx in HBV-associated HCC. However, there is a lack of direct evidence to prove the modulation of EGFR expression by HBx in controlling cellular growth of HCC.

In this study, our data surprisingly reveal that HBx decreases, but not increases, cell proliferation of HCC cells by suppressing EGFR protein expression. Mechanically, targeting EGFR mRNA 3′UTR by upregulated microRNA-7 (miR-7) in response to HBx accounts for the suppression of EGFR protein level in HBx-expressing HCC cells. Our data support the inhibitory role of HBx in the cell growth of HBV-associated HCC through the miR-7-depednent EGFR suppression.

2. Materials and Methods

2.1. Cell Culture. The human hepatocellular carcinomas Hep3B, HepG2, and their derivatives with HBx expression were cultured in Dulbecco's modified eagle medium: nutrient mixture F-12 (DMEM/F12) supplemented with 10% fetal bovine serum.

2.2. Chemicals, Antibodies, and Reagents. The antibody against EGFR was purchased from Santa Cruz (Santa Cruz, CA), and the antibody against HBx was from Abcam (Cambridge, UK). We purchased antibody against myc-tag from Sigma-Aldrich (St. Louis, MO). The validated siRNAs for negative control, HBx, miR-7 mimic, miR-7 inhibitor, and DharmaFECT 1 transfection reagent were all from Dharmacon (Lafayette, CO). We purchased TransIT-2020 transfection reagent from Mirus Bio LLC (Madison, WI). The QuickGene RNA-cultured cell kit was from Kurabo (Osaka, JP). The RevertAid H Minus First Strand cDNA synthesis kit was purchased from Fermentas (Glen Burnie, MD). The VeriQuest Fast SYBR Green qPCR Master Mix was from Affymetrix (Cleveland, OH). TaqMan Probe qPCR Master Mix was purchased from Roche (Indianapolis, IN).

2.3. Transfection and Reporter Gene Assay. The luciferase reporter gene containing full-length 3′UTR of the miR-7-targeting human EGFR gene was a gift from Dr. Keith Giles (Western Australian Institute for Medical Research). Cells with 60–80% of confluence were transfected with 0.5 μg of EGFR-3′UTR luciferase plasmid along with or without different doses of myc-HBx expression vector by using TransIT-2020 transfection reagent according to the manufacturer's instruction. After 48 hrs of transfection, cells lysates were harvested and subjected to luciferase assay system. Luciferase activity was normalized to β-gal. For siRNA/microRNA transfection, cells with 60–80% of confluence were transfected with various siRNAs by using DharmaFECT 1 transfection reagent. Cells were harvested at indicated time points and subjected to further experiment.

2.4. Reverse Transcription-Quantitative Polymerase Chain Reaction (RT-qPCR). Total RNA was extracted by using QuickGene RNA-cultured cell kit according to the manufacture's instruction. One μg of RNA was subjected to reverse transcription with the RevertAid H Minus First Strand cDNA synthesis kit. The qPCR analysis of EGFR and HBx mRNA expressions was performed on ABI 7500 system (Applied Biosystems) by using VeriQuest Fast SYBR Green qPCR Master Mix and was normalized to GAPDH or actin expression. The qPCR analysis of miR-7 expression was performed on LightCycler 480 System (Roche) by using

TaqMan Probe qPCR Master Mix and was normalized to the expression of small RNA (U47).

2.5. Cell Growth Assay. Cell growth was measured in MTT, cell counting, and crystal violet staining assays. For MTT assay, cells ($2–5 \times 10^3$ cells/well) were seeded in 96-well plates for indicated time periods, and then 1 μg/mL MTT was added to each well. After 4-hour incubation, formazan was solubilized in 100 μL DMSO/well and the absorbance was measured at 570 nm. For cell counting, cells were trypsinized and relative cell amounts were counted by using Countess Automated Cell Counter (Invitrogen, Carlsbad, CA). For crystal violet staining, cells were seeded with the same amount at the beginning. Five to seven days later, relative cell amounts were determined by crystal violet staining. In brief, cells were washed with 1X PBS once, followed by fixation, and staining with 1% crystal violet in a solvent of 30% ethanol for 15–30 minutes at room temperature. Then, cells were washed with tape water till complete elimination of the background interfered.

3. Results

3.1. The Protein Level of EGFR Was Attenuated in Response to HBx Expression in HCC Cells. To investigate the regulatory roles of HBx in EGFR expression, the protein levels of EGFR in Hep3B and HepG2 HCC cell lines and in their HBx-stable transfectants, Hep3Bx and HepG2x cells, were examined by Western blot analysis. Unexpectedly, we found that the protein level of EGFR was obviously reduced in both HBx-expressing Hep3Bx and HepG2x cells as compared with their counterpart Hep3B and HepG2 cells (Figure 1(a)). To rule out the possibility of the EGFR attenuation due to the effects of clonal selection, we transiently enforced HBx expression into Hep3B cells and analyzed EGFR protein expression. As shown in Figure 1(b), the EGFR protein level was decreased by the enforced HBx expression in Hep3B cells. In support to these findings, silencing of HBx with siRNA could restore EGFR protein level in Hep3Bx cells (Figure 1(c)). Taken together, these results indicate an inhibitory effect of HBx on EGFR protein expression in HCC cells.

3.2. The 3′UTR Activity of EGFR Was Reduced by HBx in HCC Cells. We next addressed the molecular mechanisms of HBx-mediated EGFR suppression. Since the regulations of gene expression by HBx have been widely reported [31–33], we first examined whether HBx reduces EGFR protein expression through transcriptional regulation. However, the mRNA level of EGFR was comparable in Hep3B and Hep3Bx cells (Figure 2(a), left panel) and was even slightly higher in HepG2x cells than in HepG2 cells (Figure 2(a), right panel), suggesting that HBx suppresses EGFR expression through posttranscriptional regulation. It is well documented that EGFR is subjected to polyubiquitination by Cbl and proceeds to endocytosis, followed by lysosomal degradation upon binding with ligands [34, 35]. In addition, the regulation of EGFR activity has been reported to involve proteasomal degradation with unclear molecular mechanisms [36, 37]. We thus examined whether HBx affects EGFR protein expression via these degradation pathways. To this end, both lysosomal and proteasomal inhibitors were applied. As shown in Figure 2(b), however, neither lysosomal inhibitors (bafilomycin A1 and NH_4Cl) nor proteasomal inhibitors (MG132 and bortezomib) could restore the EGFR protein expression in Hep3Bx cells, suggesting that the HBx-reduced EGFR protein expression is not mediated by enhanced receptor degradation. Moreover, enforced expression of HA-HBx into Hep3B cells did not affect the myc-EGFR protein expression, which is driven by heterologous CMV promoter (Figure 2(c)). These results further indicate that HBx has no effect on both promoter activity and protein stability of EGFR.

It is well known that microRNA (miRNA) targets the 3′UTR of mRNA to inhibit protein translation [38]. HBx was recently reported to enhance HCC progression via deregulating miRNA expression [39]. These observations and our results of Figures 2(a)–2(c) led us to further investigate whether HBx affects 3′UTR activity of EGFR mRNA through induction of miRNAs. Accordingly, the luciferase gene constructed with full-length 3′UTR of human EGFR gene was employed. As shown in Figure 2(d), the 3′UTR activity of EGFR in Hep3Bx cells was lower than that in Hep3B cells. Moreover, when the myc-HBx expression was enforced into cells, we observed an attenuation of 3′UTR activity of EGFR by myc-HBx in a dose-dependent manner (Figure 2(e)). Collectively, these results suggest that HBx suppresses EGFR protein expression through targeting its 3′UTR activity.

3.3. HBx Upregulated miRNA-7 (miR-7) Expression to Reduce EGFR Protein Level in HCC Cells. The mechanism underlying the regulation of EGFR 3′UTR activity by HBx was further explored. It is well documented that miR-7 plays critical roles in the downregulation of EGFR expression in many cancer types [40–43]. The dysregulation of miR-7 leading to HCC progression is also reported by Fang et al., more recently [44]. Thus, we clarified whether HBx upregulates miR-7 expression to target 3′UTR of EGFR mRNA and in turn leads to the attenuation of EGFR protein level. First, we examined the expression of miR-7 in both Hep3B/Hep3Bx and HepG2/HepG2x cell pairs. As shown in Figure 3(a), both Hep3Bx and HepG2x cells presented a higher expression level of miR-7 than their counterparts. To confirm the induction of miR-7 expression by HBx, HBx gene silencing with siRNA was applied. We found that the miR-7 expression in Hep3Bx cells was inhibited by HBx siRNA (Figure 3(b)), supporting that HBx suppresses EGFR protein level through inducing miR-7. That is, adjustment of miR-7 expression could modulate the protein level of EGFR presented in HCC cells. Indeed, when miR-7 expression was enforced into Hep3B cells, EGFR protein level was decreased (Figure 3(c), compared lane 2 with lane 1). On the contrary, when miR-7 expression was deprived from Hep3Bx cells by using miR-7 inhibitor, the EGFR protein expression was increased (Figure 3(c), compared lane 4 with lane 3). Altogether, these results indicate that HBx upregulates miR-7 expression to downregulate the protein level of EGFR.

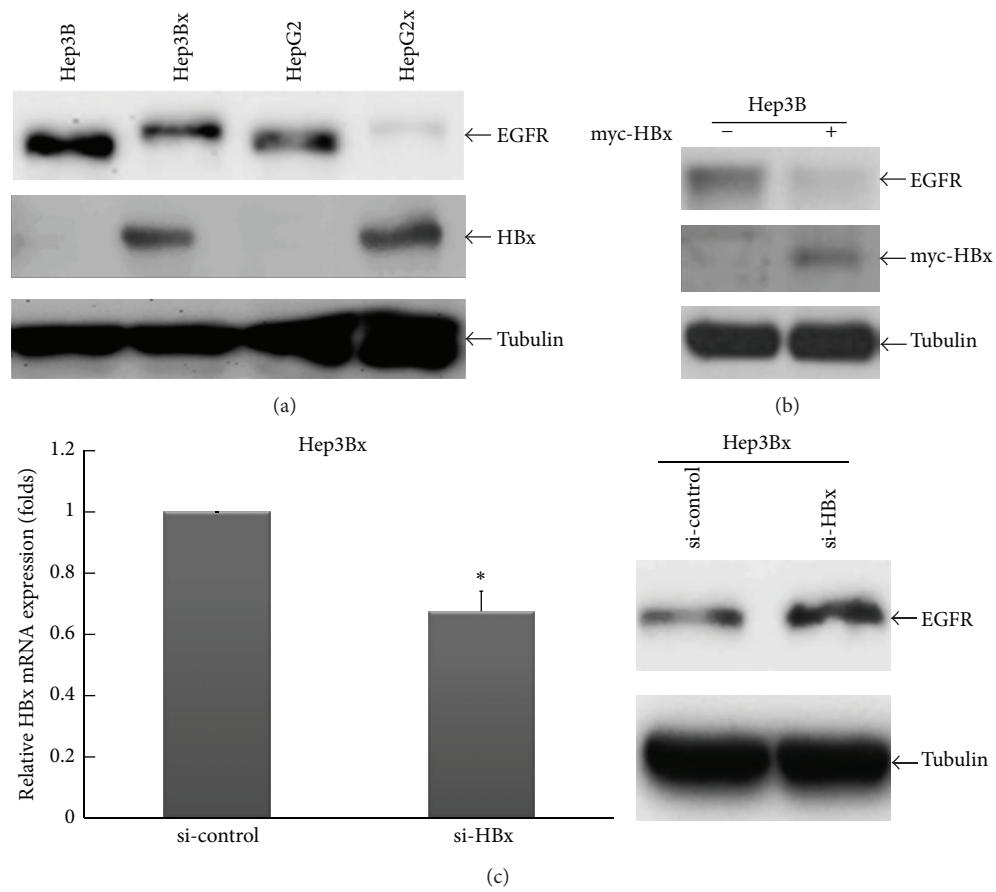

Figure 1: The protein expression of EGFR was attenuated in response to HBx expression in HCC cells. (a) The protein expressions of EGFR, HBx, and Tubulin in HCC cells were analyzed by Western blot. Tubulin acts as an internal control. (b) Hep3B cells were transiently transfected with myc-HBx expression vector for 48 hrs. EGFR protein expression was examined by Western blot. (c) Hep3Bx cells were transiently transfected with si-control or si-HBx for 3 days. The gene silencing for HBx mRNA was determined by RT-qPCR. Under the condition, EGFR protein expression was also analyzed by Western blot. Statistical analysis was performed by Student's t-test. $^{*}P < 0.05$ as compared to the control group.

3.4. The miR-7-Dependent EGFR Suppression by HBx Slows Down Cell Growth in HCC. Our above results led us to further investigate the impact of HBx-mediated EGFR suppression on HCC. It is known that EGFR signaling is a strong mitogenic stimulator for cell proliferation, and a slow cell growth is expectable when EGFR expression is reduced. Therefore, we examined the growth curve in both HCC cells lines and their HBx-expressing derivatives. As expected, HCC cells with HBx expression, including Hep3Bx and HepG2x cells, showed a retarded growth rate as compared with their counterparts (Figure 4(a)). Consistently, HBx-expressing Hep3B cells exhibited a delayed cell cycle as evidenced by the increased cell accumulation in G0/G1 phase (Figure S1(a), see in Supplementary Material available online at http://dx.doi.org/10.1155/2013/682380) and longer duration of S phase (Supplementary Figure S1(b)) when compared with their counterparts. Moreover, the cell number was increased in Hep3Bx cells after HBx expression was silenced by siRNA for 4 days (Figure 4(b)). These results suggest that HBx may slow down HCC proliferation through downregulation of EGFR expression in a miR-7-dependent manner. Indeed, introduction of miR-7 inhibitor (Figure 4(c)) or myc-EGFR (Figure 4(d)) into Hep3Bx cells could significantly increase the cell growth as determined by crystal violet staining. Collectively, these results indicate that the miR-7-dependent EGFR suppression by HBx reduces cell growth of HCC.

4. Discussion

In this study, our data showed downregulation of EGFR protein level by HBx in HCC cells (Figure 1). As a consequence, it rendered HCC cells with HBx expression to display a phenotype of slow growth (Figure 4), which is consistent with the previous findings that HBx plays an inhibitory role in the HCC cell growth both *in vivo* and *in vitro* [18, 20, 21, 45–47]. In contrast, HBx has been proposed to positively regulate cell proliferation and metastatic ability of HCC tumor cells [48]. There also has been considerable confusion regarding both proapoptotic and antiapoptotic functions of HBx mediated by p53-dependent and -independent manners during hepatocarcinogenesis [49, 50]. The differences in cell

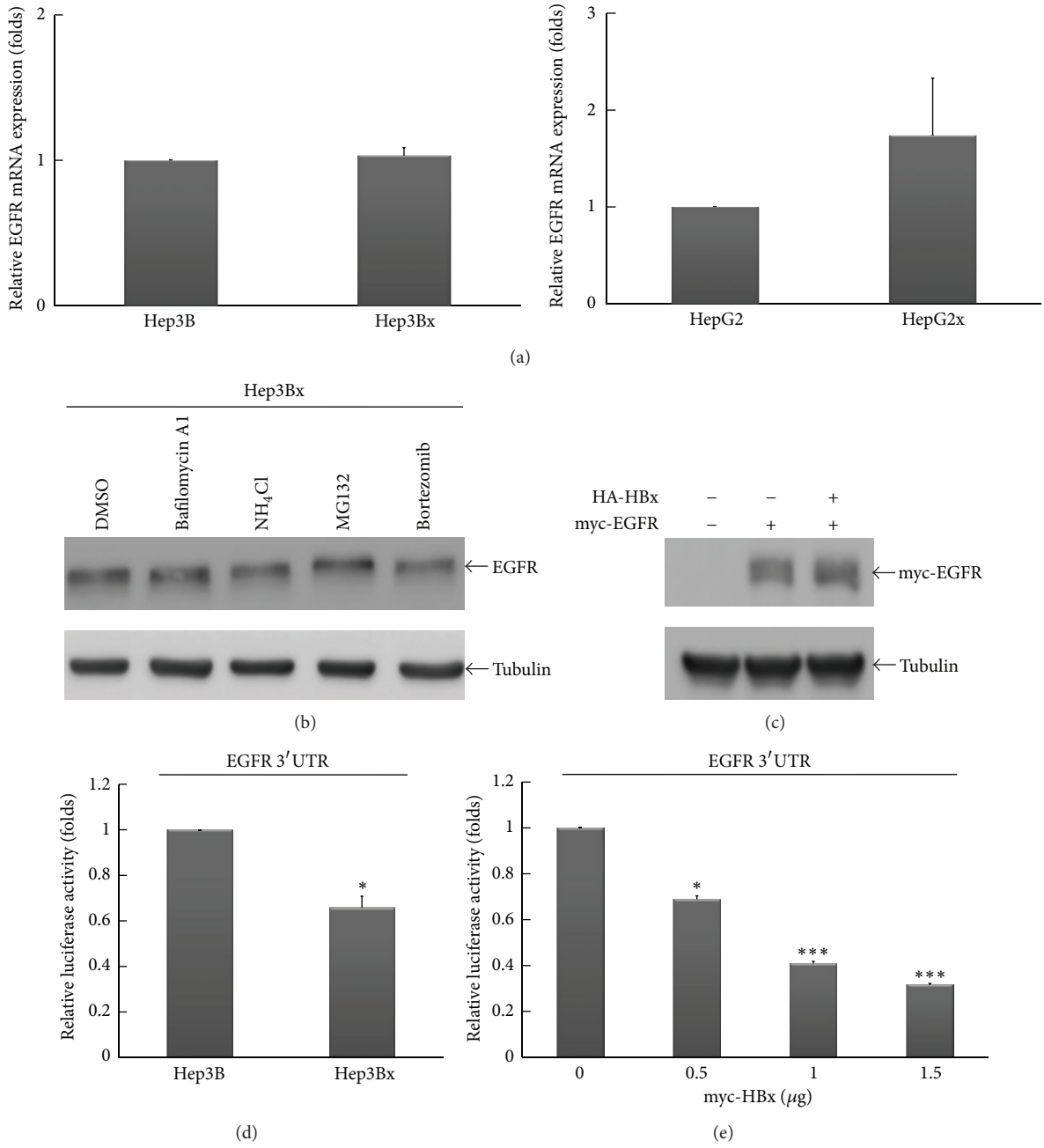

Figure 2: The 3′UTR activity of EGFR was reduced by HBx in HCC cells. (a) The mRNA expression of EGFR in HCC cells was examined by RT-qPCR. The EGFR mRNA expression was normalized to actin expression. (b) Hep3Bx cells were treated with either lysosomal inhibitors (bafilomycin A1 and NH_4Cl) or proteasomal inhibitors (MG132 and bortezomib) for 6 hrs. EGFR protein expression was analyzed by Western blot. (c) Hep3B cells were transiently transfected with myc-EGFR expression vector along with or without HA-HBx plasmid for 48 hrs. The protein expression of myc-EGFR was examined by Western blot with anti-myc antibody. (d) Hep3B and Hep3Bx cells were transiently transfected with EGFR-3′UTR luciferase plasmid for 48 hrs. Total cells lysates were harvested for luciferase activity analysis. The luciferase activities were normalized to β-gal. Values of luciferase activity were means ± SE of three determinations. Statistical analysis was performed by Student's t-test. $^{*}P < 0.05$ as compared to Hep3B cells. (e) Human embryonic kidney HEK293 cells were transiently transfected with EGFR-3′UTR luciferase plasmid as well as different doses of myc-HBx expression vector for 48 hrs. Total lysates were harvested for luciferase activity analysis. The luciferase activities were normalized to β-gal. Values of luciferase activity were means ± SE of three determinations. Statistical analysis was performed by Student's t-test. $^{*}P < 0.05$; $^{***}P < 0.001$ as compared to control group.

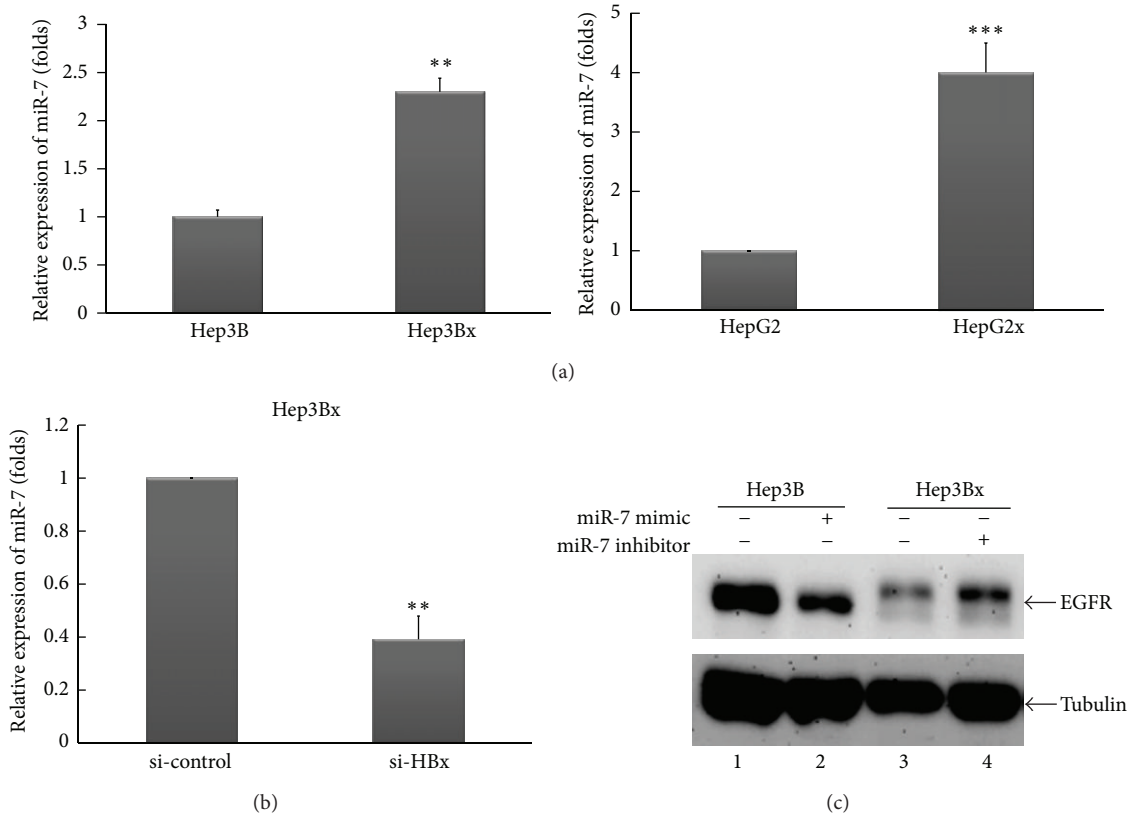

Figure 3: HBx upregulated miR-7 expression to reduce EGFR protein level in HCC cells. (a) The miR-7 expression in HCC cells was examined by RT-qPCR. The miR-7 expression was normalized to small RNA U47 level. Statistical analysis was performed by Student's t-test. $^{**}P < 0.01$; $^{***}P < 0.001$ as compared to individual parental cells. (b) Hep3Bx cells were transiently transfected with si-control or si-HBx for 3 days. The miR-7 expression was analyzed by RT-qPCR. The miR-7 expression was normalized to small RNA U47 expression. Statistical analysis was performed by Student's t-test. $^{**}P < 0.01$ as compared to control group. (c) Hep3B and Hep3Bx cells were transiently transfected with miR-7 mimic or miR-7 inhibitor, respectively. Four days later, the EGFR protein expression was analyzed by Western blot.

contexts and experimental condition used in a particular system may explain these conflict observations [5].

Of note, carboxy-terminal (C-terminal) truncation of HBx is frequently observed in HCC patients with HBV infection [51, 52]. It has further been observed that overexpression of C-terminal truncated HBx leads to cell growth of HCC [19, 46], suggesting an inhibitory role of carboxy-terminal domain of HBx in controlling cell proliferation. Consistently, overexpression of centromere protein A (CENP-A), a protein required for chromosome segregation in mitosis, has been found to be closely associated with HBx carboxy-terminal mutation in HCC [53]. The enhancement of proliferation and cyclin D1 expression by HBx carboxy-terminal deletion mutant (deleted at nucleotide 382–400) in LO2 hepatocyte cells further supports the inhibitory role of C-terminal domain of HBx in controlling cell proliferation [54]. The HBx used in this study is full-length and does not contain this deletion, raising the possibility that C-terminal domain of HBx may be responsible for HBx-mediated EGFR suppression. Since it has been shown that HBx-mediated regulation of NF-κB activity varies depending on the residues of HBx point mutations [55], it is also worthy to explore in the further studies whether any point mutation in HBx determines its ability to suppress EGFR expression.

Dysregulation of miRNA expression has been widely observed in HCC [56, 57]. Wang et al. first demonstrate that HBx can regulate miRNA expression [39]. Several studies also explore the pathological functions of aberrant miRNA expression in HCC in response to HBx [29, 58–60]. Our data further revealed that the molecular mechanism underlying HBx-mediated EGFR suppression is due to the induction of miR-7, which can bind to and target EGFR 3′UTR, leading to the downregulation of EGFR protein level (Figures 2 and 3). Disruption of the miR-7-EGFR regulatory trait increases the growth rate of HBx-expressing HCC cells, suggesting that HBx induces miR-7 to reduce EGFR expression and cell growth (Figure 4). In consistence with our findings, dysregulated miR-7 is recently detected in tumor tissues from HCC patients and functions in suppressing cell growth by targeting Akt/mTOR, a survival signaling pathway downstream of EGFR [44]. Indeed, overexpression of miR-7 resulted in the attenuation of Akt activity (Supplementary Figure S2) and it is frequently reported to have an inhibitory effect on tumor growth in various cancer types [44, 61–63], supporting the tumor suppressive roles of miR-7.

Although the induction of miR-7 by HBx was demonstrated for the first time in this study, further investigations remain to understand the underlying regulatory mechanism.

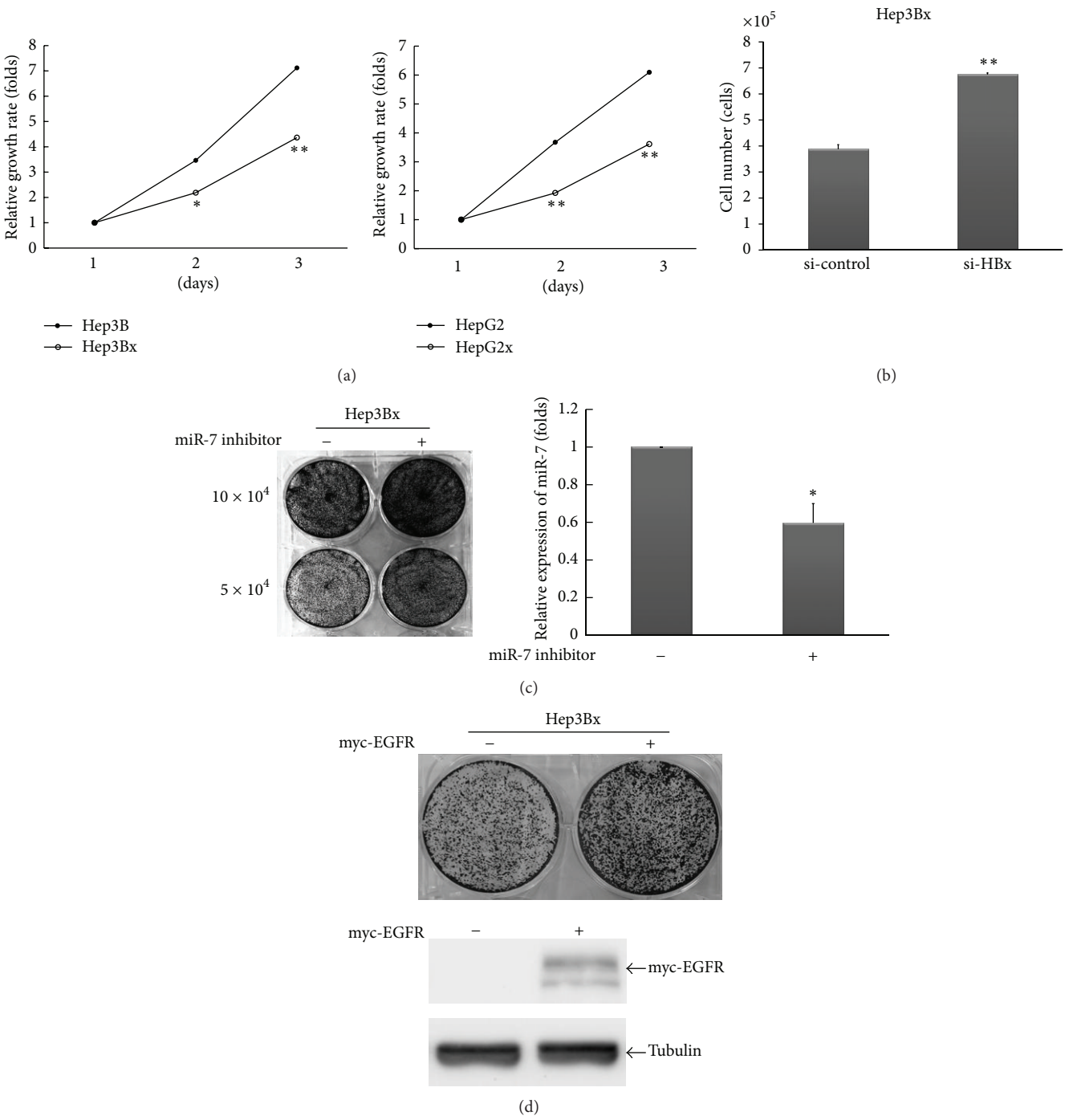

Figure 4: The regulatory trait of HBx-miR-7-EGFR conferred HCC cells a slow growth behavior. (a) The growth curves of Hep3B, HepG2, and their derivatives were determined by MTT assay. Statistical analysis was performed by Student's t-test. $^{*}P < 0.05$; $^{**}P < 0.01$ as compared to individual parental cells. (b) Hep3Bx cells were transiently transfected with si-control and si-HBx for 4 days. These cells were then trypsinized for cell number counting. Statistical analysis was performed by Student's t-test. $^{**}P < 0.01$ as compared to control group. (c) Hep3Bx cells were transiently transfected with or without miR-7 inhibitor for 1 day. Cells were reseeded at the same amount between groups and allowed for growth. The growth rate was determined by crystal violet staining. Total RNA was also collected for examination of miR-7 expression by RT-qPCR. (d) Hep3Bx cells were transiently transfected with or without myc-EGFR expression vector for 1 day. Similar procedures as described in (c) were performed. The protein expression of myc-EGFR was examined by Western blot.

In addition to being targeted by miR-7, EGFR has also been reported to induce miR-7 transcription relying on its tyrosine kinas activity [64], suggesting miR-7 as a negative feedback regulator of EGFR expression. However, our data showed that miR-7 is constitutively increased in stable HBx-expressing cells even if EGFR expression is attenuated, indicating that other mechanisms rather than EGFR signaling mediate HBx-induced miR-7 expression. Interestingly, induction of miR-7 is selectively found in differentiating neuronal progenitor cells with overexpression of IKKα, an upstream kinase for activation of NF-κB [65]. HBx has been widely found to interact with NF-κB to regulate gene expressions involved in the HCC pathogenesis [31–33]. Our previous findings also showed that IKKα is activated by HBx and translocates into the nucleus to function as a chromatin modifier for gene transcription. These observations raise the possibility that HBx may induce miR-7 expression through IKK/NF-κB and nuclear IKKα signaling pathways in HCC cells, which deserves further investigations.

5. Conclusion

This study linking viral regulatory protein HBx to EGFR suppression reveals an inhibitory role of HBx in the cell growth of HCC. HBx increases the expression of miR-7 and subsequently leads to the attenuation of EGFR protein expression, which reflects a slow-growth phenotype of HBx-expressing HCC cells. Our findings not only identify that miR-7 is a novel regulatory target of HBx, but also enhance the understandings of the pleiotropic roles of HBx in HBV-associated HCC.

Abbreviations

HBV:	Hepatitis B virus
HCC:	Hepatocellular carcinoma
HBx:	HBV-encoded X protein
EGFR:	Epidermal growth factor receptor
miR:	MicroRNA
3′UTR:	3′untranslated region
HCV:	Hepatitis C virus
ORF:	Open reading frame
NF-κB:	Nuclear factor Kappa B
c-FLIP:	FLICE inhibitor protein
C-terminal:	Carboxy-terminal
CENP-A:	Centromere protein A.

Conflict of Interests

The authors declare that they have no conflict of interests.

Acknowledgments

The authors thank Professor Keith Giles (Western Australian Institute for Medical Research, Australia) for EGFR 3′UTR-luciferase reporter. This work was supported by grants from the National Science Council of Taiwan (NSC 100-2320-B-214-008, NSC 101-2320-B-214-005, NSC-99-3112-B-039-002, NSC-101-2911-I-002-303, and NSC-101-2320-B-039-049), the National Health Research Institutes of Taiwan (NHRI-EX-101-9812BC), E-Da Hospital, Taiwan, (EDPJ101001), and I-Shou University, Taiwan, (ISU101-S-01).

References

[1] H. B. El-Serag and K. L. Rudolph, "Hepatocellular carcinoma: epidemiology and Molecular Carcinogenesis," *Gastroenterology*, vol. 132, no. 7, pp. 2557–2576, 2007.

[2] J. M. Llovet, A. Burroughs, and J. Bruix, "Hepatocellular carcinoma," *Lancet*, vol. 362, no. 9399, pp. 1907–1917, 2003.

[3] J. Fung, C.-L. Lai, and M.-F. Yuen, "Hepatitis B and C virus-related carcinogenesis," *Clinical Microbiology and Infection*, vol. 15, no. 11, pp. 964–970, 2009.

[4] D. M. Parkin, F. I. Bray, and S. S. Devesa, "Cancer burden in the year 2000. The global picture," *European Journal of Cancer*, vol. 37, supplement 8, pp. S4–S66, 2001.

[5] M. J. Bouchard and S. Navas-Martin, "Hepatitis B and C virus hepatocarcinogenesis: lessons learned and future challenges," *Cancer Letters*, vol. 305, no. 2, pp. 123–143, 2011.

[6] C. Berasain, J. Castillo, M. J. Perugorria, M. U. Latasa, J. Prieto, and M. A. Avila, "Inflammation and liver cancer: new molecular links," *Annals of the New York Academy of Sciences*, vol. 1155, pp. 206–221, 2009.

[7] S. L. Friedman, "Mechanisms of hepatic fibrogenesis," *Gastroenterology*, vol. 134, no. 6, pp. 1655–1669, 2008.

[8] L. R. Roberts and G. J. Gores, "Hepatocellular carcinoma: molecular pathways and new therapeutic targets," *Seminars in Liver Disease*, vol. 25, no. 2, pp. 212–225, 2005.

[9] M. J. Bouchard and R. J. Schneider, "The enigmatic X gene of hepatitis B virus," *Journal of Virology*, vol. 78, no. 23, pp. 12725–12734, 2004.

[10] C. Seeger and W. S. Mason, "Hepatitis B virus biology," *Microbiology and Molecular Biology Reviews*, vol. 64, no. 1, pp. 51–68, 2000.

[11] C.-M. Kim, K. Koike, I. Saito, T. Miyamura, and G. Jay, "HBx gene of hepatitis B virus induces liver cancer in transgenic mice," *Nature*, vol. 351, no. 6324, pp. 317–320, 1991.

[12] D.-Y. Yu, H.-B. Moon, J.-K. Son et al., "Incidence of hepatocellular carcinoma in transgenic mice expressing the hepatitis B virus X-protein," *Journal of Hepatology*, vol. 31, no. 1, pp. 123–132, 1999.

[13] M. Bouchard, S. Giannakopoulos, E. H. Wang, N. Tanese, and R. J. Schneider, "Hepatitis B virus HBx protein activation of cyclin A-cyclin-dependent kinase 2 complexes and G1 transit via a Src kinase pathway," *Journal of Virology*, vol. 75, no. 9, pp. 4247–4257, 2001.

[14] S. Lee, C. Tarn, W.-H. Wang, S. Chen, R. L. Hullinger, and O. M. Andrisani, "Hepatitis B virus X protein differentially regulates cell cycle progression in X-transforming Versus nontransforming hepatocyte (AML12) cell lines," *Journal of Biological Chemistry*, vol. 277, no. 10, pp. 8730–8740, 2002.

[15] J. Pan, L.-X. Duan, B. S. Sun, and M. A. Feitelson, "Hepatitis B virus X protein protects against anti-Fas-mediated apoptosis in human liver cells by inducing NF-κB," *Journal of General Virology*, vol. 82, no. 1, pp. 171–182, 2001.

[16] B. L. Slagle, T. H. Lee, D. Medina, M. J. Finegold, and J. S. Butel, "Increased sensitivity to the hepatocarcinogen diethylnitrosamine in transgenic mice carrying the hepatitis B virus X gene," *Molecular Carcinogenesis*, vol. 15, no. 4, pp. 261–269, 1996.

[17] O. Terradillos, O. Billet, C.-A. Renard et al., "The hepatitis B virus X gene potentiates c-myc-induced liver oncogenesis in transgenic mice," *Oncogene*, vol. 14, no. 4, pp. 395–404, 1997.

[18] D.-H. Yu, J. Lin, J.-H. Qu et al., "Hepatitis B virus X protein inhibits hepatoma cell growth in vitro through p14(ARF)-dependent and p14(ARF)-independent pathways," *Nan Fang Yi Ke Da Xue Xue Bao*, vol. 29, no. 6, pp. 1089–1093, 2009.

[19] H. Sirma, C. Giannini, K. Poussin, P. Paterlini, D. Kremsdorf, and C. Bréchot, "Hepatitis B virus X mutants, present in hepatocellular carcinoma tissue abrogate both the antiproliferative and transactivation effects of HBx," *Oncogene*, vol. 18, no. 34, pp. 4848–4859, 1999.

[20] H.-M. Lu, P. Cheng, Q.-Q. Tang et al., "Inhibition of tumour cells with hepatitis B virus x (HBx) gene adenoviral vector in vivo," *Sichuan Da Xue Xue Bao Yi Xue Ban*, vol. 40, no. 5, pp. 803–806, 2009.

[21] C.-Y. Kuo, C.-C. Wu, S.-L. Hsu, and G.-Y. Hwang, "HBx inhibits the growth of CCL13-HBX-stable cells via the GSK-3β/β-catenin cascade," *Intervirology*, vol. 51, no. 2, pp. 130–136, 2008.

[22] Y. Shirakata and K. Koike, "Hepatitis B virus X protein induces cell death by causing loss of mitochondrial membrane potential," *Journal of Biological Chemistry*, vol. 278, no. 24, pp. 22071–22078, 2003.

[23] K.-H. Kim and B. L. Seong, "Pro-apoptotic function of HBV X protein is mediated by interaction with c-FLIP and enhancement of death-inducing signal," *EMBO Journal*, vol. 22, no. 9, pp. 2104–2116, 2003.

[24] K. Breuhahn, T. Longerich, and P. Schirmacher, "Dysregulation of growth factor signaling in human hepatocellular carcinoma," *Oncogene*, vol. 25, no. 27, pp. 3787–3800, 2006.

[25] C. Berasain, M. J. Perugorria, M. U. Latasa et al., "The epidermal growth factor receptor: a link between inflammation and liver cancer," *Experimental Biology and Medicine*, vol. 234, no. 7, pp. 713–725, 2009.

[26] S. Kira, T. Nakanishi, S. Suemori, M. Kitamoto, Y. Watanabe, and G. Kajiyama, "Expression of transforming growth factor alpha and epidermal growth factor receptor in human hepatocellular carcinoma," *Liver*, vol. 17, no. 4, pp. 177–182, 1997.

[27] M. Daveau, M. Scotte, A. François et al., "Hepatocyte growth factor, transforming growth factor α, and their receptors as combined markers of prognosis in hepatocellular carcinoma," *Molecular Carcinogenesis*, vol. 36, no. 3, pp. 130–141, 2003.

[28] Y. Ito, T. Takeda, M. Sakon et al., "Expression and clinical significance of erb-B receptor family in hepatocellular carcinoma," *British Journal of Cancer*, vol. 84, no. 10, pp. 1377–1383, 2001.

[29] G. Kong, J. Zhang, S. Zhang, C. Shan, L. Ye, and X. Zhang, "Upregulated microRNA-29a by hepatitis B virus X protein enhances hepatoma cell migration by targeting PTEN in cell culture model," *PLoS One*, vol. 6, no. 5, Article ID e19518, 2011.

[30] T.-W. Chung, Y.-C. Lee, J.-H. Ko, and C.-H. Kim, "Hepatitis B Virus X protein modulates the expression of PTEN by inhibiting the function of p53, a transcriptional activator in liver cells," *Cancer Research*, vol. 63, no. 13, pp. 3453–3458, 2003.

[31] O. Dewantoro, R. A. Gani, and N. Akbar, "Hepatocarcinogenesis in viral Hepatitis B infection: the role of HBx and p53," *Acta Medica Indonesiana*, vol. 38, no. 3, pp. 154–159, 2006.

[32] D. Cougot, C. Neuveut, and M. A. Buendia, "HBV-induced carcinogenesis," *Journal of Clinical Virology*, vol. 34, no. 1, pp. S75–S78, 2005.

[33] Y. Lee, U.-S. Park, I. Choi, S. K. Yoon, Y. M. Park, and Y. I. Lee, "Human interleukin 6 gene is activated by hepatitis B virus-X protein in human hepatoma cells," *Clinical Cancer Research*, vol. 4, no. 7, pp. 1711–1717, 1998.

[34] H. Waterman and Y. Yarden, "Molecular mechanisms underlying endocytosis and sorting of ErbB receptor tyrosine kinases," *FEBS Letters*, vol. 490, no. 3, pp. 142–152, 2001.

[35] C. B. F. Thien, F. Walker, and W. Y. Langdon, "RING finger mutations that abolish c-Cbl-directed polyubiquitination and downregulation of the EGF receptor are insufficient for cell transformation," *Molecular Cell*, vol. 7, no. 2, pp. 355–365, 2001.

[36] S. A. Ettenberg, A. Magnifico, M. Cuello et al., "Cbl-b-dependent coordinated degradation of the epidermal growth factor receptor signaling complex," *Journal of Biological Chemistry*, vol. 276, no. 29, pp. 27677–27684, 2001.

[37] K. E. Longva, F. D. Blystad, E. Stang, A. M. Larsen, L. E. Johannessen, and I. H. Madshus, "Ubiquitination and proteasomal activity is required for transport of the EGF receptor to inner membranes of multivesicular bodies," *Journal of Cell Biology*, vol. 156, no. 5, pp. 843–854, 2002.

[38] W. Sun, Y.-S. Julie Li, H.-D. Huang, J. Y.-J. Shyy, and S. Chien, "MicroRNA: a master regulator of cellular processes for bioengineering systems," *Annual Review of Biomedical Engineering*, vol. 12, pp. 1–27, 2010.

[39] Y. Wang, Y. Lu, S. T. Toh et al., "Lethal-7 is down-regulated by the hepatitis B virus x protein and targets signal transducer and activator of transcription 3," *Journal of Hepatology*, vol. 53, no. 1, pp. 57–66, 2010.

[40] R. J. Webster, K. M. Giles, K. J. Price, P. M. Zhang, J. S. Mattick, and P. J. Leedman, "Regulation of epidermal growth factor receptor signaling in human cancer cells by MicroRNA-7," *Journal of Biological Chemistry*, vol. 284, no. 9, pp. 5731–5741, 2009.

[41] X. Li and R. W. Carthew, "A microRNA mediates EGF receptor signaling and promotes photoreceptor differentiation in the *Drosophila* eye," *Cell*, vol. 123, no. 7, pp. 1267–1277, 2005.

[42] K. M. Giles, A. Barker, P. M. Zhang, M. R. Epis, and P. J. Leedman, "MicroRNA regulation of growth factor receptor signaling in human cancer cells," *Methods in Molecular Biology*, vol. 676, pp. 147–163, 2011.

[43] B. Kefas, J. Godlewski, L. Comeau et al., "microRNA-7 inhibits the epidermal growth factor receptor and the akt pathway and is down-regulated in glioblastoma," *Cancer Research*, vol. 68, no. 10, pp. 3566–3572, 2008.

[44] Y. Fang, J. L. Xue, Q. Shen, J. Chen, and L. Tian, "MicroRNA-7 inhibits tumor growth and metastasis by targeting the phosphoinositide 3-kinase/Akt pathway in hepatocellular carcinoma," *Hepatology*, vol. 55, no. 6, pp. 1852–1862, 2012.

[45] P. Cheng, Y. Li, L. Yang et al., "Hepatitis B virus X protein (HBx) induces G2/M arrest and apoptosis through sustained activation of cyclin B1-CDK1 kinase," *Oncology Reports*, vol. 22, no. 5, pp. 1101–1107, 2009.

[46] M. Ning-Fang, S. H. Lau, L. Hu et al., "COOH-terminal truncated HBV X protein plays key role in hepatocarcinogenesis," *Clinical Cancer Research*, vol. 14, no. 16, pp. 5061–5068, 2008.

[47] T. Endoh, D. Sato, Y. Wada et al., "Galanin inhibits calcium channels via Gαi-protein mediated by GalR1 in rat nucleus tractus solitarius," *Brain Research*, vol. 1229, pp. 37–46, 2008.

[48] C. R. Madden and B. L. Slagle, "Stimulation of cellular proliferation by hepatitis B virus X protein," *Disease Markers*, vol. 17, no. 3, pp. 153–157, 2001.

[49] M. C. Kew, "Hepatitis B virus x protein in the pathogenesis of hepatitis B virus-induced hepatocellular carcinoma," *Journal of Gastroenterology and Hepatology*, vol. 26, no. 1, pp. 144–152, 2011.

[50] S. Murakami, "Hepatitis B virus X protein: a multifunctional viral regulator," *Journal of Gastroenterology*, vol. 36, no. 10, pp. 651–660, 2001.

[51] K. . Poussin, H. Dienes, H. Sirma et al., "Expression of mutated hepatitis B virus X genes in human hepatocellular carcinomas," *International Journal of Cancer*, vol. 80, no. 4, pp. 497–505, 1999.

[52] Y. Wang, S. H. Lau, J. S.-T. Sham, M.-C. Wu, T. Wang, and X.-Y. Guan, "Characterization of HBV integrants in 14 hepatocellular carcinomas: association of truncated X gene and hepatocellular carcinogenesis," *Oncogene*, vol. 23, no. 1, pp. 142–148, 2004.

[53] L. Liu, Y. Li, S. Zhang, D. Yu, and M. Zhu, "Hepatitis B virus X protein mutant upregulates CENP-A expression in hepatoma cells," *Oncology Reports*, vol. 27, no. 1, pp. 168–173, 2012.

[54] X. Fu, D. Tan, Z. Hou et al., "The effect of miR-338-3p on HBx deletion-mutant (HBx-d382) mediated liver-cell proliferation through CyclinD1 regulation," *PLoS One*, vol. 7, no. 8, Article ID e43204, 2012.

[55] J.-H. Lee, K.-H. Han, J. M. Lee, J. H. Park, and H.-S. Kim, "Impact of hepatitis B virus (HBV) X gene mutations on hepatocellular carcinoma development in chronic HBV infection," *Clinical and Vaccine Immunology*, vol. 18, no. 6, pp. 914–921, 2011.

[56] L. Santarpia, M. Nicoloso, and G. A. Calin, "MicroRNAs: a complex regulatory network drives the acquisition of malignant cell phenotype," *Endocrine-Related Cancer*, vol. 17, no. 1, pp. F51–F75, 2010.

[57] C. Braconi, J. C. Henry, T. Kogure, T. Schmittgen, and T. Patel, "The role of microRNAs in human liver cancers," *Seminars in Oncology*, vol. 38, no. 6, pp. 752–763, 2011.

[58] X. Wei, T. Xiang, G. Ren et al., "miR-101 is down-regulated by the hepatitis B virus x protein and induces aberrant DNA methylation by targeting DNA methyltransferase 3A," *Cellular Signalling*, vol. 25, no. 2, pp. 439–446, 2012.

[59] Q. H. Xie, X. X. He, Y. Chang, X. Jiang, and J. S. Lin, "HBx gene down-regulates miR-192 expression and inhibits apoptosis of human hepatoma cell line HepG2," *Zhonghua Gan Zang Bing Za Zhi*, vol. 19, no. 11, pp. 857–860, 2011 (Chinese).

[60] G. Wu, F. Yu, Z. Xiao et al., "Hepatitis B virus X protein downregulates expression of the miR-16 family in malignant hepatocytes in vitro," *British Journal of Cancer*, vol. 105, no. 1, pp. 146–153, 2011.

[61] S. Xiong, Y. Zheng, P. Jiang, R. Liu, X. Liu, and Y. Chu, "MicroRNA-7 inhibits the growth of human non-small cell lung cancer A549 cells through targeting BCL-2," *International Journal of Biological Sciences*, vol. 7, no. 6, pp. 805–814, 2011.

[62] L. Xu, Z. Wen, Y. Zhou et al., "MicroRNA-7 regulated TLR9 signaling enhanced growth and metastatic potential of human lung cancer cells by altering PIK3R3/Akt pathway," *Molecular Biology of the Cell*, vol. 24, no. 1, pp. 42–55, 2012.

[63] O. Saydam, O. Senol, T. Würdinger et al., "miRNA-7 attenuation in schwannoma tumors stimulates growth by upregulating three oncogenic signaling pathways," *Cancer Research*, vol. 71, no. 3, pp. 852–861, 2011.

[64] Y.-T. Chou, H.-H. Lin, Y.-C. Lien et al., "EGFR promotes lung tumorigenesis by activating miR-7 through a Ras/ERK/Myc pathway that targets the Ets2 transcriptional repressor ERF," *Cancer Research*, vol. 70, no. 21, pp. 8822–8831, 2010.

[65] A. Khoshnan and P. H. Patterson, "Elevated IKKalpha accelerates the differentiation of human neuronal progenitor cells and induces MeCP2-dependent BDNF expression," *PLoS One*, vol. 7, no. 7, Article ID e41794, 2012.

Hindawi Publishing Corporation
Evidence-Based Complementary and Alternative Medicine
Volume 2013, Article ID 607201, 9 pages
http://dx.doi.org/10.1155/2013/607201

Research Article

Reconstructive Effects of Percutaneous Electrical Stimulation Combined with GGT Composite on Large Bone Defect in Rats

Bo-Yin Yang,[1] Tzung-Chi Huang,[2] Yueh-Sheng Chen,[1,2] and Chun-Hsu Yao[1,2,3]

[1] *Department of Chinese Medicine, China Medical University, 91 Hsueh-Shih Road, Taichung 40402, Taiwan*
[2] *Department of Biomedical Imaging and Radiological Science, China Medical University, 91 Hsueh-Shih Road, Taichung 40402, Taiwan*
[3] *Department of Biomedical Informatics, Asia University, 500 Liou-Feng Road, Taichung 41354, Taiwan*

Correspondence should be addressed to Chun-Hsu Yao; chyao@mail.cmu.edu.tw

Received 30 October 2012; Revised 19 April 2013; Accepted 1 May 2013

Academic Editor: Wei-Chiang Lin

Previous studies have shown the electromagnetic stimulation improves bone remodeling and bone healing. However, the effect of percutaneous electrical stimulation (ES) was not directly explored. The purpose of this study was to evaluate effect of ES on improvement of bone repair. Twenty-four adult male *Sprague-Dawley rats* were used for cranial implantation. We used a composite comprising genipin cross-linked gelatin mixed with tricalcium phosphate (GGT). Bone defects of all rats were filled with the GGT composites, and the rats were assigned into six groups after operation. The first three groups underwent 4, 8, and 12 weeks of ES, and the anode was connected to the backward of the defect on the neck; the cathode was connected to the front of the defect on the head. Rats were under inhalation anesthesia during the stimulation. The other three groups only received inhalation anesthesia without ES, as control groups. All the rats were examined afterward at 4, 8, and 12 weeks. Radiographic examinations including X-ray and micro-CT showed the progressive bone regeneration in the both ES and non-ES groups. The amount of the newly formed bone increased with the time between implantation and examination in the ES and non-ES groups and was higher in the ES groups. Besides, the new bone growth trended on bilateral sides in ES groups and accumulated in U-shape in non-ES groups. The results indicated that ES could improve bone repair, and the effect is higher around the cathode.

1. Introduction

Trauma, infection, tumor resection, or skeletal abnormalities can cause bone defects of various shapes and sizes. Many methods have been applied to accelerate bone repair [1, 2]. Autografting from a tibia, fibula, iliac crest, or rib is a popular procedure but has many drawbacks such as the short supply and possible damage to the donor site. Allografting avoids these donor site problems; however, allografting has risks of immunoreaction and disease transmission [3–6]. Metal bone substitutes such as stainless steel and titanium alloys may damage the contacted normal bone and lead to inflammation from toxic ion release [1]. Bioactive ceramics, such as hydroxyapatite (HA) and tricalcium phosphate (TCP), demonstrate good biocompatibility and osteoconductive potential. Furthermore granular TCP is biodegradable [7]. In a previous study, we developed a novel composite comprising genipin cross-linked gelatin mixed with tricalcium phosphate (GGT), which is biocompatible, osteoconductive, biodegradable, and malleable [7–10]. Electromagnetic stimulation improves bone remodeling and bone healing [11–13]. Several studies have used techniques such as direct current (DC), capacitive coupling (CC), and pulsed electromagnetic field (PEMF) to stimulate bone healing. However, DC results in damage during operation; CC might cause skin hypersensitivity; and PEMF leads to the time redundant because of its time dependence [14–16]. Bone regeneration relies heavily on angiogenesis because the transportation of nutrients, oxygen, and stem cells is closely related to blood vessels [3, 17, 18]. Based on previous successful studies, the percutaneous electrical stimulation (ES) using 2 Hz and 2 mA is beneficial for angiogenesis [19, 20]. We hypothesized that the percutaneous

electrical stimulation could accelerate the bone regeneration. The evaluation of percutaneous electrical stimulation for improving bone repair was investigated in present study.

2. Materials and Methods

2.1. Implant Material Preparation. Type A gelatin (Bloom number 300, Sigma Chemical Co., Saint Louis, MO, USA) with a mass of approximately 50,000–100,000 Dalton was extracted and purified from porcine skin. A homogeneous 18% gelatin solution was made by dissolving 9 g of gelatin powder in 41 mL of distilled water in a water bath at 70°C. While the gelatin solution was cooling to 50°C, a 20% genipin solution (Challenge Bioproducts Co., Taichung, Taiwan) was added to the gelatin solution to induce cross-linking reactions at a constant temperature. After stirring for 2 min, tricalcium phosphate, $Ca_3(PO_4)_2$, ceramic particles (Merck, Germany) with grain sizes of 200–300 μm were mixed into the gelatin-genipin mixture. With an inorganic/organic ratio equivalent to that in natural bone, the weight ratio of the TCP and gelatin in the composite was 3 : 1 [7, 8, 10]. The GGT composites were manually cut and shaped to a diameter of 8 mm and a thickness of 1.5 mm. All samples were frozen at −80°C for 24 h and then dried in a freeze dryer for another 24 h.

2.2. Surgical Procedure. Twenty-four adult male *Sprague-Dawley rats* weighing 280–300 g were used as experimental animals for cranial implantation. The animals were kept in a stable following the national animal care guidelines. Prior to the beginning of the study, the protocol was approved by the Institutional Animal Care and Use Committee (IACUC) of China Medical University. All animals were anesthetized by the inhalation of isoflurane (Abbott, Taiwan). The head of each rat was shaved and prepared for surgery in an aseptic animal operation room. The head skin was incised in a T-shape. Next, the overlying parietal periosteum was excised. A circular (8 mm in diameter), full-thickness defect of the parietal bone was created with a drilling burr on a slow-speed dental handpiece; neither the dura nor the superior sagittal sinus was violated. All of these defects in the rats were then filled with the GGT composites. After each operation, the periosteum was closed with 5-0 vicryl, and the skin was sutured with 3-0 black silk [7, 21].

2.3. Percutaneous Electrical Stimulation Procedure. Percutaneous electrical stimulation using 2 Hz and 2 mA was applied in this study based on previously successful studies [19, 20]. Two points at a distance of 14 mm on the midline of the head, which were 3 mm ahead of and behind the defect, were selected for ES. After the operation, the rats were divided into six groups, with four rats each. The first three groups underwent 4, 8, and 12 weeks of percutaneous electrical stimulation (15 min/time, 3 times/week, and separated by an interval of at least one day) with stainless steel needles (0.27 mm OD, 13 mm length, Ching Ming, Taiwan) in the insertion depth of 2 mm and a stimulator (Trio 300; Ito, Tokyo, Japan). The anode was connected to a point on the back of the neck; the cathode was connected to a front point on the head, as illustrated in Figure 1. During each stimulation, the rats were under inhaled anesthesia. The other three groups, as control groups, only received inhalation anesthesia without percutaneous electrical stimulation. All the rats were examined afterward at 4, 8, and 12 weeks.

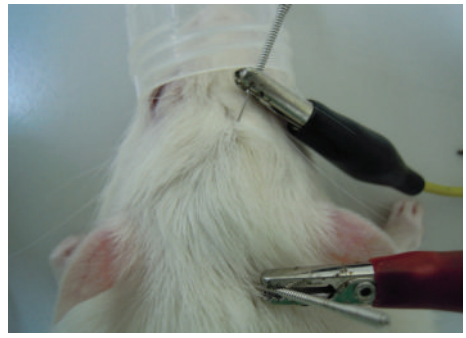

Figure 1: shows how the electrodes were positioned. The anode was connected to a point on the back of the neck; the cathode was connected to a front point on the head.

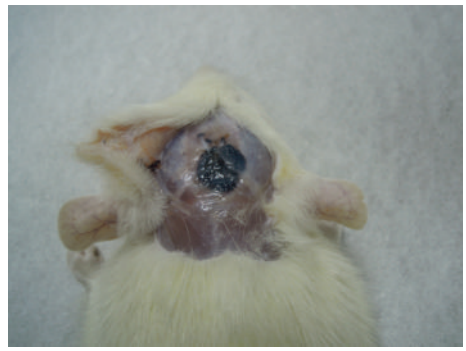

(a)

(b)

Figure 2: This figure represents the gross examination. (a) illustrates that there was no wound infection, scalp effusion, hematoma, festers or disturbed wound healing at the surgical site of the calvarial bone. No gaps between the GGT composite and the peripheral osseous tissues were noted, and no GGT composite was extruded. (b) shows that the brain tissues underlying the implantation site did not display any evidence of cortical inflammation, scar formation, or necrosis.

2.4. Harvesting, Radiomorphometry, and Histomorphometry of Tissue. The bone defect regeneration was evaluated

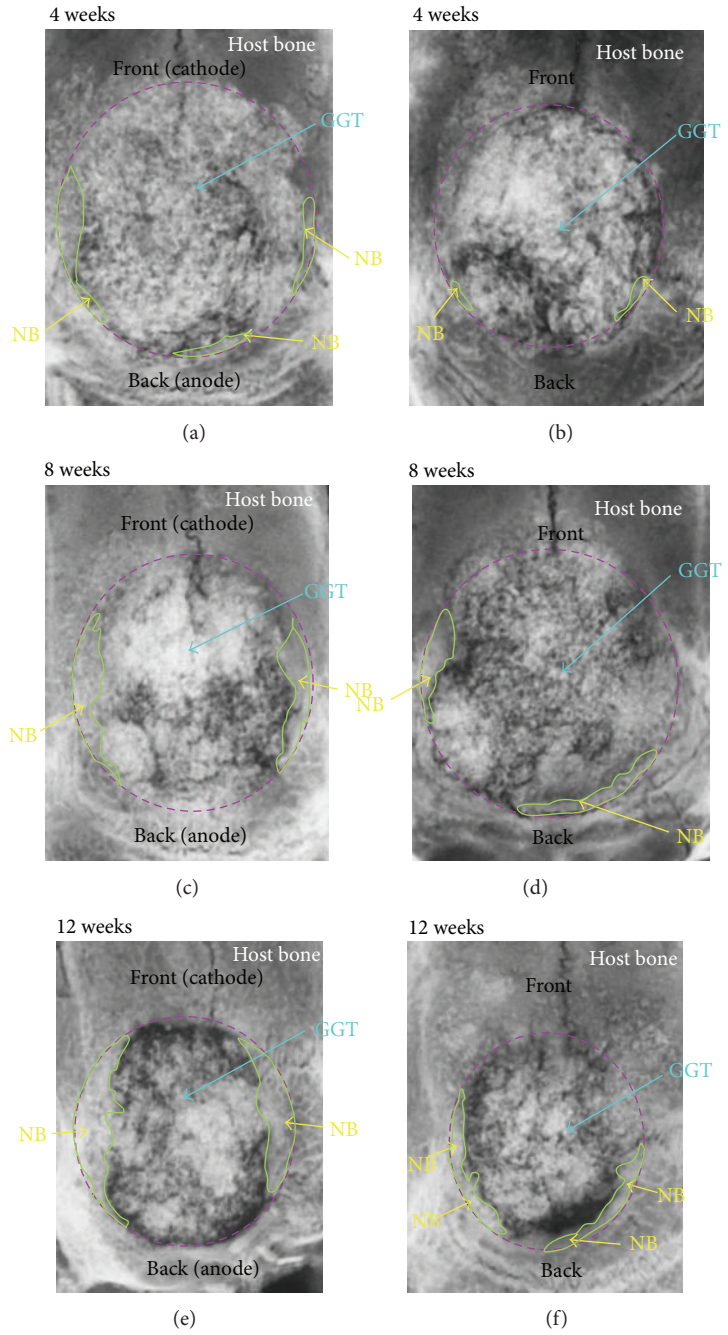

Figure 3: This figure shows the X-ray images. The top of each image corresponds to the front part of the rats, where the cathode is connected, and the bottom is the back part, where the anode is attached. (a), (c), and (e) display the results of the ES groups after 4, 8, and 12 weeks of bone repair, respectively. (b), (d), and (f) show the corresponding images of the control groups, in which non-ES was performed. In the ES groups, the new bone mostly formed on bilateral sides, whereas the new bone was U-shape in the non-ES groups (NB: new bone; GGT: genipin cross-linked gelatin mixed with tricalcium phosphate).

radiographically and histologically. Using a micro-CT scanner (SkyScan-1076, Aartselaar, Belgium) and with inhalation anesthesia, each group of animals was examined 4, 8, and 12 weeks after individual percutaneous electrical stimulation. The contrast between the gray levels of the implanted material and the new bone tissue was enhanced. The volume of newly formed bone was evaluated by counting the number of voxels using ImageJ (National Institutes of Health, USA). Next, 3D images of the new bone were obtained using Amira (Visage Imaging GmbH, Berlin, Germany) to evaluate the growth trend.

Anesthetized animals were sacrificed in a carbon-dioxide-filled box 4, 8, and 12 weeks after the operation. The craniectomy sites, along with 2-3 mm of contiguous bone,

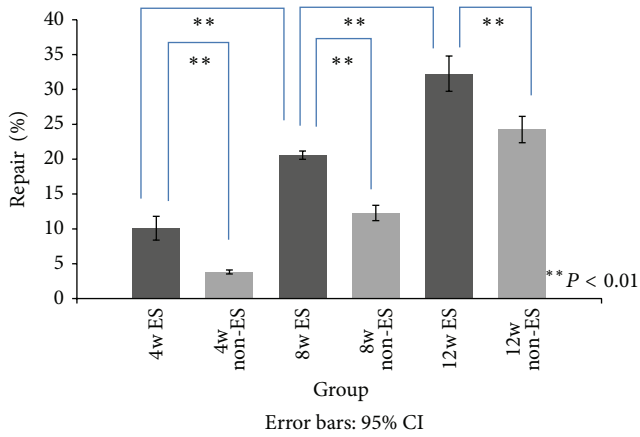

Figure 4: This figure shows that the percentage of bone regeneration in the rats is significantly higher in the ES groups than in the non-ES groups. The bone regenerated appreciably from 4 to 8 weeks and from 8 to 12 weeks.

were removed from each skull after the animal was sacrificed. Specimens were promptly placed into phosphate-buffered 10% formalin and prepared for further analysis. After 24 h of fixation, the specimens were radiographed in a cabinet X-ray machine (MGU 100A, Toshiba Company), using a high contrast X-ray film at 23 keV and 12.5 mA. The craniectomy site radiographs were analyzed using a semiautomatic histomorphometric method, and the regenerated bone was quantitatively evaluated as the percentage of infill area. Using an image analyzer system (Image-Pro Lite, Media Cybernetics, Silver Spring, MD, USA), a satisfactory contrast was achieved between the implanted materials and the new bone tissue by operator selection of a gray level sensitivity standard that was consistent for all treatments. The amount of newly grown bone tissue was calculated by moving a cursor on the digitizing plate, which was visible as a projection over the histological field, and this amount was expressed as a percentage of the ingrowth bone tissue in the created bone defect.

All of the calvarial specimens were subsequently decalcified in a solution of formic acid (10%) for 1-2 weeks and then immersed in sodium sulfate overnight. The specimens were dehydrated in a graded series of ethanol and then embedded in a tissue freezing medium (OCT). Axial sections of the decalcified bone and implants (10 μm thickness each) were prepared and stained with hematoxylin and eosin (H&E). To observe the relationship between the electrodes and osteoblasts or osteoclasts, longitudinal sections of other specimens (10 μm thickness each) were arranged and stained with either alkaline phosphatase (ALP) stain or tartrate resistant acid phosphatase (TRAP). Photomicrographs of these sections were obtained using light microscopy.

2.5. Statistical Analysis. All numerical data were presented as the mean ± one standard deviation. Significant differences among the samples were evaluated using Student's t-test (SPSS 17.0.2). Probabilities of $P < 0.05$ were considered statistically significant.

3. Results

3.1. Gross Examination. All animals in both the experimental and control groups survived for the entire experimental period without any local or general complications. There was no wound infection, scalp effusion, hematoma, festers, or disturbed wound healing at the surgical site of the calvarial bone. The results reveal that the GGT composite did not lead to histopathology or exhibit poor biocompatibility with the peripheral osseous tissues. No gaps between the GGT composite and the peripheral osseous tissues were noted, and no GGT composite was extruded (Figure 2(a)). The findings indicate that the GGT composite not only was easily molded to the calvarial bone defect without any fixation but also cohered strongly to the peripheral osseous tissues. However, cytotoxic implants may harm the underlying brain tissues because they were implanted in the calvarial bone defect and were in direct contact with brain tissue. To determine whether the brain tissue exhibited any abnormality, the calvarial bone covering implant was removed from the implantation site. The brain tissues underlying the implantation site did not display any evidence of cortical inflammation, scar formation, or necrosis (Figure 2(b)). The results revealed that the GGT composites did not cytotoxically affect the underlying brain tissue.

3.2. X-Ray Radiographic Analysis. Gross examination does not determine whether the newly formed osseous tissues were completely calcified new bones. Therefore, X-ray radiographs were obtained for further analysis. The performance both with and without ES in repairing the calvarial bone defect was evaluated to determine the efficacy of ES in accelerating the healing of defective bones. Figure 3 presents the radiographs of calvarial bone-covered implants 4, 8 and 12 weeks after the GGT composites were implanted into the calvarial bone defect. The three pictures in the left row show the ES groups, and those in the right row show the non-ES groups. In the non-ES groups, four weeks after surgery, the newly formed bone did not evidently grow into the GGT construct (Figure 3(b)); eight weeks after surgery, the implantation site had some radiopaque material in the GGT construct (Figure 3(d)); twelve weeks after surgery, the amount of radiopaque material in the GGT construct exceeded that in the radiograph obtained after 8 weeks (Figure 3(f)). The three pictures revealed that the new bone formation tended to grow in a U-shape in the non-ES groups. In the ES groups, the radiographs obtained four weeks after surgery displayed more radiopacity than those in the non-ES groups (Figure 3(a)). The radiograph obtained eight weeks after surgery showed the same pattern, and the newly formed bone accumulated on bilateral sides (Figure 3(c)). These two characteristics were more prominent in the 12-week radiograph. The newly formed bone replaced more GGT composite, and the area of the calvarial bone defect became

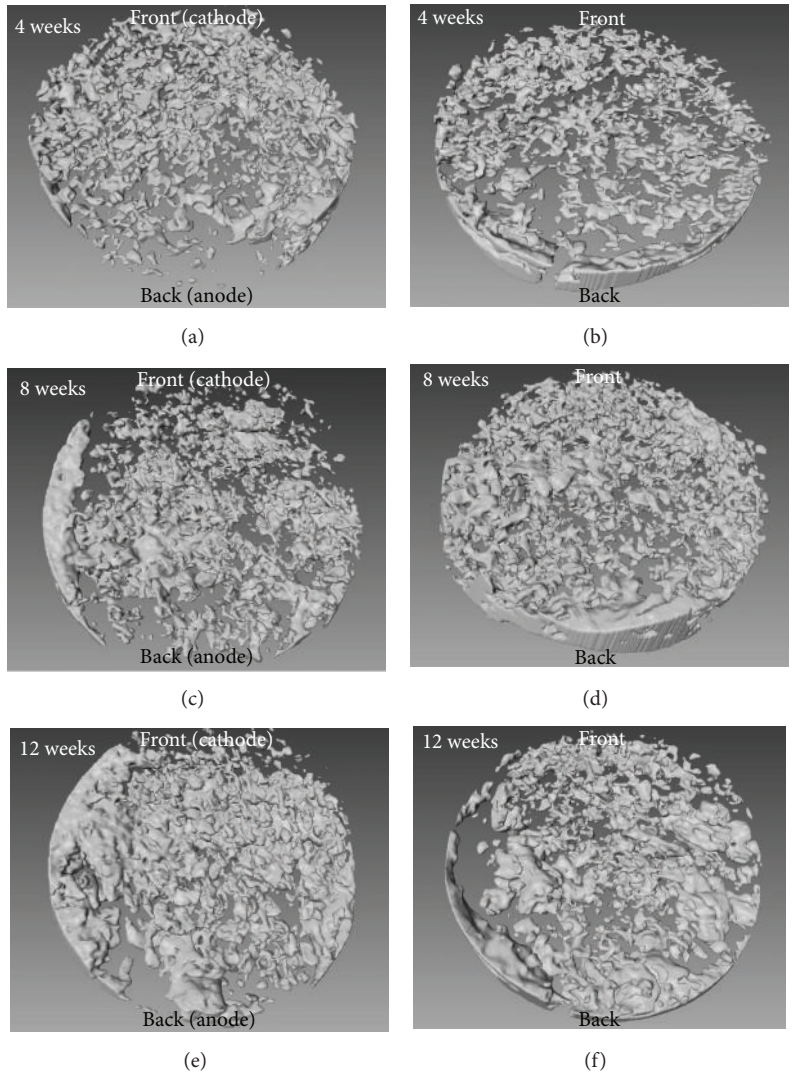

Figure 5: This figure shows the 3D images of the new bone. The top of each image corresponds to the front part of the rats, where the cathode is connected, and the bottom is the back part, where the anode is attached. (a), (c), and (e) display the results of the ES groups after 4, 8, and 12 weeks of bone repair, respectively. (b), (d), and (f) are the corresponding images of the control groups, in which non-ES was performed. In the ES groups, the new bone mostly formed on bilateral sides, whereas the new bone was U-shape in the non-ES groups.

much smaller in comparison with the 4-week and 8-week radiographs. In addition, the trend for the new bone to grow on bilateral sides was more pronounced (Figure 3(e)).

The new bone formation became more obvious as the time between implantation and examination increased. Additionally, the radiographs clearly reveal that the calvarial bone defect was repaired gradually and that the GGT composite degraded progressively. Figure 4 shows the percentage of newly formed bone to calvarial bone defect in each implantation-examination period for both groups with or without ES. The data showed augmentation in the areas of newly formed bone with time. For each implant period, the percentage of bone regeneration in the ES groups was markedly higher than that in the non-ES groups. Figure 4 and the serial postsurgery radiographs in Figure 3 exhibit progressive wound healing. The GGT composite biodegraded, and new bone infiltrated into the implant construct over time. Although the area of newly formed bone increased with implantation-examination time in the non-ES groups, it remained lower than that in the ES groups.

3.3. Three-Dimensional Micro-CT Radiographic Analysis. A new three-dimensional (3D) method, micro-CT, was applied to evaluate the amount of new bone formation. Bone repair in both the ES and non-ES groups were evaluated. Figure 5 displays the images of newly formed bone 4, 8, and 12 weeks after the GGT composites were implanted. The three pictures in the left row show the ES groups, and those in the right row show the non-ES groups.

In the non-ES groups, four weeks after surgery, some newly formed bone evidently grew into the GGT construct (Figure 5(b)); eight weeks after surgery, the implantation

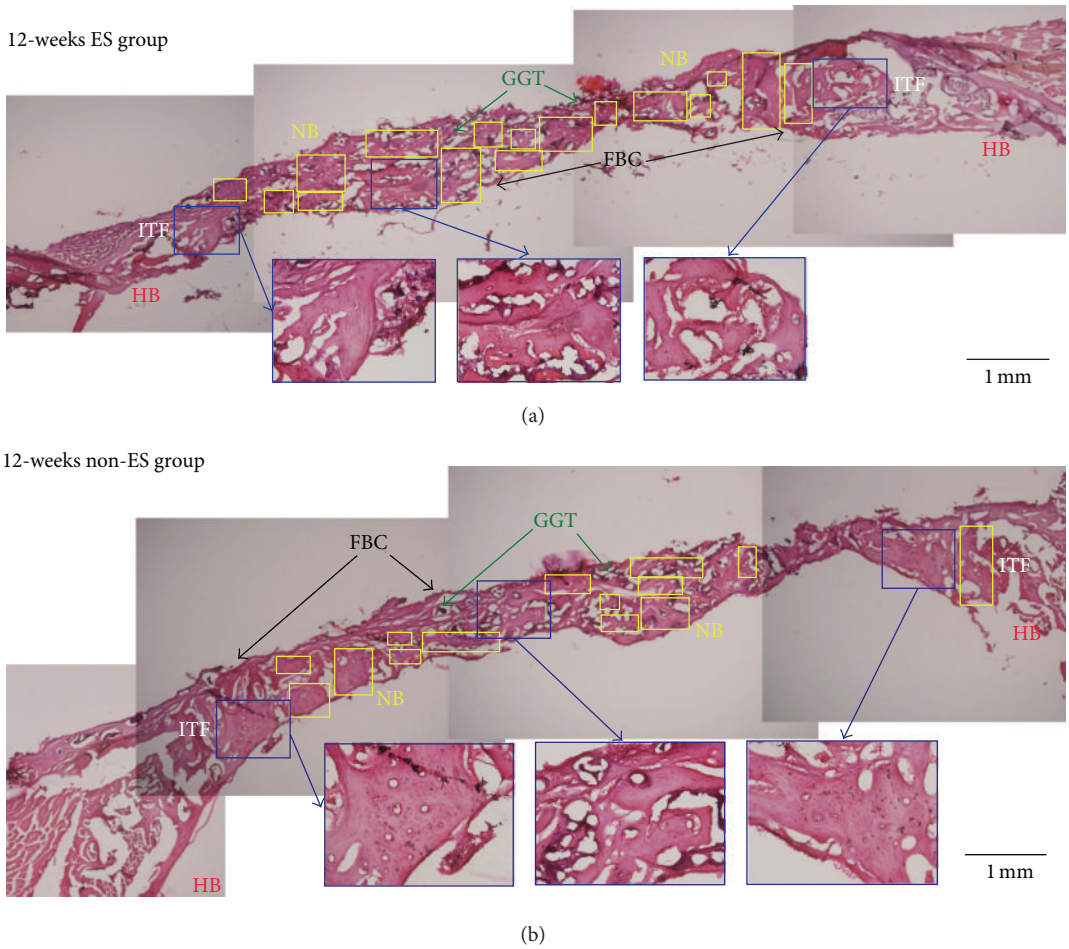

Figure 6: This figure shows transverse histological sections of calvarial defect 12 weeks after implantation with H&E stain. (a) displays the result of bone repair in the ES group. (b) shows the corresponding event for the control groups, in which non-ES was performed. The amount of bone regeneration in the rats is higher in the ES group than in the non-ES group (ITF: interface; NB: new bone; HB: host bone; FBC: foreign body capsule; original magnification: 40).

site contained more new bone in the GGT construct (Figure 5(d)); twelve weeks after surgery, the amount of bone regeneration in the GGT construct exceeded that in the radiograph obtained after 8 weeks (Figure 5(f)). The three pictures also showed a U-shape trend in the new bone formation in the non-ES groups.

The images obtained four weeks after surgery displayed a larger amount of new bone formation in the ES groups than in the non-ES groups (Figure 5(a)). The radiograph obtained eight weeks after surgery showed the same pattern, and the newly formed bone accumulated on bilateral sides (Figure 5(c)). These two observations were more pronounced in the 12-week radiograph. The newly formed bone occupied a larger volume of the calvarial bone defect than in the 4-week and 8-week radiographs. The trend of the new bone to grow on bilateral sides was more obvious (Figure 5(e)).

Table 1 shows the volume of newly formed bone for both the ES and non-ES groups for each implantation period. The volume of newly formed bone gradually increased with time. For each implant period, the volume of bone regeneration was obviously higher in the ES groups than in the non-ES groups.

Table 1: The volume of new bone formation measured with micro-CT scan.

Implantation time	With/without ES	Volume (mm^3) Mean ± SD
Four weeks*	With ES	16.70 ± 2.62
	Without ES	12.36 ± 2.24
Eight weeks*	With ES	22.03 ± 2.84
	Without ES	16.31 ± 2.49
Twelve weeks**	With ES	27.85 ± 2.16
	Without ES	18.29 ± 1.57

The volume of the newly-formed bone was determined in each implantation period ($n = 4$) ($^*P < 0.05$, $^{**}P < 0.01$).

3.4. Histological Evaluation. A histological evaluation was performed to compare the progress of restoration at the bone

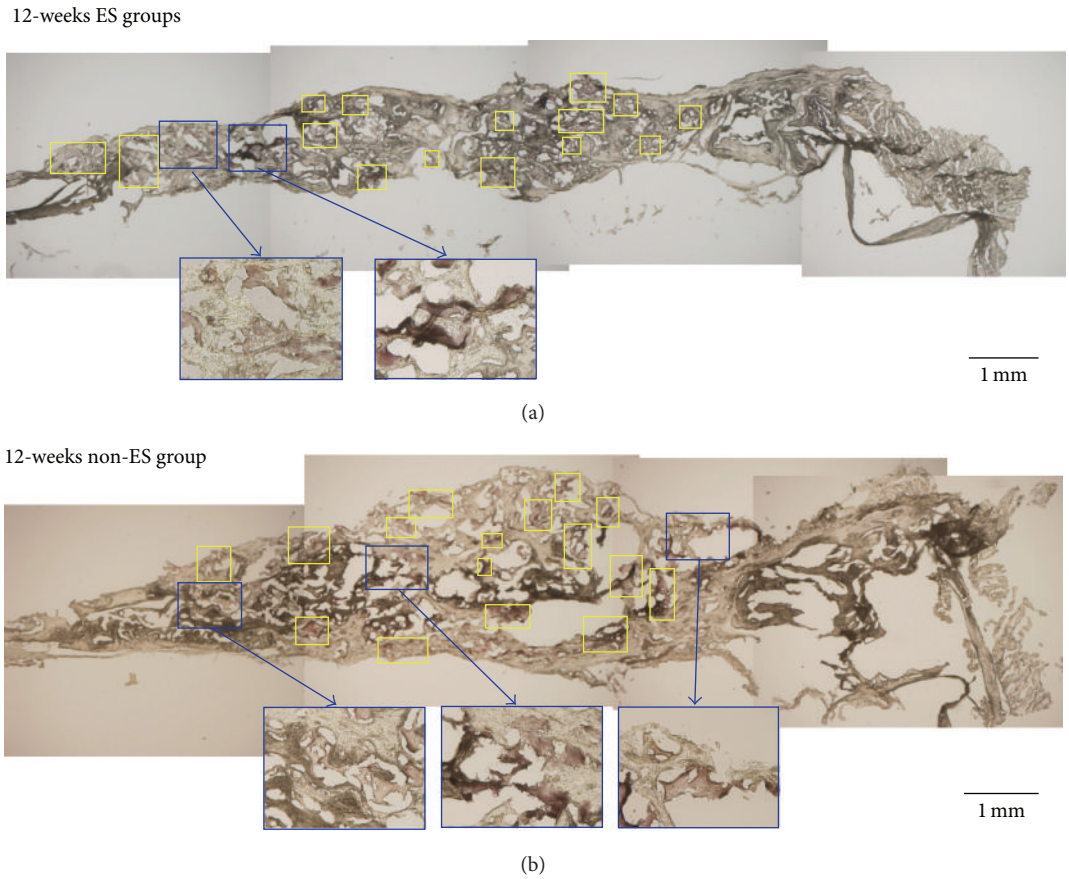

Figure 7: This figure shows longitudinal sections with ALP stain. The left side represents the far-end, in the direction of the cathode; the right side indicates the near-end, near the anode. For the ES group, the ALP accumulates on the left side after 12 weeks, as shown in (a); (b) illustrates the uniform distribution of ALP in the non-ES groups. The results indicate that osteoblasts are more active near the cathode in the ES groups.

defect in the ES and non-ES groups. Figure 6 shows the transverse sections with the H&E stain, demonstrating the difference in the growth rates of the new bone between the ES and non-ES groups. Twelve weeks after surgery, histological observation of the defective bone treated without ES indicated much new bone formation, as shown in Figure 6(b). However, compared with the control groups, the ES groups showed more new bone, indicating that ES could accelerate the restoration of defective bone (Figure 6(a)). The bone repair continued with time, and 12 weeks after implantation, the newly formed bone had replaced large amounts of the GGT composite. Substantially, more new bones were present in the defect after 12 weeks in the ES group than in the non-ES group (Figures 6(a) and 6(b)).

Longitudinal sections with the ALP and TRAP stains identified the activity of osteoblasts and osteoclasts near the electrodes. In Figures 7 and 8, the left side represents the far-end, in the direction of the cathode on the head; the right side indicates the near-end, near the anode on the neck. Figure 7 shows the slides with the ALP stain, and Figure 8 exhibits the TRAP stain. As shown in Figure 7(a), ALP accumulates on the left side in the ES groups, indicating that osteoblasts are more active near the cathode. In contrast, Figure 8(a) represents the aggregation of TRAP on the right side in the ES groups, demonstrating that osteoclasts are vigorous near the anode. When compared, Figures 7(b) and 8(b) illustrate the uniform distribution of ALP and TRAP in the non-ES groups.

4. Discussion

The GGT composite did not cause an obvious cytotoxic reaction in rabbits [7] or in the rats in this study. The radiographs from both X-ray and micro-CT showed the same trend. The new bone grew on bilateral sides of the electric current in the ES groups and grew in a U-shape in the non-ES groups. Osteogenesis depends on angiogenesis because blood vessels transport nutrients, oxygen, and stem cells. In the non-ES groups, the bottom of the U is near the heart, indicating that angiogenesis occurs from the heart to the far-end. Additionally, osteogenesis might rely on those vessels, resulting in the U-shaped formation. Previous researchers found that electric current stimulates bone regeneration at the cathode and, in contrast, bone resorption at the anode [22–24]. In the ES groups, more new bone accumulated on bilateral sides, extending to the far-end, in the direction of the cathode. Furthermore, much less new bone grew at the

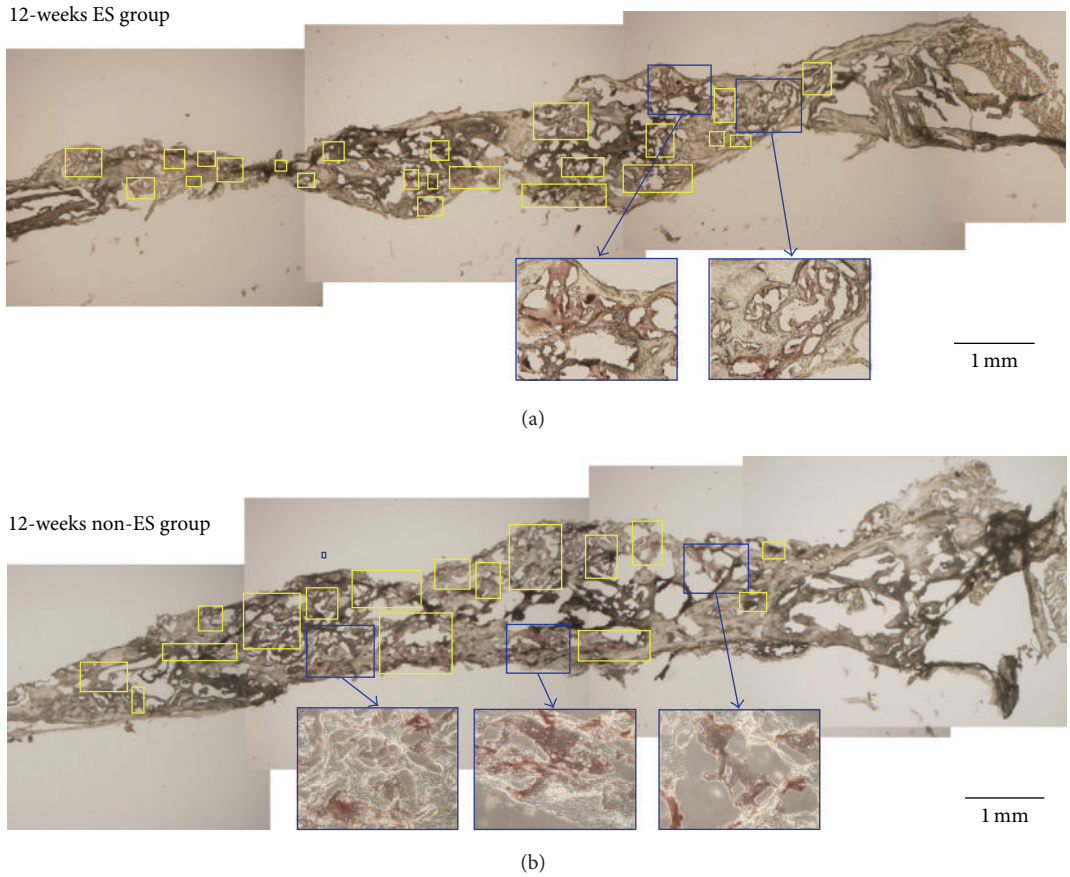

Figure 8: This figure shows longitudinal sections with TRAP stain. The left side represents the far-end, in the direction of the cathode; the right side indicates the near-end, near the anode. (a) shows the aggregation of TRAP on the right side in the ES group after 12 weeks. (b) illustrates the uniform distribution of TRAP in the non-ES groups. The results demonstrate that osteoclasts are vigorous near the anode in the ES groups.

near-heart-end, around the anode. The mechanism may be related to the increasing pH level around the cathode; the pH is raised by the electric current and results in an increase in osteoblastic bone formation and a decrease in osteoclast bone resorption [25–27].

As shown with the data in Figure 4 and Table 1, the amount of new bone measured using micro-CT was much greater than the amount measured using X-ray during the early stage of examination. However, the data were similar in the late stage. These findings might result from the fact that the bone regeneration began around the interface between the host bone and the GGT composite, and the new bone expanded after filling the interface. Furthermore, Yao et al. also found that new bone grew in the centripetal direction [7]. Thus, we may underestimate the rate of bone repair when using 2D images from X-ray data. With this explanation, the information obtained from the 3D micro-CT data is considered more accurate. In addition, the images from micro-CT are obtained with live rats. Sacrificing the animals before examination is not necessary. Thus, serial data can be acquired from each individual rat, which could reduce the number of rats used in the experiment if micro-CT is the sole imaging technique in the study.

The present study only investigated the appearance of bone regeneration using X-ray and micro-CT imaging. The hypothesis that the percutaneous electrical stimulation can accelerate the bone regeneration was confirmed in this study. However, the mechanism is still not very clear. The further study focused on the in-depth mechanism of ES which is undergoing.

5. Conclusion

The study used a calvarial bone defect model to evaluate the effect of percutaneous electrical stimulation on bone regeneration. Radiographic analyses including X-ray and micro-CT show progressive bone healing with time. The bone repair rate is higher in the ES groups than in the non-ES groups. Additionally, the new bone grows on bilateral sides in the ES groups and accumulates in a U-shape in the non-ES groups. Histological evaluations with H&E stain also confirm the higher new bone formation rate in the ES groups. The slides with ALP and TRAP stains indicate that osteoblasts are more active near the cathode and that osteoclasts are more vigorous beside the anode. The results prove the thesis that percutaneous electrical stimulation can accelerate bone

repair, and the bone regeneration is more active near the cathode than around the anode. Bone repair might rely on the activity of osteoblasts and osteoclasts by EA stimulation.

Conflict of Interests

All authors state that they have no conflict of interests.

Authors' Contribution

B.-Y. Yang and T.-C. Huang contributed equally to this work. Y.-S. Chen and Chun-Hsu Yao contributed equally to this work.

Acknowledgment

The present research is financially supported by the National Science Council of the Republic of China, Taiwan (contract no. NSC 98-2221-E-039-005-MY3) and the China Medical University (contract no. CMU99-S-44). The authors do not have a direct financial relation with the commercial identity mentioned in the paper that might lead to a conflict of interest for any of the authors.

References

[1] M. Kikuchi, S. Itoh, S. Ichinose, K. Shinomiya, and J. Tanaka, "Self-organization mechanism in a bone-like hydroxyapatite/collagen nanocomposite synthesized in vitro and its biological reaction in vivo," *Biomaterials*, vol. 22, no. 13, pp. 1705–1711, 2001.

[2] A. Ogose, N. Kondo, H. Umezu et al., "Histological assessment in grafts of highly purified beta-tricalcium phosphate (OSferion) in human bones," *Biomaterials*, vol. 27, no. 8, pp. 1542–1549, 2006.

[3] V. M. Goldberg, "Natural history of autografts and allografts," in *Bone Implant Grafting*, chapter 2, pp. 9–12, 1992.

[4] C. J. Damien and J. R. Parsons, "Bone graft and bone graft substitutes: a review of current technology and applications," *Journal of Applied Biomaterials*, vol. 2, no. 3, pp. 187–208, 1991.

[5] D. Springfield, "Autograft reconstructions," *Orthopedic Clinics of North America*, vol. 27, no. 3, pp. 483–492, 1996.

[6] T. Kaito, A. Myoui, K. Takaoka et al., "Potentiation of the activity of bone morphogenetic protein-2 in bone regeneration by a PLA-PEG/hydroxyapatite composite," *Biomaterials*, vol. 26, no. 1, pp. 73–79, 2005.

[7] C. H. Yao, B. S. Liu, S. H. Hsu, and Y. S. Chen, "Calvarial bone response to a tricalcium phosphate-genipin crosslinked gelatin composite," *Biomaterials*, vol. 26, no. 16, pp. 3065–3074, 2005.

[8] B. S. Liu, C. H. Yao, Y. S. Chen, and S. H. Hsu, "In vitro evaluation of degradation and cytotoxicity of a novel composite as a bone substitute," *Journal of Biomedical Materials Research A*, vol. 67, no. 4, pp. 1163–1169, 2003.

[9] C. H. Yao, B. S. Liu, C. J. Chang, S. H. Hsu, and Y. S. Chen, "Preparation of networks of gelatin and genipin as degradable biomaterials," *Materials Chemistry and Physics*, vol. 83, no. 2-3, pp. 204–208, 2004.

[10] C. H. Yao, B. S. Liu, S. H. Hsu, Y. S. Chen, and C. C. Tsai, "Biocompatibility and biodegradation of a bone composite containing tricalcium phosphate and genipin crosslinked gelatin," *Journal of Biomedical Materials Research A*, vol. 69, no. 4, pp. 709–717, 2004.

[11] E. Fukada and I. Yasuda, "On the piezoelectric effect of bone," *Journal of the Physical Society of Japan*, vol. 12, no. 10, pp. 1158–1162, 1957.

[12] R. O. Becker, "The bioelectric factors in amphibian-limb regeneration," *The Journal of Bone and Joint Surgery (American Volume)*, vol. 43, pp. 643–656, 1961.

[13] Z. B. Friedenberg and C. T. Brighton, "Bioelectric potentials in bone," *Journal of Bone and Joint Surgery A*, vol. 48, no. 5, pp. 915–923, 1966.

[14] C. R. Perry, "Bone repair techniques, bone graft, and bone graft substitutes," *Clinical Orthopaedics and Related Research*, no. 360, pp. 71–86, 1999.

[15] X. L. Griffin, F. Warner, and M. Costa, "The role of electromagnetic stimulation in the management of established non-union of long bone fractures: what is the evidence?" *Injury*, vol. 39, no. 4, pp. 419–429, 2008.

[16] C. Goldstein, S. Sprague, and B. A. Petrisor, "Electrical stimulation for fracture healing: current evidence," *Journal of Orthopaedic Trauma*, vol. 24, supplement 1, pp. S62–S65, 2010.

[17] K. A. Hing, "Bone repair in the twenty-first century: biology, chemistry or engineering?" *Philosophical Transactions of the Royal Society A*, vol. 362, no. 1825, pp. 2821–2850, 2004.

[18] A. L. Mescher, "Bone," in *Junqueira's Basic Histology*, chapter 8, pp. 128–132, 12th edition, 2010.

[19] M. C. Lu, C. Y. Ho, S. F. Hsu et al., "Effects of electrical stimulation at different frequencies on regeneration of transected peripheral nerve," *Neurorehabilitation and Neural Repair*, vol. 22, no. 4, pp. 367–373, 2008.

[20] M. C. Lu, C. C. Tsai, S. C. Chen, F. J. Tsai, C. H. Yao, and Y. S. Chen, "Use of electrical stimulation at different current levels to promote recovery after peripheral nerve injury in rats," *Journal of Trauma—Injury, Infection and Critical Care*, vol. 67, no. 5, pp. 1066–1072, 2009.

[21] G. C. Dong, M. C. Hueih, and C. H. Yao, "A novel bone substitute composite composed of tricalcium phosphate, gelatin and drynaria fortunei herbal extract," *Journal of Biomedical Materials Research A*, vol. 84, no. 1, pp. 167–177, 2008.

[22] C. A. L. Bassett, R. J. Pawluk, and R. O. Becker, "Effects of electric currents on bone in vivo," *Nature*, vol. 204, no. 4959, pp. 652–654, 1964.

[23] Z. B. Friedenberg and M. Kohanim, "The effect of direct current on bone," *Surgery Gynecology and Obstetrics*, vol. 127, no. 1, pp. 97–102, 1968.

[24] B. T. O'Connor, H. M. Charlton, J. D. Currey, D. R. S. Kirby, and C. Woods, "Effects of electric current on bone in vivo," *Nature*, vol. 222, no. 5189, pp. 162–163, 1969.

[25] D. A. Bushinsky, "Metabolic alkalosis decreases bone calcium efflux by suppressing osteoclasts and stimulating osteoblasts," *The American Journal of Physiology*, vol. 271, no. 1, pp. F216–F222, 1996.

[26] T. Bodamyali, J. M. Kanczler, B. Simon, D. R. Blake, and C. R. Stevens, "Effect of faradic products on direct current-stimulated calvarial organ culture calcium levels," *Biochemical and Biophysical Research Communications*, vol. 264, no. 3, pp. 657–661, 1999.

[27] D. A. Bushinsky, "Acidosis and bone," in *Nutritional Influences on Bone Health*, chapter 23, pp. 161–166, 1st edition, 2010.

Hindawi Publishing Corporation
Evidence-Based Complementary and Alternative Medicine
Volume 2013, Article ID 876327, 8 pages
http://dx.doi.org/10.1155/2013/876327

Research Article

Ferulic Acid Enhances Peripheral Nerve Regeneration across Long Gaps

Sheng-Chi Lee,[1,2] Chin-Chuan Tsai,[3,4] Chun-Hsu Yao,[5,6] Yueh-Sheng Chen,[5,6] and Ming-Chang Wu[1]

[1] *Department of Food Science, National Pingtung University of Science and Technology, Pingtung 91201, Taiwan*
[2] *Department of Orthopaedics, Pingtung Branch, Kaoshiung Veterans General Hospital, Kaohsiung 91201, Taiwan*
[3] *School of Chinese Medicine for Post-Baccalaureate, I-Shou University, Kaohsiung 82445, Taiwan*
[4] *Chinese Medicine Department, E-DA Hospital, Kaohsiung 82445, Taiwan*
[5] *Lab of Biomaterials, School of Chinese Medicine, China Medical University, Taichung 40402, Taiwan*
[6] *Department of Biomedical Imaging and Radiological Science, China Medical University, Taichung 40402, Taiwan*

Correspondence should be addressed to Ming-Chang Wu; mcwu@mail.npust.edu.tw

Received 18 December 2012; Accepted 27 March 2013

Academic Editor: Wei-Chiang Lin

This study investigated the effect of ferulic acid (FA) on peripheral nerve injury. In the *in vitro* test, the effect of FA on viability of Schwann cells was studied. In the *in vivo* test, right sciatic nerves of the rats were transected, and a 15 mm nerve defect was created. A nerve conduit made of silicone rubber tube filled with FA (5 and 25 μg/mL), or saline (control), was implanted into the nerve defect. Results show that the number of proliferating Schwann cells increased significantly in the FA-treated group at 25 μg/mL compared to that in the control group. After 8 weeks, the FA-treated group at 25 μg/mL had a higher rate of successful regeneration across the wide gap, a significantly calcitonin gene-related peptide (CGRP) staining of the lamina I-II regions in the dorsal horn ipsilateral to the injury, a significantly diminished number of macrophages recruited, and a significantly shortening of the latency and an acceleration of the nerve conductive velocity (NCV) of the evoked muscle action potentials (MAPs) compared with the controls. In summary, the FA may be useful in the development of future strategies for the treatment of peripheral nerve injury.

1. Introduction

Nerves are not homogenous tissues of monotypic cells. Peripheral nerve regeneration represents a series of highly specialized processes of healing when considered on a cellular level. Numerous investigators have bridged the stumps of a transected peripheral nerve by inserting them in conduits fabricated from a large variety of materials, either biological or artificial [1–4]. These nerve-bridging conduits provide a means for studying the nerve regenerative processes under controlled experimental conditions. However, the investigators' widespread use of a variety of gap lengths may not be able to reveal the real functions of the conduits. In the works of Zhang and Yannas [5], they analyzed a large normalized database from independent investigations, showing that the critical axon elongation, that is, the gap length between the transected sciatic nerve stumps at which the frequency of reconnection is just 50% in an empty silicone rubber nerve conduit, is 9.7 ± 1.8 mm for the rat. Their results implied that the nerve bridge technique can be successfully used to repair short nerve gaps in a rat model. However, the rat peripheral nervous system possesses a high potential for axonal regeneration across short nerve gaps. Therefore, the use of a longer gap more than 10 mm may be necessary in rats to show significant improvements in bridging injured nerves by using different modifications of nerve conduits. Various stimulatory substances such as laminin [6], fibronectin [7], and collagen [8] have been used accompanied with the nerve bridging conduits to modify their internal microenvironment in order to promote the growth of nerves across longer gaps. Recently, administration of herbal medicine has attracted the attention of investigators as a new approach to treat

peripheral nerve injuries, such as extraction of Paeoniae alba Radix [9], Chungpa-Juhn [10], Lumbricus [11], and Sanyak [12]. Components in herbs can also accelerate axonal regeneration and target muscle reinnervation, such as quercetin [13], puerarin [14], astragaloside [15], and bilobalide [16].

Ferulic acid (FA) is a component of *Angelica sinensis* (Oliv.) Diels, and *Ligusticum chuanxiong* Hort. (Figure 1), was shown to be a free radical scavenger and to have anti-inflammatory and antioxidation effects in a transient middle cerebral artery occlusion model [17]. FA could also decrease the level of intercellular adhesion molecule-1 mRNA and the number of microglia/macrophages and subsequently downregulated inflammation-induced oxidative stress and oxidative stress-related apoptosis after cerebral ischemia/reperfusion injury in rats, suggesting that FA could provide neuroprotection against oxidative stress-related apoptosis [18]. It has been also reported that the FA was better for retinal nerve cell proliferation than that of brain-derived neurotrophic factor [19]. Although the literature shows that FA has versatile biological functions, its nerve growth-promoting effect has never been characterized. Therefore, this study investigated the effect of FA on peripheral nerve injury, using a rat *in vivo* sciatic nerve transection and repair model with a long 15 mm gap and rat Schwann cell line *in vitro*.

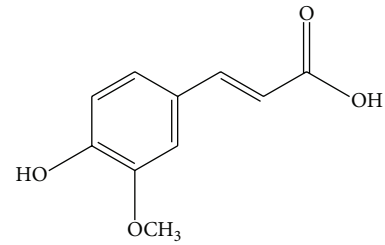

Figure 1: Structure of ferulic acid (FA).

2. Materials and Methods

2.1. Cell Culture and Treatment. Schwann cells (RSC96) were maintained at 37°C in a humidified atmosphere of 5% CO_2 and 95% air in DMEM medium supplemented with 5% fetal calf serum, 2 mM HEPES, and 2 mM L-glutamine. The Schwann cells (7×10^3 cells/cm^2) were then induced to undergo neuronal differentiation by treatment with 5 and 25 μg/mL of FA solution (Product 128708, Sigma-Aldrich, St. Louis, MO, USA) for two days. Cells that had been exposed to the vehicle alone (culture medium only) were the control. Six replicates were used in each study.

2.2. Analysis of Cell Viability. After 48 h of cell incubation, the medium was removed, replaced with 110 μL/well of 5 mg/mL of MTT solution in 1 × PBS, and further incubated in an incubator at 37°C for 4 h. Then, the MTT solution was removed and replaced with 50 μL of DMSO to dissolve the formazan. The color intensity was measured using a microplate reader (ELx800TM, Bio-Tek Instrument, Inc., Winooski, VT, USA) at the absorbance of 550 nm. Data were then expressed as a percent of control level of the optical density within an individual experiment.

2.3. Cell Imaging. After treating with the FA solution for 48 h, the Schwann cells were washed with PBS twice, fixed in 2% paraformaldehyde for 30 min, and then permeabilized with 0.1% Triton X-100/PBS for 30 min at room temperature. After washing with PBS, TUNEL assay was performed according to the manufacturer's instructions (Boehringer Mannheim). Cells were incubated in TUNEL reaction buffer in a 37°C humidified chamber for 1 h in the dark, then rinsed twice with PBS, and incubated with DAPI (1 mg/mL) at 37°C for 10 min; stained cells were visualized using a fluorescence microscope (Olympus DP70/U-RFLT50, Olympus Optical Co. Ltd., Japan). DAPI-positive and TUNEL-positive cells were counted as live and apoptotic cells, respectively.

2.4. Surgical Preparation of Animals. Adult Sprague-Dawley rats underwent placement of silicone chambers. The animals were anesthetized with an inhalational anesthetic technique (AErrane, Baxter, USA). Following the skin incision, fascia and muscle groups were separated using blunt dissection, and the right sciatic nerve was severed into proximal and distal segments. The proximal stump was then secured with a single 9-0 nylon suture through the epineurium and the outer wall of the silicone rubber chamber (1.47 mm ID, 1.96 mm OD; Helix Medical, Inc., Carpinteria, CA, USA). Animals were divided into 3 groups. In group A ($n = 9$), the chambers were filled with normal saline as the controls. In group B ($n = 9$), 5 μg/mL of FA solution was filled in the chambers. Similarly, chambers in group C ($n = 9$) were filled with 25 μg/mL of FA solution, respectively.

The volume of the chamber lumen was approximately 25.5 μL. These fillings, which were in the liquid state, were injected through a micropipette into the lumens by passing the tip of the needle inside the silicone rubber chambers as slowly as possible to prevent the leakage. As we secured the proximal stump into the end of the silicone rubber chamber, the swollen nerve end blocked the opening of the chamber. The chamber was then tilted and the distal stump secured into the other end of the chamber. Both the proximal and distal stumps were secured to a depth of 1 mm into the chamber, leaving a 15 mm gap between the stumps. The muscle layer was reapproximated with 4-0 chromic gut sutures, and the skin was closed with 2-0 silk sutures. All animals were then returned to plastic cages where a sufficient amount of sawdust was present to decrease direct contact of the paralyzed limb of the rat with the floor. These animals were housed in temperature (22°C) and humidity (45%) controlled rooms with 12-hour light cycles, and they had access to food and water *ad libitum*. All animals were maintained in facilities approved by the China Medical University for Accreditation of Laboratory Animal Care and in accordance with current ROC National Science Council of health regulations and standards.

2.5. Electrophysiological Techniques. After 8 weeks of regeneration, the animals were reanaesthetized and the silicone

rubber conduit was removed to expose their sciatic nerve. The stimulating cathode was a stainless steel monopolar needle, which was placed directly on the sciatic nerve trunk, 5 mm proximal to the transection site. The anode was another stainless steel monopolar needle placed 3 mm proximally to the cathode. Amplitude, area, and nerve conductive velocity (NCV) of the evoked muscle action potentials (MAPs) were recorded from gastrocnemius muscles with microneedle electrodes linked to a computer system (Biopac Systems, Inc., USA). The amplitude and the area under the MAP curve were calculated from the baseline to the maximal negative peak. The NCV was carried out by placing the recording electrodes in the gastrocnemius muscles and stimulating the sciatic nerve proximally and distally to the silicone rubber conduit. The NCV was then calculated by dividing the distance between the stimulating sites by the difference in latency time. All data are expressed as mean ± standard deviation. Statistical comparisons between groups were made by the one-way analysis of variance.

2.6. Histological Techniques. After perfusion, as was done for the retrograde labeling, the L4 spinal cord and the distal stump outside the nerve gap were quickly removed and postfixed in the same fixative for 3-4 h. Tissue samples were placed overnight in 30% sucrose for cryoprotection at 4°C, followed by embedding in optimal cutting temperature solution. Samples were kept at −20°C until preparation of 18 μm sections was performed using a cryostat, with samples placed upon poly-L-lysine-coated slide. Immunohistochemistry of frozen sections was carried out using a two-step protocol according to the manufacturer's instructions (Novolink Polymer Detection System, Novocastra). Briefly, frozen sections were required, endogenous peroxidase activity was blocked with incubation of the slides in 0.3% H_2O_2, and nonspecific binding sites were blocked with Protein Block (RE7102; Novocastra). After serial incubation with rabbit- anti-CGRP polyclonal antibody 1 : 1000 (Calbiochem, Germany), Post Primary Block (RE7111; Novocastra), and secondary antibody (Novolink Polymer RE7112), the L4 spinal cord sections were developed in diaminobenzidine solution under a microscope and counterstained with hematoxylin. Similar protocols were applied in the sections from the distal stump except that they were incubated with antirat CD68 1 : 100 (AbD Serotec, Kidlington, UK). Sciatic nerve sections were taken from the middle regions of the regenerated nerve in the chamber. After the fixation, the nerve tissue was postfixed in 0.5% osmium tetroxide, dehydrated, and embedded in Spurr's resin. The tissue was then cut to 5 μm thickness by using a microtome (Leica EM UC6, Leica Biosystems, Mount Waverley, Australia) with a dry glass knife, stained with toluidine blue.

2.7. Image Analysis. All tissue samples were observed under optical microscopy. CGRP immunoreactivity (IR) in dorsal horn in the lumbar spinal cord was detected by immunohistochemistry. The immunoproducts were confirmed positive labeled if their density level was over five times background levels. Under a 100x magnification, the ratio of area occupied by positive CGRP-IR in dorsal horn ipsilateral to the injury following neurorrhaphy relative to the lumbar spinal cord was measured using an image analyzer system (Image-Pro Lite, Media Cybernetics, USA) coupled to the microscope.

As counting the myelinated axons, at least 30 to 50 percent of the sciatic nerve section area randomly selected from each nerve specimen at a magnification of 400x was observed. The axon counts were extrapolated by using the area algorithm to estimate the total number of axons for each nerve. Axon density was then obtained by dividing the axon counts by the total nerve areas. Similarly, the density of macrophage was determined by dividing the macrophage counts by the total nerve areas. All data are expressed as mean ± standard deviation. Statistical comparisons between groups were made by one-way analysis of variance with Scheffe's test.

3. Results

3.1. Cell Viability. When RSC96 cells were treated with FA at 25 μg/mL for 24 h, cell viability significantly increased to 121% of control ($P < 0.05$, Figure 2(a)). Cell imaging also strongly supports the beneficial effect of FA in proliferation of Schwann cells that increases DAPI positive cells, and no TUNEL positive cells were seen in both the FA-treated groups compared to the controls (Figure 2(b)). Taken together, these data indicate that treatment with FA promotes viability of Schwann cells.

3.2. Electrophysiological Measurements. Rats having regenerated cables within the bridging conduits presented a triphasic wave of MAP indicating successful reinnervation of the gastrocnemius muscle by the regenerating sciatic nerve. The comparison of latency or NCV of the MAP waves showed significant differences between FA-treated rats at 25 μg/mL and controls ($P < 0.05$, Figures 3(a) and 3(b)). The FA-treated animals had a dramatic shortening of the latency and an acceleration of the NCV compared with the controls. The FA-treated animals also had a relatively larger area and amplitude of the MAP wave compared with the controls, though their differences did not reach the significant level at $P = 0.05$ (Figures 3(c) and 3(d)).

3.3. CGRP-IR in the Dorsal Horn following Injury. Immunohistochemical staining showed that CGRP-labeled fibers were seen in the area of lamina III–V and lamina I-II regions in the dorsal horn ipsilateral to the injury in all of the rats (Figure 4(a)) in which the FA-treated rats at 25 μg/mL had a significantly higher CGRP expression compared with the FA-treated rats at 5 μg/mL and the controls ($P < 0.05$, Figure 4(b)).

3.4. Macrophages Recruited in the Distal Nerve Ends. Within distal portions of the transection gap zone we identified clusters of macrophages labeled with CD68. Obviously, the FA could alleviate local inflammatory conditions in the regenerated nerves in which the density of macrophage was decreased as the concentration of FA was increased (Figure 5(a)). Specially, a significantly lower density of

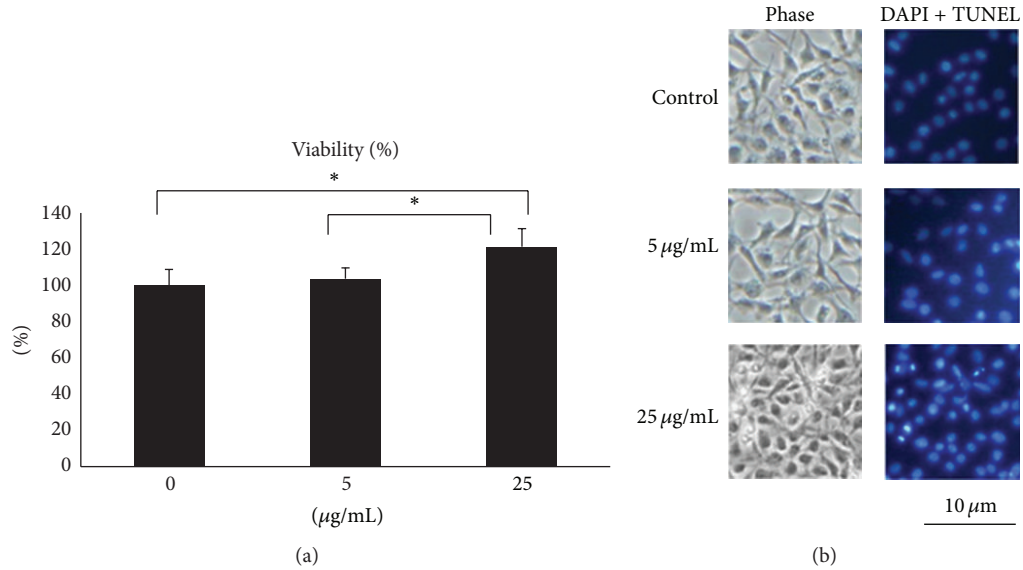

Figure 2: (a) Quantification of viability of Schwann cells treated with ferulic acid relative to controls. Values are means ± S.E.M. $^{*}P < 0.05$ indicates a significant difference from other groups. (b) Nuclei of Schwann cells characterized by DAPI and TUNEL assays and investigated via fluorescent microscopy.

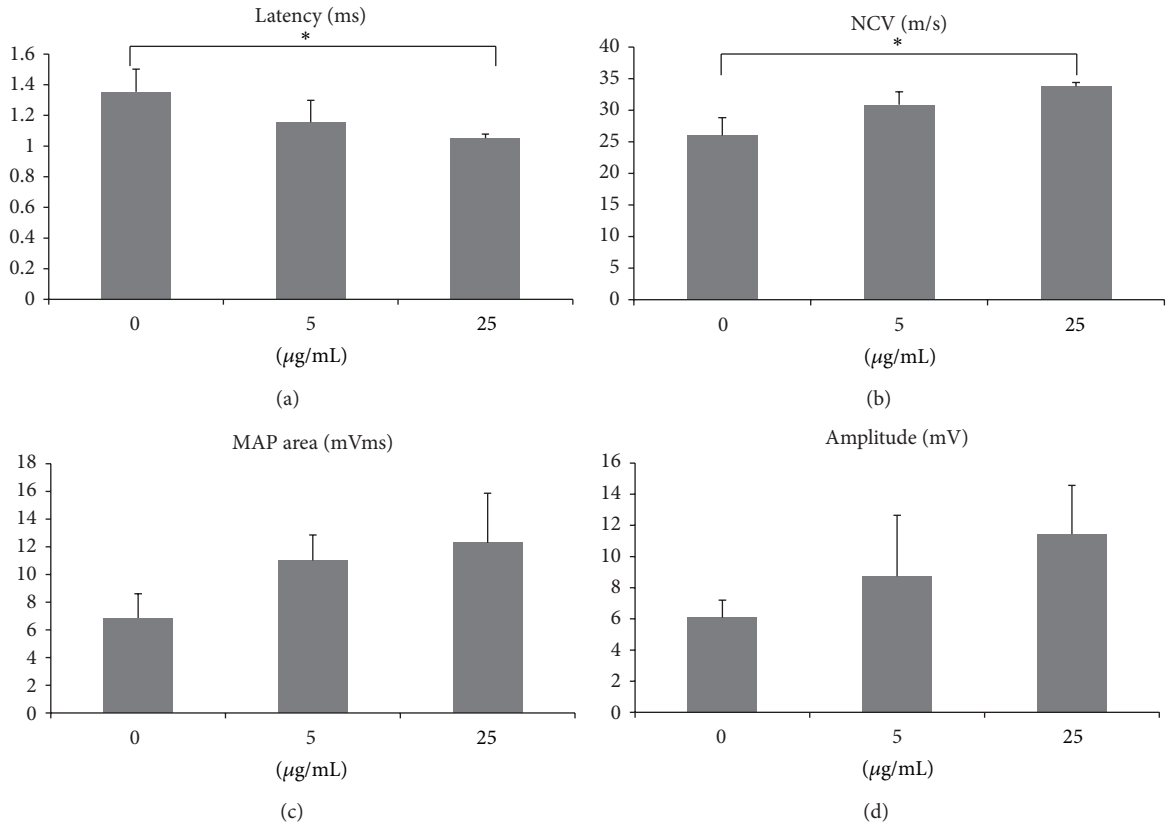

Figure 3: Analysis of evoked MAPs, including (a) latency, (b) NCV, (c) peak amplitude, and (d) area under the MAP curves. $^{*}P < 0.05$ indicates significant difference from other groups.

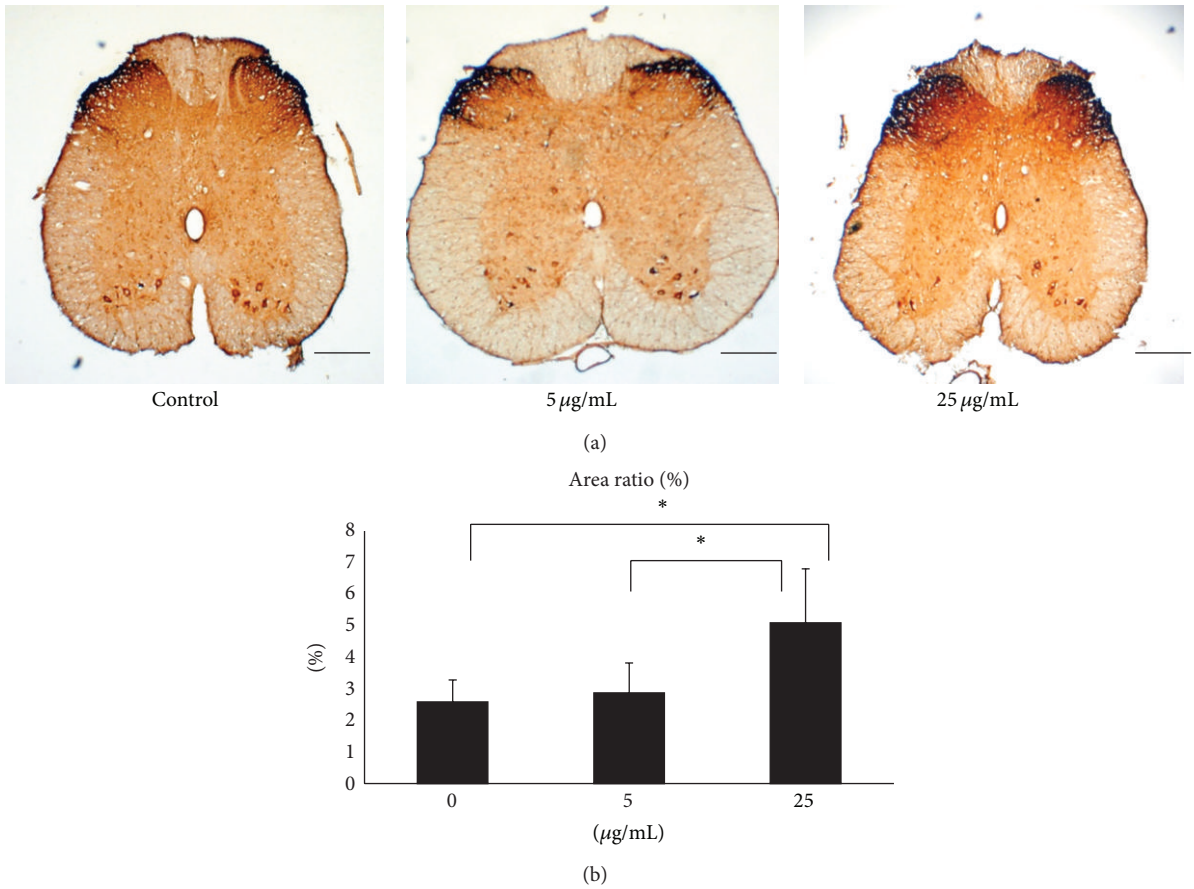

Figure 4: (a) Photomicrographs demonstrating CGRP-IR in dorsal horn in the lumbar spinal cord after injury of controls and FA-treated animals. Scale bars = 200 μm. (b) Note the significantly increased CGRP-IR area ratios in FA-treated animals at 25 μg/mL compared to those at 5 μg/mL and the controls. $^*P < 0.05$ indicates significant difference from other groups.

macrophages was recruited into the nerve stumps in the FA-treated animals at 25 μg/mL compared to that at 5 μg/mL and the controls ($P < 0.05$, Figure 5(b)). This result indicated that deliberate superimposition of FA in the bridging conduits could dramatically suppress influx of macrophages in injured nerves.

3.5. Sciatic Nerve Regeneration. Features of axon regeneration in bridging conduits have largely been described at the light and electron microscopic level. Usually, connective tissue regenerative bridges populated by a core of myelinated axons surrounded by layers of perineurial and epineurial cells could be identified. In this study, we found that two of nine conduits in the control group developed regenerative bridges by the 8-week end point (Figure 6(a)). Only one of them had evidence of axon regrowth (number: 3592) and penetration into the bridge. In conduits exposed to FA at 5 μg/mL, two of nine had bridges (Figure 6(b)), and the mean axonal number was 1627 (range: 1600–1653). By comparison, four of nine rats treated with 25 μg/mL of FA developed the regenerative bridges (Figure 6(c)) and three of which contained a sizeable population of myelinated axons (mean axon number was 2437; range: 691–3963).

4. Discussion

Most of the studies in the literature associated with the nerve regeneration using herbal medicine to repair injured rat nerves have reported that the interstump gap lengths used were shorter than 10 mm. A 10 mm gap is considered the critical gap length within a tubular prosthesis above which neural components usually will not cross the gap when no growth substances are distributed in the chambers at the time of implantation [20]. Therefore, to demonstrate the real effect of herbal medicine on nerve regeneration we chose a 15 mm gap in the rat transaction model.

Before examining the *in vivo* action of FA on nerve regeneration, we first found that FA could increase Schwann cell viability in a dose-dependent fashion *in vitro*. Schwann cells are the principal glia as well as myelinating cells of the peripheral nervous system, which are involved in many important aspects of peripheral nerve regeneration, such as secreting neurotrophic factors and physically supporting

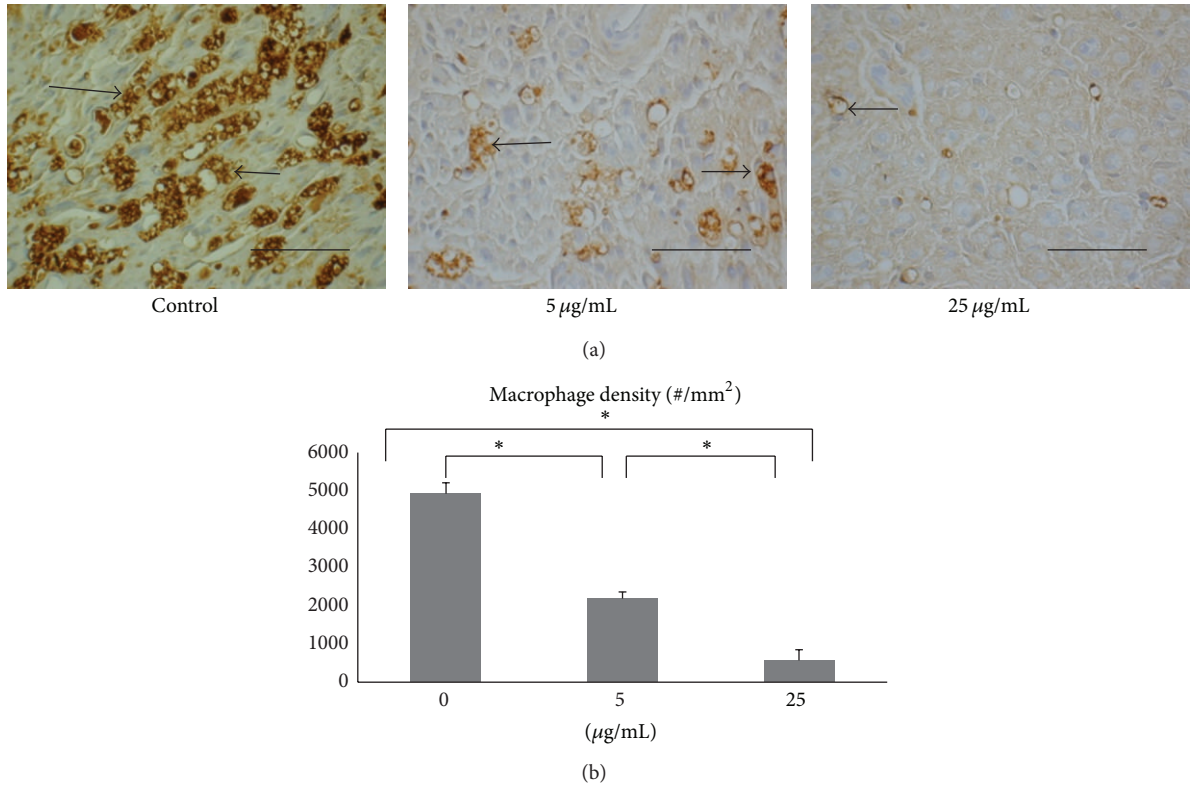

Figure 5: (a) Photomicrographs demonstrating antirat CD68 immunoreactivity in macrophages (arrows) from cross sections of distal nerve cables of controls and FA-treated animals. Scale bars = 100 μm. (b) Note the dramatically decreased density of macrophages with the concentration of FA. $^{*}P < 0.05$ indicates significant difference from other groups.

regenerating axons [21]. Therefore, the FA should have significant nerve growth-promoting potential. The *in vivo* study supports and extends these initial *in vitro* findings by showing that FA could enhance formation of regenerated nerve cables in the bridging conduits, especially in the group of FA at 25 μg/mL (4 of 9). By comparison, the complete interruption of regenerative bridge formation was dramatic in the controls (7 of 9) and the FA-treated rats at 5 μg/mL (7 of 9). In addition, histological observations of regenerated nerve also strongly support the beneficial effect of FA in axonal regrowth that only one of the regenerated cables in the controls showing myelinated axons. Similar to the morphometric analyses, the FA effect was also observed in the MAP measurements. For example, the FA group at 25 μg/mL showed bundles of myelinated axons in morphometric analysis with a relatively larger amplitude, area, NCV, and shorter latency during electrophysiological assay as compared to those in the other two groups. To address how regenerative events might fare in bridges exposed to FA, we also examined CGRP-labeled components in the spinal cord sections. Unlike control or low-dose FA infused sections, the FA-treated rats at 25 μg/mL had a dramatic high CGRP expression. The CGRP is crucial for interactions between axons and Schwann cells during peripheral nerve regrowth [22] and plays important roles in nerve function and repair when axons are severed [23]. Taken together, these data indicate that treatment with FA at 25 μg/mL could promote functional recovery by accelerating axonal regeneration after sciatic nerve transaction in the rat.

Finally, in this study, a surface marker, CD68, was employed to characterize macrophages participating in nerve regeneration. It was found that population of macrophages was significantly diminished as the dosage of FA was increased. Macrophages have been reported, playing an important role during early nerve regeneration [24]. Within days of peripheral nerve injury, activated macrophages begin tasks of debris removal, secretion of growth factors, and remodeling of the extracellular matrix of the distal nerve stump. However, at later stage of nerve regeneration inflammation caused by macrophages becomes harmful since nitric oxide (NO) generated by inducible nitric oxide synthase (iNOS) can collapse growth cones and cause axonal degeneration [25]. Since this study focused on late regenerative events associated with axon growth across a critical defect gap, population of macrophages suppressed by administering FA in the bridging conduits was beneficial to the regenerating axons.

5. Conclusions

Our data demonstrates that FA appears to promote peripheral nerve regeneration across a 15 mm critical defect gap in the

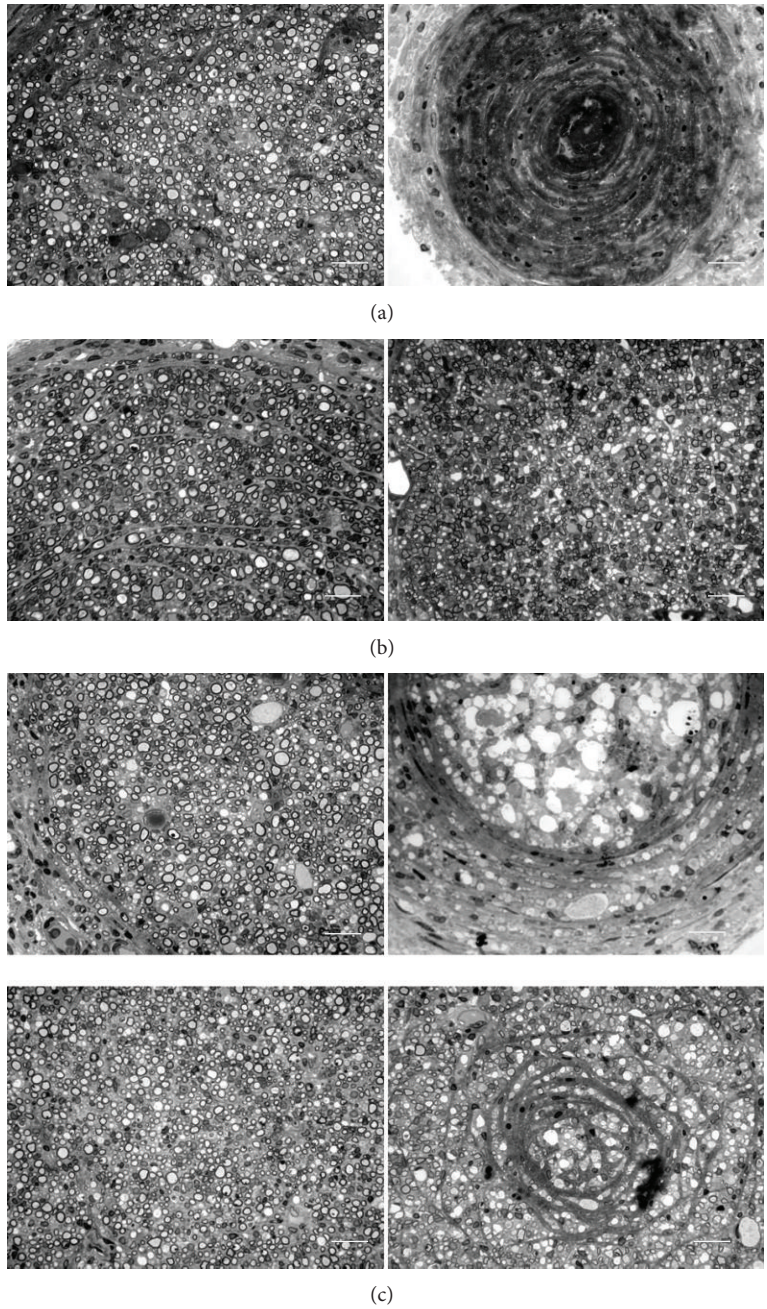

(a)

(b)

(c)

Figure 6: Photomicrographs showing regenerated nerve cross sections of (a) controls and FA-treated animals at (b) 5 μg/mL and (c) 25 μg/mL. Scale bars = 20 μm.

rat sciatic nerve injury model. Suppression of macrophages by FA at the site of peripheral nerve injury may contribute to its nerve growth-promoting capability.

Acknowledgments

The authors would like to thank Miss. I-Ching Chen for her assistance in the experiment. M.-C. Wu and Y.-S. Chen contributed equally to this work. Part of this work was supported by research grants from the China Medical University and Hospital (CMU100-S-37; DMR-98-054) and Taiwan Department of Health Clinical Trial and Research Center of Excellence (DOH102-TD-B-111-004).

References

[1] S. W. Hsiang, C. C. Tsai, F. J. Tsai, T. Y. Ho, C. H. Yao, and Y. S. Chen, "Novel use of biodegradable casein conduits for guided peripheral nerve regeneration," *Journal of the Royal Society Interface*, vol. 8, no. 64, pp. 1622–1634, 2011.

[2] A. M. McGrath, M. Brohlin, P. J. Kingham, L. N. Novikov, M. Wiberg, and L. N. Novikova, "Fibrin conduit supplemented

with human mesenchymal stem cells and immunosuppressive treatment enhances regeneration after peripheral nerve injury," *Neuroscience Letters*, vol. 516, no. 2, pp. 171–176, 2012.

[3] V. Magnaghi, V. Conte, P. Procacci et al., "Biological performance of a novel biodegradable polyamidoamine hydrogel as guide for peripheral nerve regeneration," *Journal of Biomedical Materials Research A*, vol. 98, no. 1, pp. 19–30, 2011.

[4] V. Penna, B. Munder, G. B. Stark, and E. M. Lang, "An *in vivo* engineered nerve conduit-fabrication and experimental study in rats," *Microsurgery*, vol. 31, no. 5, pp. 395–400, 2011.

[5] M. Zhang and I. V. Yannas, "Peripheral nerve regeneration," *Advances in Biochemical Engineering/Biotechnology*, vol. 94, pp. 67–89, 2005.

[6] J. Cao, C. Sun, H. Zhao et al., "The use of laminin modified linear ordered collagen scaffolds loaded with laminin-binding ciliary neurotrophic factor for sciatic nerve regeneration in rats," *Biomaterials*, vol. 32, no. 16, pp. 3939–3948, 2011.

[7] T. Ding, W. W. Lu, Y. Zheng, Z. Y. Li, H. B. Pan, and Z. Luo, "Rapid repair of rat sciatic nerve injury using a nanosilver-embedded collagen scaffold coated with laminin and fibronectin," *Regenerative Medicine*, vol. 6, no. 4, pp. 437–447, 2011.

[8] W. T. Daly, L. Yao, M. T. Abu-rub et al., "The effect of intraluminal contact mediated guidance signals on axonal mismatch during peripheral nerve repair," *Biomaterials*, vol. 33, no. 28, pp. 6660–6671, 2012.

[9] Y. S. Chen, K. S. Huang, J. G. Lin et al., "Paeoniae alba radix promotes peripheral nerve regeneration," *Evidence-Based Complementary and Alternative Medicine*, vol. 2011, Article ID 109809, 8 pages, 2011.

[10] T. H. Kim, S. J. Yoon, W. C. Lee et al., "Protective effect of GCSB-5, an herbal preparation, against peripheral nerve injury in rats," *Journal of Ethnopharmacology*, vol. 136, no. 2, pp. 297–304, 2011.

[11] S. Wei, X. Yin, Y. Kou, and B. Jiang, "Lumbricus extract promotes the regeneration of injured peripheral nerve in rats," *Journal of Ethnopharmacology*, vol. 123, no. 1, pp. 51–54, 2009.

[12] J. M. Lee, U. K. Namgung, and K. E. Hong, "Growth-promoting activity of sanyak (*Dioscoreae rhizoma*) extract on injured sciatic nerve in rats," *Journal of Acupuncture and Meridian Studies*, vol. 2, no. 3, pp. 228–235, 2009.

[13] W. Wang, C. Y. Huang, F. J. Tsai, C. C. Tsai, C. H. Yao, and Y. S. Chen, "Growth-promoting effects of quercetin on peripheral nerves in rats," *The International Journal of Artificial Organs*, vol. 34, no. 11, pp. 1095–1105, 2011.

[14] S. W. Hsiang, H. C. Lee, F. J. Tsai, C. C. Tsai, C. H. Yao, and Y. S. Chen, "Puerarin accelerates peripheral nerve regeneration," *The American Journal of Chinese Medicine*, vol. 39, no. 6, pp. 1207–1217, 2011.

[15] C. Y. Cheng, C. H. Yao, B. S. Liu, C. J. Liu, G. W. Chen, and Y. S. Chen, "The role of astragaloside in regeneration of the peripheral nerve system," *Journal of Biomedical Materials Research A*, vol. 76, no. 3, pp. 463–469, 2006.

[16] Y. S. Chen, C. J. Liu, C. Y. Cheng, and C. H. Yao, "Effect of bilobalide on peripheral nerve regeneration," *Biomaterials*, vol. 25, no. 3, pp. 509–514, 2004.

[17] Q. Wang, S. Y. Chen, L. Z. Xiong, W. L. Jin, and J. Yang, "Neuroprotective effect of sodium ferulate on transient focal cerebral ischemia by weakening activation of postsynaptic density-95 in rats," *Chinese Journal of Traumatology*, vol. 8, no. 5, pp. 297–302, 2005.

[18] C. Y. Cheng, S. Y. Su, N. Y. Tang, T. Y. Ho, S. Y. Chiang, and C. L. Hsieh, "Ferulic acid provides neuroprotection against oxidative stress-related apoptosis after cerebral ischemia/reperfusion injury by inhibiting ICAM-1 mRNA expression in rats," *Brain Research*, vol. 1209, pp. 136–150, 2008.

[19] G. L. Li, J. J. Wang, J. Z. Wang, Y. Y. Liu, and Y. Jin, "Effect of ferulic acid on the proliferation of nerve cells of retinas *in vitro*," *Chinese Journal of Ophthalmology*, vol. 39, no. 11, pp. 650–654, 2003.

[20] A. L. Woolley, J. P. Hollowell, and K. M. Rich, "Fibronectin-laminin combination enhances peripheral nerve regeneration across long gaps," *Otolaryngology—Head and Neck Surgery*, vol. 103, no. 4, pp. 509–518, 1990.

[21] W. Daly, L. Yao, D. Zeugolis, A. Windebank, and A. Pandit, "A biomaterials approach to peripheral nerve regeneration: bridging the peripheral nerve gap and enhancing functional recovery," *Journal of the Royal Society Interface*, vol. 9, no. 67, pp. 202–221, 2012.

[22] C. C. Toth, D. Willis, J. L. Twiss et al., "Locally synthesized calcitonin gene-related peptide has a critical role in peripheral nerve regeneration," *Journal of Neuropathology and Experimental Neurology*, vol. 68, no. 3, pp. 326–337, 2009.

[23] X. Q. Li, V. M. K. Verge, J. M. Johnston, and D. W. Zochodne, "CGRP peptide and regenerating sensory axons," *Journal of Neuropathology and Experimental Neurology*, vol. 63, no. 10, pp. 1092–1103, 2004.

[24] D. S. McDonald, C. Cheng, J. A. Martinez, and D. W. Zochodne, "Regenerative arrest of inflamed peripheral nerves: role of nitric oxide," *NeuroReport*, vol. 18, no. 16, pp. 1635–1640, 2007.

[25] N. Mokarram, A. Merchant, V. Mukhatyar, G. Patel, and R. V. Bellamkonda, "Effect of modulating macrophage phenotype on peripheral nerve repair," *Biomaterials*, vol. 33, no. 34, pp. 8793–8801, 2012.

Hindawi Publishing Corporation
Evidence-Based Complementary and Alternative Medicine
Volume 2013, Article ID 514049, 9 pages
http://dx.doi.org/10.1155/2013/514049

Research Article

Anti-Inflammatory and Neuroprotective Effects of Constituents Isolated from *Rhodiola rosea*

Yeonju Lee,[1] Jae-Chul Jung,[1] Soyong Jang,[1] Jieun Kim,[1] Zulfiqar Ali,[2] Ikhlas A. Khan,[2] and Seikwan Oh[1]

[1] *Department of Neuroscience and Tissue Injury Defense Research Center, School of Medicine, Ewha Womans University, Seoul 158-710, Republic of Korea*
[2] *National Center for Natural Products Research, School of Pharmacy, Thad Cochran Research Center, University of Mississippi, MS 38677-1848, USA*

Correspondence should be addressed to Seikwan Oh; skoh@ewha.ac.kr

Received 26 September 2012; Revised 2 January 2013; Accepted 27 March 2013

Academic Editor: Wei-Chiang Lin

To determine the biological activity of *Rhodiola rosea*, the protein expression of iNOS and proinflammatory cytokines was measured after the activation of murine microglial BV2 cells by LPS under the exposure of constituents of *Rhodiola rosea*: crude extract, rosin, rosarin, and salidroside (each 1–50 μg/mL). The LPS-induced expression of iNOS and cytokines in BV2 cells was suppressed by the constituents of *Rhodiola rosea* in a concentration-dependent manner. Also the expression of the proinflammatory factors iNOS, IL-1β, and TNF-α in the kidney and prefrontal cortex of brain in mice was suppressed by the oral administration of *Rhodiola rosea* crude extract (500 mg/kg). To determine the neuroprotective effect of constituents of *Rhodiola rosea*, neuronal cells were activated by L-glutamate, and neurotoxicity was analyzed. The L-glutamate-induced neurotoxicity was suppressed by the treatment with rosin but not by rosarin. The level of phosphorylated MAPK, pJNK, and pp38 was increased by L-glutamate treatment but decreased by the treatment with rosin and salidroside. These results indicate that *Rhodiola rosea* may have therapeutic potential for the treatment of inflammation and neurodegenerative disease.

1. Introduction

Rhodiola rosea (*R. rosea*) is known as a golden or arctic root and belongs to the plant family of Crassulaceae, subfamily of Sedoideae, and genus Rhodiola [1]. *R. rosea* is widely distributed in the Arctic and mountainous regions throughout Europe and Asia. It is a popular plant in traditional medical systems and has been used to stimulate the nervous system, decrease depression, enhance work performance, and prevent high altitude sickness [2]. Of the Rhodiola species, *R. rosea* has been extensively studied for its phytochemical and toxicological properties [3]. *R. rosea* root contains about 28 compounds, of which salidroside (rhodioloside), rosavins, and p-tyrosol are thought to have the most critical therapeutic activity [4]. It was reported that *R. rosea* ingestion can improve cognitive function [5], reduce mental fatigue [6, 7], promote free radical mitigation, have antioxidative [8] and neuroprotective [9] effects, increase endurance performance [10, 11], and enhance learning and memory [11]. *R. rosea* may play a role in the amelioration of neurodegenerative diseases, such as Alzheimer's disease (AD), via its anti-inflammatory and neuroprotective properties.

Alzheimer's disease is the common neurodegenerative disease characterized by the inflammation and neuronal loss in the specific regions of the forebrain. Therefore, any compound that has the antineurotoxicity and the anti-inflammatory properties can be a good candidate for AD therapy. The central nervous system includes two major cell types, neurons, and glial cells; glial cells are represented by astrocytes, oligodendrocytes, and microglia [12]. Once the microglia is activated by lipopolysaccharide, the affected microglia can produce a series of proinflammatory and cytotoxic factors, such as tumor necrosis factor- (TNF-) α and interleukin- (IL-) 1β, which have been implicated in the

neuropathogenesis of AD [13]. Moreover, the release of these proinflammatory factors from the activated cells enhances LPS-induced cytotoxic activations [14] and develops a continuous cycle of inflammatory stimuli.

L-Glutamate (L-glu) is the most abundant excitatory neurotransmitter in the vertebrate central nervous system (CNS) and plays a crucial role in the neurological processes including cognition, learning, and memory [15]. However, excessive stimulation of glutamate receptors, under pathophysiological conditions, leads to the neuronal damage and death. This phenomenon is well known as "excitotoxicity," since neurotoxicity is correlated with excitatory properties of various L-glu analogs [16]. Glutamate neurotoxicity has also been postulated to play important roles in the pathophysiology of numerous neurological diseases including hypoxic-ischemic brain injury [17, 18], epileptic seizures [19], and neurodegenerative diseases including AD [20, 21] and Parkinson's disease [22, 23]. Accordingly, substances which can prevent L-glu-induced neurotoxicity are expected to be potential tools in the therapy of various neurological and neurodegenerative diseases. If one compound reduces the L-glu-induced neurotoxicity, it would become a candidate means of improving the neurodegenerative diseases. This experiment was aimed to investigate the effects of the various constituents of *R. rosea* on inflammation and neurotoxicity.

2. Materials and Methods

2.1. Reagents. LPS (*Escherichia coli*, O111:B4) were obtained from Sigma-Aldrich (St. Louis, MO, USA). Cell culture ingredients were obtained from Invitrogen (Carlsbad, CA, USA). All other reagents were obtained from Sigma-Aldrich. Roots' water extract (230 g) of *Rhodiola rosea* was soaked in MeOH at room temperature. The soluble part was evaporated under reduced pressure to afford a dry brown material (extract, 165 g) and subjected to vacuum liquid chromatography over flash silica gel. Through column fraction, rosin (322 mg), rosarin (339 mg), and salidroside (908 mg) were purified and identified as described in detail [24]. *R. rosea* extract and constituents (Figure 1) were kindly supplied from Dr. Ikhlas Khan (NCNPR, University of Mississippi, MS, USA).

2.2. Cell Culture. The murine BV2 cell line (a generous gift from W. Kim, Korea Research Institute of Bioscience and Biotechnology, Daejeon, Republic of Korea), which is immortalized after infection with a *v-raf/v-myc* recombinant retrovirus, exhibits the phenotypic and functional properties of reactive microglial cells. BV2 cells were maintained at 37°C at 5% CO_2 in Dulbecco's modified Eagle's medium (DMEM) supplemented with 10% FBS, 100 μg/mL streptomycin, and 100 U/mL penicillin. BV2 cells were grown in 24-well plates at a concentration of 1×10^5 cells/well followed by proper treatment.

2.3. Nitrite Assay. NO production from activated microglial cells was determined by measuring the amount of nitrite, a relatively stable oxidation product of NO, as described previously [25]. Cells were incubated with or without LPS in the presence or absence of various concentrations of compounds for 18 h. The nitrite accumulation in the supernatant was assessed by the Griess reaction. In brief, an aliquot of the conditioned medium 50 μL was mixed with an equal volume of 1% sulfanilamide in water and 0.1% *N*-1-naphthylethylenediamine dihydrochloride in 5% phosphoric acid. The absorbance was determined at 540 nm in an automated microplate reader.

2.4. Immunoblot Analysis. BV2 and cortical neuronal cells were washed twice with ice-cold phosphate-buffered saline (PBS) and then lysed in ice-cold modified lysis buffer (150 mM NaCl, 50 mM Tris, 1 mM EDTA, 0.01% Triton

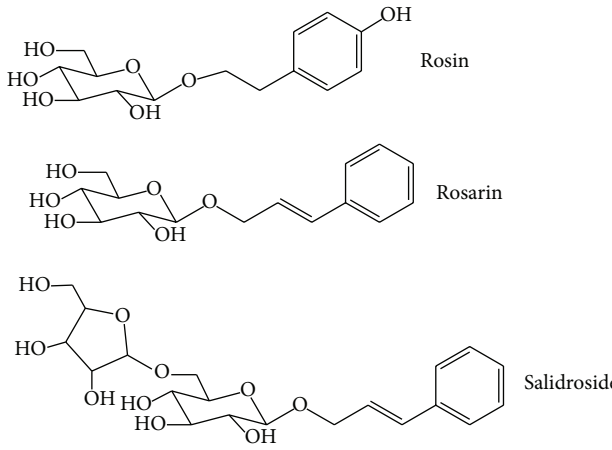

Figure 1: The structures of a constituent of *R. rosea*.

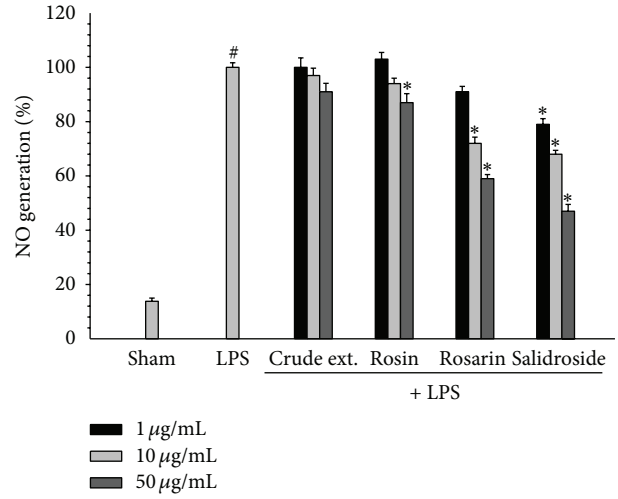

Figure 2: The suppression of NO generation in LPS-treated BV2 microglial cells. Cells were treated with 100 ng/mL LPS with or without *R. rosea* constituents (1, 10, 50 μg/mL) for 18 h. At the end of incubation, 50 μL of the medium was collected to measure nitrite production. The amount of NO in the supernatant fractions was measured by using the Griess reagent. All values are expressed as mean ± S.E.M. from three independent experiments. Data were analyzed by one-way ANOVA for multiple comparison and Student-Newman-Keuls test as post hoc test. $^{\#}P < 0.01$ as compared with the vehicle group; $^{*}P < 0.05$ as compared with the LPS-treated group.

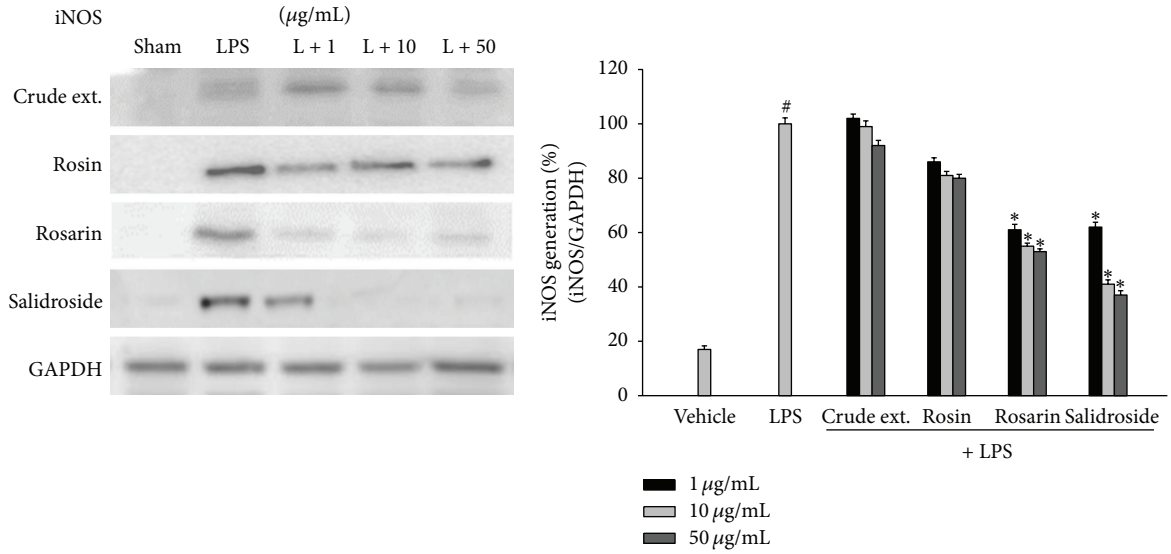

Figure 3: Effects of *R. rosea* constituents on iNOS protein expression in LPS-treated microglial cell. BV2 microglial cells were treated with the *Rhodiola rosea* constituents (1, 10, 50 μg/mL) 30 min prior to activation by 100 ng/mL LPS. The protein was collected after 18 h. The iNOS protein levels were measured using immunoblot analysis. *R. rosea* active components suppressed the LPS-induced expression of iNOS protein in activated microglia. Results are representative of three independent experiments. Data were analyzed by one-way ANOVA for multiple comparison and Student-Newman-Keuls test as post hoc test. $^{\#}P < 0.01$ as compared with the vehicle group; $^{*}P < 0.05$ as compared with the LPS treated group.

X-100, and protease inhibitors, pH 8.0), and cellular debris was cleared by centrifugation. Samples were assayed for protein concentration using bicinchoninic acid reagents (Pierce Chemical, Rockford, IL, USA). The supernatants were aliquoted and stored at −70°C until use. Proteins were separated by SDS-polyacrylamide gel electrophoresis and transferred to a polyvinylidene difluoride membrane. The membrane was blocked with 5% skim milk in Tris-buffered saline/Tween 20 solution. The blots were incubated with the TNF-α, IL-6, and iNOS (Cell Signaling Technology Inc., Danvers, MA, USA). GAPDH (Santa Cruz Biotechnology, Inc., Santa Cruz, CA, USA) was performed as an internal control. After washing with Tris-buffered saline/Tween 20, horseradish peroxidase-conjugated secondary antibodies (Cell Signaling Technology Inc. Danvers, MA, USA) were applied, and the blots were developed using the enhanced chemiluminescence detection kit (GE Healthcare, Chalfont St. Giles, Buckinghamshire, UK).

2.5. Animals. All the experiments were carried out using male ICR mice weighing 28–30 g purchased from the Orient Co., Ltd. (Seoul, Republic of Korea), according to the guidelines of the Animal Care and Use Committee of the School of Medicine, Ewha Womans University in Seoul, Republic of Korea. The mice were housed 6 or 8 per cage, allowed access to water and food *ad libitum*, and maintained at an ambient temperature of 23°C with 40–50% humidity and a 12 h diurnal light cycle (light on 07:00–19:00). Seven-week-old ICR male mice were injected with saline or LPS from *Escherichia coli* (0111:B4, Sigma-Aldrich, St. Louis, MO, 1 mg/kg). LPS was dissolved in saline and injected intraperitoneally. *R. rosea* crude extract (500 mg/kg) was administered orally 1 h before LPS injection. Control animals were injected with equivalent volumes of saline. The tissue was collected from mice after 6 h of kidney and 16 h for frontal cortex of brain LPS injection, and changes of proinflammatory cytokine expression were measured by PCR.

2.6. Mixed Cortical Culture. After CO_2 anesthesia, cerebral cortices were removed from the brains of 16-day-old ICR fetal mice. The neocortices were triturated and plated on 24-well plates (with approximately 1×10^6 cells/well), which were precoated with 100 μg/mL poly-D-lysine and 4 μg/mL laminin in modified Eagle's medium (MEM) and supplemented with 5% horse serum, 5% fetal bovine serum (FBS), 2 mM glutamine, and 20 mM glucose. After 6 days in vitro (DIV), the cultures were shifted to the plating media containing 10 μM cytosine arabinoside without FBS. The cultures were then fed twice per week. After 12 to 13 days, more than 90% of neurons were MAP2-positive to immunocytochemical staining and sat on the top of a confluent monolayer of astrocytes. Mixed cortical cell cultures containing neurons and glia (DIV 12–14) were exposed to the excitatory amino acid, L-glutamate, in MEM without 10% horse serum for 24 h to measure the condition of the cells.

2.7. Measurement of Neurotoxicity. Cell death was assessed by measuring the activity of lactate dehydrogenase (LDH) released in the culture medium according to the method described by Koh and Choi [26]. Culture medium collected after 18 to 24 h drug treatment was used unless otherwise indicated. An aliquot of 25 μL of culture medium was transferred to a microplate, and 100 μL of NADH solution (0.3 mg/mL NADH and 0.1 M potassium phosphate, pH 7.4) was added to the medium. After 2 min, 25 μL of pyruvate solution (22.7 mM pyruvate and 0.1 M potassium phosphate,

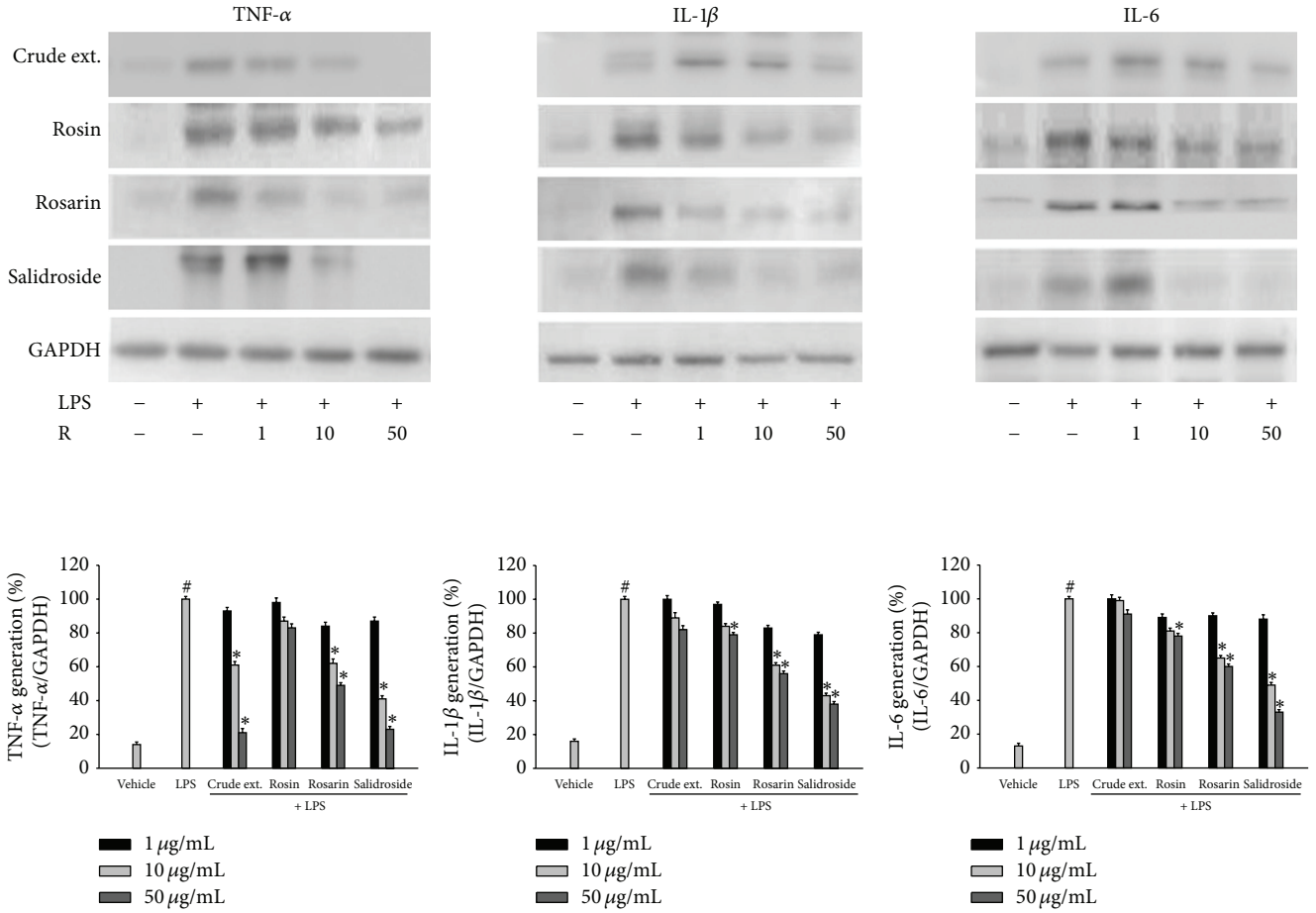

Figure 4: Effects of *R. rosea* constituents on the LPS-induced expressions of TNF-α, IL-1β, and IL-6 in microglial cells. BV2 microglial cells were treated with the *Rhodiola rosea* constituents (1, 10, 50 μg/mL) 30 min prior to activation by 100 ng/mL LPS for 18 h. Cell extracts were collected from cultured microglia after activation by LPS with treatment of *R. rosea* constituents, and immunoblot analysis was performed using TNF-α, IL-1β, and IL-6. *R. rosea* suppressed the expression of TNF-α, IL-1β, and IL-6 in activated microglia, respectively. GAPDH was used as an internal control. Results are representative of three independent experiments. Data were analyzed by one-way ANOVA for multiple comparison and Student-Newman-Keuls test as post hoc test. $^{\#}P < 0.01$ as compared with the vehicle group; $^{*}P < 0.05$ as compared with the LPS treated group.

pH 7.4) was added. After adding the pyruvate solution, the decrease in absorbance at 340 nm, indicating the conversion of NADH to NAD, was measured using a SpectraMax microplate reader (Molecular Devices, Sunnyvale, CA, USA). LDH activity was normalized on the basis of the reference scale such that the sham-treated culture and culture showing complete cell death were taken as 0 and 100%, respectively, and normalized LDH activity was regarded as an indicator of cell death.

2.8. Polymerase Chain Reaction. ICR mice were administered with LPS in the absence or presence of crude extract of *R. rosea* for 6 h or 16 h. Total RNA was isolated from kidney or prefrontal cortex of brain of ICR mice using TRIzol (Invitrogen, CA, USA) according to the manufacturer's instructions. For cDNA synthesis, 2 μg of total RNA was reverse-transcribed using the SuperScript First-Strand Synthesis System (Invitrogen, CA, USA). cDNA was amplified by polymerase chain reaction (PCR) using primers for iNOS (F: GTGTTCCACCAGGAGATGTTG, R: CTCCTGCCCACTGAGTTCGTC), IL-1β (F: AGCAACGACAAAATACCTGT, R: CAGTCCAGCCCATACTTTAG), and IL-6 (F: CCACTTCACAAGTCGGAGGC, R: CCAGCTTATCTGTTAGGAGA). Thermal cycling conditions included initial denaturation at 95°C for 2 min, followed by 30 cycles of 1 min at 95°C, 1 min at 56°C and 30 s at 72°C, and then a dissociation step. PCR products were separated by 1% agarose gel electrophoresis and visualized by ethidium bromide staining.

2.9. Statistical Analysis. All values were expressed as mean ± S.E.M., and comparisons between groups were performed using analysis of variance followed by the Student-Newman-Keuls test for multiple comparisons. The results are representative of three independent experiments done. Differences with $P < 0.05$ and $P < 0.01$ were considered as statistically significant.

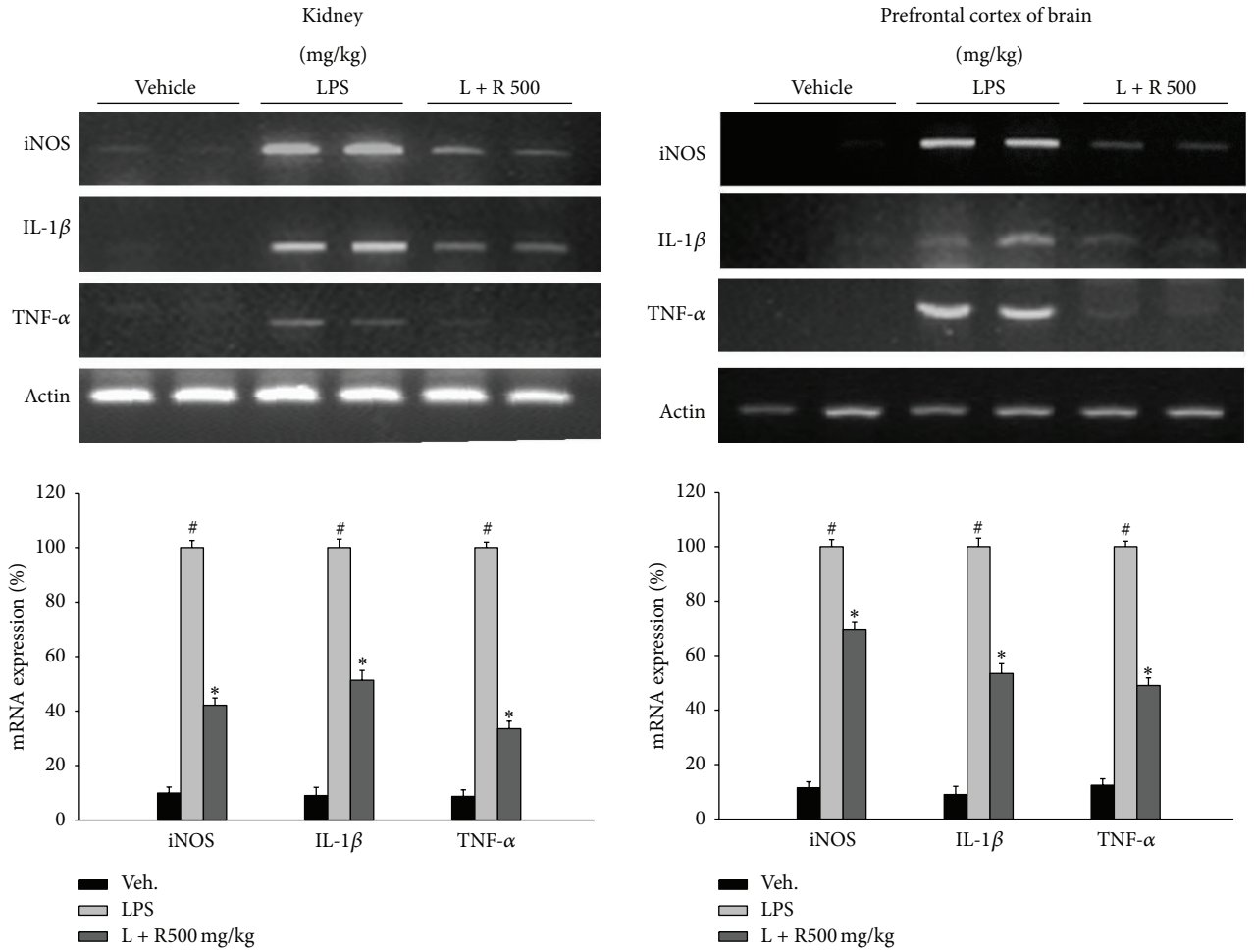

Figure 5: Effects of *R. rosea* extract on cytokines mRNA expression in LPS-treated mice. ICR mice were orally administered with the *R. rosea* extract (500 mg/kg); 30 min later mice were injected (i.p.) by 1 mg/kg LPS. Expressions of iNOS, IL-1β, and TNF-α were measured by PCR analysis at 6 h or 16 h after LPS treatment. *R. rosea* extract suppressed the expression of iNOS, IL-1β, and TNF-α in mice 6 h later for kidney and 16 h later for prefrontal cortex of brain. β-actin was used as an internal control. All values are expressed as mean ± S.E.M. from three independent experiments. Data were analyzed by one-way ANOVA for multiple comparisons and Student-Newman-Keuls test as post hoc test. $^{\#}P < 0.01$ as compared with the vehicle group; $^{*}P < 0.05$ as compared with the LPS injected group.

3. Results

3.1. Rhodiola rosea Constituents Suppressed the LPS-Induced NO Generation and iNOS Expression in Microglia. To investigate the anti-inflammatory effect of *R. rosea* constituents, the LPS-induced production of NO was measured in the presence or absence of constituents of *R. rosea* in BV2 microglial cells. Microglial cells were treated with *R. rosea* constituents 30 min prior to the LPS treatment for 18 h. The constituents, rosarin and salidroside, suppressed the generation of NO in activated microglia in a dose-dependent manner (Figure 2). These findings suggest that *R. rosea* constituents may suppress the LPS-induced inflammatory response through the inhibition of NO generation. The expression of iNOS protein was highly induced by LPS, and this expression was inhibited by rosarin and salidroside as did in NO generation (Figure 3). These results implied that suppression of NO generation by *R. rosea* might be due to the inhibition of iNOS protein expression by components of *R. rosea*.

3.2. Rhodiola rosea Constituents Reduced the LPS-Induced Expression of Proinflammatory Cytokines. Constituents of *R. rosea* exerted an anti-inflammatory effect on LPS-induced responses accompanied by the expression of proinflammatory cytokines. Microglial cells were treated with constituents of *R. rosea* and LPS for 18 h. The expression levels of the proinflammatory cytokines, TNF-α, IL-1β, and IL-6 were reduced by the treatment with constituents of *R. rosea* in dose-dependent manners (Figure 4). The crude extract of *R. rosea* showed suppressing activity to the LPS-induced TNF-α expression but did not inhibit the IL-1β or IL-6 expression. These results indicated that constituents of *R. rosea* (rosin, rosarin, and salidroside) showed the suppression of LPS-induced expression of proinflammatory cytokines in microglia.

3.3. Rhodiola rosea Extract Reduced the LPS-Induced Elevation of Proinflammatory Cytokine Expression in Mice. The *R. rosea*

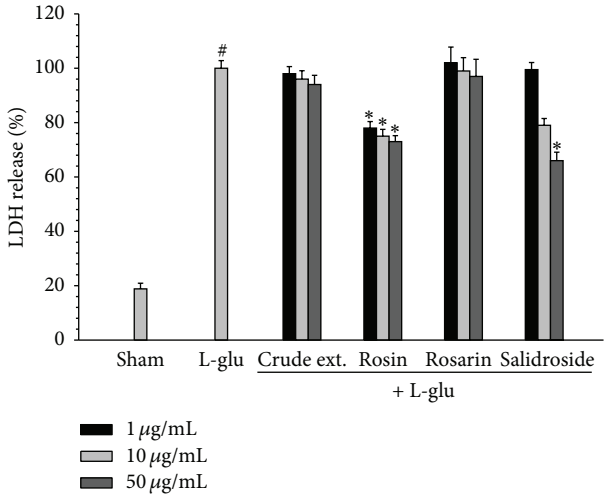

Figure 6: Effects of *R. rosea* constituents on L-glutamate toxicity in cultured cortical cells. Neurons were treated by *R. rosea* constituents (1, 10, 50 μg/mL) with L-glu (60 μM) for 18 h. Neuronal toxicity was measured by using LDH assay. Data were analyzed by one-way ANOVA for multiple comparisons and Student-Newman-Keuls test as post hoc test. All values are expressed as mean ± S.E.M. from three independent experiments. $^{\#}P < 0.01$ as compared with the vehicle group; $^{*}P < 0.05$ as compared with the L-glu-treated group.

extracts exerted an anti-inflammatory effect on LPS-induced responses accompanied by the expression of proinflammatory cytokines in mice. Kidney and brain prefrontal cortex of ICR mice were collected after 6 h (kidney) or 16 h (brain) of oral administration of *R. rosea* extract (500 mg/kg) and LPS treatment. The mRNA expression levels of the iNOS, IL-1β, and TNF-α were reduced by treatment with *R. rosea* extracts (Figure 5). These results indicated that *R. rosea* extracts have an anti-inflammatory effect on the expression of LPS-induced proinflammatory cytokines in mice centrally and peripherally.

3.4. Rhodiola rosea Constituents Suppressed the L-Glu-Induced Neurotoxicity in Primary Cortical Neurons. To investigate the antineurotoxic effect of constituents of *R. rosea*, the L-glutamate-induced neurotoxicity was measured after treating cortical neuronal cells with L-glutamate (60 μM) in the presence of *R. rosea* constituents for 18 h. The neuronal toxicity was measured by using LDH assay. The neuroprotective effects of constituents of *R. rosea*, rosin and salidroside, were evidenced by the significant decrease of LDH release (Figure 6).

3.5. Rhodiola rosea Constituents Reduced the L-Glu-Induced Expression of MAPK in Primary Cortical Neurons. *R. rosea* exerted an antineurotoxicity effect by the suppression of MAPK. Primary cortical neuronal cells were treated with constituents of *R. rosea* and L-glu for 18 h. The elevated levels of the pJNK and pp38 were reduced by crude extract and constituents of *R. rosea*, rosin and salidroside, in a dose-dependent manner (Figure 7). These results indicated that rosin and salidroside had an antineurotoxic effect on the suppression of L-glu-induced MAPK expression in primary cortical neurons.

4. Discussion

Over the past few decades, many researchers have attempted to develop antineurotoxic agents that are capable of preventing the release of glutamate [27], activation of microglia [28], oxidative stress [29], and apoptosis [30]. Therefore, we also searched for active natural products with better neuroprotective effects and fewer side effects. The main purpose of this study was to determine the anti-inflammatory and neuroprotective effects of *R. rosea* constituents in microglial and neuronal cells.

The functional characteristics of microglia have received increasing attention, as these cells play a key role in the inflammatory reaction [31, 32]. Activation of microglia occurred during the development of neurodegenerative pathologies such as Alzheimer's and Parkinson's diseases [33]. In vivo studies also proved that activated microglia produce large amounts of reactive oxygen species (ROS), nitric oxide (NO), and proinflammatory cytokines such as TNF-α, interleukin-1β (IL-1β), and interleukin-6 (IL-6), which, in turn, cause neuronal damage [34–36]. Therefore, treatment with anti-inflammatory drugs can appear to be the most promising option for neurodegenerative disease like Alzheimer's disease. Since nitric oxide is one of the main inflammatory mediators and plays an important role in neuroinflammatory disease, the effect of the *R. rosea* constituents on the NO production was investigated in LPS-stimulated microglial cells. The present study also suggested that *R. rosea* constituents strongly inhibit NO production and the expression of iNOS, the key enzyme for NO in LPS-stimulated BV2 microglial cells. LPS is a stimulator which is responding to the inflammation to generate TNF-α. Currently, the treatment of inflammation-mediated diseases has been studied to suppress the TNF-α production which is released by LPS-stimulated microglia [37]. In the following studies, the inhibitory effect of constituents of *R. rosea* against TNF-α, IL-1β, and IL-6 was investigated because these cytokines are also known as major proinflammatory mediators in the progress of neuroinflammatory disease. In these studies, constituents of *R. rosea* treatment decreased the production of TNF-α, Il-1β, and IL-6 which are induced by LPS in BV2 microglia cells in a dose-dependent manner. In particular, TNF-α, which may potentiate damage to neuronal cell, is a proinflammatory cytokine and costimulator which is thought to be mediated in the regulation of iNOS gene, predominantly through the mitogen-activated protein kinase (MAPK) and NF-κB signaling pathway [38, 39]. And then regarding the anti-inflammatory role of R. roesa, we determined whether *R. rosea* decreased the proinflammatory cytokine expression in mice. This idea is showing that disruption or attenuation of peripheral organ function is linked to an increased risk for chronic inflammatory disease [40–43]. In the present study, oral administration of *R. rosea* extract significantly decreases iNOS and proinflammatory cytokines responses in not only kidney but also prefrontal cortex of brain. These results suggest that *R. rosea* constituents can be delivered to the brain

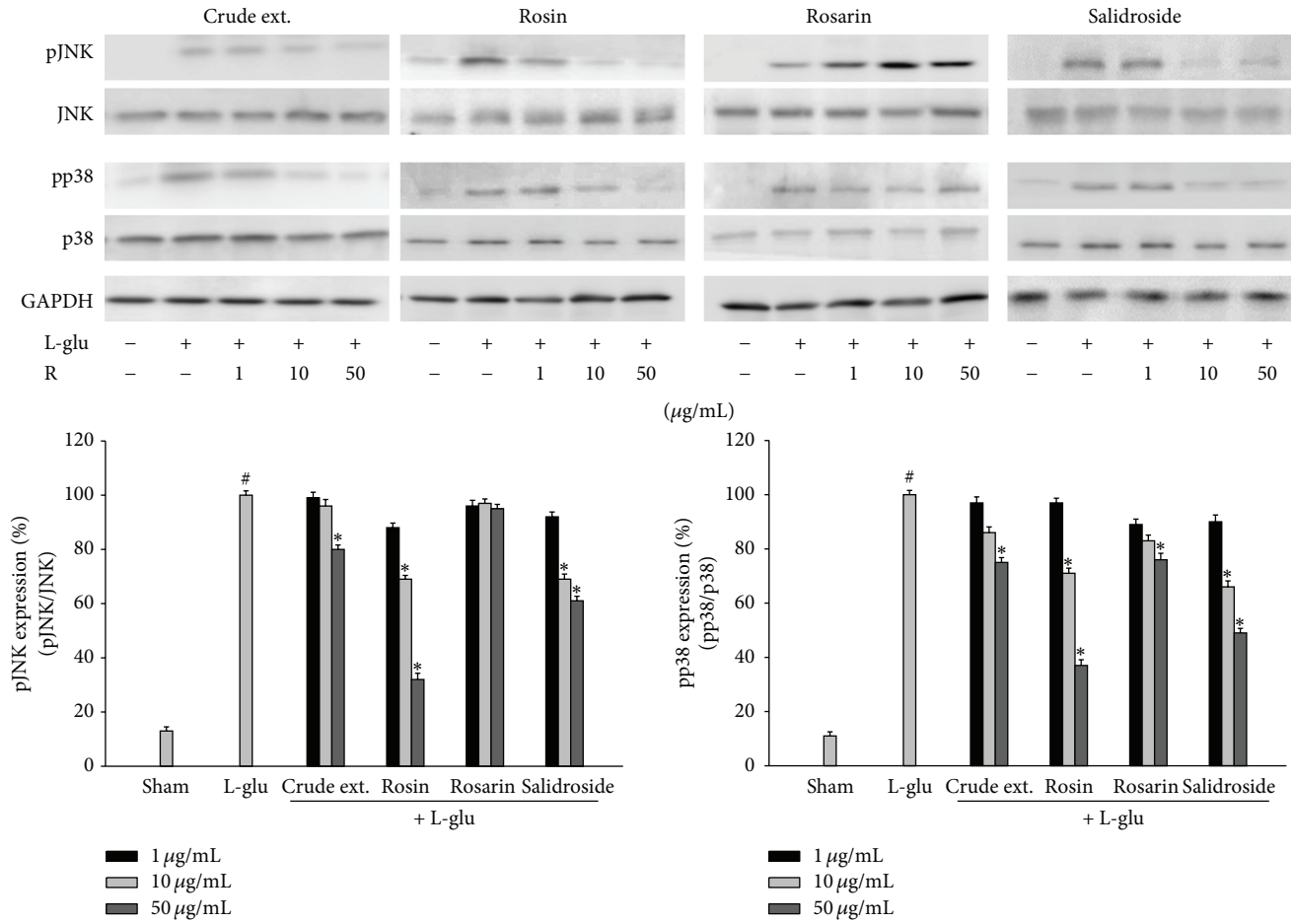

Figure 7: Effects of *R. rosea* constituents on the L-glu-induced expressions of MAPK expression in primary neuronal cells. Primary cortical neuronal cell extracts were collected after activation by L-glu (60 μM) with or without treatment of *R. rosea* constituents for 18 h and immunoblot analysis was performed using phospho- or total JNK, p38 antibodies. GAPDH was used as an internal control. All values are expressed as mean ± S.E.M. from three independent experiments. Data were analyzed by one-way ANOVA for multiple comparison and Student-Newman-Keuls test as post hoc test. $^{\#}P < 0.01$ as compared with the vehicle group; $^{*}P < 0.05$ as compared with the L-glu treated group.

and suppress the inflammation in the CNS. Further experiment of the anti-inflammatory effect of *R. rosea* to determine the signal cascade from TLR-4 which induces a signaling cascade leading to the activation of NF-κB is under investigation.

Alzheimer's disease is a progressive neurodegenerative disease characterized by the presence of two types of abnormal deposits, senile plaques and neurofibrillary tangles, and by extensive neuronal loss [44]. Other studies have suggested the involvement of glutamate cytotoxicity in various neurodegenerative diseases [45] and that amyloid-β increases the vulnerability of cultured cortical neurons to glutamate cytotoxicity [20]. Thus, glutamate may play an important role in amyloid β-induced cytotoxicity in the cerebral cortex. Therefore, we investigated the modulation of signaling pathways in the neurotoxic conditions induced by L-glutamate treatment with *R. rosea*. L-glutamate release and subsequent excitotoxic cell damage has been proposed as a major mechanism producing neuronal cell death in several experimental paradigms of human neurodegenerative disorders [46]. Examination of the intracellular mechanism of neuroprotection against acute L-glu-induced neurotoxicity demonstrated that *R. rosea* treatment protects against L-glu-induced neurotoxicity.

In AD brain, the association between neurotoxicity and MAPK activation has been observed in dystrophic neuritis and astroglial cells [47]. Neurotoxicity is one of the major stimuli for MAPK cascades which are involved in the apoptotic signal transduction. It has been reported that the activation of JNK and p38 MAPK is closely related with cytotoxicity by insults, while the activation of ERK is associated with cell proliferation and serves as an anti-apoptotic signal [48]. In fact, regulators upstream of ERK are distinct from those involved in JNK and p38 activation.

In the present study, *R. rosea* constituents inhibit L-glu-induced JNK and p38 MAPK, but not ERK phosphorylation

(data not shown). Further study on whether L-glu could stimulate a rapid, transient activation of ERK in cortical neuronal cells, and whether *R. rosea* has any effects on expression is now under investigation.

In summary, *R. rosea* constituents could ameliorate the inflammation and neurotoxicity in cortical neuronal cells. The protective effects of *R. rosea* constituents not only were related to modulate endogenous anti-inflammatory, but also affected the neuronal over activation. As far as we know, this is the first report to demonstrate that *R. rosea* has the neuroprotective effects against L-glu-induced neurotoxicity in cortical neuronal cells. The protective effects of *R. rosea* against neurotoxicity may provide the pharmacological basis of its clinical usage in the treatment of neurodegenerative diseases.

Conflict of Interests

The authors declare that they have no conflict of interests.

Acknowledgment

This work was supported by the Korea Research Foundation Grant (MRC, 2010-0029355) funded by the Korean Government (MEST).

References

[1] F. Khanum, A. S. Bawa, and B. Singh, "*Rhodiola rosea*: a versatile adaptogen," *Comprehensive Reviews in Food Science and Food Safety*, vol. 4, no. 3, pp. 55–62, 2005.

[2] V. D. Petkov, D. Yonkov, A. Mosharoff et al., "Effects of alcohol aqueous extract from *Rhodiola rosea* L. roots on learning and memory," *Acta Physiologica et Pharmacologica Bulgarica*, vol. 12, no. 1, pp. 3–16, 1986.

[3] V. A. Kurkin and G. G. Zapesochnaya, "Chemical composition and pharmacological characteristics of *Rhodiola rosea*," *Journal of Medicinal Plants*, vol. 10, pp. 1231–1245, 1985.

[4] I. I. Brekhman and I. V. Dardymov, "New substances of plant origin which increase nonspecific resistance," *Annual Review of Pharmacology*, vol. 9, pp. 419–430, 1969.

[5] A. A. Spasov, G. K. Wikman, V. B. Mandrikov, I. A. Mironova, and V. V. Neumoin, "A double-blind, placebo-controlled pilot study of the stimulating and adaptogenic effect of *Rhodiola rosea* SHR-5 extract on the fatigue of students caused by stress during an examination period with a repeated low-dose regimen," *Phytomedicine*, vol. 7, no. 2, pp. 85–89, 2000.

[6] V. A. Shevtsov, B. I. Zholus, V. I. Shervarly et al., "A randomized trial of two different doses of a SHR-5 *Rhodiola rosea* extract versus placebo and control of capacity for mental work," *Phytomedicine*, vol. 10, no. 2-3, pp. 95–105, 2003.

[7] V. Darbinyan, A. Kteyan, A. Panossian, E. Gabrielian, G. Wikman, and H. Wagner, "*Rhodiola rosea* in stress induced fatigue—a double blind cross-over study of a standardized extract SHR-5 with a repeated low-dose regimen on the mental performance of healthy physicians during night duty," *Phytomedicine*, vol. 7, no. 5, pp. 365–371, 2000.

[8] S. L. Wing, E. W. Askew, M. J. Luetkemeier, D. T. Ryujin, G. H. Kamimori, and C. K. Grissom, "Lack of effect of rhodiola or oxygenated water supplementation on hypoxemia and oxidative stress," *Wilderness and Environmental Medicine*, vol. 14, no. 1, pp. 9–16, 2003.

[9] X. Chen, J. Liu, X. Gu, and F. Ding, "Salidroside attenuates glutamate-induced apoptotic cell death in primary cultured hippocampal neurons of rats," *Brain Research*, vol. 1238, no. C, pp. 189–198, 2008.

[10] M. Abidov, F. Crendal, S. Grachev, R. Seifulla, and T. Ziegenfuss, "Effect of extracts from *Rhodiola rosea* and *Rhodiola crenulata* (Crassulaceae) roots on ATP content in mitochondria of skeletal muscles," *Bulletin of Experimental Biology and Medicine*, vol. 136, no. 6, pp. 585–587, 2003.

[11] K. De Bock, B. O. Eijnde, M. Ramaekers, and P. Hespel, "Acute *Rhodiola rosea* intake can improve endurance exercise performance," *International Journal of Sport Nutrition and Exercise Metabolism*, vol. 14, no. 3, pp. 298–307, 2004.

[12] Y. Murabe and Y. Sano, "Morphological studies on neuroglia. V. Microglial cells in the cerebral cortex of the rat, with special reference to their possible involvement in synaptic function," *Cell and Tissue Research*, vol. 223, no. 3, pp. 493–506, 1982.

[13] H. Akiyama, S. Barger, S. Barnum et al., "Inflammation and Alzheimer's disease," *Neurobiology of Aging*, vol. 21, no. 3, pp. 383–421, 2000.

[14] J. Hu and L. J. Van Eldik, "Glial-derived proteins activate cultured astrocytes and enhance beta amyloid-induced glial activation," *Brain Research*, vol. 842, no. 1, pp. 46–54, 1999.

[15] G. L. Collingridge and R. A. J. Lester, "Excitatory amino acid receptors in the vertebrate central nervous system," *Pharmacological Reviews*, vol. 41, no. 2, pp. 143–210, 1989.

[16] J. W. Olney, O. L. Ho, and V. Rhee, "Cytotoxic effects of acidic and sulphur containing amino acids on the infant mouse central nervous system," *Experimental Brain Research*, vol. 14, no. 1, pp. 61–76, 1971.

[17] D. W. Choi, "Glutamate neurotoxicity and diseases of the nervous system," *Neuron*, vol. 1, no. 8, pp. 623–634, 1988.

[18] B. Meldrum and J. Garthwaite, "Excitatory amino acid neurotoxicity and neurodegenerative disease," *Trends in Pharmacological Sciences*, vol. 11, no. 9, pp. 379–387, 1990.

[19] J. W. Olney, T. DeGubareff, and R. S. Sloviter, ""Epileptic" brain damage in rats induced by sustained electrical stimulation of the perforant path—II. Ultrastructural analysis of acute hippocampal pathology," *Brain Research Bulletin*, vol. 10, no. 5, pp. 699–712, 1983.

[20] Y. J. Koh, L. L. Yang, and C. W. Cotamn, "beta-Amyloid protein increases the vulnerability of cultured cortical neurons to exitotoxic damage," *Brain Research*, vol. 553, no. 2, pp. 315–320, 1990.

[21] W. D. Le, L. V. Colom, W. J. Xie, R. G. Smith, M. Alexianu, and S. H. Appel, "Cell death induced by β-amyloid 1-40 in MES 23.5 hybrid clone: the role of nitric oxide and NMDA-gated channel activation leading to apoptosis," *Brain Research*, vol. 686, no. 1, pp. 49–60, 1995.

[22] H. Sawada, S. Shimohama, Y. Tamura, T. Kawamura, A. Akaike, and J. Kimura, "Methylphenylpyridium ion (MPP+) enhances glutamate-induced cytotoxicity against dopaminergic neurons in cultured rat mesencephalon," *Journal of Neuroscience Research*, vol. 43, no. 1, pp. 55–62, 1996.

[23] F. Bladini, R. H. P. Porter, and J. T. Greenamyre, "Glutamate and Parkinson's disease," *Molecular Neurobiology*, vol. 12, pp. 73–94, 1996.

[24] Z. Ali, F. R. Fronczek, and I. A. Khan, "Phenylalkanoids and monoterpene analogues from the roots of *Rhodiola rosea*," *Planta Medica*, vol. 74, no. 2, pp. 178–181, 2008.

[25] L. C. Green, D. A. Wagner, and J. Glogowski, "Analysis of nitrate, nitrite, and [15N]nitrate in biological fluids," *Analytical Biochemistry*, vol. 126, no. 1, pp. 131–138, 1982.

[26] J. Y. Koh and D. W. Choi, "Quantitative determination of glutamate mediated cortical neuronal injury in cell culture by lactate dehydrogenase efflux assay," *Journal of Neuroscience Methods*, vol. 20, no. 1, pp. 83–90, 1987.

[27] O. Hurtado, M. A. Moro, A. Cárdenas et al., "Neuroprotection afforded by prior citicoline administration in experimental brain ischemia: effects on glutamate transport," *Neurobiology of Disease*, vol. 18, pp. 336–345, 2005.

[28] W. K. Kim, P. G. Jang, M. S. Woo et al., "A new anti-inflammatory agent KL-1037 represses proinflammatory cytokine and inducible nitric oxide synthase (iNOS) gene expression in activated microglia," *Neuropharmacology*, vol. 47, no. 2, pp. 243–252, 2004.

[29] I. G. Gazaryan, I. P. Krasinskaya, B. S. Kristal, and A. M. Brown, "Zinc irreversibly damages major enzymes of energy production and antioxidant defense prior to mitochondrial permeability transition," *Journal of Biological Chemistry*, vol. 282, no. 33, pp. 24373–24380, 2007.

[30] Y. Miao, Q. Xia, Z. Hou, Y. Zheng, H. Pan, and S. Zhu, "Ghrelin protects cortical neuron against focal ischemia/reperfusion in rats," *Biochemical and Biophysical Research Communications*, vol. 359, no. 3, pp. 795–800, 2007.

[31] B. Hauss-Wegrzyniak, P. Dobrzanski, J. D. Stoehr, and G. L. Wenk, "Chronic neuroinflammation in rats reproduces components of the neurobiology of Alzheimer's disease," *Brain Research*, vol. 780, no. 2, pp. 294–303, 1998.

[32] E. Hirsch, V. L. Katanaev, C. Garlanda et al., "Central role for G protein-coupled phosphoinositide 3-kinase γ in inflammation," *Science*, vol. 287, no. 5455, pp. 1049–1052, 2000.

[33] E. G. McGeer and P. L. McGeer, "Brain inflammation in Alzheimer disease and the therapeutic implications," *Current Pharmaceutical Design*, vol. 5, no. 10, pp. 821–836, 1999.

[34] F. González-Scarano and G. Baltuch, "Microglia as mediators of inflammatory and degenerative diseases," *Annual Review of Neuroscience*, vol. 22, pp. 219–240, 1999.

[35] L. Minghetti and G. Levi, "Microglia as effector cells in brain damage and repair: focus on prostanoids and nitric oxide," *Progress in Neurobiology*, vol. 54, no. 1, pp. 99–125, 1998.

[36] K. M. Boje and P. K. Arora, "Microglial-produced nitric oxide and reactive nitrogen oxides mediate neuronal cell death," *Brain Research*, vol. 587, no. 2, pp. 250–256, 1992.

[37] S. Pawate, Q. Shen, F. Fan, and N. R. Bhat, "Redox regulation of glial inflammatory response to lipopolysaccharide and interferonγ," *Journal of Neuroscience Research*, vol. 77, no. 4, pp. 540–551, 2004.

[38] L. Gautron, P. Lafon, M. Chaigniau, G. Tramu, and S. Layé, "Spatiotemporal analysis of signal transducer and activator of transcription 3 activation in rat brain astrocytes and pituitary following peripheral immune challenge," *Neuroscience*, vol. 112, no. 3, pp. 717–729, 2002.

[39] M. B. Marrero, V. J. Venema, H. He, R. B. Caldwell, and R. C. Venema, "Inhibition by the JAK/STAT pathway of IFNγ- and LPS-stimulated nitric oxide synthase induction in vascular smooth muscle cells," *Biochemical and Biophysical Research Communications*, vol. 252, no. 2, pp. 508–512, 1998.

[40] A. Buske-Kirschbaum, A. Geiben, H. Höllig, E. Morschhäuser, and D. Hellhammer, "Altered responsiveness of the hypothalamus-pituitary-adrenal axis and the sympathetic adrenomedullary system to stress in patients with atopic dermatitis," *Journal of Clinical Endocrinology & Metabolism*, vol. 87, no. 9, pp. 4245–4251, 2002.

[41] I. J. Elenkov and G. P. Chrousos, "Stress hormones, proinflammatory and antiinflammatory cytokines, and autoimmunity," *Annals of the New York Academy of Sciences*, vol. 966, pp. 290–303, 2002.

[42] F. Eskandari and E. M. Sternberg, "Neural-immune interactions in health and disease," *Annals of the New York Academy of Sciences*, vol. 966, pp. 20–27, 2002.

[43] C. Heesen, S. M. Gold, I. Huitinga, and J. M. H. M. Reul, "Stress and hypothalamic-pituitary-adrenal axis function in experimental autoimmune encephalomyelitis and multiple sclerosis—a review," *Psychoneuroendocrinology*, vol. 32, no. 6, pp. 604–618, 2007.

[44] M. A. Winker, K. Ritchie, D. Kildea, P. Giannakopoulos, P. R. Hof, and C. Bouras, "Age versus ageing as a cause of dementia," *Lancet*, vol. 346, no. 8988, pp. 1486–1487, 1995.

[45] G. H. Bresnick, "Excitotoxins: a possible new mechanism for the pathogenesis of ischemic retinal damage," *Archives of Ophthalmology*, vol. 107, no. 3, pp. 339–341, 1989.

[46] J. W. Olney, "New insights and new issues in developmental neurotoxicology," *NeuroToxicology*, vol. 23, no. 6, pp. 659–668, 2002.

[47] B. Webster, L. Hansen, A. Adame et al., "Astroglial activation of extracellular-regulated kinase in early stages of Alzheimer disease," *Journal of Neuropathology and Experimental Neurology*, vol. 65, no. 2, pp. 142–151, 2006.

[48] M. R. Junttila, S. P. Li, and J. Westermarck, "Phosphatase-mediated crosstalk between MAPK signaling pathways in the regulation of cell survival," *FASEB Journal*, vol. 22, no. 4, pp. 954–965, 2008.

Hindawi Publishing Corporation
Evidence-Based Complementary and Alternative Medicine
Volume 2013, Article ID 801374, 9 pages
http://dx.doi.org/10.1155/2013/801374

Research Article

A New Type of Biphasic Calcium Phosphate Cement as a Gentamicin Carrier for Osteomyelitis

Wen-Yu Su,[1,2,3] Yu-Chun Chen,[1,2] and Feng-Huei Lin[1,2]

[1] *Division of Medical Engineering Research, National Health Research Institutes, Miaoli county 350, Taiwan*
[2] *Institute of Biomedical Engineering, National Taiwan University, Taipei 100, Taiwan*
[3] *Institute of Biomedical Engineering and Material Science, Central Taiwan University of Science and Technology, Taichung 406, Taiwan*

Correspondence should be addressed to Feng-Huei Lin; double@ntu.edu.tw

Received 2 January 2013; Accepted 8 February 2013

Academic Editor: Yueh-Sheng Chen

Osteomyelitis therapy is a long-term and inconvenient procedure for a patient. Antibiotic-loaded bone cements are both a complementary and alternative treatment option to intravenous antibiotic therapy for the treatment of osteomyelitis. In the current study, the biphasic calcium phosphate cement (CPC), called α-TCP/HAP (α-tricalcium phosphate/hydroxyapatite) biphasic cement, was prepared as an antibiotics carrier for osteomyelitis. The developed biphasic cement with a microstructure of α-TCP surrounding the HAP has a fast setting time which will fulfill the clinical demand. The X-ray diffraction and Fourier transform infrared spectrometry analyses showed the final phase to be HAP, the basic bone mineral, after setting for a period of time. Scanning electron microscopy revealed a porous structure with particle sizes of a few micrometers. The addition of gentamicin in α-TCP/HAP would delay the transition of α-TCP but would not change the final-phase HAP. The gentamicin-loaded α-TCP/HAP supplies high doses of the antibiotic during the initial 24 hours when they are soaked in phosphate buffer solution (PBS). Thereafter, a slower drug release is produced, supplying minimum inhibitory concentration until the end of the experiment (30 days). Studies of growth inhibition of *Staphylococcus aureus* and *Pseudomonas aeruginosa* in culture indicated that gentamicin released after 30 days from α-TCP/HAP biphasic cement retained antibacterial activity.

1. Introduction

Osteomyelitis is defined as inflammation of bone and marrow cavity [1]. Osteomyelitis causes major morbidity and remains the most feared and difficult infection to treat in orthopedic surgery. In general, it is a protracted commitment to antibiotic therapy for 6~8 weeks. The course of treatment is a long-term and inconvenient procedure for patients. For the treatment of osteomyelitis and prosthesis infection, continuous irrigation and antibiotic-impregnated bone cement beads have become popular because of the resulting higher antibiotic concentration in soft tissue or bone [2, 3].

Various studies have suggested that the local application of antimicrobials clearly provides higher local antibiotic concentrations than those achieved with intravenous application and additionally avoids toxicity with high plasma levels [4, 5]. Antibiotic beads are both a complementary and alternative treatment option to intravenous antibiotic therapy for the treatment of osteomyelitis. Polymethylmethacrylate (PMMA) antibiotic beads were introduced clinically 30 years ago and have been the main local antibiotic delivery system in osteomyelitis therapy until recently [6, 7]. The beads can be impregnated with one or more antibiotics and placed within the wound site at the time of surgery. Ideally, the antibiotics then diffuse out of the beads, maintaining a local concentration above the minimum inhibitory concentration for a period of days or weeks, thereby preventing or diminishing bacterial infection at the site. PMMA beads, however, are associated with some serious disadvantages including uncertain period of antibiotic delivery, as the carrier material is not degradable, and induction of foreign body reaction [8–10].

Recently, much attention has been paid to calcium phosphate cement (CPC) and it has been applied to fractures, filling bone defects, and intensification of bone as bone replacement and augmentation [3, 11]. Calcium phosphate cement, which has a chemical composition close to that of bone, has

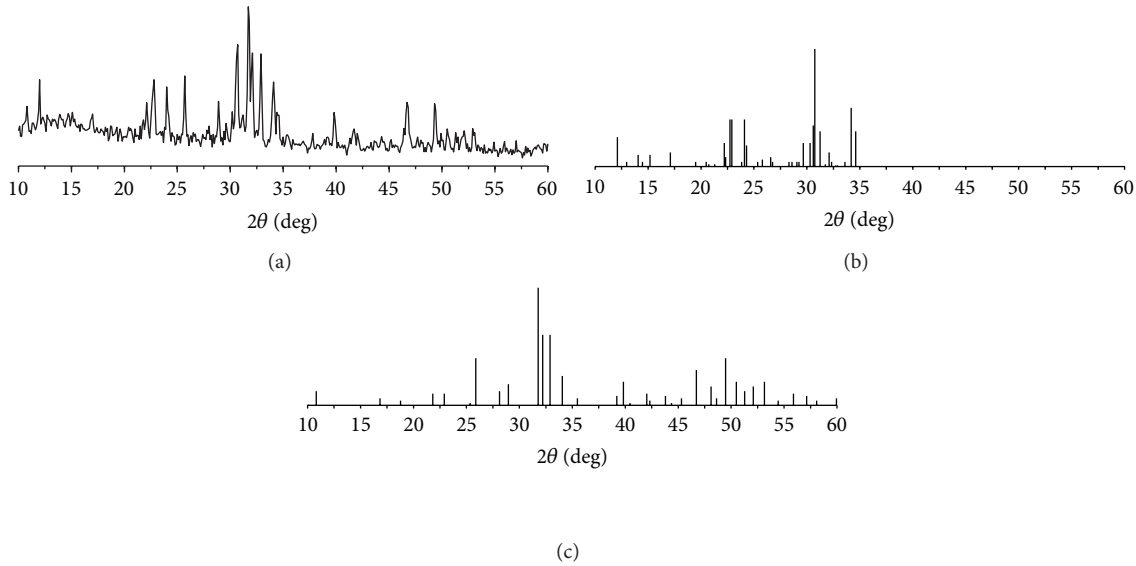

Figure 1: XRD patterns of (a) α-TCP/HAP; (b) JCPDS card 9–348 alpha-TCP; (c) JCPDS card 9–432 HAP.

been extensively explored as bone graft materials [12]. The possibility to use CPCs not only as bone substitutes, but also as carriers for local and controlled release of drugs is very attractive and can be useful in treatments of different skeletal diseases, such as bone tumors, osteoporosis, or osteomyelitis, which normally require long and painful therapies. Several studies have shown that CPC could also be used as a delivery system for therapeutic peptides or antibiotics [13–15]. In general, most of CPCs are composed of one or more calcium phosphates, which upon mixing with a liquid phase, usually water or an aqueous solution, to form a paste, are able to set and harden after being implanted within the body [16–18].

In the present study, we developed a biphasic calcium phosphate cement, which consisted of α-tricalcium phosphate (α-TCP) and hydroxyapatite (HAP). The HAP doped with ammonium hydrogen phosphate [$(NH_4)_2HPO_4$] could partially convert HAP into α-TCP on heating to a temperature up to 1350°C–1450°C. With different concentrations of ammonium hydrogen phosphate addition, we could prepare series of biphasic calcium phosphates in different α-TCP/HAP ratios. The prepared α-TCP/HAP biphasic cement can set in aqueous environment because the α-TCP can be hydrolyzed in water solution and perform segregation. Apatite crystal generated in segregation can interactively set with each other similar to the coagulation of cement.

α-TCP/HAP biphasic cement is a self-setting materials consisting of α-TCP and HAP that can harden completely into a uniform microporous hydroxyapatite when mixed in an aqueous solution. By replacing water with an antibiotic solution, α-TCP/HAP biphasic cement might be a convenient carrier material for local antibiotic delivery. It might be possible to maintain high concentrations of antibiotics within an infected lesion and allow bone formation in a bone defect at the same time. Since the morbidity of chronic osteomyelitis is due in part to bone loss and the need of multiple surgical procedures, using these antibiotic-loaded CPC in the bone-defect-filling manner may potentially minimize the risk of infection and avoid additional surgical procedures.

For this reason, the aim of this study was to investigate α-TCP/HAP biphasic cement as a drug carrier for gentamicin released in the treatment of chronic osteomyelitis. Gentamicin is the primary choice of orthopedic surgeons for local treatment of osteomyelitis [19, 20]. In the current study, the setting properties of gentamicin-loaded α-TCP/HAP biphasic cement were evaluated by X-ray diffraction (XRD), fourier transform infrared (FTIR) spectroscopy, and scanning electron microscope (SEM) observation. The release behavior of gentamicin from α-TCP/HAP was evaluated over a period of 30 days and the efficacy of the released gentamicin was performed in the germ culture of *staphylococcus aureus* and *pseudomonas aeruginosa*.

2. Material and Methods

2.1. Preparation of α-TCP/HAP Biphasic Cement. α-TCP/HAP biphasic cement was prepared by heating a mixture that contains hydroxyapatite (HAP) and ammonium hydrogen phosphate [$(NH_4)_2HPO_4$]. First, we dissolve 2.19 g of $(NH_4)_2HPO_4$ powder in 70 mL distilled water uniformly and then add 40 g of HAP powder into the solution. After stirring, the mixture was dried in an oven at 60°C for 72 hours. The dried mixture was crushed with a mortar and ground into fine powder for the following thermal treatment. The powder mixture was heated to 1350°C at a heating rate of 10°C/min and kept at 1350°C for one hour, and then the powder mixture was quenched to room temperature immediately to obtain the α-TCP/HAP biphasic cement.

2.2. Preparation and Evaluation of Gentamicin-Loaded α-TCP/HAP Biphasic Cement. Gentamicin sulfate powder was

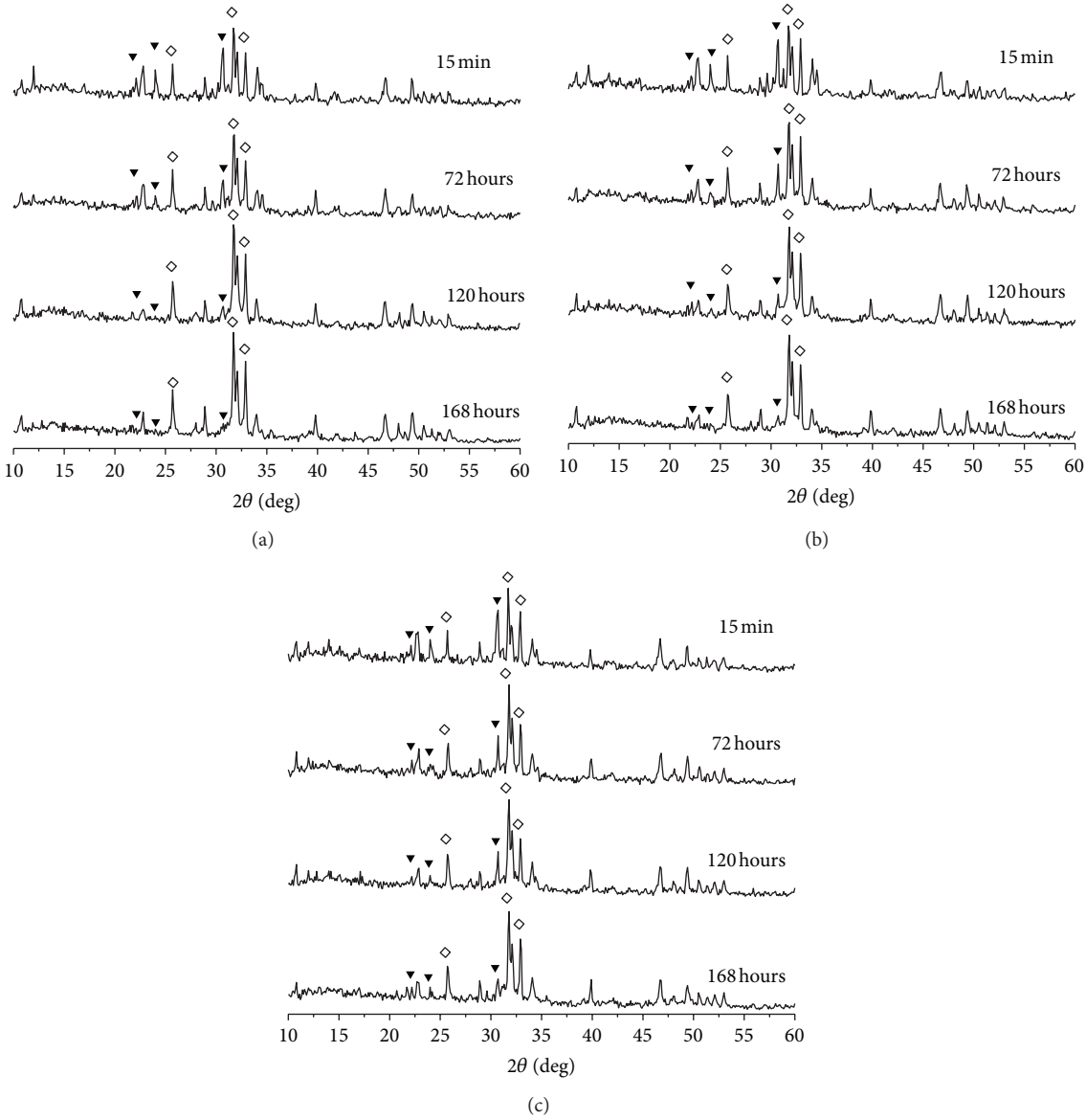

Figure 2: XRD patterns of α-TCP/HAP biphasic cement containing (a) 0 wt%; (b) 4 wt%; (c) 16 wt% gentamicin sulfate immersed in distilled water for 15 minutes, 72 hours, 120, and 168 hours. Peak description: (◊) HAP; (▼) alpha-TCP.

dissolved in distilled water with different concentrations. The gentamicin-loaded α-TCP/HAP biphasic cement was prepared by mixing 0.5 g of α-TCP/HAP biphasic cement powder and 0.1 mL of gentamicin sulfate solution. The mixed cement pastes were kneaded to a cube with a dimension of 5 mm × 5 mm × 5 mm.

In the study, we prepared three different groups of gentamicin-loaded α-TCP/HAP biphasic cements, which were loaded with various concentrations of gentamicin sulfate (0 wt%, 4 wt% and 16 wt%, resp.) respectively. Each group of gentamicin-loaded α-TCP/HAP biphasic cement involved 12 samples, and then the samples were immersed into 10 mL distilled water for 15 min, 2 hr, 4 hr, 8 hr, 16 hr, 24 hr, 48 hr, 72 hr, 96 hr, 120 hr, 144 hr, and 168 hr, respectively. Draw out samples at the end of each period of time, and then immerse them into pure alcohol immediately to stop transferring of α-TCP. After 168 hr, all of the samples were analyzed by scanning electron microscope (SEM), X-ray diffraction (XRD), and fourier transform infrared spectroscopy (FTIR).

2.3. Antibiotic Release Experiments. The gentamicin-loaded α-TCP/HAP biphasic cements were prepared as described previously; four samples (containing 0, 4, 8, and 16 wt% of gentamicin sulfate) were prepared and then immersed in 10 mL of phosphate buffer solution (PBS) at 37°C incubator, respectively. The PBS was changed and collected at regular time interval. The collected PBS was analyzed by UV-VIS spectrometer to measure the concentration of released gentamicin sulfate.

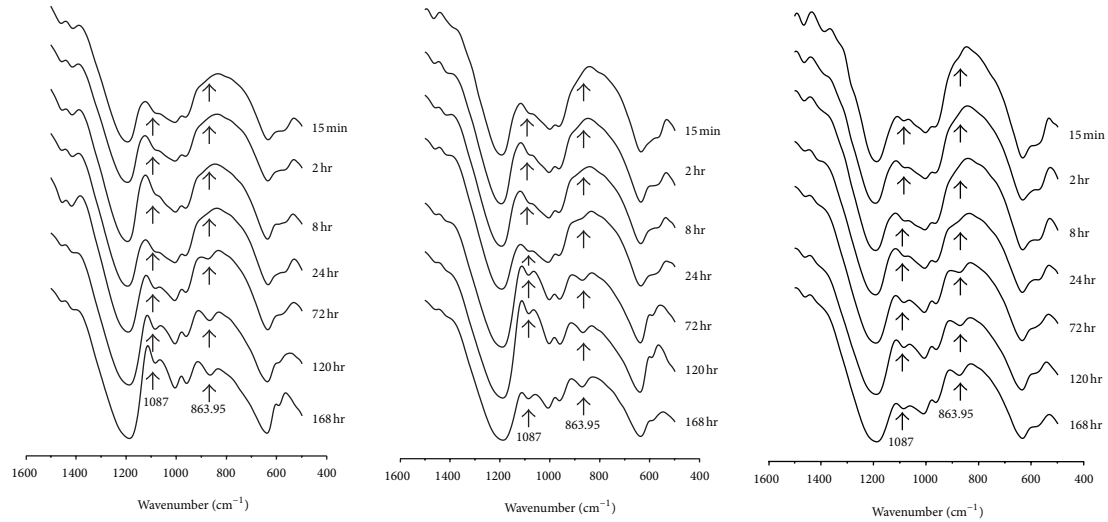

Figure 3: FTIR spectra of α-TCP/HAP biphasic cement containing (a) 0 wt%; (b) 4 wt%; (c) 16 wt% gentamicin sulfate immersed in distilled water for 15 minutes, 72 hours, 120, and 168 hours.

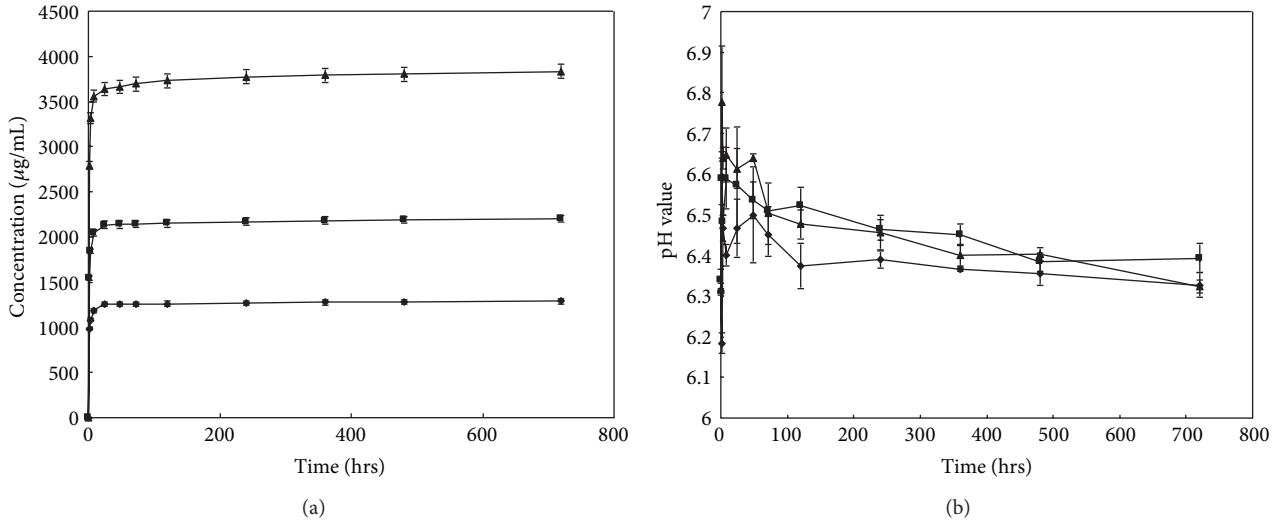

Figure 4: (a) Release curve of gentamicin-loaded α-TCP/HAP biphasic cement containing 4 wt% (⧫), 8 wt% (■), and 16 wt% (▲) of gentamicin sulfate immersed in distilled water for 15 minutes, 72 hours, 120, and 168 hours. (b) pH value of released media of α-TCP/HAP biphasic cement containing 4 wt% (⧫), 8 wt% (■), and 16 wt% (▲) gentamicin sulfate.

2.4. Bacteria Growth Inhibition by GS Released from α-TCP/HAP Biphasic Cements. In order to evaluate the activity of released gentamicin sulfate, two kinds of bacteria, *Staphylococcus aureus* ATCC 29213 and *Pseudomonas aeruginosa* ATCC 27853, were used to culture with the solution collected from antibiotic release experiments (Section 2.3). The Mueller-Hinton Broth and sterile test tubes (13 × 100 mm) were used in the experiments. First, add bacteria into a test tube that contained 2 mL of Mueller-Hinton Broth, and then adjust the concentration of bacteria to 10^7/mL, which was used as coordinated bacteria solution for following experiments. After that, 0.1 mL of the coordinated bacteria solution and 0.5 mL of released gentamicin sulfate solution at each time point (obtained from Section 2.3) were added to sterile test tube that contained 2 mL of Mueller-Hinton Broth. Furthermore, test tubes containing broth and bacteria without released gentamicin sulfate solution were used as control groups. All of these test tubes were incubated in an atmosphere containing 5% CO_2 at 35°C for 18 hours.

3. Results

3.1. Preparation and Characterization of α-TCP/HAP Biphasic Cement. Figure 1(a) shows the XRD patterns of α-TCP/HAP biphasic cements. The JCPDS cards 9–348 (Figure 1(b)) and

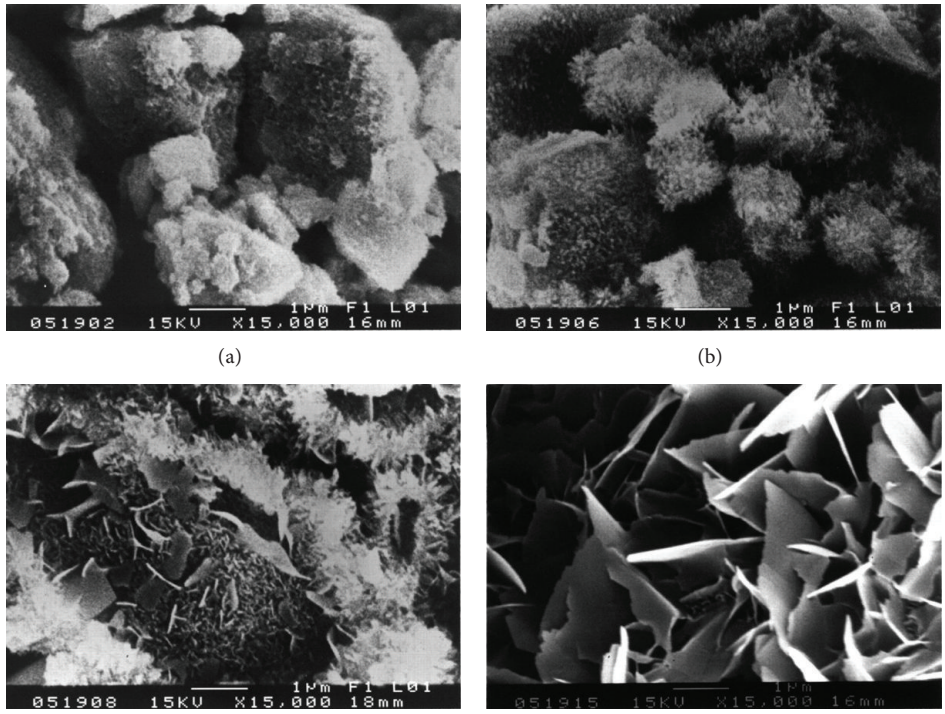

(a) (b) (c) (d)

Figure 5: SEM observation of α-TCP/HAP biphasic cement immersed in distilled water for a period of time of (a) 15 min; (b) 72 hours; (c) 120 hours; (d) 168 hours.

9–432 (Figure 1(c)) are the standard diffraction pattern of α-TCP and HAP, respectively. The major diffraction peak of HAP at $2\theta = 30.6^{\circ}$ and α-TCP at $2\theta = 31.8^{\circ}$ could be observed in XRD pattern of α-TCP/HAP biphasic cements, which means the end product of thermal treatment consisted of HAP and α-TCP.

3.2. Preparation and Evaluation of Gentamicin-Loaded α-TCP/HAP Biphasic Cement. The effects of adding gentamicin sulfate on the transition of α-TCP are shown in Figure 2. Figure 2(a) shows the XRD patterns of α-TCP/HAP biphasic cements without gentamicin sulfate obtained from different setting time points. At $t = 15$ min, the peaks of α-TCP and HAP can be observed clearly. As the soaking time increased, the α-TCP peak intensities decreased and HAP peaks intensity increased. Finally, the α-TCP peaks almost disappear at $t = 168$ hours. Figures 2(b) and 2(c) show that the XRD patterns of α-TCP/HAP biphasic cements contained 4% and 16% gentamicin sulfate obtained from different setting time points. The diffraction peaks of α-TCP still could be observed even after being immersed in distilled water for 168 hours, which means the phase transition of α-TCP is not completed.

AS we know, α-TCP would be gradually converted into apatite in aqueous solution as immersed time increased. However, from the XRD patterns we cannot distinguish HAP from d-HAP. It is known that the deficient HAP has the same crystal structure as HAP, which can be presented by a formula: (d-HAP, $Ca_{10-X}(HPO_4)_X(PO_4)_{6-X}(OH)_{2-X}$). In order to confirm the formation of d-HAP in the CPC system, FTIR analysis was needed. Figure 3 shows the FTIR spectra of the α-TCP/HAP biphasic cements without/with gentamicin sulfate obtained at different setting times. As the soaking time increased, the HPO_4^- band at 865 cm^{-1} was observed and increased in all the spectra of α-TCP/HAP biphasic cement with/without gentamicin sulfate; it indicated that the calcium-deficient hydroxyapatite could be formed by the transition of α-TCP.

3.3. Antibiotic Release Experiments. Figure 4(a) shows the drug release behavior of α-TCP/HAP biphasic cement containing various amounts (4 wt%, 8 wt%, and 16 wt%) of gentamicin sulfate. The drug delivery system showed two-stage release curve. Firstly, gentamicin sulfate was released rapidly from the cement at the initial stage within 24 hours. Secondly, after 24 hours the sustained release of gentamicin sulfate could be observed for 30 days. At the end of release experiments conducted with 4 wt%, 8 wt%, and 16 wt% gentamicin sulfate, the concentrations in the release medium are 7.11 ± 1.01, 12.76 ± 1.03, and 28.76 ± 1.56 μg/mL. The pH value of gentamicin sulfate-released medium was maintained between 6.7 and 6.4 within the release period, as shown in Figure 4(b).

The SEM photos in Figure 5 show the microstructure of the α-TCP/HAP biphasic cement without gentamicin sulfate at different setting time points (15 min, 72 hours, 120 hours, and 168 hours). Small needle-like crystals are occasionally observed on the surface of α-TCP/HAP particles at early time (15 min). At 72 hours, lots of needle-like crystallites

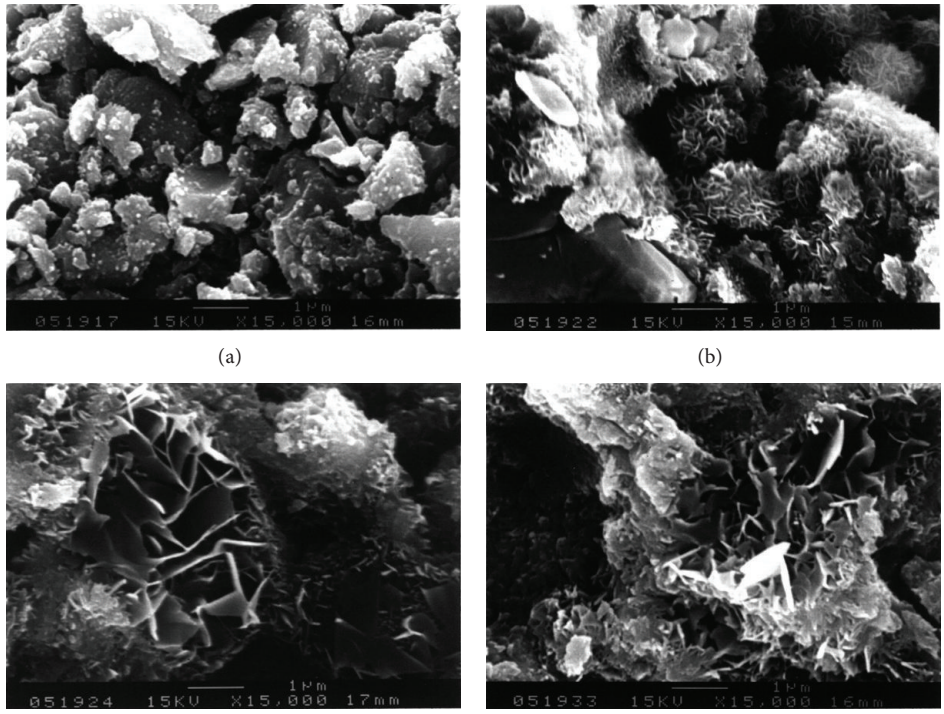

Figure 6: SEM observation of α-TCP/HAP biphasic cement containing 4% gentamicin sulfate which was immersed in distilled water for a period of time of (a) 15 min; (b) 72 hours; (c) 120 hours; (d) 168 hours.

can be observed on the surface of the particles (Figure 5(b)); the crystallites continuously grown and then transformed to plate-like structure after 120 hours, shown in Figure 5(c). Finally, the majority of the α-TCP/HAP particles are covered with plate-like of HAP, and area of petal-like crystals significantly increased as the soaking time increased. The microstructures of the cement with different concentrations (4 wt% and 16 wt%) of gentamicin sulfate are showed in Figures 6 and 7, respectively. The similar results were observed when adding various concentration of gentamicin sulfate into cement. However, compared with Figures 5(d), 6(d), and 7(d), the addition of gentamicin sulfate might lead to a thinner and smaller average crystal size.

3.4. Bacteria Growth Inhibition by GS Released from α-TCP/HAP Biphasic Cements. Figure 8 shows some representative digital pictures of the released gentamicin sulfate solution cultured with *Staphylococcus aureus* ATCC 29213 and *Pseudomonas aeruginosa* ATCC 27853 in Mueller-Hinton Broth. The released gentamicin sulfate solutions were collected from the previous release experiments and then used for bacteria growth inhibition experiments. At the end of release experiments (30 days) conducted with 4 wt%, 8 wt%, and 16 wt% gentamicin sulfate, the concentrations in the release medium are 7.11 ± 1.01, 12.76 ± 1.03, and 28.76 ± 1.56 μg/mL, respectively. The antibacterial efficacy was evaluated by the clarity of solution; the turbid solution indicated the bacterial growth. In these photos, the left test tube was a control group that did not contain released gentamicin sulfate, and the right test tube contained the released gentamicin sulfate at different time points. It is easy to distinguish the clarity from the line behind test tubes, and it indicated that the released gentamicin sulfate at each time point could inhibit bacteria growth significantly. According to the results of germ culture, the antibiotic-loaded α-TCP/HAP biphasic cement could release effective concentration of gentamicin sulfate to inhibit the growth both of *Staphylococcus aureus* and *Pseudomonas aeruginosa* for 30 days.

4. Discussion

When treating osteomyelitis and prosthesis infection, it is often difficult to cure them by antibiotics administered systemically. Usually, osteomyelitis treatment requires prolonged antibiotic therapy, with a course lasting a matter of weeks or months. Further, there is a need of high parenteral dose of antibiotic to achieve effective therapeutic drug concentrations in the infected bone [1]. Therefore, antibiotic-loaded bone cements have become a complementary treatment because of the resulting higher antibiotic concentration in the infected area [2, 5, 8, 20]. Calcium phosphate cement has been used for bone replacement and augmentation because of good biocompatibility and osteoconductivity. There have been some studies about the efficacy and release of antibiotic-impregnated bone cement [21–24]. The present study showed the efficacy of α-TCP/HAP biphasic cement as a biocompatible carrier material that allows prolonged release of antibiotics, gentamicin sulfate.

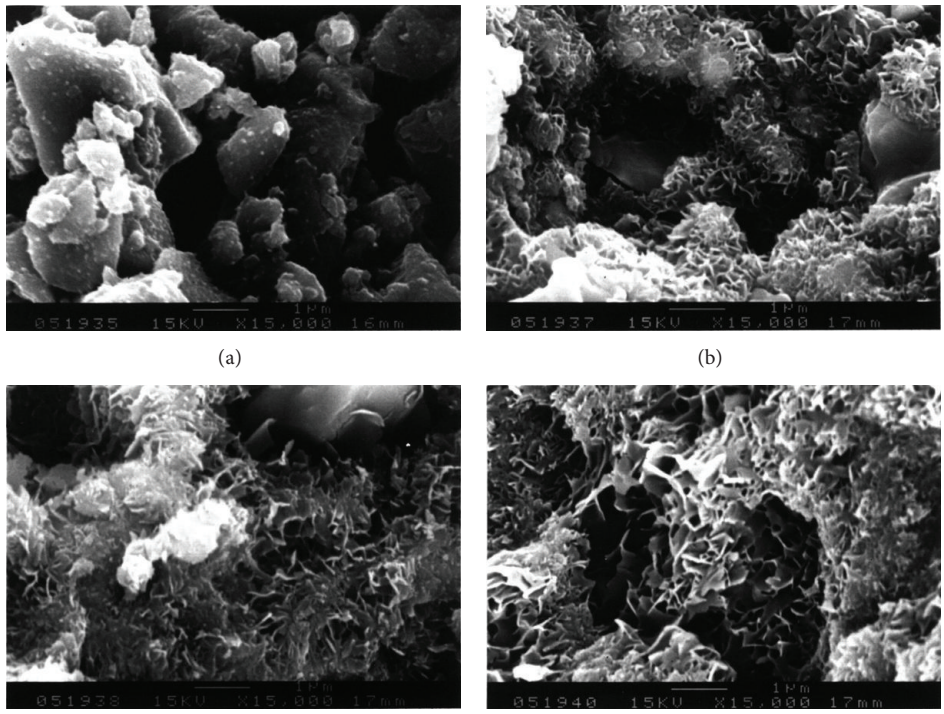

Figure 7: SEM observation of α-TCP/HAP biphasic cement containing 16% gentamicin sulfate which was immersed in distilled water for a period of time of (a) 15 min; (b) 72 hours; (c) 120 hours; (d) 168 hours.

Calcium phosphate cements have the significant advantage of setting at ambient temperatures, which means that antibiotics can be incorporated into the matrices during preparation.

The significant effect of gentamicin sulfate on the setting properties of the α-TCP/HAP biphasic cement is to obstruct the phase transformation of α-TCP to HAP. The addition of gentamicin sulfate led to a thinner and smaller precipitate grain size (Figures 5, 6, and 7) because sulfate ions might create more nucleation sites and block the crystal growth [25]. Comparing between Figures 5(a), 6(a), and 7(a), it can be observed that there is a large amount of needle-like d-HAP in Figure 5(a), but it could not be observed that there are conspicuous needle-like precipitates in Figures 6(a) and 7(a). Furthermore, comparing between Figures 5(d), 6(d), and 7(d), the average crystal size in Figure 5(d) was larger than that in Figures 6(d) and 7(d). This phenomenon conjectured that due to the higher concentration of sulfate, the sulfate ions would be the nucleation sites when α-TCP hydrolyzed and crystallized in aqueous solution. On the other hand, the large molecular structure of gentamicin sulfate may also be obstacles in the process of grain growth.

The release curves of different concentrations of gentamicin sulfate in this study are similar in shape, suggesting that the drug release was controlled by diffusion through the interconnected porous structure of the cement. The release behavior of this drug delivery system showed two-stage release; initial stage and sustained stage, respectively. In initial stage, it showed bursting release, the high concentration of released gentamicin sulfate conjectured that due to the adsorbent gentamicin sulfate near the surface of cement. Furthermore, the cement did not form enough needle-like or plate-like structure to block the release of gentamicin in initial stage. So, a large amount of gentamicin sulfate was released in this stage. In fact, bursting release is an advantage for the treatment of osteomyelitis. The effectiveness of antibiotic delivery systems for the local prevention of bacterial infections related to orthopedic implants is strongly dependent on the drug release profile. Since the concentration of bacteria was very high at local in early infection, it is needed to maintain a high local concentration of antibiotic to inhibit bacteria. In sustained stage, the release rate became slower due to the formation of needle-like and plate-like structure. The therapeutic concentration of GS is ≥ 4 μg/mL for sensitive microorganisms and ≥ 8 μg/mL for more-resistant microorganisms [26]. At the end of release experiments (30 days) conducted with 4 wt%, 8 wt%, and 16 wt% gentamicin sulfate, the concentrations in the release medium are 7.11 ± 1.01, 12.76 ± 1.03, and 28.76 ± 1.56 μg/mL, respectively. According to the result of our study, the amount of released gentamicin sulfate collected from the three groups (α-TCP/HAP biphasic cement containing 4%, 8%, and 16% gentamicin sulfate) in vitro clearly exceeded the minimum inhibitory concentration for *Staphylococcus aureus* and *Pseudomonas aeruginosa*. Many species of organisms, such as *Staphylococcus*, *Enterobacteriaceae,* and *Pseudomonas* species, have been implicated in the etiology of osteomyelitis, with *Staphylococcus aureus* being the most commonly isolated organism. The antibacterial experiments further confirm the activity and

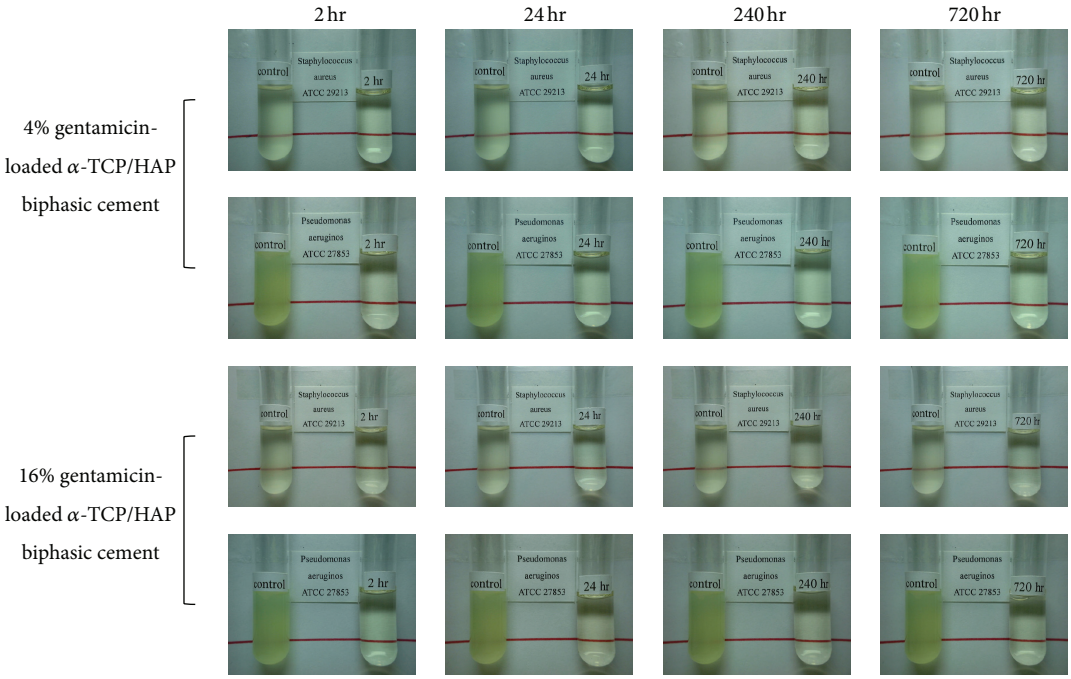

Figure 8: Antibacterial experiments of gentamicin-loaded α-TCP/HAP biphasic cement. The left test tube was control group that did not contain released gentamicin sulfate, and the right test tube contained various period of time of released gentamicin sulfate. At the end of release experiments (30 days) conducted with 4 wt%, 8 wt% and 16 wt% gentamicin sulfate, the concentration in the release medium are 7.11 ± 1.01, 12.76 ± 1.03 and 28.76 ± 1.56 μg/mL, respectively. The gentamicin loaded α-TCP/HAP biphasic cement can release effective concentration of gentamicin sulfate to inhibit the growth both of *staphylococcus aureus* and *pseudomonas aeruginosa* for 30 days.

efficacy of released gentamicin sulfate at regular time interval (Figure 8).

Most antibiotics, except for aminoglycosides such as gentamicin and tobramycin, are heat labile. The characteristics of calcium phosphate cement are a high release rate of antibiotics and no heating during the setting process. Many antibiotics have been shown to maintain efficacy when mixed with bone cement [11, 14, 15, 21–24]. The requirements of such antibiotics are that they are heat stable and hydrophilic. Release of the antibiotic in such bone cement systems depends on the rate of dissolution of drug in its matrix allowing its penetration through the porous structure of the carrier. The most commonly used antibiotics include gentamicin, tobramycin, and vancomycin. Gentamicin remains the most effective antibiotic to incorporate with bone cement due to its high solubility, heat stability, and bactericidal activity at low concentration [20]. Vancomycin and tobramycin are both water-soluble and available in powder form. Mixing of more than one antibiotic into bone cement has been shown to have a synergistic effect [27, 28]. The combination of different antibiotics can increase the antimicrobial spectrum, and also it would potentially lead to increased concentrations of antibiotics in the local area. The combination of antibiotics is supposed not only to be more powerful, but also to prevent the emergency of resistant strains through the synergistic action of two antibiotics at the same time [29].

Prevention of osteomyelitis and its treatment are still a challenge not only to the veterinary orthopedic surgery but also to the human subjects. Low systemic toxicity and high local antibiotic concentrations are the major advantages of local antibiotic delivery system. Furthermore, there is a possibility that CPC allows bone formation in a bone defect caused by infection because CPC has a character of bone replacement and augmentation.

5. Conclusion

The use of α-TCP/HAP biphasic cement as a drug delivery system for gentamicin sulfate appears to be very promising because gentamicin sulfate could be sustainably released for at least 30 days and the biological activity of gentamicin sulfate was preserved when mixed with the α-TCP/HAP biphasic cement. For clinical application, gentamicin-loaded α-TCP/HAP biphasic cement may be able to maintain a high local concentration of gentamicin sulfate, which was beneficial to the treatment of osteomyelitis or prosthesis infection.

References

[1] N. H. Mast and D. Horwitz, "Osteomyelitis: a review of current literature and concepts," *Operative Techniques in Orthopaedics*, vol. 12, no. 4, pp. 232–241, 2002.

[2] S. K. Nandi, P. Mukherjee, S. Roy, B. Kundu, D. K. De, and D. Basu, "Local antibiotic delivery systems for the treatment of osteomyelitis—a review," *Materials Science and Engineering C*, vol. 29, no. 8, pp. 2478–2485, 2009.

[3] M. P. Ginebra, C. Canal, M. Espanol, D. Pastorino, and E. B. Montufar, "Calcium phosphate cements as drug delivery materials," *Advanced Drug Delivery Reviews*, vol. 64, pp. 1090–1010, 2012.

[4] J. H. Calhoun and J. T. Mader, "Treatment of osteomyelitis with a biodegradable antibiotic implant," *Clinical Orthopaedics and Related Research*, no. 341, pp. 206–214, 1997.

[5] J. S. Gogia, J. P. Meehan, P. E. Di Cesare, and A. A. Jamali, "Local antibiotic therapy in osteomyelitis," *Seminars in Plastic Surgery*, vol. 23, pp. 100–107, 2009.

[6] K. Garvin and C. Feschuk, "Polylactide-polyglycolide antibiotic implants," *Clinical Orthopaedics and Related Research*, no. 437, pp. 105–110, 2005.

[7] M. S. Rouse, K. E. Piper, M. Jacobson, D. J. Jacofsky, J. M. Steckelberg, and R. Patel, "Daptomycin treatment of *Staphylococcus aureus* experimental chronic osteomyelitis," *Journal of Antimicrobial Chemotherapy*, vol. 57, no. 2, pp. 301–305, 2006.

[8] K. Kanellakopoulou and E. J. Giamarellos-Bourboulis, "Carrier systems for the local delivery of antibiotics in bone infections," *Drugs*, vol. 59, no. 6, pp. 1223–1232, 2000.

[9] M. J. Patzakis, K. Mazur, J. Wilkins, R. Sherman, and P. Holtom, "Septopal beads and autogenous bone grafting for bone defects in patients with chronic osteomyelitis," *Clinical Orthopaedics and Related Research*, no. 295, pp. 112–118, 1993.

[10] C. L. Nelson, S. G. Hickmon, and B. H. Harrison, "Elution characteristics of gentamicin-PMMA beads after implantation in humans," *Orthopedics*, vol. 17, no. 5, pp. 415–416, 1994.

[11] H. P. Stallmann, C. Faber, A. L. J. J. Bronckers, A. V. N. Amerongen, and P. I. J. M. Wuisman, "In vitro gentamicin release from commercially available calcium-phosphate bone substitutes influence of carrier type on duration of the release profile," *BMC Musculoskeletal Disorders*, vol. 7, article 18, 2006.

[12] T. Hisatome, Y. Yasunaga, Y. Ikuta, and Y. Fujimoto, "Effects on articular cartilage of subchondral replacement with polymethylmethacrylate and calcium phosphate cement," *Journal of Biomedical Materials Research*, vol. 59, no. 3, pp. 490–498, 2002.

[13] M. P. Ginebra, T. Traykova, and J. A. Planell, "Calcium phosphate cements as bone drug delivery systems: a review," *Journal of Controlled Release*, vol. 113, no. 2, pp. 102–110, 2006.

[14] T. Sasaki, Y. Ishibashi, H. Katano, A. Nagumo, and S. Toh, "In vitro elution of vancomycin from calcium phosphate cement," *Journal of Arthroplasty*, vol. 20, no. 8, pp. 1055–1059, 2005.

[15] A. E. Watts, A. J. Nixon, M. G. Papich, H. D. Sparks, and W. S. Schwark, "In vitro elution of amikacin and ticarcillin from a resorbable, self-setting, fiber reinforced calcium phosphate cement," *Veterinary Surgery*, vol. 40, no. 5, pp. 563–570, 2011.

[16] M. P. Ginebra, E. Fernández, E. A. P. De Maeyer et al., "Setting reaction and hardening of an apatitic calcium phosphate cement," *Journal of Dental Research*, vol. 76, no. 4, pp. 905–912, 1997.

[17] E. Verron, I. Khairoun, J. Guicheux, and J. M. Bouler, "Calcium phosphate biomaterials as bone drug delivery systems: a review," *Drug Discovery Today*, vol. 15, no. 13-14, pp. 547–552, 2010.

[18] S. Bose and S. Tarafder, "Calcium phosphate ceramic systems in growth factor and drug delivery for bone tissue engineering: a review," *Acta Biomaterialia*, vol. 8, pp. 1401–1421, 2012.

[19] J. Schnieders, U. Gbureck, R. Thull, and T. Kissel, "Controlled release of gentamicin from calcium phosphate-poly(lactic acid-co-glycolic acid) composite bone cement," *Biomaterials*, vol. 27, no. 23, pp. 4239–4249, 2006.

[20] D. Campoccia, L. Montanaro, P. Speziale, and C. R. Arciola, "Antibiotic-loaded biomaterials and the risks for the spread of antibiotic resistance following their prophylactic and therapeutic clinical use," *Biomaterials*, vol. 31, no. 25, pp. 6363–6377, 2010.

[21] U. Joosten, A. Joist, T. Frebel, B. Brandt, S. Diederichs, and C. Von Eiff, "Evaluation of an in situ setting injectable calcium phosphate as a new carrier material for gentamicin in the treatment of chronic osteomyelitis: studies in vitro and in vivo," *Biomaterials*, vol. 25, no. 18, pp. 4287–4295, 2004.

[22] U. Joosten, A. Joist, G. Gosheger, U. Liljenqvist, B. Brandt, and C. Von Eiff, "Effectiveness of hydroxyapatite-vancomycin bone cement in the treatment of Staphylococcus aureus induced chronic osteomyelitis," *Biomaterials*, vol. 26, no. 25, pp. 5251–5258, 2005.

[23] O. Kisanuki, H. Yajima, T. Umeda, and Y. Takakura, "Experimental study of calcium phosphate cement impregnated with dideoxy-kanamycin B," *Journal of Orthopaedic Science*, vol. 12, no. 3, pp. 281–288, 2007.

[24] P. J. Jiang, S. Patel, U. Gbureck, R. Caley, and L. M. Grover, "Comparing the efficacy of three bioceramic matrices for the release of vancomycin hydrochloride," *Journal of Biomedical Materials Research Part B*, vol. 93, no. 1, pp. 51–58, 2010.

[25] M. Bohner, J. Lemaitre, and T. A. Ring, "Effects of sulfate, pyrophosphate, and citrate ions on the physicochemical properties of cements made of β-tricalcium phosphate-phosphoric acid-water mixtures," *Journal of the American Ceramic Society*, vol. 79, no. 6, pp. 1427–1434, 1996.

[26] M. Bohner, J. Lemaître, P. Van Landuyt, P. Y. Zambelli, H. P. Merkle, and B. Gander, "Gentamicin-loaded hydraulic calcium phosphate bone cement as antibiotic delivery system," *Journal of Pharmaceutical Sciences*, vol. 86, no. 5, pp. 565–572, 1997.

[27] M. J. Penner, B. A. Masri, and C. P. Duncan, "Elution characteristics of vancomycin and tobrarnycin combined in acrylic bone-cement," *Journal of Arthroplasty*, vol. 11, no. 8, pp. 939–944, 1996.

[28] C. S. Che Nor Zarida, O. Fauziah, A. K. Arifah, A. Azfar Rizal, M. Y. Nazri, and Z. Ahmad Hafiz, "In vitro elution and dissolution of tobramycin and gentamicin from calcium phosphate," *African Journal of Pharmacy and Pharmacology*, vol. 5, pp. 2283–2291, 2011.

[29] A. Bistolfi, G. Massazza, E. Verne, A. Masse, D. Deledda, and S. Ferraris, "Antibiotic-loaded cement in orthopedic surgery: a review," *ISRN Orthopedics*, vol. 2011, Article ID 290851, 8 pages, 2011.

Hindawi Publishing Corporation
Evidence-Based Complementary and Alternative Medicine
Volume 2013, Article ID 846740, 16 pages
http://dx.doi.org/10.1155/2013/846740

Review Article

Experimental and Clinical Pharmacology of *Andrographis paniculata* and Its Major Bioactive Phytoconstituent Andrographolide

Thanasekaran Jayakumar,[1] Cheng-Ying Hsieh,[2] Jie-Jen Lee,[1,3,4] and Joen-Rong Sheu[1,2]

[1] *Department of Pharmacology, Taipei Medical University, Taipei 110, Taiwan*
[2] *Graduate Institute of Medical Sciences, Taipei Medical University, 250 Wu-Hsing Street, Taipei 110, Taiwan*
[3] *Department of Surgery, Mackay Memorial Hospital, Taipei 104, Taiwan*
[4] *Department of Nursing, Mackay Medicine, Nursing and Management College, Taipei 112, Taiwan*

Correspondence should be addressed to Jie-Jen Lee; jjlee1957@gmail.com and Joen-Rong Sheu; sheujr@tmu.edu.tw

Received 23 November 2012; Revised 12 February 2013; Accepted 12 February 2013

Academic Editor: Yueh-Sheng Chen

Andrographis paniculata (Burm. F) Nees, generally known as "king of bitters," is an herbaceous plant in the family Acanthaceae. In China, India, Thailand, and Malaysia, this plant has been widely used for treating sore throat, flu, and upper respiratory tract infections. Andrographolide, a major bioactive chemical constituent of the plant, has shown anticancer potential in various investigations. Andrographolide and its derivatives have anti-inflammatory effects in experimental models asthma, stroke, and arthritis. In recent years, pharmaceutical chemists have synthesized numerous andrographolide derivatives, which exhibit essential pharmacological activities such as those that are anti-inflammatory, antibacterial, antitumor, antidiabetic, anti-HIV, antifeedant, and antiviral. However, what is noteworthy about this paper is summarizing the effects of andrographolide against cardiovascular disease, platelet activation, infertility, and NF-κB activation. Therefore, this paper is intended to provide evidence reported in relevant literature on qualitative research to assist scientists in isolating and characterizing bioactive compounds.

1. Introduction

Andrographis paniculata (Burm. F) Nees, commonly known as the "king of bitters," is an herbaceous plant belonging to the Acanthaceae and is found throughout tropical and subtropical Asia, Southeast Asia, and India. In India, *A. paniculata* is known as "Kalmegh"; in China it is known as "Chuan-Xin-Lian"; in Thailand it is known as "Fah Tha Lai"; in Malaysia it is known as "Hempedu bumi"; in Japan it is known as "Senshinren"; and in Scandinavian countries it is known as "green chiretta" [1]. Extracts of this plant and andrographolide exhibit pharmacological activities such as those that are immunostimulatory [1, 2], antiviral [3], and antibacterial [4]. As major active constituent, andrographolide exhibits a broad range of biological activities, such as anti-inflammatory, antibacterial, antitumor, antidiabetic, antimalarial, and hepatoprotective [5]. Because of the impressive variety of these biological activities, researchers propose obtaining various leads by structurally modifying andrographolide. In recent decades, numerous andrographolide derivatives have emerged and their pharmacological activities have also been evaluated. However, studies that have comprehensively summarized or analyzed *A. paniculata* and its derivatives have been minimal. Therefore, to contribute to the advanced trends of research on andrographolide, this paper provides thorough information regarding the pharmacological activities of *A. paniculata* and its major compound andrographolide.

1.1. Chemical Structure. Andrographolide is a major bioactive phytoconstituent found in various parts of *A. paniculata* (Figure 1), but particularly in the leaves. The chemical

Figure 1: Morphology of *Andrographis paniculata*.

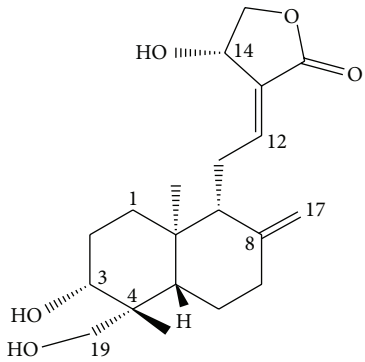

Figure 2: Chemical structure of andrographolide.

name of andrographolide is 3α, 14, 15, 18-tetrahydroxy-5β, 9βH, 10α-labda-8, 12-dien-16-oic acid γ-lactone (Figure 2), and its molecular formula and weight are $C_{20}H_{30}O_5$ and 350.4 (C 68.54%, H 8.63%, and O 22.83%), respectively. The structure of andrographolide has been analyzed by using X-ray, 1H,13 C-NMR, and ESI-MS [6–10]. Although andrographolide is not very soluble in water, it is soluble in acetone, chloroform, ether, and hot ethanol. Crystalline andrographolide was reported to be highly stable, over a period of three months [11]. Rajani et al. [8] reported a simple and rapid method for isolating andrographolide from the leaf of *A. paniculata*. They extracted it using a 1 : 1 mixture of dichloromethane and methanol and then isolated the andrographolide directly from the extract by performing recrystallization. The purity of the compound has been evaluated with thin-layer chromatography (TLC), UV absorption spectrum, high-performance liquid chromatography (HPLC), liquid chromatography-mass spectrometry (LCMS), and differential scanning calorimetry (DSC), which revealed the melting point of andrographolide to be 235.3°C [8, 9].

1.2. Biological Activities of Andrographolide. Andrographolide has been reported to have a wide range of biological activities, such as those that are anti-inflammatory [12], antiallergic [13], antiplatelet aggregation [14, 15], hepatoprotective [16], and anti-HIV [17]. In addition to these activities, the ability of ethanol or an aqueous extract of *A. paniculata* to decrease blood glucose levels in normal rats or streptozotocin diabetic rats has been documented [18]. In biological systems, andrographolide can interact with many inter- and intracellular constituents as a bipolar compound, thus ensuing in many biological responses. A recent study demonstrated that *A. paniculata* polysaccharides combined with andrographolide can ease the recovery of diabetic nephropathy [18].

2. Experimental Studies

2.1. Effects on Antioxidant Defense. Antioxidant defense systems may only partially prevent oxidative damage [19]. Hence, there is interest in using dietary supplements containing antioxidants to protect the components of the human body from oxidative damage. Currently, the most commonly used synthetic antioxidants are butylated hydroxyanisole (BHA), butylated hydroxytoluene (BHT), propyl gallate, and *tert*-butylhydroquinone. However, BHA and BHT have restricted use in foods because they are suspected to be carcinogenic and to cause liver damage [20]. Therefore, there is growing interest in using natural additives as potential antioxidants [21, 22].

Several studies have reported the antioxidant activities of *A. paniculata* and its constituents. Verma and Vinayak [23] reported that the aqueous extract of *A. paniculata* significantly increased the activities of antioxidant defense enzymes

such as catalase, superoxide dismutase, and glutathione-S-transferase and reduced glutathione content. The extract significantly inhibits lipid peroxidation by lowering the levels of thiobarbituric-acid-reactive substances in the liver and kidney of diabetic rats (as compared to normal rats) and also significantly increases the level of hepatic glutathione concentrations [24]. A pretreatment of andrographolide was reported to significantly attenuate the accumulation of the phorbol-12-myristate-13-acetate- (PMA-) induced formation of ROS and N-formyl-methionyl-leucyl-phenylalanine- (fMLP-) inducing adhesion of rat neutrophils [25]. Andrographolide exhibited free radical-scavenging ability, thus reduced oxidative stress and thiobarbituric-acid-reactive substance formation [26].

2.2. Anti-Inflammatory Effects. Andrographolide has been reported to significantly reduce the inflammation caused by histamine, dimethyl benzene, and adrenaline [27]. Overproduction of NO and prostaglandin E2 (PGE2), because of the expression of inducible isoforms of nitric oxide synthase (iNOS) and cyclooxygenase-2 (COX-2), plays a significant role in the inflammatory processes of activated macrophages. The secretion of proinflammatory cytokines from macrophages stimulated and promoted by lipopolysaccharide, which causes induction of iNOS, results in increased production of NO. The methanol extract of *A. paniculata* and andrographolide incubated with macrophages have been reported to inhibit LPS-stimulated NO production in a concentration-dependent manner [28, 29]. Chiou et al. [30] observed that andrographolide inhibits lipopolysaccharide-induced nitric oxide (NO) production and inducible NO synthase (iNOS) expression in the murine macrophage-like cell line RAW 264.7. Administering andrographolide to rats fully restored the maximal contractile response of the thoracic aorta to phenylephrine after incubation with LPS and alleviated the decrease in the mean arterial blood pressure of anesthetized rats. Andrographolide has also been reported to suppress IL-2 production and T-cell proliferation in a mixed lymphocyte reaction and to inhibit dendritic cell maturation and antigen presentation [31].

2.3. Anticancer Activity. Natural products are recognized as sources for drugs used to treat several human ailments including cancers. Vincristine, irinotecan, etoposide, and paclitaxel are examples of many natural pharmaceuticals derived from plants [32]. Despite the discovery of numerous drugs of natural origin, searching for new anticancer agents is still necessary to provide drugs that are less toxic and more effective and to increase their variety and availability. Samples with pharmacological usage should be accounted for when selecting plants to treat cancer because several ailments reflect disease states bearing relevance to cancer or cancer-like symptoms [33]. Andrographolide exhibited potent cytotoxic activity against KB (human epidermoid leukemia) and P388 (lymphocytic leukemia) cells [34]. Among the diterpenoid lactones isolated from the ethyl acetate fraction of *A. paniculata*, andrographolide had strong anticancer activity by inducing cell differentiation in mouse myeloid leukemia cells [35]. Andrographolide was found to inhibit the proliferation of various cell lines including leukemia, breast cancer, lung cancer, and melanoma cells [2, 36]. Furthermore, this compound has strong anticancer activity against human colorectal carcinoma LoVo cells by inhibiting cell cycle progression [37]. A potent growth inhibitory effect of andrographolide has been demonstrated in acute promyelocytic leukemic cells (HL-60 and NB4) that are mediated by inducing cell differentiation and apoptosis [38, 39]. Andrographolide was also reported to suppress the adhesion of gastric cancer cells which express high-level sialyl Lewis X to human vascular endothelial cells by blocking E-selectin expression and, thus, may represent a candidate therapeutic agent for cancer [40]. Lim et al. [41] demonstrated that the anticancer mechanisms for andrographolide include the inhibition of Janus tyrosine kinases-signal transducers and activators of transcription, phosphatidylinositol 3-kinase and NF-κB signalling pathways, suppression of heat shock protein 90, cyclins and cyclin-dependent kinases, metalloproteinases and growth factors, and the induction of tumour suppressor proteins p53 and p21, leading to the inhibition of cancer cell proliferation, survival, metastasis, and angiogenesis.

In vivo models of the anticancer activity of andrographolide have been used against MCF-7 and HT-29 tumor xenografts and B16F0 melanoma [38]. In a radiation therapy study, andrographolide was found to sensitize Ras-transformed cells and significantly delay tumor growth [42]. Sheeja and Kuttan [43] demonstrated that *A. paniculata* extract or andrographolide alone could stimulate cytotoxic T lymphocyte production through the enhanced secretion of IL-2 and IFN-c by T cells, thereby inhibiting tumor growth *in vivo*. Inhibition of angiogenesis is currently perceived as a promising strategy in treating cancer. In a significant invention, *A. paniculata* and andrographolide alone were found to inhibit tumor-specific angiogenesis by regulating the production of various pro- and antiangiogenic factors, such as proinflammatory cytokines, NO, vascular endothelial growth factor, IL-2, and the tissue inhibitor of metalloproteinase-1 [43]. A recent study demonstrated that andrographolide inhibits breast cancer cell proliferation, migration, and cell cycle arrest at the G2/M phase and induces apoptosis through a caspase-independent pathway. Their experimental evidence suggests that andrographolide attenuates endothelial cell motility and tumor-endothelial cell interaction [44]. The antitumor activity of andrographolide in an *in vivo* model was correlated with the downregulation of PI3 kinase/Akt activation, inhibition of proangiogenic molecules, such as OPN, and VEGF expressions [44].

2.4. Immunomodulatory Activity. Purified andrographolide (1 mg/kg body weight) or intragastric administration of ethanol extracts of the stems and leaves (25 mg/kg body weight) to mice stimulate antibody production and the delayed-type hypersensitivity response to sheep red blood cells [45]. The extract and purified andrographolide were also reported to stimulate an innate immune response in mice, which was measured according to the macrophage migration index, phagocytosis of leucine-labelled *Escherichia coli*, and proliferation of splenic lymphocytes stimulated by *A. paniculata* extract [45]. The immunomodulatory property

of a diterpene lactone andrographolide was reported to be associated with the enhancement of the proliferation of human peripheral blood lymphocytes, as well as the production of key cytokines and the expression of Y Xu 21 immune activation markers in whole blood cells in culture *in vitro* [46]. Rajagopal et al. [2] and Kumar et al. [1] have reported the immunostimulatory activity of andrographolide *in vitro* in PHA-stimulated human peripheral blood lymphocytes (HPBLs) by increased proliferation of lymphocytes and production of IL-2. *In vivo* immune responses, such as an antibody response to a thymus-dependent antigen and delayed-type hypersensitivity, were considerably lessened in mice treated with andrographolide. In addition, Iruretagoyena et al. [47] reported that andrographolide enhanced the tolerogenic properties of immature dendritic cells (DCs) in experimental autoimmune encephalomyelitis (EAE) by inhibiting NF-kappa B activation in murine DCs. Andrographolide was also reported to reduce IFN-γ and IL-2 production in murine T cells stimulated with concanavalin A (Con A) *in vitro* [48]. Moreover, andrographolide was reported to inhibit the production of TNF-α and IL-12 in macrophages stimulated by lipopolysaccharide [49].

2.5. Hepatoprotective Activity. Liver diseases of various origins remain a serious health problem and a major cause of mortality. In the absence of reliable hepatoprotective drugs in modern medicine, herbs and plants play a vital role in managing several liver disorders [50, 51]. Extensive literature related to the hepatoprotective activity of molecules from herbal sources shows that there is a vast array of molecules exhibiting potent hepatoprotective efficacy. The Indian systems of medicine have long used *A. paniculata* as a hepatostimulant and hepatoprotective agent [16]. *A. paniculata* is also an ingredient in several polyherbal preparations used as hepatoprotectants [52], one of which has been reported to be efficacious in chronic hepatitis B viral infection [53]. A recent study showed that andrographolide attenuated concanavalin A-induced liver injury and inhibited hepatocyte apoptosis [54]. Shukla et al. [55] reported observing choleretic effects of andrographolide in conscious rats and anesthetized guinea pigs. The effect of andrographolide was found to be more potent than silymarin against acetaminophen-induced reduction of the volume and contents of bile. Andrographolide was also shown to protect against ethanol-induced hepatotoxicity in mice with an equivalent efficacy of silymarin [56]. Oral pre- and posttreatments of adult rats with an extract of *A. paniculata* were protective against an ethanol-induced increase in serum transaminases. A protective effect of a single oral dose each of the extract and of andrographolide has been studied in carbon tetrachloride- (CCl_4-) induced hepatic microsomal lipid peroxidation. Rana and Avadhoot [57] reported the hepatoprotective effects of the crude alcohol extract of leaves against CCl_4-induced liver damage; these effects have had also been established against paracetamol-induced toxicity in an *ex vivo* rat model of isolated hepatocytes [58]. Plant extracts of *A. paniculata* showed hepatoprotective characters consistent with the folk use and pharmacology [59].

2.6. Antimicrobial Effects. Antimicrobial drugs have caused a dramatic change not only in the treatment of infectious diseases but to the fate of mankind. Antimicrobial chemotherapy has made noteworthy advances, resulting in positive observations that infectious diseases might be dominated in the near future. However, in reality, emerging and reemerging infectious diseases have indicated a countercharge from infections. Infections with drug-resistant organisms hang back an imperative problem in clinical practice that is complicated to explain. If an unsuitable antimicrobial agent is preferred over the treatment of infection with drug-resistant microorganisms, the therapy may not achieve beneficial effects and may lead to a worse prognosis. *A. paniculata* and andrographolide have been reported to exhibit potent antimicrobial activity against various microbial organisms.

In vitro antibacterial activity of the crude powder of *A. paniculata* has been reported against *Salmonell*a, *Shigella, E. coli*, gram A streptococci, and *Staphylococcus aureus*, even at a concentration of 25 mg/mL. Singha et al. [4] found significant antibacterial activity in an aqueous extract with andrographolide. A similar result was found in a crude aqueous extract of leaves that exhibit significant antimicrobial activity against gram-positive *S. aureus*, methicillin-resistant *S. aureus*, and gram-negative *Pseudomonas aeruginosa* [60]. Significant activity against enterohemorrhagic strains of *E. coli* was found in the ethanol extract of *A. paniculata* [61]. The virucidal activity of andrographolide has been reported against herpes simplex virus 1 (HSV-1) without having any significant cytotoxicity [62]. At a concentration of 0.05 mg/mL of a chloroform extract of *A. paniculata,* the plant completely inhibits malarial parasitic growth within 24 h of incubation; and the same inhibition has been noted within 48 h with methanol extract concentration of 2.5 mg/mL [63]. A methanol extract was found to inhibit *Plasmodium falciparum* substantially at a 50% inhibitory concentration (IC50) of 7.2 μg/mL [64]. The ethanolic extract of *A. paniculata* was effective against upper respiratory tract infection [65]. The antimicrobial activity of *A. paniculata* against nine bacterial strains, *Salmonella typhimurium, E. coli, Shigella sonnei, Staphylococcus aureus, Pseudomonas aeruginosa, Streptococcus pneumonia, Streptococcus pyogenes, Legionella pneumophila,* and *Bordetella pertussis,* has also been reported [66].

2.7. Antiviral Effects. The antiviral activities of plant extracts have been renewed and have been the topic of passionate scientific investigation. Several medicinal plant extracts have shown antiviral activities against some RNA and DNA viruses. Among these plants is *A. paniculata* which exhibits a neutralizing activity against the human immunodeficiency virus (HIV) [67]. Andrographolide was investigated for antiviral activity against herpes simplex virus (HSV) [62, 68], HIV [3], flaviviruses, and pestiviruses [69]. Lin et al. [70] demonstrated that 25 μg/mL of ethanolic extract of *A. paniculata* and 5 μg/mL of andrographolide effectively inhibit the expression of Epstein-Barr virus (EBV) lytic proteins, Rta, Zta, and EA-D, during the viral lytic cycle in P3HR1 cells. A recent study has demonstrated that *A. paniculata* has the most

antiviral inhibitory effects among six medicinal plants tested against DENV1-infected Vero E6 cells [71].

2.8. Antipyretic and Analgesic Effects. In Asian countries, *A. paniculata* has been widely used for its antipyretic, analgesic, protozoacidal, antihepatotoxic, anti-HIV, immunostimulant, anticancer effects [36]. It had been reported that andrographolide, with oral doses of 100 and 300 mg/kg, produced a significant antipyretic effect after 3 h administration of brewer's yeast-induced fever in rats [72]. In addition, doses of 180 or 360 mg/kg of andrographolide were also found to relieve fever in humans by the third day after administration [73]. Madav et al. [72] have also reported that 300 mg/kg of andrographolide, administered orally, had significant analgesic activity on acetic-induced writhing in mice and on the Randall-Selitto test in rats, but without any effect on the hot plate test in mice. These authors have also reported that intraperitoneal administration of 4 mg/kg of andrographolide exhibited an analgesic effect, whereas the former study, 300 mg/kg administered orally did not. The different routes of administration between these experiments could contribute to this discrepancy [72].

2.9. Antimalarial Effects. *In vitro* and *in vivo* studies performed by Rahman et al. [63] showed that *A. paniculata* produced significant antimalarial effects. Chloroform extract of this plant shows better effect than the methanol extract because it showed complete parasite growth inhibition as low as 0.05 mg/mL drug dose within 24 h incubation period as compared to methanol extract of drug dose of 2.5 mg/mL but under incubation time of 48 h of the same plant species. *In vivo* activity of *A. paniculata* also demonstrated higher antimalarial effect [63]. Fractions isolated from *A. paniculata* also exhibited antimalarial activity [74]. Misra et al. [75] have isolated andrographolide, neoandrographolide, deoxyandrographolide and andrographolide from the leaves of *A. paniculata* that showed anti-malarial activity against *Plasmodium berghei* NK65 in *Mastomys natalensis*.

2.10. Larvicidal and Ovicidal Effects. Plant products have been used by traditionally human communities in many parts of the earth against the vectors and species of insects. The phytochemicals derived from plant sources can act as larvicides, insect growth regulators, repellents, and ovipositional attractants and have deterrent actions as observed by many researchers [76–80]. The treatment of different products of *A. paniculata* greatly affected the larval growth of *Anopheles stephensi* and caused malformation and mortality in a dose-dependent manner [81]. An ethanolic extract of *A. paniculata* caused moderate ovicidal activity against various age groups of *Aedes stephensi*, but it inflicted delayed effects such as high larval, pupal, and adult mortality, thereby suppressing the vector population and adversely influencing transmission of the disease pathogen [82]. The leaf extract of *A. paniculata* with different solvents of benzene, hexane, ethyl acetate, methanol, and chloroform exhibited larvicidal and ovicidal activities against *Culex quinquefasciatus* Say and *Aedes aegypti* L., whereas ethyl acetate and methanol extracts of the plant showed only ovicidal activity against *Culex quinquefasciatus* and *Aedes aegypti* [83]. They have also found 100% mortality against two mosquito species exerted by ethyl acetate and methanol extracts of the plant. A recent study performed by Sheeja et al., 2012 suggest that the leaf extracts of *A. paniculata* may have the potential to be used as an ideal eco-friendly approach for the control of the filarial vector *Culex quinquefasciatus* [76].

2.11. Renoprotective Effects. The recurrence of urolithiasis is critical; thus, preventing and treating stone formation are highly recommended. The most recent data suggest that 27 million people have chronic kidney disease, representing nearly one in seven adults and a 30% increase over the past decade [84]. In the Unites States, more than 200 thousand people suffer from kidney failure. A similar increase in the incidence of end-stage renal failure caused by an increasing incidence of the risk factors for renal disease has occurred in many Asian countries [85]. A study found that the aqueous extract of *A. paniculata* could considerably alleviate the nephrotoxic action of gentamicin in male albino rats, thus exhibiting marked renoprotective activity [86].

2.12. Antifertility Effects. Efforts are underway to develop antifertility products from plants. Many plants are reported to have fertility-regulating properties in ancient Indian literature [87]. Numerous plants have been tested for their antifertility activities in laboratory animals [88, 89] and several animal studies have reported an effect of *A. paniculata* on male and female reproduction. Early reports of oral administration of the powdered stem of *A. paniculata* have shown an antifertility effect on male Wistar mice, but no impact on fertility in female mice [90]. It has also been reported that administering *A. paniculata* results in abortion in pregnant rabbits. Moreover, the herb is reported to suppress the growth of human placental chorionic trophoblastic cells in vitro [91]. Zoha et al. [92] reported feeding sun-dried *Andrographis* powder to female mice at a dose of 2 g/kg bw/day for 6 weeks and then mated them with untreated males of proven fertility, thus inhibiting pregnancy in 100% of the tested animals. Oral administration of *Andrographis paniculata* extract during the first 19 days of pregnancy in doses of 200, 600, and 2000 mg/kg did not exhibit any effect on the elevated level of progesterone in the blood plasma of rats [46]. Animal studies have also shown that *A. paniculata* may have contraceptive or antifertility effects following long-term treatment at high doses (20 mg/rat) [93]. However, there was a large degree of discrepancy in the results, with some studies demonstrating no untoward effects even at the 1000 mg/kg dose [48]. Administering dry leaf powder to male albino rats (20 mg daily for 60 days) has been shown to inhibit spermatogenesis, degenerative changes in the seminiferous tubules, regression of Leydig cells, and regressive or degenerative changes in the epididymis, seminal vesicle, ventral prostate, and coagulating glands [94]. Andrographolide also produced similar results when orally administered to male Wistar albino rats for 48 days. A study reported no toxicity of andrographolide (50 mg/kg) treatment for up to 8 weeks in the number and motility of sperm [95]. It was reported that the effect of andrographolide or *A. paniculata* on sex

hormones in patients with an impaired testosterone level might be able to return hormone levels to normal and treat decreased libidos and decreased mental and physical sexual activity.

2.13. Antihyperglycemic Activities. Diabetic nephropathy has become the leading cause of end-stage renal disease in developed countries, thus creating an increasing clinical problem [96]. To prevent and treat diabetic nephropathy, current methods using agents such as angiotensin-converting enzyme inhibitors, angiotensin-II receptor blockers, and antihypertensive drugs have been attempted in clinical practice [97]. Despite these treatments, numerous patients still develop intractable diabetic nephropathy. This has prompted considerable interest in using traditional medicines to treat this condition. Orally administered glucose-induced hyperglycemia in nondiabetic rabbits was reported to be prevented by the extract of *A. paniculata*. Six weeks of chronic administration of the extract showed no effect on fasting blood glucose levels [98]. The ethanolic extract of *A. paniculata* at a dose of 400 mg/kg body weight twice daily for 2 weeks to diabetic rats was shown to produce a 49.8% reduction in fasting serum triglyceride levels. This was reported to be greater than the 27.7% decline that was achieved with 500 mg/kg body weight twice daily for 14 days [24]. An aqueous extract (50 mg/kg body weight) administered to streptozotocin-diabetic rats resulted in a 52.9% reduction in blood glucose levels. Dry powder of the plant material significantly decreased blood glucose levels by 61.8% at a lower dose of 6.25 mg/kg body weight [99]. Comparable results were observed by Dandu and Inamdar [100] with oral administration of an aqueous extract of *A. paniculata* leaves. A dose of 400 mg/kg was found to lower the blood glucose levels of streptozotocin-induced animals and increased the activity of superoxide dismutase and catalase. Oral administration of the decoction also significantly reduced blood glucose levels in alloxan-induced diabetic rats and reduced food and water intake when compared to vehicle-treated diabetic controls [100]. Extended mean estrous cycles were reduced from 8 to 5 days in treated diabetic rats [101]. Andrographolide appears to reduce plasma glucose concentration dose-dependently in streptozotocin-induced diabetic and normal rats, with the potential effect observed in normal rats rather than in diabetic rats [102]. This is a significant difference from the water extract, which did not show a glucose-lowering effect in a study on normoglycemic rats [100].

Andrographolide also attenuates the increase in plasma glucose in response to an intravenous glucose challenge in normal rats and enhances the uptake of radioactive glucose by isolating the soleus muscle of streptozotocin-diabetic rats in a concentration-dependent manner. Repeated intravenous administration of andrographolide in diabetic rats for three days resulted in an increase in mRNA and protein levels of glucose transporter in the soleus muscle, indicating that the glucose-lowering effect of andrographolide could be caused by more effective glucose use of the skeletal muscle [102]. However, an *in vitro* experiment concluded that the hypoglycemic effect of *A. paniculata* is caused by insulin release from pancreatic cells through ATP-sensitive potassium channels, an effect that is similar to that of other insulinotropic antidiabetic agents [103]. Subramanian et al. [104] conducted *in vitro* experiments and suggested that the inhibition of alpha-glucosidase and alpha-amylase enzyme could be the mechanism by which the ethanol extract of *A. paniculata* and andrographolide produce hypoglycemic effects. Water extract seems to be a more suitable candidate for further study because it does not affect the fasting blood glucose levels of nondiabetic animals. Therefore, identifying blood glucose-lowering constituents in both water and ethanol extracts may be of value.

2.14. Hypolipidemic Effects. Hyperlipidemia is a crucial factor, particularly in patients with high cholesterol levels and abnormal lipoprotein metabolisms, and has a direct relationship with cardiovascular diseases [105, 106]. Hence, the research and development of new functional foods and medicines for preventing coronary heart disease are crucial. Cholesterol and other fatty substances combine in the bloodstream and are deposited in the blood vessels to form a material called plaque [107]. The increase in lipids can cause plaque to grow over time and lead to obstructions in blood flow. If an obstruction occurs in the coronary arteries, it could result in a heart attack. Furthermore, an obstruction occurring in the arteries of the brain could lead to a stroke [108]. Hence, it is critical to actively decrease blood lipid counts to prevent and cure cardiovascular and cerebrovascular diseases. A recent study thoroughly demonstrated that andrographolide has potent hypolipidemic effects and protects the cardiovascular system without significant liver damage by lowering TC, TG, HDL-TC, and LDL-TC in mice and rats [109]. Nugroho et al. [110] reported that the purified extract of andrographolide significantly ($P < 0.05$) decreased the levels of blood glucose, triglycerides, and LDL.

2.15. Effects on Cardiovascular Disease. A. paniculata has demonstrated an increase of blood-clotting time; hence, pre- and posttreatments of the extract of *A. paniculata* after surgery significantly prevent the constriction of blood vessels, thus decreasing the risk of the subsequent closing of blood vessels after angioplasty procedures [111]. Several studies have used animal models to investigate the effects of aqueous extracts and active constituents of *A. paniculata*, both before and after experimental myocardial infarction. An extract of the plant produced antihypertensive effects because it relaxed smooth muscles in the walls of blood vessels and prevented the blood vessels from constricting and limiting blood flow to the brain, heart, and other organs [112]. A time-dependent protection of rat cardiomyocytes against hypoxia injury was reported to be caused by the pretreatment of andrographolide; this effect was reported to be associated with upregulation of cellular reduced glutathione (GSH) level and antioxidant enzyme activities [113]. Awang et al. [114] demonstrated that the dichloromethane extract of *A. paniculata* significantly reduced coronary perfusion pressure by up to 24.5 ± 3.0 mm Hg at a 3 mg dose and also reduced the heart rate by up to 49.5 ± 11.4 beats/min at this dose. The arterial constriction caused by high cholesterol in the

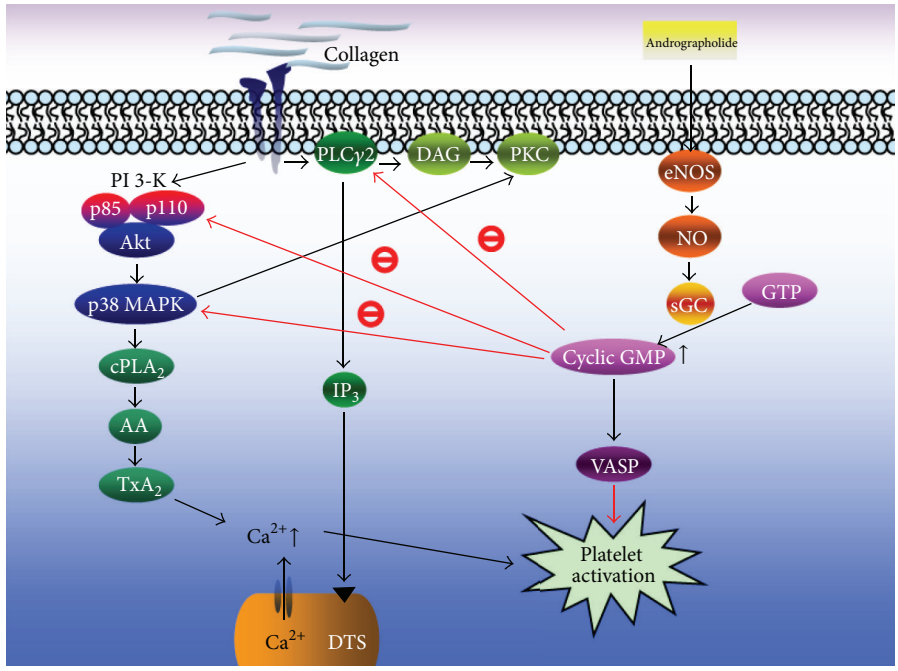

FIGURE 3: Hypothetical scheme shows the inhibitory signaling of andrographolide in platelet activation. Andrographolide can activate the endothelial nitric oxide synthase- (eNOS-) NO-cyclic GMP pathway, followed by the inhibition of both the PLCγ2-DAG-PKC and PI3 kinase/Akt cascades, and ultimately inhibits platelet aggregation [120].

diet and by injury to the inner lining of the blood vessel was also found to be diminished by *A. paniculata* [115]. It was reported that *A. paniculata* decreased the damage of the heart muscle, when it is administered to dogs one hour after the development of myocardial infarction [116]. These findings imply the promising use of *A. paniculata* as a favorable alternative for cardiovascular therapy.

2.16. Inhibitory Effects on Platelet Aggregation. An intravascular thrombosis is among the generators of a wide variety of cardiovascular diseases. Initiation of an intraluminal thrombosis is believed to involve platelet adherence and aggregation. Thus, platelet aggregation may play a crucial role in the atherothrombotic process [117]. Blood platelet activation and aggregation are common denominators in atherothrombotic events and various inflammatory diseases. Platelets have been viewed exclusively as mediators of thrombosis and hemostasis; their function has been extended to include prominent roles in inflammation and immunity [118]. Therefore, the use of antiplatelet agents, which can inhibit thromboembolic diseases (myocardial infarction, ischemic stroke, and vascular death) in the platelets, warrants investigation. Amroyan et al. [14] found that andrographolide inhibited PAF-induced human platelet aggregation. Moreover, Thisoda et al. [119] reported that the extract of *A. paniculata* (10–100 μg/mL) significantly inhibited platelet aggregation in washed rat platelets. Our recent study demonstrated for the first time that andrographolide exhibits potent antiplatelet activity through the activation of the eNOS-NO/cyclic GMP pathway and inhibition of both the PLCγ2-PKC and PI3 kinase/Akt-MAPK (i.e., p38 MAPK) cascades in washed human platelets (Figure 3) [120]. Our earlier study also showed that andrographolide may involve an increase in cyclic GMP/PKG, followed by inhibition of the p38 MAPK/$^{\bullet}$HO-NF-κB-ERK2 cascade in activated platelets. In that study, we also suggested that andrographolide may have a high therapeutic potential to treat thromboembolic disorders and may also be considered for treating various inflammatory diseases [15].

Aqueous extract, andrographolide, and DDA inhibit thrombin-induced platelet aggregation in time- and concentration-dependent manners [119]. Andrographolide inhibits platelet-activating factor- (PAF-) induced platelet aggregation in a dose-dependent manner without affecting the biosynthesis of eicosanoids. An extract of *A. paniculata* significantly inhibited *ex vivo* ADP-induced platelet aggregation in 63 patients with cardiac and cerebral vascular diseases 3 h after administration. Thirty-three of these patients, who were observed for platelet aggregation after 1 week, experienced even more significant effects. Serotonin release from platelets was significantly reduced in 20 extract-treated volunteers, although the plasma serotonin levels remained unchanged [121].

2.17. Inhibitory Effects on NF-kappa B (NF-κB) Transcription Factors. NF-κB plays a pivotal role in the pathogenesis of inflammation, prompting various drugs designed to treat human inflammatory disease to be focused on inhibiting NF-κB activation [122]. Many natural compounds or herbal extracts reportedly exhibit anti-inflammatory activities that generally involve NF-κB activation [123, 124]. Phytochemicals, especially flavonoids, are currently of interest because

of their essential biological and pharmacological properties, including the inhibition of NF-κB activation [125].

NF-kappa B comprises a family of inducible transcription factors that serve as crucial regulators of the host immune and inflammatory responses. The NF-kappa B transcription factor regulates the expression of various components of the immune system, including proinflammatory cytokines, chemokines, adhesion molecules, and inducible enzymes such as cyclooxygenase-2 and inducible nitric oxide synthase, as well as proteins that regulate the specific immune response, such as interleukin- (IL-) 2, IL-12, and interferon-γ that control lymphocyte proliferation and differentiation. Therefore, dysregulation of this transcription factor can lead to inflammatory and autoimmune diseases [126]. Andrographolide has been proven to attenuate inflammation by inhibiting NF-kappa B activation through the covalent modification of reduced Cys62 of p50. Mechanistically, andrographolide formed a covalent adduct with a reduced cysteine of p50, thus blocking the binding of NF-kappa B oligonucleotide to nuclear proteins. Andrographolide suppressed the activation of NF-kappa B in stimulated endothelial cells, thereby reducing the expression of the cell adhesion molecule E-selectin and prevented E-selectin-mediated leukocyte adhesion under flow [13]. Andrographolide also abrogated the cytokine- and endotoxin-induced peritoneal deposition of neutrophils, attenuated septic shock, and prevented allergic lung inflammation *in vivo*.

Other researchers have analyzed the effect of andrographolide on the activation of NF-kappa B induced by a platelet-activating factor (PAF) and N-formyl-methionyl-leucyl-phenylalanine (fMLP) in HL-60 cells differentiated to neutrophils. Andrographolide has been shown to inhibit the NF-kappa B luciferase activity induced by PAF. Andrographolide also reduced the DNA binding of NF-kappa B in whole cells and in nuclear extracts induced by PAF and fMLP. Therefore, andrographolide exerts its anti-inflammatory effects by inhibiting NF-kappa B binding to DNA, thus reducing the expression of proinflammatory proteins, such as COX-2 [127].

Several lines of evidence indicate that inhibition of NF-κB transcriptional activity contributes to the protective anti-inflammatory actions of andrographolide [128, 129]. Andrographolide inhibits nuclear factor kappa B (NF-κB) activation by blocking the binding of NF-κB oligonucleotides to nuclear proteins [30, 128]. Recently, we demonstrated that andrographolide enhances the NF-κB subunit p65 Ser536 dephosphorylation through the activation of protein phosphatase 2A in vascular smooth muscle cells [129]. We also demonstrated for the first time that andrographolide inhibited p65 Ser536 phosphorylation, reduced nuclear translocation of p65, and diminished p65 kB oligonucleotide binding in LPS/IFN-γ-stimulated rat VSMCs [129]. In addition, PP2A may contribute to these actions of andrographolide in rat VSMCs.

3. Clinical Studies

3.1. Antidiarrheal Effects. In the tropical and subtropical regions of the world, diarrhea is still one of the major causes of death. In developing countries, it is a principal cause of death in children under 5 years of age and the causes include infectious agents, plant toxins, and gastrointestinal disorders [130]. Many Western medicines, such as kaolin-pectin, bismuth, and loperamide, have long been used to alleviate the symptoms but have included undesirable side effects. It was reported that the ethanol extract of *A. paniculata* cured 88.3% of acute bacillary dysentery and 91.3% of acute gastroenteritis cases [91]. Administering andrographolide was reported to cure 91% of acute bacillary dysentery cases. The same cure rate (91.1%) was also achieved by administering a compound tablet containing andrographolide and neoandrographolide (at a ratio of 7 : 3) in cases of bacillary dysentery. This was reported to be higher than cure rates obtained with furazolidrne or chloramphenicol [91]. This compound has also been used traditionally to sluggish live as an antidote for colic dysentery and dyspepsia, and has been employed successfully in cases of general debility in convalescence after fever, livero disorders and advanced stages of dysentery. The juice of fresh leaves of *A. paniculata*, which generally contains andrographolide, is used as a domestic remedy to treat colic pain, loss of appetite, irregular stool, and diarrhea [131].

Table 1: Effect of andrographolide on mortality of acute pulmonary thrombosis caused by intravenous injection of ADP in experimental mice.

	Total no. of mice	Number of deaths	Mortality rate (%)
Solvent control (0.5 DMSO)	6	0	0
ADP (700 mg/kg)	10	9	90
ADP (700 mg/kg) + andrographolide (μg, kg)			
22	10	6	60*
55	10	5	50*

ADP: adenosine diphosphate; DMSO: dimethyl sulfoxide.
*$P < 0.05$ (compared with ADP control).

3.2. Anti-HIV Effects. Studies on the development of new anti-HIV drugs have begun worldwide in the past few years [132]. The growing incidence of drug-resistant HIV strains is one of the main problems in treating HIV infection, although current anti-HIV drugs can inhibit HIV infection. To avoid existing therapeutic difficulties, current searches for new anti-HIV agents are focused on discovering compounds with novel structures and different mechanisms of action [133]. Natural products and their derivatives have long been invaluable as a source of therapeutic agents for the development of medicine. The development of anti-HIV drugs derived from natural products is an area of research in which considerable effort should be dedicated in the future [134]. A clinical trial of andrographolide was conducted to examine 13 HIV-positive patients and five HIV-negative healthy volunteers. A planned protocol began with a dose of 5 mg/kg body weight for the first 3 weeks, increased to 10 mg/kg body weight for 3 weeks, and then increased to 20 mg/kg body weight for the final 3 weeks. Andrographolide administration significantly improved the $CD4^+$ lymphocyte count from

Table 2: Dosage and toxicity of *Andrographis paniculata* and its major natural product andrographolide.

Products name	Dosage/duration/route	Experimental models	Toxic effects	References
Andrographolide	10 mg/kg for 3 weeks	Human	No	[3]
Andrographolide	500 mg/kg bw for 7 days i.p.	Mice	No	[4]
Andrographolide	25–75 μM	Platelets	No cytotoxicity	[15]
A. paniculata	20 mg/kg bw for 60 days, oral	Rats	No	[71]
Andrographolide	22–55 μg/kg, i.v.	Mice	Lower mortality	[97]
A. paniculata	1 g/kg/day for 4, 6, and 8 weeks	Rats	No	[120]
Andrographolide	100 mg/kg, i.p.	Mice	No	[121]
Andrographolide	10 mg/kg, i.v.	Rats	No	[123]

i.p.: intraperitoneal; i.v.: intravenous; and bw: body weight.

a baseline mean of 405 cells/mm^3 to 501 cells/mm^3 in HIV-positive patients. There was no statistically significant change in mean plasma HIV-1 RNA levels [3]. A recent study summarized that andrographolide derivatives may be promising candidates for preventing HIV infection [135], suggesting that andrographolide inhibited the gp120-mediated cell fusion of HL2/3 cells with TZM-bl cells.

3.3. Effects on Upper Respiratory Tract Infections. *A. paniculata* has been widely used for upper respiratory tract infections (URTIs). In a randomized, double-blind, and controlled study, Thamlikitkul et al. [73] administered *A. paniculata* at a dose of 6 g/day for 7 days to 152 Thai adults suffering from pharyngotonsillitis, and the efficiency has been reported to be similar to that of acetaminophen in relieving the symptoms of fever and sore throat. Cáceres et al. [136] clearly demonstrated that the treatment of *Andrographis paniculata* extract SHA-10 reduces the intensity of the symptoms of tiredness (OR = 1.28; 95% CI 1.07–1.53), sleeplessness (OR = 1.71; 95% CI 1.38–2.11), sore throat (OR = 2.3; 95% CI 1.69–3.14), and, HSP, (OR = 2.51; 95% CI 1.82–3.46) as compared with the placebo group in a duration-dependent manner. They have found that *Andrographis paniculata* extract treatment for 4 days significantly decreases in the intensity of all symptoms than in 2-day treatment group.

4. Dosage and Safety of Andrographolide

Numerous studies have been performed in different countries on the toxicity of *A. paniculata,* finding that it is extremely nontoxic, even at high doses (Table 2). Sakila et al. [137] conducted an antifertility study and found no toxicity, even at a high dose of *A. paniculata* that was administered to rats. The LD50 of andrographolide in male mice through the intraperitoneal route was reported to be 11.46 g/kg [138]. In a study of HIV-positive patients, a dose of 1,500–2,000 mg of andrographolide was administered daily for 6 weeks. The study was discontinued early despite some improvements in CD4$^+$ counts [3], and the side effects were common. Intravenous administration of andrographolide (10 mg/kg) to rabbits showed no abnormal cardiovascular responses. Results from liver enzyme tests indicated that the heart, liver, kidney, and spleen of these rabbits were found to be normal [139]. Mice receiving an oral plant extract (10 g/kg) once a day for 7 days proved that no mortality was observed. In another test for toxicity, rats or rabbits receiving 1 g/kg of andrographolide orally showed no changes in body weight, blood count, or the functions of the liver, kidney, or other vital organs [94]. Singha et al. [56] noticed that pretreatment of *A. paniculata* and andrographolide at 500 mg/kg body weight and 125 mg/kg body weight, respectively, could minimize the toxicity when compared with the ethanol-treated group, as evidenced by different enzymatic assays in the liver and kidney tissues; the results were comparable with those of administering silymarin.

Our recent study show that andrographolide concentrations of 22 μg/kg and 55 μg/kg markedly lowered the mortality rate in mice challenged with ADP (700 mg/kg) from 90% to 60%, respectively, indicating that andrographolide effectively prevents thromboembolism (Table 1) [120]. Suo et al. [140] investigated the pharmacokinetics of andrographolide (10 mg/kg, i.v.) in rats and observed that the blood concentration of andrographolide was approximately 11 μg/mL (approximately 30 μM). Moreover, administering andrographolide causes no cytotoxic effects on platelets at concentrations between 35 and 150 mM [15]. Therefore, andrographolide is recommended to be clinically tested as a pharmaceutical agent.

5. Conclusion

Andrographolide, which exhibits notable pharmacological activities (Table 3), has attracted the interest of numerous researchers. Because of its rational activity, numerous andrographolide derivatives have been synthesized for the development of biological activities. Thus, this paper summarizes various experimental and clinical pharmacological activities of andrographolide, such as those that are antioxidant, anti-inflammatory, anticancer, antimicrobial and parasitic, hepatoprotective, antihyperglycemic, and antihypoglycemic. Evidence from clinical studies suggests that andrographolide reduces HIV symptoms, uncomplicated upper respiratory tract infections, including sinusitis and the common cold, and rheumatoid arthritis. Nevertheless, summarizing the effects on cardiovascular disease, NF-κB, and platelet activation of this natural product is worthy of review, and additional studies must be conducted to confirm the toxicological properties of this novel molecule before

Table 3: Experimental and clinical pharmacology of *Andrographis paniculata* and its major phytoconstituent andrographolide.

Pharmacological effects	Mechanisms	References
	(I) Experimental studies	
Antioxidant activity	↑ CAT, SOD, and GST; ↓ LDH	[23]
	↑ CAT, SOD, and GSH	[24]
	↓ TBARS	[26]
Anti-inflammatory effects	↓ LPS-induced NO production	[28–30]
Anticancer effects	↑ Cell differentiation	[35]
	↓ Proliferation of cancer cells	[3, 36]
	↑ IL-2 and IFN-c	[38]
	↓ Tumour growth	
	↓ Cell proliferation, migration, and cell cycle arrest at G2/M phase	[42]
	↓ E-selectin expression	[40]
	↓ Janus tyrosine kinases-signal transducers and activators of transcription, phosphatidylinositol 3-kinase and NF-κB signalling pathways, suppression of hsp 90, cyclins, and cyclin-dependent kinases, MMPs and growth factors	
	↑ Tumor suppressor proteins p53 and p21	[41]
Immunomodulatory effect	↑ Antibody production	[43]
	↓ Delayed-type hypersensitivity response	
	↑ Proliferation of human peripheral blood lymphocytes	
	Key cytokines and the expression	[1, 2, 44]
Hepatoprotective effects	↓ ALT activity	[50]
	↓ Concanavalin A-induced liver injury and hepatocyte apoptosis	[52]
	↓ GOT, GPT, ACP, and ALP levels Losses of HBsAg, HBeAg, and HBV DNA	[54, 56]
Antimicrobial effects	Acted against herpes simplex virus 1 (HSV-1)	[59]
	Acted against nine bacterial strains such as *Salmonella typhimurium, Escherichia coli, Shigella sonnei, Staphylococcus aureus, Pseudomonas aeruginosa, Streptococcus pneumonia, Streptococcus pyogenes, Legionella pneumophila,* and *Bordetella pertussis*	[63]
Antiviral effects	↓ Herpes simplex virus (HSV)	[62, 68]
	Human immunodeficiency virus (HIV)	[3, 67]
	Flaviviruses and pestiviruses	[69]
	Dengue virus (DENV1)	[71]
Larvicidal and ovicidal effects	Affected the larval growth of *Anopheles stephensi*	[81]
	Ovicidal activity against various age groups of *Aedes Stephens*	[82]
	Larvicidal and ovicidal activities against *Culex quinquefasciatus* Say and *Aedes aegypti* L.	[83]
Renoprotective effects	↓ Gentamicin-induced increase in serum creatinine, serum urea, and blood urea nitrogen levels	[86]
Antifertility effects	↓ Spermatogenesis	[94]
	↓ Degenerative changes in the seminiferous tubules, regression of Leydig cells, and regressive and/or degenerative changes in the epididymis, seminal vesicle,	[94]

Table 3: Continued.

Pharmacological effects	Mechanisms	References
	↓ ventral prostate, and coagulating glands	[94]
Antihyperglycemic activity	↓ TG	[24]
	↓ Blood glucose level	[99, 100, 102]
Hypolipidemic effects	↓ TC, TG, HDL-TC, and LDL-TC	[109]
	↓ Blood glucose, triglyceride, and LDL	[110]
Cardiovascular effects	Limiting blood flow to the brain, heart, and bodies of other organs	[112]
	Protect rat cardiomyocytes against hypoxia injury by increasing GSH and antioxidant enzyme	[113]
	↓ Coronary perfusion pressure	[114]
Inhibitory effects on platelet aggregation	↓ Platelet-activating factor (PAF)	[15]
	↑ eNOS-NO/cyclic GMP pathway	[120]
	↓ PLCγ2-PKC and PI3 kinase/Akt-MAPKs	
Inhibitory effects on NF-kappa B activation	↓ NF-κB via the covalent modification of reduced Cys62 of p50	[13]
	↓ NF-κB via blocking the binding of NF-κB oligonucleotides to nuclear proteins	[128]
(II) Clinical studies		
Anti-HIV effect	↑ CD4+ lymphocyte count	[3]
	↓ gp120-mediated cell fusion of HL2/3 cells with TZM-bl cells	[135]
Effects on upper respiratory tract infections	↓ Relieving the symptoms of fever and sore throat	[73]
	Tiredness, sleeplessness, sore throat, and nasal secretion	[136]

CAT: catalase; SOD: superoxide dismutase; GST: glutathione-S-transferase; LDH: lactate dehydrogenase; TBARS: thiobarbituric-acid-reactive substances; LPS: lipopolysaccharides; NO: nitric oxide; IL-2: interleukin-2; IFN-c: interferon-c; GOT: glutamate oxaloacetate transaminase; GPT: glutamate pyruvate transaminase; ALP: alkaline phosphatase; ACP: acid phosphatase; HBsAg: hepatitis B surface antigen; HBeAg: hepatitis B "e" antigen; ALT: alanine aminotransferase; TC: total cholesterol; TG: triglyceride; LDL: low-density lipoprotein; HDL: high-density lipoprotein; GHS: reduced glutathione; PLC-γ2: phospholipase C; PKC: protein kinase C; MAPK: mitogen-activated protein kinase; cGMP: cyclic guanosine monophosphate; eNOS: endothelial nitric oxide synthase; HSP: heat shock protein; MMP: matrix metalloproteinases.

taking place in clinical studies in patients. This summary offers pharmaceutical chemists and plant scientists additional thoughts for drug discovery. The combined drug discovery of andrographolide analogues will likely transform them into an effective assemblage of inflammation and cancer treatment in the future.

Acknowledgment

This work was supported by Grants from the National Science Council of Taiwan (NSC97-2320-B-038-016-MY3 and NSC100-2320-B-038-021-MY3).

References

[1] R. A. Kumar, K. Sridevi, N. Vijaya Kumar, S. Nanduri, and S. Rajagopal, "Anticancer and immunostimulatory compounds from *Andrographis paniculata*," *Journal of Ethnopharmacology*, vol. 92, no. 2-3, pp. 291–295, 2004.

[2] S. Rajagopal, R. A. Kumar, D. S. Deevi, C. Satyanarayana, and R. Rajagopalan, "Andrographolide, a potential cancer therapeutic agent isolated from *Andrographis paniculata*," *Journal of Experimental Therapeutics and Oncology*, vol. 3, no. 3, pp. 147–158, 2003.

[3] C. Calabrese, S. H. Berman, J. G. Babish et al., "A phase I trial of andrographolide in HIV positive patients and normal volunteers," *Phytotheraphy Research*, vol. 14, no. 5, pp. 333–338, 2000.

[4] P. K. Singha, S. Roy, and S. Dey, "Antimicrobial activity of *Andrographis paniculata*," *Fitoterapia*, vol. 74, no. 7-8, pp. 692–694, 2003.

[5] K. Jarukamjorn and N. Nemoto, "Pharmacological aspects of *Andrographis paniculata* on health and its major diterpenoid constituent andrographolide," *Journal of Health Science*, vol. 54, no. 4, pp. 370–381, 2008.

[6] T. Fujita, R. Fujitani, Y. Takeda et al., "On the ditrpenoids of *Andrographis paniculata*: X-ray crystallographic analysis of andrographolide and structure determination of new minor diterpenoids," *Chemical & Pharmaceutical Bulletin*, vol. 32, no. 6, pp. 2117–2125, 1984.

[7] C. J. Medforth, R. S. Chang, G. Q. Chen, M. M. Olmstead, and K. M. Smith, "A conformational study of diterpenoid lactones isolated from the Chinese medicinal herb *Andrographis*

paniculata," *Journal of the Chemical Society, Perkin Transactions 2*, no. 6, pp. 1011–1016, 1990.

[8] M. Rajani, N. Shrivastava, and M. N. Ravishankara, "A rapid method for isolation of andrographolide from *Andrographis paniculata* Nees (Kalmegh)," *Pharmaceutical Biology*, vol. 38, no. 3, pp. 204–209, 2000.

[9] Q. Du, G. Jerz, and P. Winterhalter, "Separation of andrographolide and neoandrographolide from the leaves of *Andrographis paniculata* using high-speed counter-current chromatography," *Journal of Chromatography A*, vol. 984, no. 1, pp. 147–151, 2003.

[10] L. Cui, F. Qiu, and X. Yao, "Isolation and identification of seven glucuronide conjugates of andrographolide in human urine," *Drug Metabolism and Disposition*, vol. 33, no. 4, pp. 555–562, 2005.

[11] L. Lomlim, N. Jirayupong, and A. Plubrukarn, "Heat-accelerated degradation of solid-state andrographolide," *Chemical & Pharmaceutical Bulletin*, vol. 51, no. 1, pp. 24–26, 2003.

[12] Y. C. Shen, C. F. Chen, and W. F. Chiou, "Andrographolide prevents oxygen radical production by human neutrophils: possible mechanism(s) involved in its anti-inflammatory effect," *British Journal of Pharmacology*, vol. 135, no. 2, pp. 399–406, 2002.

[13] Y. F. Xia, B. Q. Ye, Y. D. Li et al., "Andrographolide attenuates inflammation by inhibition of NF-κB activation through covalent modification of reduced cysteine 62 of p 50," *Journal of Immunology*, vol. 173, no. 6, pp. 4207–4217, 2004.

[14] E. Amroyan, E. Gabrielian, A. Panossian, G. Wikman, and H. Wagner, "Inhibitory effect of andrographolide from *Andrographis paniculata* on PAF-induced platelet aggregation," *Phytomedicine*, vol. 6, no. 1, pp. 27–31, 1999.

[15] W. J. Lu, J. J. Lee, D. S. Chou et al., "A novel role of andrographolide, an NF-kappa B inhibitor, on inhibition of platelet activation: the pivotal mechanisms of endothelial nitric oxide synthase/cyclic GMP," *Journal of Molecular Medicine*, vol. 89, no. 12, pp. 1263–1271, 2011.

[16] N. P. Trivedi and U. M. Rawal, "Hepatoprotective and antioxidant property of *Andrographis paniculata* (Nees) in BHC induced liver damage in mice," *Indian Journal of Experimental Biology*, vol. 39, no. 1, pp. 41–46, 2001.

[17] V. L. N. Reddy, S. M. Reddy, V. Ravikanth et al., "A new bis-andrographolide ether from *Andrographis paniculata* nees and evaluation of anti-HIV activity," *Natural Product Research*, vol. 19, no. 3, pp. 223–230, 2005.

[18] J. Xu, Z. Li, and M. Caoa, "Synergetic effect of *Andrographis paniculata* polysaccharide on diabetic nephropathy with andrographolide," *International Journal of Biological Macromolecule*, vol. 51, no. 5, pp. 738–742, 2012.

[19] M. G. Simic, "Mechanisms of inhibition of free-radical processes in mutagenesis and carcinogenesis," *Mutation Research*, vol. 202, no. 2, pp. 377–386, 1988.

[20] E. R. Sherwin, A. L. Branen, P. M. Davidson, and S. Salminen, *Food Additives*, Marcel Dekker, New York, NY, USA, 1990.

[21] G. K. Jayaprakasha, T. Selvi, and K. K. Sakariah, "Antibacterial and antioxidant activities of grape (Vitis vinifera) seed extracts," *Food Research International*, vol. 36, no. 2, pp. 117–122, 2003.

[22] M. Oktay, I. Gülçin, and O. I. Küfrevioğlu, "Determination of *in vitro* antioxidant activity of fennel (Foeniculum vulgare) seed extracts," *LWT-Food Science and Technology*, vol. 36, no. 2, pp. 263–271, 2003.

[23] N. Verma and M. Vinayak, "Antioxidant action of *Andrographis paniculata* on lymphoma," *Molecular Biology Reports*, vol. 35, no. 4, pp. 535–540, 2008.

[24] X. F. Zhang and B. K. H. Tan, "Anti-diabetic property of ethanolic extract of *Andrographis paniculata* in streptozotocin-diabetic rats," *Acta Pharmacologica Sinica*, vol. 21, no. 12, pp. 1157–1164, 2000.

[25] Y. C. Shen, C. F. Chen, and W. F. Chiou, "Suppression of rat neutrophil reactive oxygen species production and adhesion by the diterpenoid lactone andrographolide," *Planta Medica*, vol. 66, no. 4, pp. 314–317, 2000.

[26] F. L. Lin, S. J. Wu, S. C. Lee, and L. T. Ng, "Antioxidant, antioedema and analgesic activities of *Andrographis paniculata* extracts and their active constituent andrographolide," *Phytotherapy Research*, vol. 23, no. 7, pp. 958–964, 2009.

[27] W. L. Deng, "Outline of current clinical and pharmacological research on *Andrographis paniculata* in China," *Newsletters Chinese Herbal Medicine*, vol. 10,, pp. 27–31, 1978.

[28] J. Batkhuu, K. Hattori, F. Takano, S. Fushiya, K. I. Oshiman, and Y. Fujimiya, "Suppression of NO production in activated macrophages *in vitro* and *ex vivo* by neoandrographolide isolated from *Andrographis paniculata*," *Biological & Pharmaceutical Bulletin*, vol. 25, no. 9, pp. 1169–1174, 2002.

[29] J. Liu, Z. T. Wang, L. L. Ji, and B. X. Ge, "Inhibitory effects of neoandrographolide on nitric oxide and prostaglandin E2 production in LPS-stimulated murine macrophage," *Molecular and Cellular Biochemistry*, vol. 298, no. 1-2, pp. 49–57, 2007.

[30] W. F. Chiou, C. F. Chen, and J. J. Lin, "Mechanisms of suppression of inducible nitric oxide synthase (iNOS) expression in RAW 264.7 cells by andrographolide," *British Journal of Pharmacology*, vol. 129, no. 8, pp. 1553–1560, 2000.

[31] M. I. Iruretagoyena, S. E. Sepúlveda, J. P. Lezana et al., "Inhibition of nuclear factor-κB enhances the capacity of immature dendritic cells to induce antigen-specific tolerance in experimental autoimmune encephalomyelitis," *The Journal of Pharmacology and Experimental Therapeutics*, vol. 318, no. 1, pp. 59–67, 2006.

[32] A. B. Da Rocha, R. M. Lopes, and G. Schwartsmann, "Natural products in anticancer therapy," *Current Opinion in Pharmacology*, vol. 1, no. 4, pp. 364–369, 2001.

[33] G. A. Cordell, C. W. W. Beecher, and J. M. Pezzuto, "Can ethnopharmacology contribute to the development of new anticancer drugs?" *Journal of Ethnopharmacology*, vol. 32, no. 1–3, pp. 117–133, 1991.

[34] P. Siripong, B. Kongkathip, K. Preechanukool, P. Picha, K. Tunsuwan, and W. C. Taylor, "Cytotoxic diterpenoid constituents from *A. paniculata* Nees leaves," *Journal of Scientific Soceity of Thailand*, vol. 18, pp. 187–194, 1992.

[35] T. Matsuda, M. Kuroyanagi, S. Sugiyama, K. Umehara, A. Ueno, and K. Nishi, "Cell differentiation-inducing diterpenes from *Andrographis paniculata* NEES," *Chemical & Pharmaceutical Bulletin*, vol. 42, no. 6, pp. 1216–1225, 1994.

[36] S. Nanduri, V. K. Nyavanandi, S. S. R. Thunuguntla et al., "Synthesis and structure-activity relationships of andrographolide analogues as novel cytotoxic agents," *Bioorganic & Medicinal Chemistry Letters*, vol. 14, no. 18, pp. 4711–4717, 2004.

[37] M. D. Shi, H. H. Lin, Y. C. Lee, J. K. Chao, R. A. Lin, and J. H. Chen, "Inhibition of cell-cycle progression in human colorectal carcinoma Lovo cells by andrographolide," *Chemico-Biological Interactions*, vol. 174, no. 3, pp. 201–210, 2008.

[38] J. Li, H. Y. Cheung, Z. Zhang, G. K. L. Chan, and W. F. Fong, "Andrographolide induces cell cycle arrest at G2/M phase and

cell death in HepG2 cells via alteration of reactive oxygen species," *European Journal of Pharmacology*, vol. 568, no. 1–3, pp. 31–44, 2007.

[39] S. D. Manikam and J. Stanslas, "Andrographolide inhibits growth of acute promyelocytic leukaemia cells by inducing retinoic acid receptor-independent cell differentiation and apoptosis," *The Journal of Pharmacy and Pharmacology*, vol. 61, no. 1, pp. 69–78, 2009.

[40] C. G. Jiang, J. B. Li, F. R. Liu, T. Wu, M. Yu, and H. M. Xu, "Andrographolide inhibits the adhesion of gastric cancer cells to endothelial cells by blocking E-selectin expression," *Anticancer Research*, vol. 27, no. 4 B, pp. 2439–2447, 2007.

[41] J. C. Lim, T. K. Chan, D. S. Ng, S. R. Sagineedu, J. Stanslas, and W. S. Wong, "Andrographolide and its analogues: versatile bioactive molecules for combating inflammation and cancer," *Clinical and Experimental Pharmacology & Physiology*, vol. 39, no. 3, pp. 300–310, 2012.

[42] S. K. Hung, L. C. Hung, C. D. Kuo et al., "Andrographolide sensitizes Ras-transformed cells to radiation *in vitro* and *in vivo*," *International Journal of Radiation Oncology Biology Physics*, vol. 77, no. 4, pp. 1232–1239, 2010.

[43] K. Sheeja and G. Kuttan, "Activation of cytotoxic T lymphocyte responses and attenuation of tumor growth *in vivo* by *Andrographis paniculata* extract and andrographolide," *Immunopharmacology and Immunotoxicology*, vol. 29, no. 1, pp. 81–93, 2007.

[44] S. Kumar, H. S. Patil, P. Sharma et al., "Andrographolide inhibits osteopontin expression and breast tumor growth through down regulation of PI3 kinase/Akt signaling pathway," *Current Molecular Medicine*, vol. 12, no. 8, pp. 952–966, 2012.

[45] A. Puri, R. Saxena, R. P. Saxena, K. C. Saxena, V. Srivastava, and J. S. Tandon, "Immunostimulant agents from *Andrographis paniculata*," *Journal of Natural Products*, vol. 56, no. 7, pp. 995–999, 1993.

[46] A. Panossian, A. Kochikian, E. Gabrielian et al., "Effect of *Andrographis paniculata* extract on progesterone in blood plasma of pregnant rats," *Phytomedicine*, vol. 6, no. 3, pp. 157–162, 1999.

[47] M. I. Iruretagoyena, J. A. Tobar, P. A. González et al., "Andrographolide interferes with T cell activation and reduces experimental autoimmune encephalomyelitis in the mouse," *The Journal of Pharmacology and Experimental Therapeutics*, vol. 312, no. 1, pp. 366–372, 2005.

[48] R. A. Burgos, E. E. Caballero, N. S. Sánchez, R. A. Schroeder, G. K. Wikman, and J. L. Hancke, "Testicular toxicity assesment of *Andrographis paniculata* dried extract in rats," *Journal of Ethnopharmacology*, vol. 58, no. 3, pp. 219–224, 1997.

[49] L. H. Qin, L. Kong, G. J. Shi, Z. T. Wang, and B. X. Ge, "Andrographolide inhibits the production of TNF-α and interleukin-12 in lipopolysaccharide-stimulated macrophages: role of mitogen-activated protein kinases," *Biological & Pharmaceutical Bulletin*, vol. 29, no. 2, pp. 220–224, 2006.

[50] K. Maiti, A. Gantait, K. Mukherjee, B. P. Saha, and P. K. Mukherjee, "Therapeutic potentials of andrographolide from *Andrographis paniculata*: a review," *Journal of Natural Remedies*, vol. 6, no. 1, pp. 1–13, 2006.

[51] P. K. Mukherjee, *Quality Control on Herbal Drugs*, Business Horizons, New Delhi, India, 1st edition, 2002.

[52] V. J. Ram, "Herbal preparations as a source of hepatoprotective agents," *Drug News and Perspectives*, vol. 14, no. 6, pp. 353–363, 2001.

[53] J. S. Rajkumar, M. G. Sekar, and S. K. Mitra, "Safety and efficacy of oral HD-03/ES given for six months in patients with chronic hepatitis B virus infection," *World Journal of Gastroenterology*, vol. 13, no. 30, pp. 4103–4107, 2007.

[54] G. Shi, Z. Zhang, R. Zhang et al., "Protective effect of andrographolide against concanavalin A-induced liver injury," *Naunyn's Schmiedebergs Archives of Pharmacology*, vol. 385, no. 1, pp. 69–79, 2012.

[55] B. Shukla, P. K. S. Visen, G. K. Patnaik, and B. N. Dhawan, "Choleretic effect of andrographolide in rats and guinea pigs," *Planta Medica*, vol. 58, no. 2, pp. 146–149, 1992.

[56] P. K. Singha, S. Roy, and S. Dey, "Protective activity of andrographolide and arabinogalactan proteins from *Andrographis paniculata* Nees. against ethanol-induced toxicity in mice," *Journal of Ethnopharmacology*, vol. 111, no. 1, pp. 13–21, 2007.

[57] A. C. Rana and Y. Avadhoot, "Hepatoprotective effects of Andrograhphis paniculata against carbon tetrachloride-induced liver damage," *Archives of Pharmacal Research*, vol. 14, no. 1, pp. 93–95, 1991.

[58] P. K. S. Visen, B. Shukia, G. K. Patnaik, and B. N. Dhawan, "Andrographolide protects rat hepatocytes against paracetamol-induced damage," *Journal of Ethnopharmacology*, vol. 40, no. 2, pp. 131–136, 1993.

[59] R. M. Kunwar, K. P. Shrestha, and R. W. Bussmann, "Traditional herbal medicine in far-west Nepal: a pharmacological appraisal," *Journal of Ethnobiology and Ethnomedicine*, vol. 6, article 35, pp. 1–18, 2010.

[60] M. R. Zaidan, A. Noor Rain, A. R. Badrul, A. Adlin, A. Norazah, and I. Zakiah, "*In vitro* screening of five local medicinal plants for antibacterial activity using disc diffusion method," *Tropical Biomedicine*, vol. 22, no. 2, pp. 165–170, 2005.

[61] S. P. Voravuthikunchai and S. Limsuwan, "Medicinal plant extracts as anti-Escherichia coli O157:H7 agents and their effects on bacterial cell aggregation," *Journal of Food Protection*, vol. 69, no. 10, pp. 2336–2341, 2006.

[62] C. Wiart, K. Kumar, M. Y. Yusof, H. Hamimah, Z. M. Fauzi, and M. Sulaiman, "Antiviral properties of ent-labdene diterpenes of *Andrographis paniculata* Nees, inhibitors of herpes simplex virus type 1," *Phytotherapy Research*, vol. 19, no. 12, pp. 1069–1070, 2005.

[63] N. N. N. A. Rahman, T. Furuta, S. Kojima, K. Takane, and M. Ali Mohd, "Antimalarial activity of extracts of Malaysian medicinal plants," *Journal of Ethnopharmacology*, vol. 64, no. 3, pp. 249–254, 1999.

[64] K. Mishra, A. P. Dash, B. K. Swain, and N. Dey, "Anti-malarial activities of *Andrographis paniculata* and Hedyotis corymbosa extracts and their combination with curcumin," *Malaria Journal*, vol. 8, no. 1, article 26, 2009.

[65] N. Poolsup, C. Suthisisang, S. Prathanturarug, A. Asawamekin, and U. Chanchareon, "*Andrographis paniculata* in the symptomatic treatment of uncomplicated upper respiratory tract infection: systematic review of randomized controlled trials," *Journal of Clinical Pharmacy and Therapeutics*, vol. 29, no. 1, pp. 37–45, 2004.

[66] Y. Xu, R. L. Marshall, and T. K. S. Mukkur, "An investigation on the antimicrobial activity of *Andrographis paniculata* extracts and andrographolide *in vitro*," *Asian Journal of Plant Sciences*, vol. 5, no. 3, pp. 527–530, 2006.

[67] R. S. Chang, L. Ding, G. Q. Chen, Q. C. Pan, Z. L. Zhao, and K. M. Smith, "Dehydroandrographolide succinic acid monoester as an inhibitor against the human immunodeficiency virus (43225)," *Proceedings of the Society for Experimental Biology and Medicine*, vol. 197, no. 1, pp. 59–66, 1991.

[68] S. Seubsasana, C. Pientong, T. Ekalaksananan, S. Thongchai, and C. Aromdee, "A potential andrographolide analogue against the replication of herpes simplex virus type 1 in vero cells," *Medicinal Chemistry*, vol. 7, no. 3, pp. 237–244, 2011.

[69] King Spalding LLP, "Andrographolide derivatives to treat viral infections," US20060333785; 2006.

[70] T. P. Lin, S. Y. Chen, P. D. Duh, L. K. Chang, and Y. N. Liu, "Inhibition of the Epstein-Barr virus lytic cycle by andrographolide," *Biological & Pharmaceutical Bulletin*, vol. 31, no. 11, pp. 2018–2023, 2008.

[71] L. I. C. Tang, A. P. K. Ling, R. Y. Koh, S. M. Chye, and K. G. L. Voon, "Screening of anti-dengue activity in methanolic extracts of medicinal plants," *BMC Complementary and Alternative Medicine*, vol. 12, no. 3, pp. 1–10, 2012.

[72] S. Madav, H. C. Tripathi, Tandan, and S. K. Mishra, "Analgesic, antipyretic and antiulcerogenic effects of andrographolide," *Indian Journal of Pharmaceutical Sciences*, vol. 57, no. 3, pp. 121–125, 1995.

[73] V. Thamlikitkul, S. Theerapong, P. Boonroj et al., "Efficacy of *Andrographis paniculata*, nees for pharyngotonsillitis in adults," *Journal of the Medical Association of Thailand*, vol. 74, no. 10, pp. 437–442, 1991.

[74] V. K. Dua, V. P. Ojha, S. Biswas, N. Valecha, N. Singh, and V. P. Sharma, "Antimalarial activity of different fractions isolated from the leaves of *Andrographis paniculata*," *Journal of Medicinal and Aromatic Plant Sciences*, vol. 21, pp. 1069–1073, 1999.

[75] P. Misra, N. L. Pal, P. Y. Guru, J. C. Katiyar, V. Srivastava, and J. S. Tandon, "Antimalarial activity of *Andrographis paniculata* (Kalmegh) against Plasmodium berghei NK 65 in Mastomys natalensis," *International Journal of Pharmacognosy*, vol. 30, no. 4, pp. 263–274, 1992.

[76] B. D. Sheeja, D. Sindhu, J. Ebanasar, and S. Jeeva, "The Larvicidal activity of *Andrographis paniculata* (Burm. f) Nees against Culex quinquefasciatus Say (Insecta: Diptera-Culicidae), a filarial vector," *Asian Pacific Journal of Tropical Disease*, pp. S574–S578, 2012.

[77] R. Babu, K. Murugan, and v, "Interactive effect of neem seed kernel and neem gum extracts on the control of Culex quinquefasciatus say," *Neem Newsletterno*, vol. 15, no. 2, pp. 9–11, 1998.

[78] M. R. Venkatachalam and A. Jebanesan, "Larvicidal activity of Hydrocotyle javanica Thunb. (Apiaceae) extract against Culex quinquefasciatus," *Journal of Experimental Zoology*, vol. 4, no. 1, pp. 99–101, 2001.

[79] T. Pushpanathan, A. Jebanesan, and M. Govindarajan, "Larvicidal, ovicidal and repellent activities of Cymbopogan citratus Stapf (Graminae) essential oil against the filarial mosquito Culex quinquefasciatus (Say) (Diptera : Culicidae)," *Tropical biomedicine*, vol. 23, no. 2, pp. 208–212, 2006.

[80] S. Mandal, "Exploration of larvicidal and adult emergence inhibition activities of Ricinus communis seed extract against three potential mosquito vectors in Kolkata, India," *Asian Pacific Journal of Tropical Medicine*, vol. 3, no. 8, pp. 605–609, 2010.

[81] C. Kuppusamy and K. Murugan, "Mosquitocidal effect of Andographis paniculata Nees against the malaria vector, *Anopheles stephensi* Liston (Diptera: culicidae)," *International Journal of Integrative Biology*, vol. 5, no. 2, pp. 75–81, 2009.

[82] K. Chenniappan and M. Kadarkarai, "Oviposition deterrent, ovicidal and gravid mortality effects of ethanolic extract of *Andrographis paniculata* Nees against the malarial vector Anopheles stephensi Liston (Diptera: Culicidae)," *Entomological Research*, vol. 38, no. 2, pp. 119–125, 2008.

[83] M. Govindarajan, "Evaluation of *Andrographis paniculata* Burm.f. (Family:Acanthaceae) extracts against Culex quinquefasciatus (Say.) and Aedes aegypti (Linn.) (Diptera:Culicidae)," *Asian Pacific Journal of Tropical Medicine*, vol. 4, no. 3, pp. 176–181, 2011.

[84] J. Coresh, E. Selvin, L. A. Stevens et al., "Prevalence of chronic kidney disease in the United States," *Journal of the American Medical Association*, vol. 298, no. 17, pp. 2038–2047, 2007.

[85] S. A. Jaffar Naqvi, "Commentary on acute renal failure in Asian region," *Nephrology*, vol. 2, p. 213, 2007.

[86] P. Singh, M. M. Srivastava, and L. D. Khemani, "Renoprotective effects of *Andrographis paniculata* (Burm. f.) Nees in rats," *Upsala Journal of Medical Sciences*, vol. 114, no. 3, pp. 136–139, 2009.

[87] R. N. Chopra, S. L. Nayar, and I. C. Chopra, *Glossary of Indian Medicinal Plants*, Publications and Information Directorate, CSIR, New Delhi, India, 1990.

[88] M. L. Dhar, M. M. Dhar, B. N. Dhawan, B. N. Mehrotra, and C. Ray, "Screening of Indian plants for biological activity: I," *Indian Journal of Experimental Biology*, vol. 6, no. 4, pp. 232–247, 1968.

[89] D. S. Bhakuni, M. L. Dhar, M. M. Dhar, B. N. Dhawan, and B. N. Mehrotra, "Screening of Indian plants for biological activity. II," *Indian Journal of Experimental Biology*, vol. 7, no. 4, pp. 250–262, 1969.

[90] M. Shamsuzzoha, M. S. Rahman, M. M. Ahmed, and A. K. Islam, "Antifertility effect in mice of medicinal plant of family acanthaceae," *The Lancet*, vol. 2, no. 8095, p. 900, 1978.

[91] H. M. Chang and P. P. H. But, *Pharmacology and Applications of Chinese Materia Medica*, vol. 2, World Scientific, Singapore, 1987, English translation by Shem Chang-Shing Yeung, Sih Cheng-Yao and Lai-Ling Wang (Chinese Medicinal Material Research Centre, the Chinese University of Hong Kong).

[92] M. S. Zoha, A. H. Hussain, and S. A. Choudhury, "Antifertility effect of *Andrographis paniculata* in mice," *Bangladesh Medical Research Council Bulletin*, vol. 15, no. 1, pp. 34–37, 1989.

[93] M. A. Akbarsha, B. Manivannan, K. S. Hamid, and B. Vijayan, "Antifertility effect of *Andrographis paniculata* (Nees) in male albino rat," *Indian Journal of Experimental Biology*, vol. 28, no. 5, pp. 421–426, 1990.

[94] M. A. Akbarsha and P. Murugaian, "Aspects of the male reproductive toxicity/male antifertility property of andrographolide in albino rats: effect on the testis and the cauda epididymidal spermatozoa," *Phytother Research*, vol. 14, no. 6, pp. 432–435, 2000.

[95] J. Sattayasai, S. Srisuwan, T. Arkaravichien, and C. Aromdee, "Effects of andrographolide on sexual functions, vascular reactivity and serum testosterone level in rodents," *Food and Chemical Toxicology*, vol. 48, no. 7, pp. 1934–1938, 2010.

[96] F. N. Ziyadeh and K. Sharma, "Overview: combating diabetic nephropathy," *Journal of the American Society of Nephrology*, vol. 14, no. 5, pp. 1355–1357, 2003.

[97] B. M. Brenner, M. E. Cooper, D. De Zeeuw et al., "Effects of losartan on renal and cardiovascular outcomes in patients with type 2 diabetes and nephropathy," *The New England Journal of Medicine*, vol. 345, no. 12, pp. 861–869, 2001.

[98] M. Borhanuddin, M. Shamsuzzoha, and A. H. Hussain, "Hypoglycaemic effects of *Andrographis paniculata* Nees on non-diabetic rabbits," *Bangladesh Medical Research Council Bulletin*, vol. 20, no. 1, pp. 24–26, 1994.

[99] R. Husen, A. H. L. Pihie, and M. Nallappan, "Screening for antihyperglycaemic activity in several local herbs of Malaysia," *Journal of Ethnopharmacology*, vol. 95, no. 2-3, pp. 205–208, 2004.

[100] A. M. Dandu and N. M. Inamdar, "Evaluation of beneficial effects of antioxidant properties of aqueous leaf extract of *Andrographis paniculata* in STZ-induced diabetes," *Pakistan Journal of Pharmaceutical Sciences*, vol. 22, no. 1, pp. 49–52, 2009.

[101] B. A. S. Reyes, N. D. Bautista, N. C. Tanquilut et al., "Anti-diabetic potentials of Momordica charantia and *Andrographis paniculata* and their effects on estrous cyclicity of alloxan-induced diabetic rats," *Journal of Ethnopharmacology*, vol. 105, no. 1-2, pp. 196–200, 2006.

[102] B. C. Yu, C. R. Hung, W. C. Chen, and J. T. Cheng, "Antihyperglycemic effect of andrographolide in streptozotocin-induced diabetic rats," *Planta Medica*, vol. 69, no. 12, pp. 1075–1079, 2003.

[103] A. Wibudi, B. Kiranadi, W. Manalu, A. winarto, and S. Suyono, "The traditional plant, *Andrographis paniculata* (Sambiloto), exhibits insulin-releasing actions *in vitro*," *Acta medica Indonesiana*, vol. 40, no. 2, pp. 63–68, 2008.

[104] R. Subramanian, M. Z. Asmawi, and A. Sadikun, "*In vitro* α-glucosidase and α-amylase enzyme inhibitory effects of *Andrographis paniculata* extract and andrographolide," *Acta Biochimica Polonica*, vol. 55, no. 2, pp. 391–398, 2008.

[105] J. Stamler, M. L. Daviglus, D. B. Garside, A. R. Dyer, P. Greenland, and J. D. Neaton, "Relationship of baseline serum cholesterol levels in 3 large cohorts of younger men to long-term coronary, cardiovascular, and all-cause mortality and to longevity," *Journal of the American Medical Association*, vol. 284, no. 3, pp. 311–318, 2000.

[106] M. Briel, I. Ferreira-Gonzalez, J. J. You et al., "Association between change in high density lipoprotein cholesterol and cardiovascular disease morbidity and mortality: systematic review and meta-regression analysis," *British Medical Journal*, vol. 338, no. 7693, p. b92, 2009.

[107] F. M. Refaie, A. Y. Esmat, S. M. A. Gawad, A. M. Ibrahim, and M. A. Mohamed, "The antihyperlipidemic activities of 4(3H) quinazolinone and two halogenated derivatives in rats," *Lipids in Health and Disease*, vol. 4, article 22, 2005.

[108] A. M. Al-Attar, "Hypolipidemic effects of coenzyme Q10 in experimentally induced hypercholesterolemic model in female rats," *American Journal of Pharmacology and Toxicology*, vol. 5, no. 1, pp. 14–23, 2010.

[109] T. Yang, H. X. Shi, Z. S. Wang, and Z. H. Wang, "Hypolipidemic effects of andrographolide and neoandrographolide in mice and rats," *Phytotherapy Research*, 2012.

[110] A. E. Nugroho, M. Andrie, N. K. Warditiani, E. Siswanto, S. Pramono E, and Lukitaningsih, "Antidiabetic and antihiperlipidemic effect of *Andrographis paniculata* (Burm. f.) Nees and andrographolide in high-fructose-fat-fed rats," *Indian Journal of Pharmacology*, vol. 44, no. 3, pp. 377–381, 2012.

[111] H. W. Wang, H. Y. Zhao, and S. Q. Xiang, "Effects of *Andrographis paniculata* component on nitric oxide, endothelin and lipid peroxidation in experimental atherosclerotic rabbits," *Zhongguo Zhong Xi Yi Jie He Za Zhi*, vol. 17, no. 9, pp. 547–549, 1997.

[112] L. Y. Huang, "The effects of andrographolide on experimental blood deficiency of cardiac muscle," *Chinese Herbal Medicine*, vol. 18, pp. 26–28, 1987.

[113] A. Y. H. Woo, M. M. Y. Waye, S. K. W. Tsui, S. T. W. Yeung, and C. H. K. Cheng, "Andrographolide up-regulates cellular-reduced glutathione level and protects cardiomyocytes against hypoxia/reoxygenation injury," *The Journal of Pharmacology and Experimental Therapeutics*, vol. 325, no. 1, pp. 226–235, 2008.

[114] K. Awang, N. H. Abdullah, A. H. Hadi, and Y. S. Fong, "Cardiovascular activity of labdane diterpenes from *Andrographis paniculata* in isolated rat hearts," *Journal of Biomedicine and Biotechnology*, vol. 2012, Article ID 876458, 5 pages, 2012.

[115] D. Wang and H. Zhao, "Experimental studies on prevention of atherosclerotic arterial stenosis and restenosis after angioplasty with *Andrographis paniculata* Nees and Fish Oil," *Journal of Tongji Medical University*, vol. 13, no. 4, pp. 193–198, 1993.

[116] H. Zhao and W. Fang, "Protective effects of *Andrographis paniculata* Nees on post-infarction myocardium in experimental dogs," *Journal of Tongji Medical University*, vol. 10, no. 4, pp. 212–217, 1990.

[117] G. Hsiao, K. H. Lin, Y. Chang et al., "Protective mechanisms of inosine in platelet activation and cerebral ischemic damage," *Arteriosclerosis, Thrombosis, and Vascular Biology*, vol. 25, no. 9, pp. 1998–2004, 2005.

[118] P. von Hundelshausen and C. Weber, "Platelets as immune cells: bridging inflammation and cardiovascular disease," *Circulation Research*, vol. 100, no. 1, pp. 27–40, 2007.

[119] P. Thisoda, N. Rangkadilok, N. Pholphana, L. Worasuttayangkurn, S. Ruchirawat, and J. Satayavivad, "Inhibitory effect of *Andrographis paniculata* extract and its active diterpenoids on platelet aggregation," *European Journal of Pharmacology*, vol. 553, no. 1–3, pp. 39–45, 2006.

[120] W. J. Lu, K. H. Lin, M. J. Hsu, D. S. Chou, G. Hsiao, and J. R. Sheu, "Suppression of NF-κB signaling by andrographolide with a novel mechanism in human platelets: regulatory roles of the p38 MAPK-hydroxyl radical-ERK2 cascade," *Biochemical Pharmacology*, vol. 84, pp. 914–924, 2012.

[121] Y. Z. Zhang, J. Z. Tang, and Y. J. Zhang, "Study of *Andrographis paniculata* extracts on antiplatelet aggregation and release reaction and its mechanism," *Zhongguo Zhong Xi Yi Jie He Za Zhi*, vol. 14, no. 1, pp. 28–5, 1994.

[122] M. Karin, Y. Yamamoto, and Q. M. Wang, "The IKK NF-κB system: a treasure trove for drug development," *Nature Reviews Drug Discovery*, vol. 3, no. 1, pp. 17–26, 2004.

[123] K. T. Ku, Y. L. Huang, Y. J. Huang, and W. F. Chiou, "Miyabenol A inhibits LPS-induced NO production via IKK/IκB inactivation in RAW 264.7 macrophages: possible involvement of the p38 and PI3K pathways," *Journal of Agricultural and Food Chemistry*, vol. 56, no. 19, pp. 8911–8918, 2008.

[124] Y. H. Hong, W. W. Chao, M. L. Chen, and B. F. Lin, "Ethyl acetate extracts of alfalfa (Medicago sativa L.) sprouts inhibit lipopolysaccharide-induced inflammation *in vitro* and *in vivo*," *Journal of Biomedical Science*, vol. 16, no. 1, article 64, 2009.

[125] K. J. Yun, D. J. Koh, S. H. Kim et al., "Anti-inflammatory effects of sinapic acid through the suppression of inducible nitric oxide synthase, cyclooxygase-2, and proinflammatory cytokines expressions via nuclear factor-κB inactivation," *Journal of Agricultural and Food Chemistry*, vol. 56, no. 21, pp. 10265–10272, 2008.

[126] Y. Yamamoto and R. B. Gaynor, "Therapeutic potential of inhibition of the NF-κB pathway in the treatment of inflammation and cancer," *The Journal of Clinical Investigation*, vol. 107, no. 2, pp. 135–142, 2001.

[127] M. A. Hidalgo, A. Romero, J. Figueroa et al., "Andrographolide interferes with binding of nuclear factor-κB to DNA in HL-60-derived neutrophilic cells," *British Journal of Pharmacology*, vol. 144, no. 5, pp. 680–686, 2005.

[128] Z. Bao, S. Guan, C. Cheng et al., "A novel antiinflammatory role for andrographolide in asthma via inhibition of the nuclear factor-κb pathway," *American Journal of Respiratory and Critical Care Medicine*, vol. 179, no. 8, pp. 657–665, 2009.

[129] C. Y. Hsieh, M. J. Hsu, G. Hsiao et al., "Andrographolide enhances nuclear factor-κB subunit p65 Ser 536 dephosphorylation through activation of protein phosphatase 2A in vascular smooth muscle cells," *The Journal of Biological Chemistry*, vol. 286, no. 8, pp. 5942–5955, 2011.

[130] E. A. Susan and A. Mays, "Pharmacology," in *The Merck Vetrinary Manual*, p. 1638, Merck and Co., New York, NY, USA, 9th edition, 2005.

[131] S. Mishra, S. K. Tiwary, A. Kakkar, and A. K. Pandey, "Chemoprofiling of *Andrographis paniculata* (kalmegh) for its andrographolide conten in Mathya predesh, India," *International Journal of Phrama and Biological Science*, vol. 1, no. 2, pp. 1–5, 2010.

[132] Y. El Safadi, J. C. Paillarte, G. Laumond et al., "5-modified-2′-dU and 2′-dC as mutagenic anti HIV-1 proliferation agents: synthesis and activity," *Journal of Medicinal Chemistry*, vol. 53, no. 4, pp. 1534–1545, 2010.

[133] X. K. Zhu, J. Guan, Z. Xiao, L. M. Cosentino, and K. H. Lee, "Anti-AIDS agents. Part 61: anti-HIV activity of new podophyllotoxin derivatives," *Bioorganic and Medicinal Chemistry*, vol. 12, no. 15, pp. 4267–4273, 2004.

[134] Y. Mehellou and E. De Clercq, "Twenty-six years of anti-HIV drug discovery: where do we stand and where do we go?" *Journal of Medicinal Chemistry*, vol. 53, no. 2, pp. 521–538, 2010.

[135] M. M. Uttekar, T. Das, R. S. Pawar et al., "Anti-HIV activity of semisynthetic derivatives of andrographolide and computational study of HIV-1 gp120 protein binding," *European Journal of Medicinal Chemistry*, vol. 56, pp. 368–374, 2012.

[136] D. D. Cáceres, J. L. Hancke, R. A. Burgos, F. Sandberg, and G. K. Wikman, "Use of visual analogue scale measurements (VAS) to asses the effectiveness of standardized *Andrographis paniculata* extract SHA-10 in reducing the symptoms of common cold. A randomized double blind-placebo study," *Phytomedicine*, vol. 6, no. 4, pp. 217–223, 1999.

[137] S. Sakila, N. Begum, S. Kawsar, Z. A. Begum, and M. S. Zoha, "Relationship of anti-fertility effects of *Andrographis paniculata* and hormonal assay in female rats," *Bangladesh Journal of Medical Science*, vol. 8, no. 1-2, pp. 10–14, 2009.

[138] S. S. Handa and A. Sharma, "Hepatoprotective activity of Andrographolide from *Andrographis paniculata* against carbontetrachloride," *Indian Journal of Medical Research. Section B*, vol. 92, pp. 276–283, 1990.

[139] S. Y. Guo, D. Z. Li, W. S. Li, A. H. Fu, and L. H. Zhang, "Study of the toxicity of andrographolide in rabbits," *The Journal of Beijing Medical University*, vol. 5, pp. 422–428, 1988.

[140] X. B. Suo, H. Zhang, and Y. Q. Wang, "HPLC determination of andrographolide in rat whole blood: study on the pharmacokinetics of andrographolide incorporated in liposomes and tablets," *Biomedical Chromatography*, vol. 21, no. 7, pp. 730–734, 2007.

Hindawi Publishing Corporation
Evidence-Based Complementary and Alternative Medicine
Volume 2013, Article ID 514610, 7 pages
http://dx.doi.org/10.1155/2013/514610

Research Article

Electroacupuncture and Acupuncture Promote the Rat's Transected Median Nerve Regeneration

C. Y. Ho,[1,2] C. H. Yao,[1,3] W. C. Chen,[1] W. C. Shen,[1] and D. T. Bau[4]

[1] *School of Chinese Medicine, Institute of Chinese Medicine, China Medical University, 404 Yuh-Der Road, Taichung 40447, Taiwan*
[2] *Departments of Family Medicine, China Medical University Hospital, 404 Yuh-Der Road, Taichung 40447, Taiwan*
[3] *Department of Biomedical Imaging and Radiological Science, China Medical University Hospital, 404 Yuh-Der Road, Taichung 40447, Taiwan*
[4] *Graduate Institute of Clinical Medical Science, China Medical University, 404 Yuh-Der Road, Taichung 40447, Taiwan*

Correspondence should be addressed to D. T. Bau; samsam172@yahoo.com.tw

Received 26 December 2012; Accepted 9 February 2013

Academic Editor: Yueh-Sheng Chen

Background. Acupuncture and electroacupuncture treatments of damaged nerves may aid nerve regeneration related to hindlimb function, but the effects on the forelimb-related median nerve were not known. *Methods*. A gap was made in the median nerve of each rat by suturing the stumps into silicone rubber tubes. The influences of acupuncture and electroacupuncture treatments on transected median nerve regeneration were evaluated from morphological, electrophysiological, and functional angles. *Results*. Morphologically, the group receiving acupuncture and electroacupuncture treatments had larger total nerve area and blood vessel number compared with the controls. Electrophysiologically, the group receiving electroacupuncture had significantly larger amplitude and larger area of the evoked muscle action potentials compared with the controls. Functionally, the acupuncture and electroacupuncture treatments enhanced the injured paw's ability to regain its grasping power and resulted in a faster efficiency to a new bilateral balance. *Conclusion*. Our findings provide multiapproach evidence of the efficacy of acupuncture and electroacupuncture treatments to the regeneration of median nerve. Indeed, acupuncture and electroacupuncture appear to have positive effects on the regeneration processes. This platform is beneficial to further study the clinical application of acupuncture and electroacupuncture alternative treatments on nerve-injured patients.

1. Introduction

Peripheral nerve injury is an important issue in the world and represents a series of highly specialized processes of nerve regeneration [1]. The techniques of using silicone rubber to bridge a severed nerve provide a method for observing the regenerative processes. While most researches focus on the lower limbs injury model, upper limbs injuries are in fact more commonly observed in clinical trauma, especially median nerve injury [2, 3]. Recently, application of combining traditional Chinese acupuncture and electroacupuncture to stimulate nerve regeneration has become the mainstream treatment in clinical rehabilitation and related basic research [4, 5]. However, the effects of acupuncture and electroacupuncture were still controversial and seldom compared together, and had been evaluated from multiple approaches. Therefore, it is of great interest and urgent need to evaluate the influences of acupuncture and electroacupuncture on median nerve regeneration simultaneously and from multiple angles.

Acupuncture and electroacupuncture cause physiobiological effects that promote movement and function after peripheral nerve injury in individuals [6, 7]. Several researches have revealed that a low frequency electroacupuncture is a better approach to promote nerve regeneration after trauma injury [8, 9]. Therefore, it is reasonable to assume that electrical stimulation can have positive impacts on nerve regeneration. As a clinical physician, the clinical outcomes that resulted from rehabilitation medicine must be taken into consideration at first priority in which treatment is most likely to be safe and effective. Acupuncture and electroacupuncture provide a safe and effective way to help patients' rehabilitation after trauma accident. To the best of

our knowledge, there are two pilot studies reported by Yao et al. using the conduit tube to investigate the effects of electrical stimulation at different frequencies and current levels on regenerating sciatica nerves [10, 11]. Besides Bertelli's model, there was little literature available that described the rat's upper limb's nerve injury model and discussed the different nerve regeneration rates, especially for common diseases like median nerve injury [12]. Because allograft and autograft nerve implantation lacks the availability of experimental models to evaluate the nerve regeneration condition, the nerve conduit provides a state-of-the-art platform. Therefore, the objective of this study is to determine whether acupuncture and/or electroacupuncture can serve as an effective clinical strategy for improving functional recovery after a median nerve transection.

2. Methods

2.1. Silicone Rubber Tube Entubulation. Twenty-one adult Sprague-Dawley rats received placement of silicone rubber tube. First, all of the rats were surgical with inhalation anesthetic technique (AErrane; Baxter, Deerfield, IL, USA). The left arms and forelimbs of the rats were sheaved. Then, fascia and muscle were separated using blunt dissection after incising skin, and the left median nerve was severed into proximal and distal segments at, forelimb. Continuously the proximal and distal stumps were fixed with a simple 9-0 nylon direct suture through the nerve epineurium and silicone rubber tube (1.47 mm inter diameter, 1.96 mm outer diameter; Helix Medical, Carpinteria, CA, USA). Both the proximal and distal nerve segments were severed to the depth of 1 mm into the chamber, leaving a 5 mm gap between the bridge stumps. The muscle layer was sutured with 4-0 chromic gut sutures, and the skin was closed with 2-0 silk sutures. All animals were reared in temperature (22°C)- and humidity (45%)-controlled rooms with 12-hour light-dark cycles, and they had access to food and water ad libitum.

2.2. Acupuncture and Electroacupuncture Protocols. The acupuncture and electroacupuncture treatment protocols are similar to that previously reported [13]. Briefly, their left forearms were extended, and left paws were held in place by rubber tapes. One stainless steel needle electrode (0.35 mm outer diameter, 12 mm length) connected to the negative wick (cathode) of a stimulator (Trio 300, Ito, Japan) was inserted aseptically into the middle aspect of the wrist (Da-Ling, PC7), and another positive electrode (anode) was positioned around the site of the arm (Quze, PC3) along with pericardium meridian. The positive and negative stimulating sites were located near the proximal and distal ends of the implanted silicone tubes, respectively. The depth of insertion varied from 0.5 cm to 1 cm according to the thickness of skin and fatty tissues. The stimulation was applied to the animals for 15 minutes every other day beginning a week after the nerve repair. The reason that we did not perform the electrical stimulation on animals immediately after the nerve repair was to avoid the loosening of suture line on the skin because of muscle contraction, which might cause serious inflammatory reactions. All the animals were divided into three groups according to the current intensity of the electrical stimulation they received. In group A ($n = 7$), animals were the controls which received empty silicone rubber chambers, and the stimulator did not deliver current to the two stainless steel needle electrodes. In group B ($n = 7$), animals received a treatment of acupuncture stimulation after their injured nerves were bridged with the silicone rubber tubes. Similarly, animals in groups C ($n = 7$) received electrical stimulation of frequency 2 Hz, and the current intensity was 1 mA to produce a visual muscle contraction as the proper response of acupuncture.

2.3. Electrophysiological Measurements. After the entubulation duration of 5 weeks, all rats were reanesthetized, and the left hand median nerve was exposed. Then, the nerve was stimulated with supramaximal stimulus intensity through a pair of needle electrodes placed directly on the median nerve trunk, 5 mm proximal to the transection site. Latency, amplitude, muscle action potentials (MAPs) area, and nerve conduction velocity (NCV) were recorded from the thenar muscle with microneedle electrodes linked to a computer system (Biopac Systems, Goleta, CA, USA). The latency was recorded from the stimulus to the starting points of the first negative skew. The amplitude and the area under the MAP curve from the baseline to the maximal negative peak were measured. The MAP was used to evaluate the NCV, which was performed by placing the recording electrodes in the thenar muscle and stimulating the median nerve proximally. The NCV was then calculated by dividing the distance between the stimulating sites by the difference in latency period.

2.4. Histological Measurements. After the electrophysiologic MAP measurements, rapidly the regenerated median nerve was taken out. The median nerve sections were taken from the middle regions of the regenerated nerve in the chamber. After the fixation of glutaraldehyde (Merck, Whitehouse Station, NJ, USA), the nerve tissue was postfixed in 0.5% osmium tetroxide (Sigma Chemical Co., St. Louis, MO, USA), dehydrated in a series of graded alcohols (70, 80, 95, and 100%; Merck, Whitehouse Station, NJ, USA) for 60 minutes each, and embedded using a JB-4 Embedding Kit (Polysciences, Warrington, PA, USA). The tissue was then cut to 5 mm thickness by using a microtome with a dry glass knife and stained with toluidine blue (Sigma Chemical Co., St. Louis, MO, USA). Using an optical microscope (Olympus IX70, Olympus Optical Co., Japan) with an image analyzer system (Image-Pro Lite, Media Cybernetics, Bethesda, MD, USA), the number of neural components in each nerve section was counted. Myelinated axons in a frame of image randomly selected from each nerve specimen at a magnification of 400x were counted. When the axons in one image had been counted, those of a second image were counted, and so on until all images had been included. The total number of myelinated axons and their areas was then determined from the number of components in each image and the total number of images occupied by the nerve cross section. In addition, the total nerve areas including the epineurial and the endoneurial areas were measured under the microscope at 40x. Similarly, the areas of blood vessels were also measured.

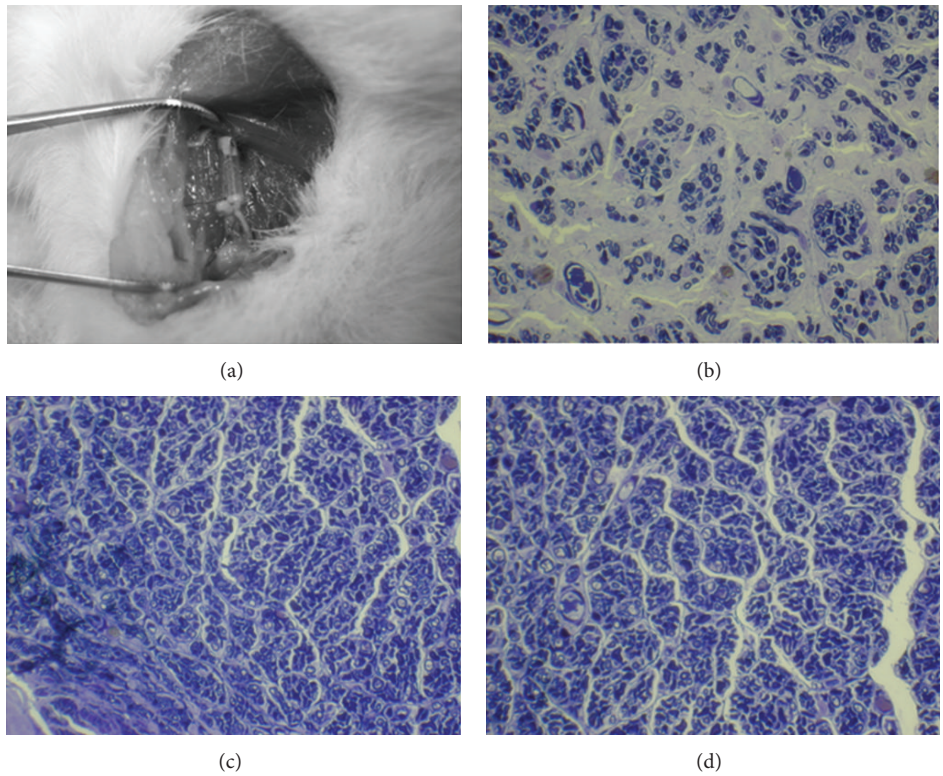

Figure 1: The sampling of median nerve from the rat (a) and light micrographs of the regenerated nerve cross sections of control (b); acupunctured (c), and electrical stimulation plus acupunctured (d) rats.

2.5. Grasping Test Analyses. The analyzing system of a rats' grasp pattern by recording their grip power of the forepaw movements has been well established and widely employed for the assessment of motor nerve recovery after median nerve injury. In this study, a grasp methodology was designed by modifying that of Bertelli and Mira to assess the forelimb median nerve function of the rat [14]. Briefly, a mesh pull-bar assembly was placed via a threaded adaptor to a digital force gauge. The mesh was 8 cm × 15 cm inches with 2.5 square grids. The bars of the grids were 8 mm thick. The rats were gently lifted by holding their tails and then lowered toward the mesh and continued while the body was in a line where forepaw catch can reach for the mesh. When the digits of the forepaw had grasped the mesh, the rat was rapidly pulled vertically away from the mesh in a smooth and constant motion. The rats would hold onto the mesh until they can no longer resist the pull. When the grasp was broken, the report from the gauge was recorded as the grasp strength (Kgw, Newton). When the rats grasp the mesh, a digital video camera (Sony TCR19) was used to record their forelimb grasp movements. These movements were calculated three times, and the average of the measurements was taken. The measurements of the bilateral hands at 6 weeks postoperatively were recorded. All the measurements were done by the same observer and data expressed as mean ± SD.

2.6. Statistical Analysis. Statistical comparisons between groups were made by the one-way analysis of variance (SPSS 16.0). The Turkey test was then used as post hoc test.

3. Results

To focus on investigating the influence of acupuncture and electroacupuncture on the regenerative process, all other confounding factors, such as carious acupoints, permeability of biomaterial, surface morphology, and electrical properties, were eliminated by using nondegradable silicone rubber as the guide channel. After an implantation time of 5 weeks, the silicone conduit, together with the regenerated nerves in it, was then retrieved from the rats and evaluated. Swelling or deformation of the silicone tubes was not obvious, and no nerve dislocation was seen in all the investigated rats. It was found that the regenerated nerve, which was surrounded by fluid, occupied a central location within the tube (Figure 1(a)). Rough examination of the silicone rubber chambers revealed 100% rates of successful nerve regeneration in all the three groups (A: control, B: acupuncture, and C: electroacupuncture groups) with the animals exhibiting a regenerated nerve cable across the 5 mm gap. Figures 1(b)–1(d) showed representative cross sections of nerve specimen retrieved from the A (Figure 1(b)), B (Figure 1(c)), and C (Figure 1(d)) groups. The influence of acupuncture and electroacupuncture on the regeneration of the nerve will be investigated from three angles: nerve morphology, nerve electrophysiology, and integrate function of nerve-recovered grasping capacity.

First, the morphometry examined with quantification helped us to understand the alterations of nerve regeneration and the effects of acupuncture and electroacupuncture on

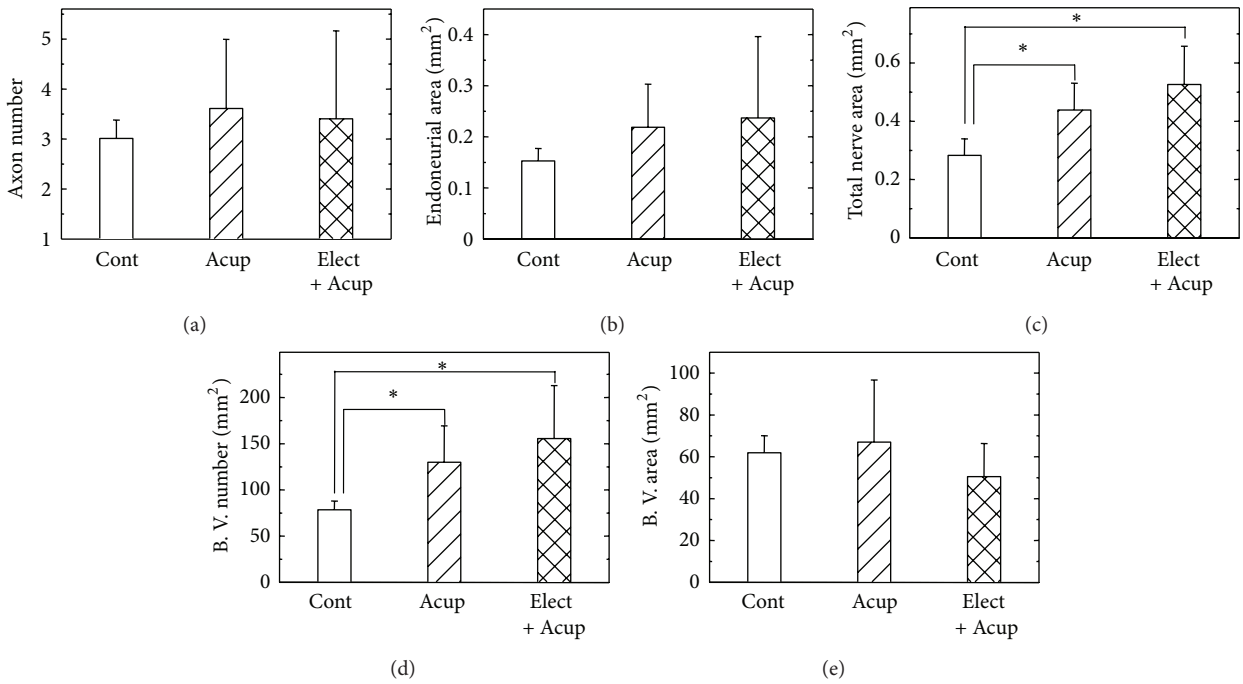

Figure 2: Morphometric analysis from the regenerated nerves in the chambers receiving electrical stimulation at different current intensities, including axon number (a), endoneurial area (b), total nerve area (c), blood vessel number (d), and blood vessel area (e). Cont: untreated control group; Acup: acupuncture group; Elect + Acup: electroacupuncture group. *Statistically different compared with the control group, $P < 0.05$.

Table 1: The morphometric, electrophysiological, and grasping analysis of the influences of acupuncture and electroacupuncture on nerve regeneration.

Measuring index	Control	Acupuncture	Electroacupuncture
Morphometric analysis			
Axon number#	3009 ± 977	3612 ± 1381	3404 ± 1528
Endoneurial area (mm^2)	0.15 ± 0.06	0.22 ± 0.09	0.24 ± 0.15
Total nerve area (mm^2)	0.28 ± 0.15	0.40 ± 0.17*	0.52 ± 0.17*
B. V. number#	78 ± 25	130 ± 39*	154 ± 63*
B. V. area (μm^2)	62 ± 21	67 ± 30	51 ± 17
Electrophysiological analysis			
Latency (ms)	5.11 ± 0.8	4.39 ± 1.02	4.69 ± 0.57
Amplitude (mv)	12.49 ± 1.31	12.82 ± 3.67	16.50 ± 3.18*
MAP area (mvms)	16.41 ± 2.96	15.54 ± 5.57	21.85 ± 5.17*
NCV (m/s)	24.07 ± 1.3	24.97 ± 4.55	27.44 ± 5.58
Grasping analysis			
Right paw (healthy)	100.26 ± 30.94	47.45 ± 18.66*	39.80 ± 12.33*
Left paw (injured)	20.51 ± 5.80	23.31 ± 14.44	29.74 ± 6.86*

*$P < 0.05$ compared with the control group; B. V.: blood vessel; MAP: muscle action potential; NCV: nerve conductive velocity.
#Cell number.

nerve regeneration (Figure 2). The indexes included the mean values of axon number, endoneurial area, total area, blood vessel number, and blood vessel area, which were positively indexes for better regeneration. In the results, we can find that in the acupuncture and electroacupuncture groups, the total nerve areas and blood vessel numbers were larger than those in the control group ($P < 0.05$). Also, all the other indexes in the acupuncture and electroacupuncture groups seemed to be slightly higher than those in the controls, except the areas of blood vessel in the electroacupuncture group (Figure 2 and Table 1).

Second, we were interested in the effects of acupuncture and electroacupuncture on the reconstruction of nerve virtue electrofunction. To estimate the effect from multiple approaches, the MAP indexes included the latency, the amplitude, the MAP area, and the NCV as described in Section 2.

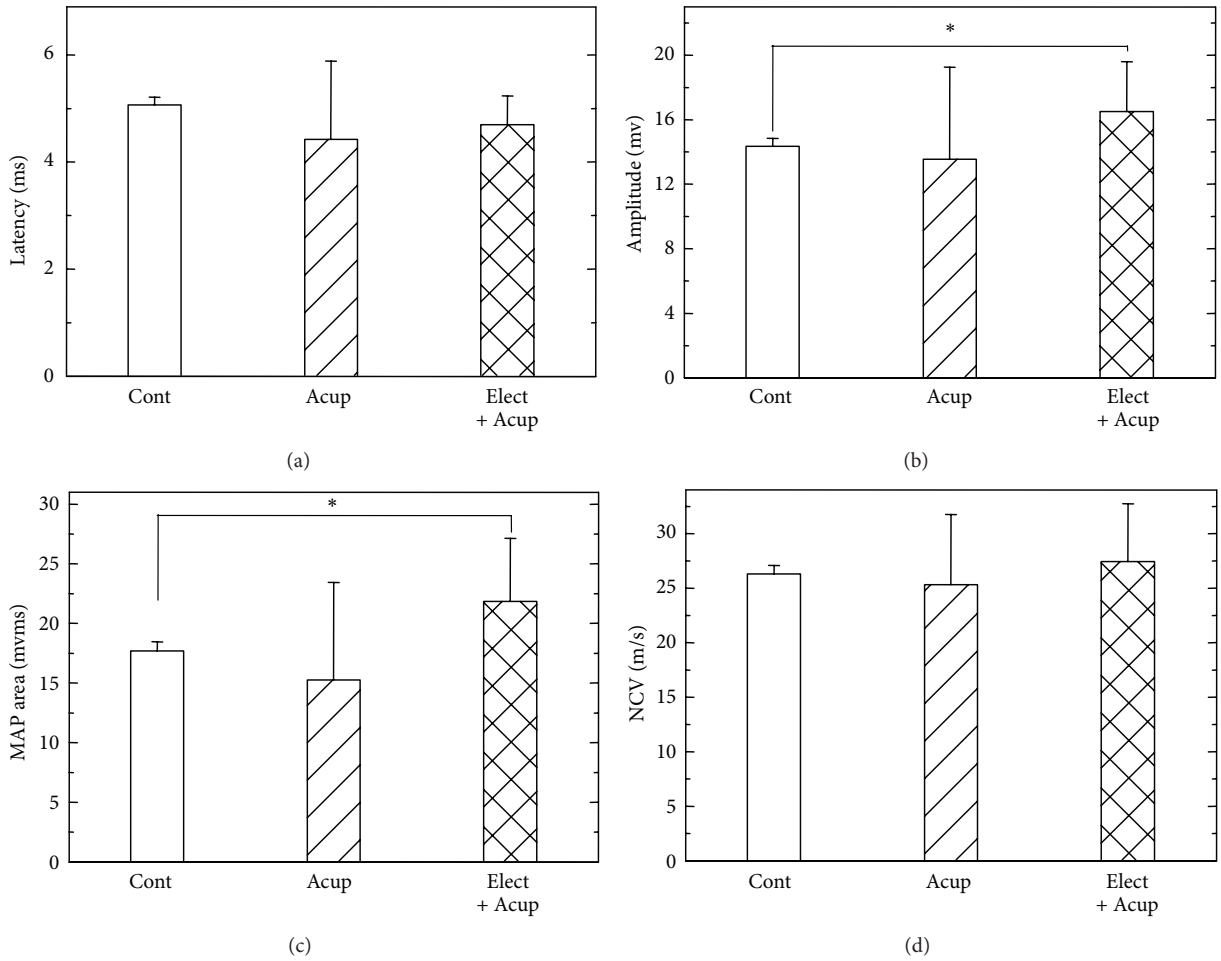

Figure 3: Electrophysiological analysis of the evoked MAPs, including latency (a), amplitude (b), area under the MAP curves (c), and NCV (d). Cont: untreated control group; Acup: acupuncture group; Elect + Acup: electroacupuncture group. *Statistically different compared with the control group, $P < 0.05$.

As for the MAP indexes, the regenerated nerves treated with electrical stimulation in addition to acupuncture had relatively larger amplitude and larger MAP area compared with the controls (Figure 3). The latency was slightly shorter, and the NCV was slightly faster. As for the acupuncture group, the effects were too small to make any difference in the electrophysiological measurements (Figure 3 and Table 1).

Finally, we investigated the integrate function of nerve regeneration by analyzing the recovered grasping capacity (Figure 4). In the design, we had measured not only the grasping capacity of the injured left paw but also the healthy right paws as well. The results showed that in the control group, the injured paw had regained only 39.6% of the original strength after nerve regeneration. In the other two groups, acupuncture and electroacupuncture improved the recovery rates up to 45% and 57.4%, respectively. Obviously, the electroacupuncture treatment had a better and significant improvement compared with the controls while grasping the mesh ($P < 0.05$).

4. Discussion

It is believed that acupuncture and electroacupuncture would do well to ameliorate nerve regeneration and movement function recovery. However, there is very few evidence available to support this theory. In the previous literature, it has been reported that low frequency electroacupuncture and acupuncture could improve sciatica nerve regeneration [10, 12, 15–17]. Koppes et al. indicated that alternation of neurite growth could be manipulated by extracellular direct current [18]. The in vitro nerve growth promoting effects of electrical stimulation have also been demonstrated with the in vivo experiments showing that nerve regeneration could be enhanced by applying direct current to the sciatic nerve of rats as the cathode was placed toward the distal end of the injured nerve conduits. Zhang et al. provided the peripheral nerve regeneration with a definite theory stating that the nerve's successful rate was decided via the balance of contact guidance substance, basement microtube

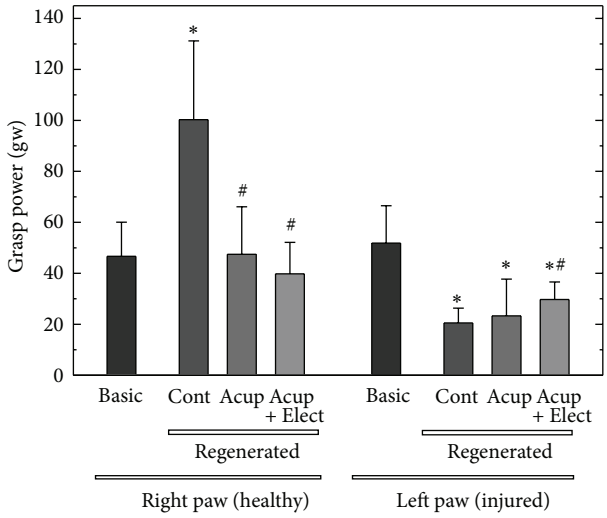

Figure 4: Functional analysis of the grasping power from the right (healthy) and left (injured) paws of the rats. Cont: untreated control group; Acup: acupuncture group; Elect + Acup: electroacupuncture group. *Statistically different compared with the basic (intact) group, $P < 0.05$; #statistically different compared with the control group, $P < 0.05$.

formation, neurotrophic factor, and contractile fibroblast capsule [19, 20]. McCaig et al. revealed that electroacupuncture could stimulate two cascade pathways: one was related to the activation of phospho-inositide-3 kinase (PI-3K) and phospholipase C (PLC); the other is to trigger laminin to secret integrins [21]. At the same time, the electroacupuncture could lead to an increase of calcium concentration and consequently an increase in the concentration of cAMP and cAMP-dependent protein kinase A, which would promote nerve regeneration [21]. It has also been explored that placing direct current at the cathode would form adhesion-associated proteoglycan to accelerate nerve regeneration [22]. In our previous researches in which we studied injured nerves related to the hindlimbs, we recognized that acupuncture and electroacupuncture could accelerate the maturity of regenerated nerves with larger mean values of axon number, endoneurial area, blood vessel number, and blood vessel area as compared with the controls [13, 23]. This was similar to our current study of the injured median nerve related to the forelimbs. The electroacupuncture could significantly improve the overall recovery at the indexes of the enlarged total nerve area, blood vessel numbers, nerve amplitude, and MAP area. Most importantly, electroacupuncture could help our rats to regain grasping power (Figures 2–4 and Table 1). However, in our current study, the effects of acupuncture were only significant in the increasing of the total nerve area and blood vessel numbers.

Chen et al.'s and Lu et al.'s studies revealed that acupuncture and electroacupuncture increase regenerated nerve Schwann cell proliferation and provide blood supply for treatments. Some investigators had pointed out that when the nerve was transacted, the electrical stimulation would help blood reconstruction via somatic/autonomic reflex arc to provide enough blood flow for the regenerated nerve [11, 13]. In our study, the effects of acupuncture and electroacupuncture on blood vessel reconstruction were not as obvious as the previous findings, which may also be due to the different targets that were investigated. In his experiment, Bertelli and Mira first used the median nerve model and grasp test for the evaluation of functional median nerve recovery [12, 14]. As a result, the regenerated nerves treated with electroacupuncture had relatively shorter latency, larger amplitude, and larger MAP area as compared with the controls. These results indicated that the transected nerves receiving acupuncture and electroacupuncture have undergone an enhanced regeneration with more mature nerve fibers that have reinnervated the muscle fibers [12, 14]. Although it is uncertain whether electrical stimulation promotes an outgrowth of neural components in developing nerves, the movement function-improving capability of electrical stimulation on regenerated nerves is obvious. The kinematic grasp analysis to median nerve function evaluation is usually designed to assess individual upper motor functions, which can prevent the interference of compensatory movements from healthy limbs. However, in previous designs, the healthy limb's function was not measured simultaneously as ours. It is interesting to find that the rats in the control group depended so much on the healthy right paw that the grasping strength could reach almost twice as much as the other groups after the duration of the nerve regeneration (Figure 4). More interestingly, the rats in the acupuncture and electroacupuncture groups exhibited better balance and coordination between their left and right limbs. In other words, the acupuncture and the electroacupuncture treatment would do more benefit to enhance the injured forepaw grasp strength but reduce the dependency on the healthy forelimb than the control groups. It is promising that median nerve injured patients receiving acupuncture and electroacupuncture treatment may recover faster and better and may regain a bilateral balance of normal life.

This study provides a better strategy to assist the recovery of nerve-injured patients in clinical practices. However, there is still much work to be done before this practice can be performed in a real setting. These include an overall examination of the various types of electrical stimulation (continuous or pulsed), meridian acupoints, the stimulation parameters, the sites for the placement of electrodes, and most importantly the length of the nerve gap, which may affect the efficacy of electrical stimulation on nerve regeneration. Our animal models provide a platform for further studies on establishing a palette of electrical stimulation with different stimulus combinations and an efficient multiapproach examination for figuring out the optimal way to promote the growth of the regenerating nerves.

5. Conclusions

The current study provides evidence indicating that traditional acupuncture and electroacupuncture have potential rehabilitating effects on the regeneration of the dissected median nerves from the angles of morphology, electrophysiology, and grasping function.

Conflict of Interests

All the authors state that they have no conflict of interests.

Acknowledgments

The study is supported by the Grant of China Medical University Hospital (DMR-102-066). The authors sincerely thank Miss Du for the expert assistance in nerve surgery.

References

[1] S. F. Swaim, "Peripheral nerve surgery," in *VeterInary Neurology*, J. E. Oliver, B. F. Hoerlein, and I. G. Mayhew, Eds., pp. 493–512, WB Saunders, Pennsylvania, Pa, USA, 1987.

[2] E. N. Bontioti, M. Kanje, and L. B. Dahlin, "Regeneration and functional recovery in the upper extremity of rats after various types of nerve injuries," *Journal of the Peripheral Nervous System*, vol. 8, no. 3, pp. 159–168, 2003.

[3] J.-L. Shen, Y.-S. Chen, J.-Y. Lin et al., "Neuron regeneration and proliferation effects of danshen and tanshinone IIA," *Evidence-Based Complementary and Alternative Medicine*, vol. 2011, Article ID 378907, 9 pages, 2011.

[4] Y.-C. Lee, T.-M. Li, C.-Y. Tzeng et al., "Electroacupuncture at the Zusanli (ST-36) acupoint induces a hypoglycemic effect by stimulating the cholinergic nerve in a rat model of streptozotocine-induced insulin-dependent diabetes mellitus," *Evidence-Based Complementary and Alternative Medicine*, vol. 2011, Article ID 650263, 6 pages, 2011.

[5] Y. Piao and X. Liang, "Chinese medicine in diabetic peripheral neuropathy: experimental research on nerve repair and regeneration," *Evidence-Based Complementary and Alternative Medicine*, vol. 2012, Article ID 191632, 13 pages, 2012.

[6] P. H. Gorman, "An update on functional electrical stimulation after spinal cord injury," *Neurorehabilitation and Neural Repair*, vol. 14, no. 4, pp. 251–263, 2000.

[7] R. K. Shields and S. Dudley-Javoroski, "Musculoskeletal adaptations in chronic spinal cord injury: effects of long-term soleus electrical stimulation training," *Neurorehabilitation and Neural Repair*, vol. 21, no. 2, pp. 169–179, 2007.

[8] A. A. Al-Majed, C. M. Neumann, T. M. Brushart, and T. Gordon, "Brief electrical stimulation promotes the speed and accuracy of motor axonal regeneration," *Journal of Neuroscience*, vol. 20, no. 7, pp. 2602–2608, 2000.

[9] M. Inoue, T. Hojo, T. Yano, and Y. Katsumi, "The effects of electroacupuncture on peripheral nerve regeneration in rats," *Acupuncture in Medicine*, vol. 21, no. 1-2, pp. 9–17, 2003.

[10] C. H. Yao, R. L. Chang, S. L. Chang, C. C. Tsai, F. J. Tsai, and Y. S. Chen, "Electrical stimulation improves peripheral nerve regeneration in streptozotocin-induced diabetic rats," *Journal of Trauma and Acute Care Surgery*, vol. 72, no. 1, pp. 199–205, 2012.

[11] Y. S. Chen, C. L. Hu, C. L. Hsieh et al., "Effects of percutaneous electrical stimulation on peripheral nerve regeneration using silicone rubber chambers," *Journal of Biomedical Materials Research*, vol. 57, no. 4, pp. 541–549, 2001.

[12] J. A. Bertelli and J. C. Mira, "Behavioral evaluating methods in the objective clinical assessment of motor function after experimental brachial plexus reconstruction in the rat," *Journal of Neuroscience Methods*, vol. 46, no. 3, pp. 203–208, 1993.

[13] M. C. Lu, C. Y. Ho, S. F. Hsu et al., "Effects of electrical stimulation at different frequencies on regeneration of transected peripheral nerve," *Neurorehabilitation and Neural Repair*, vol. 22, no. 4, pp. 367–373, 2008.

[14] J. A. Bertelli and J. C. Mira, "The grasping test: a simple behavioral method for objective quantitative assessment of peripheral nerve regeneration in the rat," *Journal of Neuroscience Methods*, vol. 58, no. 1-2, pp. 151–155, 1995.

[15] Y. S. Chen, C. H. Yao, T. H. Chen, C. L. Hsieh, C. J. Lao, and C. C. Tsai, "Effect of acupuncture stimulation on peripheral nerve regeneration using silicone rubber chambers," *American Journal of Chinese Medicine*, vol. 29, no. 3-4, pp. 377–385, 2001.

[16] J. Huang, L. Lu, J. Zhang et al., "Electrical stimulation to conductive scaffold promotes axonal regeneration and remyelination in a rat model of large nerve defect," *PLoS ONE*, vol. 7, no. 6, Article ID e39526, 2012.

[17] F. Liang, R. Chen, and E. L. Cooper, "Neuroendocrine mechanisms of acupuncture," *Evidence-Based Complementary and Alternative Medicine*, vol. 2012, Article ID 792793, 2 pages, 2012.

[18] A. N. Koppes, A. M. Seggio, and D. M. Thompson, "Neurite outgrowth is significantly increased by the simultaneous presentation of Schwann cells and moderate exogenous electric fields," *Journal of Neural Engineering*, vol. 8, no. 4, Article ID 046023, 2011.

[19] M. Zhang and I. V. Yannas, "Peripheral nerve regeneration," *Advances in Biochemical Engineering/Biotechnology*, vol. 94, pp. 67–89, 2005.

[20] I. V. Yannas, M. Zhang, and M. H. Spilker, "Standardized criterion to analyze and directly compare various materials and models for peripheral nerve regeneration," *Journal of Biomaterials Science, Polymer Edition*, vol. 18, no. 8, pp. 943–966, 2007.

[21] C. D. McCaig, A. M. Rajnicek, B. Song, and M. Zhao, "Has electrical growth cone guidance found its potential?" *Trends in Neurosciences*, vol. 25, no. 7, pp. 354–359, 2002.

[22] B. Pomeranz and J. J. Campbell, "Weak electric current accelerates motoneuron regeneration in the sciatic nerve of ten-month-old rats," *Brain Research*, vol. 603, no. 2, pp. 271–278, 1993.

[23] M. C. Lu, C. C. Tsai, S. C. Chen, F. J. Tsai, C. H. Yao, and Y. S. Chen, "Use of electrical stimulation at different current levels to promote recovery after peripheral nerve injury in rats," *Journal of Trauma*, vol. 67, no. 5, pp. 1066–1072, 2009.